

Numerical Studies on Groundwater Flow in Coastal Aquifers

Dissertation
zur Erlangung des
Doktorgrades der Naturwissenschaften
im Fachbereich Geowissenschaften
der Universität Bremen

vorgelegt von
Tomas Feseker

Bremen

2004

Dank

Besonders möchte ich mich bei Herrn Prof. Dr. Horst D. Schulz für die Betreuung der Arbeit, die stets freundliche Unterstützung und nicht zuletzt für seine Geduld bedanken. Herrn Prof. Dr. Michael Schlüter danke ich für die freundliche Übernahme des zweiten Gutachtens und den Ansporn in der Endphase dieser Arbeit.

Ein besonderer Dank gilt Dr. Martin Kölling und Dr. Sabine Kasten für Ihre stete Diskussions- und Hilfsbereitschaft.

Bei allen Kollegen aus dem Doktorandenkolleg Nordseeküste, die die letzten Jahre nicht nur fachlich bereichert haben, möchte ich mich herzlich bedanken. Ein spezielles Dankeschön gilt Dr. Jens Dannenberg, mit dessen Hilfe sich so mancher Knoten im Hirn leichter lösen ließ.

Für zahlreiche sprachliche Korrekturen und Anregungen zum ersten Teil der Arbeit bedanke ich mich bei Dr. Antje Weitz.

Ganz besonders möchte ich meinen Eltern danken, die mich während meiner gesamten Studienzzeit in jeder Hinsicht unterstützt haben.

Ein riesengroßes Dankeschön gilt meiner Frau Gudrun Tegeder, die immer da war, wenn die Gefahr bestand, daß ich mich im Grundwasser auflöse.

Preface

This study was conducted as part of an interdisciplinary research project on sustainable use of the coastal region in north-western Germany (“Doktorandenkolleg Lebensraum Nordseeküste”) funded by the University of Bremen. This work is submitted as a dissertation and has been supervised by Prof. Dr. Horst D. Schulz. The thesis consists of five separate manuscripts which have either been published, or submitted for publication in international journals or on the internet. Their thematic context as well as a brief introduction into the subject of groundwater flow in coastal aquifers is given in an introductory chapter.

The first part of the thesis consists of the user’s guide to a new computer program for simulating density-dependent groundwater flow which was developed in the context of this study. Both the software “SWIMMOC” and the user’s guide is available on the internet. The second part describes a study that was conducted in co-operation with Jens Seeberg-Elverfeldt, who participated in the field work and provided the laboratory results in the context of his diploma thesis. The third manuscript presents an application of the new density-dependent flow model. The fourth and the fifth part of the thesis are the user’s guide to a new computer program for visualizing groundwater flow to a well and a short description of the application to a well in Portugal. The software was developed during a stay as guest scientist at the Laboratório Nacional de Engenharia Civil (LNEC) in Lisbon, Portugal. My own contribution consists of the development of the software and authorship of the user’s guide and the publication “Delineation of wellhead-protection zones: a simplified approach”, which was published in an international newsletter on coastal research. Dr. João Paulo Lobo Ferreira inspired and supervised the work. The software “WellFlow” and the user’s guide will be available on the internet.

Contents

1	Introduction	1
I	User's Guide to SWIMMOC	5
2	Introduction	9
3	Density-dependent groundwater flow	11
3.1	Pressure head and piezometric head	11
3.2	Darcy's law	12
3.3	Density differences	14
3.4	Leakage and drainage	16
3.5	The groundwater flow equation	18
4	Numerical solution of the flow equation	21
4.1	Method of finite differences	21
4.2	Explicit solution	27
4.3	Implicit solutions	27
4.3.1	Convergence condition for iteration methods	29
4.3.2	Jacobi method	29
4.3.3	Gauss-Seidel method	30
4.3.4	Iterative Alternating Direction Implicit method (IADI) .	30
4.3.5	Thomas algorithm	33

5	Solute transport	37
5.1	Advection	37
5.2	Dispersion	38
5.3	Diffusion	41
5.4	Solute mass flux at sources and sinks	42
5.5	Transport equation	43
6	Method of characteristics	47
6.1	Particle tracking	49
6.1.1	Linear interpolation	51
6.1.2	Bilinear interpolation	55
6.1.3	Concentration after advection	56
6.1.4	Redistributions	58
6.2	Dispersion, diffusion, sources and sinks	58
6.2.1	Mean effective porosity	61
6.2.2	Velocity components at cell faces	61
6.2.3	Concentration gradients at cell faces	63
6.2.4	Concentration changes at the nodes	64
6.3	Determination of the transport time step	66
6.3.1	Travel distance criterion	66
6.3.2	Neumann-criterion	67
6.3.3	Source criterion	68
7	Coupling flow and transport	69
7.1	Conversion from concentration to density	69
7.2	Simulation process	70

8	Initial values and boundary conditions	73
8.1	Initial values	73
8.2	Definition of boundary conditions	74
8.2.1	No-flow boundaries	74
8.2.2	Constant observed head boundary	75
8.2.3	Constant concentration boundary	75
8.2.4	Constant flux boundary	75
8.2.5	Leakage boundary	76
8.3	Particle tracking at boundaries	76
8.3.1	Reflection at no-flow boundaries	77
8.3.2	Replacing and removing particles at sources and sinks	78
9	Accuracy of the simulation	83
9.1	Water balance	83
9.2	Solute mass balance	86
9.3	Numerical instabilities	90
10	Observation points	93
10.1	Shepard's method of inverse distance interpolation	93
10.2	Bilinear interpolation of concentration values	94
11	Review of assumptions	97
12	Introduction to SWIMMOC	99
12.1	Overview of the general program features	99
12.2	The File-menu	100
12.3	The Edit-menu	101
12.4	The Model-menu	101
12.5	The Units-menu	102
12.6	The Boundaries-menu	102
12.7	The Parameters-menu	103

CONTENTS

12.8	The View-menu	104
12.9	The Simulation-menu	104
12.10	The Evaluation-menu	105
13	Numerical solution of the Henry problem	107
13.1	Step 1: Creation of the model grid	109
13.2	Step 2: Specification of the aquifer properties	109
13.3	Step 3: Definition of the boundary conditions	110
13.4	Step 4: Specification of the initial values	110
13.5	Step 5: Specification the simulation options	111
13.6	Step 6: Running the simulation	112
13.7	Step 7: Evaluation of the simulation results	112
13.8	Numerical solution of the modified Henry problem	114
13.9	Comparison of the simulation results	117
14	Summary	119
II	Streambed hydraulic conductivity	121
15	In-situ measurement of low streambed hydraulic conductivity	123
15.1	Introduction	123
15.2	Materials and methods	124
15.2.1	Grain size analysis	124
15.2.2	In-situ tests	125
15.3	Results	131
15.3.1	Estimated hydraulic conductivity values based on the grain size distribution	131
15.3.2	Results of the in-situ tests	133
15.3.3	Comparison of the results	134
15.4	Discussion	137
15.5	Conclusions	140

III	Numerical studies on saltwater intrusion	141
16	Numerical studies on saltwater intrusion in a coastal aquifer in north-western Germany	143
16.1	Introduction	143
16.1.1	Geology	144
16.1.2	Hydrogeology	145
16.2	Method	148
16.2.1	Conceptual model of a representative cross-section	148
16.2.2	Numerical model	149
16.3	Results	152
16.3.1	Sensitivity analysis	155
16.4	Discussion	161
16.5	Conclusion	162
IV	Modeling Groundwater Flow to a Well	165
17	Introduction	169
17.1	Wellhead protection areas	170
18	Groundwater flow to a well	173
18.1	Wells in single layer systems	173
18.1.1	Unconfined aquifer settings	173
18.1.2	Confined aquifer settings	174
18.1.3	Analytical solutions for single aquifer settings	174
18.2	Wells in multi-layer systems	177
18.2.1	Three-layer aquifer settings	177
18.2.2	Analytical solutions for three-layer aquifer settings	177
18.2.3	Settings with more than three layers	178

19 Modeling groundwater flow to a well	181
19.1 Concept of modeling axisymmetric flow	181
19.2 Grid design	182
19.3 Finite differences flow equation	182
19.4 Calculating times of travel	188
20 The computer program WellFlow	193
20.1 Input data	193
20.1.1 Hydrogeological units	193
20.1.2 Well properties	194
20.1.3 Model properties	194
20.1.4 Loading and saving input data sets	195
20.2 Simulation	195
20.3 Evaluation	196
21 Examples	197
21.1 Example A: Single confined aquifer	197
21.2 Example B: Single unconfined aquifer	198
21.3 Example C: Three-layer aquifer system	199
22 Summary	203
V Delineation of wellhead protection zones	205
23 Delineation of wellhead protection zones – A simplified approach	207
23.1 Introduction	207
23.2 Problem definition	208
23.3 Concepts of modeling axisymmetric flow	208
23.4 The computer program “WellFlow”	209
23.5 Application of WellFlow – A case study	209
23.6 Conclusion	210

References

213

CONTENTS

List of Figures

3.1	Pressure head and piezometric head	13
3.2	Equivalent freshwater head	15
3.3	Leakage and drainage	18
4.1	Spatial discretization of the cross-section	22
4.2	Flow chart of the iteration process	26
4.3	Iterative Alternating Direction Implicit (IADI) scheme	32
5.1	Dispersion	38
6.1	Numerical dispersion	48
6.2	Initial distribution of tracer points	50
6.3	Linear particle tracking	54
6.4	Bilinear interpolation	57
6.5	Concentration gradients at cell faces	65
7.1	Simulation flow chart	71
8.1	Reflection of particles at no-flow boundaries	77
8.2	Particle replacement in source cells adjacent to no-flow boundaries	79
8.3	Particle replacement in internal source cells	80
8.4	Strong and weak sinks	81
13.1	Geometry and boundary conditions of the Henry problem	108
13.2	Mass accumulation for the standard Henry problem	113

LIST OF FIGURES

13.3	Concentration distribution for the standard Henry problem . . .	115
13.4	Observed piezometric heads and equivalent freshwater heads for the standard Henry problem	116
13.5	Comparison of the simulation results for the standard Henry problem using different grid resolutions	117
13.6	Mass accumulation during the simulation of the modified Henry problem	118
13.7	Comparison of numerical and semi-analytical solutions for the modified Henry problem	118
15.1	Measuring device for in-situ tests	127
15.2	Location of the test site	132
15.3	Grain size distribution	133
15.4	Water level in the measuring tube versus time	135
15.5	Time versus the natural logarithm of the corresponding ratio of hydraulic heads	137
15.6	Comparison of estimated and measured values of hydraulic con- ductivity	138
15.7	Relation of uniformity and estimated hydraulic conductivity . .	138
16.1	Location of the Coastal Aquifer Test-field (CAT-field)	145
16.2	Characteristic structures of the post-Permian geology in north- western Germany	146
16.3	Conceptual model of a representative cross-section through the upper aquifer	149
16.4	Model grid, subdomains, and boundary conditions	151
16.5	Solute mass accumulation during the progression of the saltwa- ter intrusion	153
16.6	Hypothetical steady-state position of the saltwater / freshwater interface	154
16.7	Drainage rates for the hypothetical steady-state condition	155
16.8	The effect of reduced recharge on the position of the saltwater / freshwater interface	156
16.9	The effect of increased recharge on the position of the freshwa- ter/saltwater interface	157

16.10	Drainage rates for reduced and increased groundwater recharge .	158
16.11	The effect of lowering the drainage level on the position of the freshwater/saltwater interface	159
16.12	The effect of a sea level rise on the position of the freshwa- ter/saltwater interface	160
16.13	Drainage rates for the lowered drainage level and for sea level rise	161
17.1	Wellhead protection areas	170
18.1	Well in an unconfined aquifer	173
18.2	Well in a confined aquifer	174
18.3	Thiem equation	176
18.4	Well in a three-layer aquifer system with downward leakage . . .	178
18.5	Well in a three-layer aquifer system with upward leakage	179
19.1	Axisymmetric flow to a well	182
19.2	Discretization of the cross-section for modeling	183
19.3	Steady-state balance of flows	184
19.4	Pattern of known hydraulic heads and velocity components in the grid	187
19.5	Linear particle tracking	191
21.1	Comparison of the simulation results for example A and the analytical solution	198
21.2	Comparison of the simulation results for example B and the analytical solution	199
21.3	Time of travel contours for example C - I	201
21.4	Time of travel contours for example C - II	202
23.1	50 days isochronal line for a well in Ramalhal, Portugal	211

LIST OF FIGURES

List of Tables

4.1	Single index numbering of the grid cells	28
13.1	Parameters for the standard Henry problem	108
13.2	Grid definition for the Henry problem	109
15.1	Values of the proportionality factor used to estimate the hydraulic conductivity from the grain size distribution	125
15.2	Estimated values of hydraulic conductivity using the grain size distribution	134
15.3	Values of hydraulic conductivity measured in-situ	136
16.1	Model subdomains	150
16.2	Boundary conditions used to obtain a steady-state position of the freshwater/saltwater interface	153
21.1	Parameters for defining the aquifer in example A	197
21.2	Sequence of hydrogeological layers in example C	200

LIST OF TABLES

Chapter 1

Introduction

The coastal regions are the most densely populated areas in the world. *Cohen et al.* (1997) estimate that in 1994, more than one third of the world's population lived within 100 km of a coastline. At the same time, the coastal regions provide about one third of the world's ecosystem services and natural capital (*Costanza et al.*, 1997). In order to preserve this valuable and unique biosphere for future generations, it is important to understand the effects of climate change and human interference in order to ensure the sustainable use of coastal resources. The growth of human settlements is accompanied by an increasing demand for water supply and excessive drainage for land reclamation purposes. Expected climate changes will additionally influence the coastal groundwater system. As a consequence, the coastal groundwater resources are increasingly threatened by over-exploitation, pollution and saltwater intrusion.

The phenomenon of seawater intrusion in coastal aquifers was first observed by *Badon Ghijben and Drabbe* (1889) during the exploration of groundwater resources close to Amsterdam, The Netherlands. Several years later, *Herzberg* (1901) described saline groundwater on German islands in the North Sea. *Badon-Ghijben* and *Herzberg* independently developed an equation that expresses the depth of the freshwater/saltwater interface below sea level as a function of the elevation of the groundwater table above sea level:

$$h_s = \frac{\rho_f}{\rho_s - \rho_f} h_f \quad (1.1)$$

where

h_s is the depth of the freshwater/saltwater interface below sea level,

ρ_f is the density of freshwater,

ρ_s is the density of saltwater, and

h_f is the elevation of the groundwater table above sea level.

Due to the density difference between freshwater and saltwater, the freshwater experiences a buoyancy force and floats on top of the saltwater. Consequently, saltwater intrusion is a natural process that results from the equilibration of pressures in the ocean and in the adjacent coastal aquifer. However, the assumption of a steady-state of equilibrium implies that equation (1.1) can greatly underestimate or overestimate the thickness of freshwater in case of non-hydrostatic conditions (*Izuka and Gingerich, 1998*). Furthermore, the presence of a brackish transition zone between saltwater and freshwater which results from dispersive and diffusive mixing is neglected.

In order to correctly describe the pattern of groundwater flow and the salt distribution in coastal aquifers, numerical modeling is required. In the context of this study, the two-dimensional density-dependent groundwater flow model SWIMMOC was developed. SWIMMOC can be used to analyze groundwater flow at variable densities in vertical cross-sections and to compute the salt transport in aquifers. The program is especially suited to simulate groundwater flow in coastal aquifers. The first part of this thesis consists of the user's guide to SWIMMOC and introduces the concepts of modeling density-dependent groundwater flow. The hydrogeological and numerical background of the software are explained in detail and examples are presented.

How accurately a numerical model represents a situation observed in the field always depends on the quality of the input parameters. In the course of the study, it soon turned out that the exchange of water between the aquifers and drainage networks in marsh areas is an important process that influences saltwater intrusion. Therefore, a new method was developed for accurately measuring the hydraulic conductivity of the drainage channel streambeds in-situ, which is described in the second part of this thesis. The new measuring technique was applied successfully on a section of a drainage channel close to the city of Cuxhaven in north-western Germany.

The measured values were directly included into simulations of the freshwater/saltwater interface in a coastal aquifer in north-western Germany, which are presented in the third part of this thesis. Saltwater intrusion into a representative aquifer is modeled and the effects of climate changes and land reclamation are investigated.

A different aspect of groundwater protection is considered in the fourth and fifth part of this thesis. The European Water Framework directive demands the delineation of wellhead protection area to protect wells that are used for public drinking water supply. For most of the required protection areas, the boundaries are defined by the time it takes for groundwater to reach the well. Consequently, the groundwater velocity field and the streamlines in the vicinity of the well must be calculated. The computer program WellFlow was developed to visualize the path of particles flowing to a well and to calculate the corresponding times of travel. Since WellFlow is based on an axisymmetric approach, the program is especially useful for wells in coastal regions, which are commonly characterized by very small regional hydraulic gradients. The

fourth manuscript consists of the user's guide to WellFlow, which explains the background of axisymmetric flow modeling and presents a number of simple examples. The fifth part is a brief description of the new computer program and includes the results of an application of WellFlow to a well in Ramalhal, Portugal.

Part I

A Saltwater Intrusion Model Based on the Method of Characteristics – User's Guide to SWIMMOC

License

The computer program SWIMMOC is free software. It can be redistributed and/or modified under the terms of the GNU General Public License as published by the Free Software Foundation; either version 2 of the license, or (at your option) any later version. This program is distributed in the hope that it will be useful, however, it comes WITHOUT ANY WARRANTY. The software does not even hold the implied warranty of MERCHANTABILITY or FITNESS FOR A PARTICULAR PURPOSE. See the GNU General Public License for more details.

An electronic copy of the GNU General Public License should be included with the copy of the program. In case it is missing, write to the Free Software Foundation, Inc., 59 Temple Place - Suite 330, Boston, MA 02111-1307, USA.

Software Availability

The RealBasic source code of the computer program SWIMMOC as well as precompiled executables can be downloaded from <http://www.geochemie.uni-bremen.de>.

Chapter 2

Introduction

A variety of numerical models for the simulation of density-dependent groundwater flow have been developed during the past two decades. In general, three different approaches can be distinguished: finite-elements models (e.g. SUTRA by *Voss*, 1987), finite-differences models (e.g. SEAWAT by *Guo and Langevin*, 2002), and models based on the method of characteristics (e.g. MOC DENSE by *Sanford and Konikow*, 1985). *Oude Essink* (1996) evaluated and discussed these three different approaches with respect to their ability to simulate the groundwater flow in coastal aquifers in the Netherlands and concluded that models based on the method of characteristics are superior to finite-elements or finite-differences codes in terms of accuracy, stability, and computational effort, because they allow the use of relatively coarse grids without numerical dispersion. He adapted the method of characteristics program MOC (*Konikow and Bredehoeft*, 1978) to simulate density-dependent groundwater flow, and successfully applied the new model, describing saltwater intrusion in coastal aquifers (*Oude Essink*, 1996).

Oude Essink (1996) changed and extended the original code of MOC. As a result, the adapted MOC profits from robust and widely accepted techniques implemented in the original MOC. However, it is also restricted to limitations inherent in the original code; e.g. neither constant concentration boundaries nor constant head boundaries can be used directly in simulations. Also, since the original MOC was intended for two-dimensional groundwater flow in a horizontal plane, the adapted MOC model requires further changes in the code in order to use leakage boundary conditions. Compared to the original model, the possibilities to perform mass balance calculations are limited in the adapted MOC code.

The well-documented adaption of the original MOC code (*Oude Essink*, 1996) gave rise to the idea of developing a new model from scratch, using the robust and proven method, while facilitating at the same time the use of boundary conditions that are typical for coastal aquifers. Implementing visualization features into the new code provides options to gain a profound insight into

the numerical methods and to avoid that the model is used merely as a ‘black box’.

SWIMMOC is a numerical model for the simulation of two-dimensional density-dependent groundwater flow. The purpose of the model is to compute the pattern of groundwater flow and the distribution of salt in a vertical cross-section through an aquifer. SWIMMOC can be applied to analyze the dynamics of saltwater intrusion in coastal aquifers with respect to climate change and anthropogenic influences. The model is capable of simulating groundwater flow at a steady-state equilibrium as well as transient flow problems. This document describes the theoretical background of the computer program and presents an example of a simulation run.

Chapter 3 introduces the reader to the theory of groundwater flow at variable densities following the concept of equivalent freshwater heads. Different numerical methods to solve the governing equation for two-dimensional density-dependent groundwater flow (chapter 4) as well as the relevant processes of solute transport in groundwater are described (chapter 5). In chapter 6, the numerical solution of the transport equation using the method of characteristics is explained in detail; it is coupled to the numerical solutions of the groundwater flow equation in chapter 7. The definition of initial values and boundary conditions is described in chapter 8. Chapter 9 introduces possible strategies to evaluate and influence the precision and accuracy of numerical simulations with SWIMMOC. The theoretical part of this documentation rounds up with a brief review of the used assumptions (chapter 11).

The practical introduction to the computer program SWIMMOC begins with a brief description of the menus and dialogs (chapter 12). The classic Henry problem of saltwater intrusion is employed in chapter 13, demonstrating how to set up a new simulation in SWIMMOC. The solution of a modified version of the Henry problem illustrates the features and practical power of the new simulation tool SWIMMOC.

Chapter 3

Density-dependent groundwater flow

The theory of two-dimensional density-dependent groundwater flow forms the background of the numerical model SWIMMOC. It is assumed that groundwater flow is two-dimensional in a vertical plane. The horizontal x -axis of the plane is positive to the right. The vertical z -axis is parallel to gravity, but pointing in the opposite direction, therefore z is positive upward. It is assumed that the vertical cross-section has unit thickness. For this reason, the thickness is not included into the equations as a third variable.

In hydrogeology, next to the International System of Units (SI), the foot-pound-second (FPS) system of units is still widely used. Moreover, the units of quantities are often adjusted to the scale of the problem, e.g. specific discharge as well as hydraulic conductivity are frequently expressed in meters per day. In order to account for this common practice, the quantities are characterized by their dimensions rather than through SI units: [L] is length, [M] is mass, and [T] is time.

3.1 Pressure head and piezometric head

It is assumed that water is an incompressible fluid. Inside any hydrostatic body of water that is exposed to a gravitational field, the water pressure increases with depth. Consequently, the hydrostatic pressure of groundwater can be expressed as a function of the depth below the water table:

$$p(z) = \rho g (z_{wt} - z) \quad (3.1)$$

where

p	is the pressure at the point of observation $[\text{ML}^{-1}\text{T}^{-2}]$,
ρ	is the density of the water $[\text{ML}^{-3}]$,
g	is the acceleration due to gravity $[\text{LT}^{-2}]$,
z_{wt}	is the elevation of the water table $[\text{L}]$, and
z	is the elevation head at the point of observation $[\text{L}]$.

The distance between the point of observation to the water table is equal to the height of a column of water needed to generate the pressure p and can be expressed as:

$$z_{wt} - z = \frac{p(z)}{\rho g} \quad (3.2)$$

The quotient on the right hand side of equation (3.2) is referred to as pressure head. The sum of the pressure head and the elevation head is called piezometric head:

$$h(z) = \frac{p(z)}{\rho g} + z \quad (3.3)$$

where

$h(z)$ is the piezometric head at the observation depth z $[\text{L}]$.

Figure 3.1 illustrates that inside a body of water at rest, thus at hydrostatic conditions, the water pressure increases with depth while the piezometric head remains constant. Groundwater flow between two points in the same aquifer occurs only if there is a difference in piezometric head.

3.2 Darcy's law

Two-dimensional groundwater flow in a vertical cross-section through an anisotropic, heterogeneous aquifer can be described using Darcy's law (e.g. *Freeze and Cherry, 1979; Bear, 1979*):

$$q_x = -K_x \frac{\partial h}{\partial x} \quad (3.4)$$

$$q_z = -K_z \frac{\partial h}{\partial z} \quad (3.5)$$

where

q_x, q_z are the specific discharges $[\text{LT}^{-1}]$, and

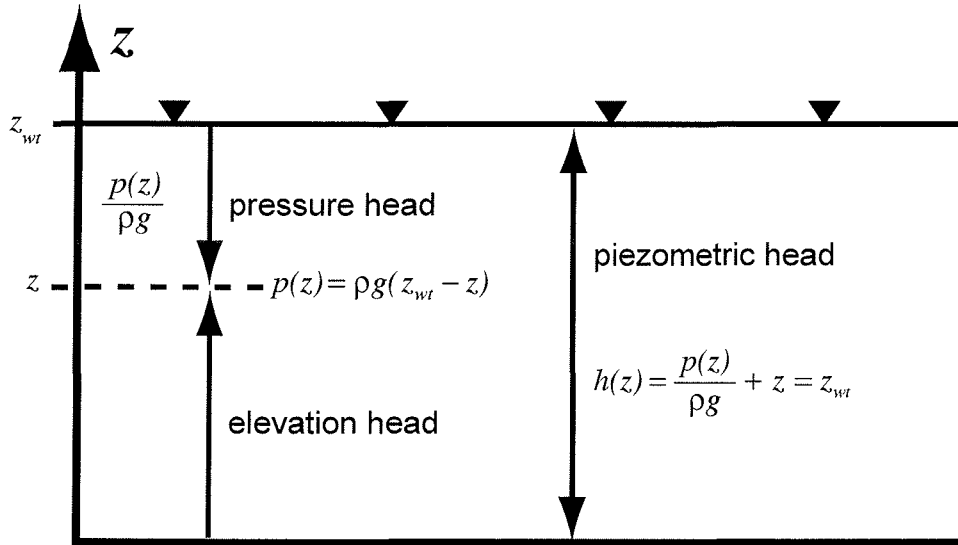


Figure 3.1: At hydrostatic conditions, the pressure increases with depth. The piezometric head is constant throughout the aquifer, because it is the sum of the pressure head and the elevation head.

K_x, K_z are the hydraulic conductivities [LT^{-1}] in horizontal and vertical direction, respectively.

Darcy's law indicates that the specific discharge is proportional to the gradient in the piezometric head. The proportionality constant K is called the hydraulic conductivity. K depends on both the permeability of the porous medium and the viscosity of the fluid. Commonly, the value of the hydraulic conductivity refers to freshwater at a temperature of ten degrees Celsius, which is considered the standard state of groundwater. At different temperatures and densities of the fluid, the hydraulic conductivity may vary significantly. The specific discharge is the flow of groundwater per unit area of the aquifer perpendicular to the direction of flow. This area consists of both sediment and porespace. The velocity of groundwater flow is calculated by dividing the specific flow by the effective porosity:

$$v_x = \frac{q_x}{n_e} \quad (3.6)$$

$$v_z = \frac{q_z}{n_e} \quad (3.7)$$

where

v_x, v_z are the horizontal and vertical components of groundwater velocity [LT^{-1}], and

n_e is the effective porosity [-].

3.3 Density differences

Given the presence of density differences within a water body, either the hydraulic conductivities must be calculated as functions of the density or the piezometric heads must be transformed such that they refer to the same density. The pressure at the bottom of a water column of the density ρ is calculated according to equation (3.1). After inserting the density of freshwater ρ_f into equation (3.3) and substitution of the right hand side of equation (3.1) for the pressure, the piezometric head can be expressed with respect to freshwater density:

$$h_f(z) = (z_{wt} - z) \frac{\rho}{\rho_f} + z \quad (3.8)$$

where

$h_f(z)$ is the equivalent freshwater head at the depth z [L], and

ρ_f is the density of freshwater [ML⁻³].

Since the equivalent freshwater head is not a real quantity that can be measured in nature, it is sometimes also called ‘fictive’ freshwater head. The difference between the real piezometric head and the equivalent freshwater head is illustrated in figure 3.2. Within a groundwater body at rest the real piezometric head is constant throughout the aquifer. The freshwater head increases with depth because the density of the groundwater is greater than the density of freshwater. The conversion of observed piezometric heads into equivalent freshwater heads creates a fictive vertical gradient in the profile:

$$\frac{\partial h_f}{\partial z} = 1 - \frac{\rho}{\rho_f} \quad (3.9)$$

In order to prevent the introduction of a fictive groundwater flow when applying Darcy’s law to equivalent freshwater heads, a buoyancy term must be added to equation (3.5), to compensate for fictive gradients :

$$q_z = -K_z \left(\frac{\partial h_f}{\partial z} + B \right) \quad \text{with } B = \frac{\rho}{\rho_f} - 1 \quad (3.10)$$

The fictive vertical gradient given by equation (3.9) is negative if the density of the groundwater is greater than the density of freshwater. Consequently, in the hydrostatic case, the buoyancy term must be positive to balance the fictive gradient. If the density of groundwater varies within the aquifer, the buoyancy term becomes a function of the location within the vertical plane of the aquifer and the time:

$$B(x, z, t) = \frac{\rho(x, z, t)}{\rho_f} - 1 \quad (3.11)$$

where

t is the time [T].

Equation (3.11) simply indicates that water of a greater density will obey the law of gravity and move downward. Thus a positive correlation exists between groundwater density and downward flow created by the density term.

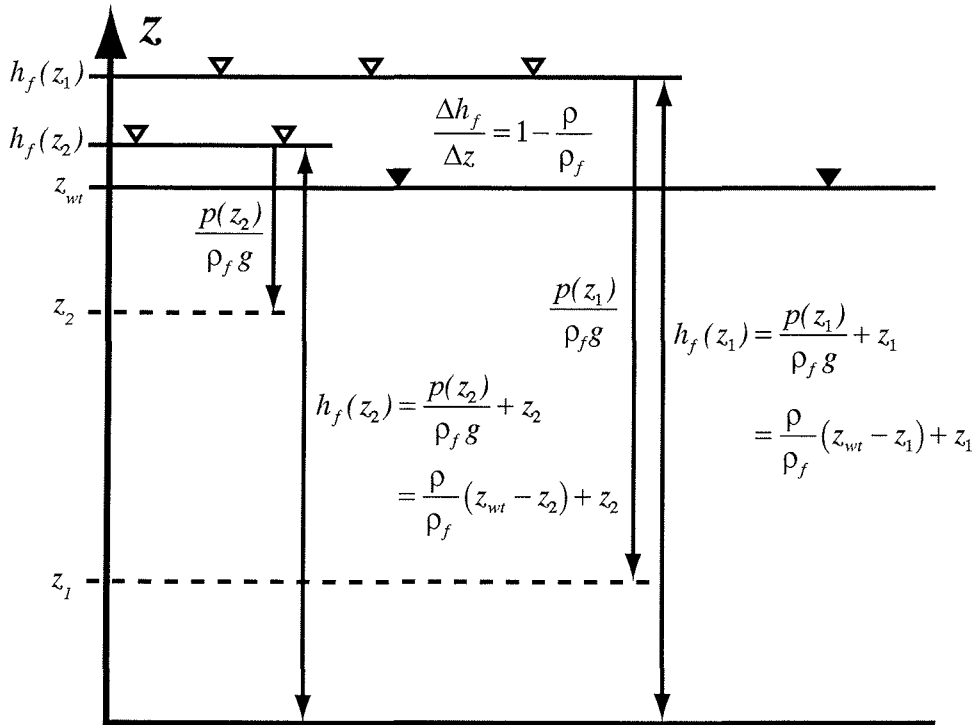


Figure 3.2: The groundwater in this illustration has the density ρ , which is greater than the density of fresh groundwater ρ_f . Assuming hydrostatic conditions, the observed piezometric heads (solid triangles) at the depths z_1 and z_2 are equal ($h_{obs} = z_{wt}$). Expressing the piezometric head with respect to freshwater density (open triangles) introduces a fictive hydraulic gradient to the profile.

Assuming hydrostatic conditions, equation (3.8) can be used to calculate the equivalent freshwater head using the pressure and the depth of observation. In the presence of vertical hydraulic gradients, the pressure head can be different from the distance to the water table. Thus, the pressure must be expressed in terms of the observed piezometric head:

$$p(z) = \rho g (h - z) \quad (3.12)$$

Combining equations (3.12) and (3.3) yields the formulas for the conversion between equivalent freshwater heads and observed piezometric heads in water

bodies that are not hydrostatic:

$$h_f = (h - z) \frac{\rho}{\rho_f} + z \quad (3.13)$$

$$h = (h_f - z) \frac{\rho_f}{\rho} + z \quad (3.14)$$

3.4 Leakage and drainage

In areas where the groundwater table is close to the surface, the exchange of water between surface water bodies, e.g. lakes and rivers, and the aquifer may play an important role for groundwater flow. Commonly, surface water and groundwater bodies are separated by a semi-pervious layer, such as e.g. a riverbed or a lakebed. Even though usually the hydraulic conductivity of such layers is low, groundwater may pass through it in both directions. In case the water level of the surface water body is higher than the piezometric head of the groundwater in the aquifer below, then surface water will leak through the riverbed or lakebed sediments and enter the aquifer. Drainage from the aquifer into a river, lake, or creek occurs if the piezometric head of the groundwater is higher than the water level of the surface water body. In this document, leakage flux into an aquifer has a positive sign, while drainage is simply considered as negative leakage (figure 3.3).

If the water exchange between a surface water body and the aquifer is controlled mainly by the hydraulic conductivity and the thickness of the semi-pervious layer, then the leakage flux across the semi-pervious layer can be written as:

$$q_L^* = (H_f - h_f) \frac{K_L}{m_L} \quad (3.15)$$

where

- q_L^* is the specific leakage flux across the semi-pervious layer [LT^{-1}],
- H_f is the freshwater head at the bottom of the surface water [L],
- K_L is the (vertical) hydraulic conductivity of the semi-pervious layer [LT^{-1}], and
- m_L is the thickness of the semi-pervious layer [L].

Some authors refer to the quotient of the conductivity and the thickness of the semi-pervious layer as leakage factor. On a regional scale, the absolute leakage flow depends on the leakage factor, and on the size of the surface water body. Therefore, it is convenient to define the specific conductance as an entity that

includes the leakage factor and the surface area of the aquifer that is exposed to leakage:

$$C_S = \frac{K_L}{m_L} a_L \quad (3.16)$$

where

C_S is the specific conductance [T^{-1}], and

a_L is the fraction of the aquifer surface that is exposed to leakage [-].

Hence, the specific steady leakage flux through an area that is only partly covered by a surface water body is:

$$q_L = (H_f - h_f) C_S \quad (3.17)$$

where

q_L is the leakage flux through the surface of the aquifer [LT^{-1}].

According to equation (3.8), the freshwater head at the bottom of the surface water body can be calculated from the density of the surface water:

$$H_f = (H_S - z_{bottom}) \frac{\rho_S}{\rho_f} + z_{bottom} \quad (3.18)$$

where

H_S is the surface water level [L], and

z_{bottom} is the elevation of the bottom of the surface water [L].

Inserting equation (3.18) into equation (3.17) delivers:

$$q_L = \left[(H_S - z_{bottom}) \frac{\rho_S}{\rho_f} + z_{bottom} - h_f \right] C_S \quad (3.19)$$

The leakage flux into the aquifer becomes independent of the hydraulic gradient between the surface water and the aquifer in case the freshwater head in the aquifer falls below the base of the semi-pervious layer. Then the leakage flux is controlled by the distance between the equivalent freshwater head at the bottom of the surface water and the base of the semi-pervious layer (*Kinzelbach and Rausch, 1995*). As a result, equation 3.19 can be simplified to:

$$q_L = \left[(H_S - z_{bottom}) \frac{\rho_S}{\rho_f} + m_L \right] C_S \quad (3.20)$$

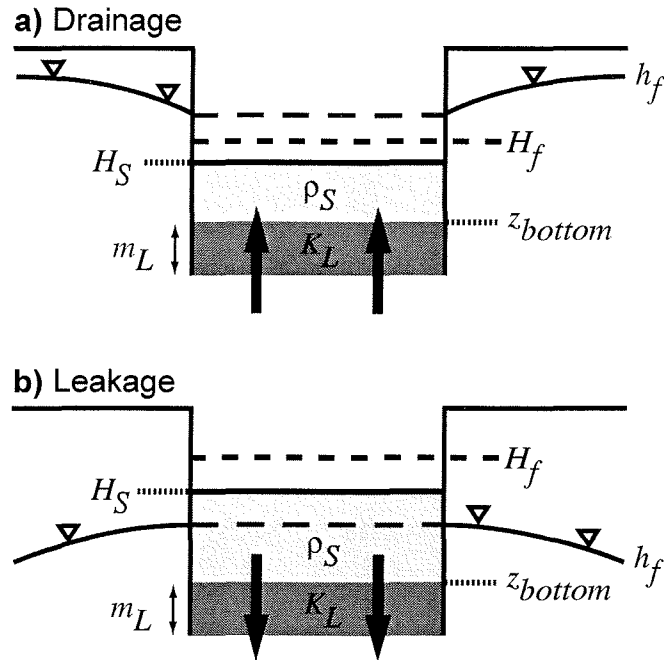


Figure 3.3: The freshwater head in the aquifer at the elevation of the base of the semi-pervious layer is indicated by h_f . In order to calculate the hydraulic gradient across the semi-pervious layer, the observed water level (H_S) of the surface water body must first be expressed with respect to freshwater density (H_f). In the illustrated example, the density of the surface water is significantly greater than the density of freshwater. Arrows indicate the direction of leakage flow. In case H_f is lower than h_f , groundwater is flowing from the aquifer into the surface water body (a). Leakage from the surface water body into the aquifer occurs in case H_f is higher than h_f (b).

3.5 The groundwater flow equation

Assuming that groundwater flow is two-dimensional in a vertical plane, the groundwater flow equation for a vertical cross-section can be derived from the flow budget for an infinitesimal control volume. For reasons of continuity, a change in the net flux into or out of the control volume must lead to a change in the amount of water stored inside the control volume, unless the change is balanced by sources or sinks. Besides the exchange of groundwater and surface water, recharge from precipitation and injection or abstraction of water through wells are possible sources or sinks. Since a change in groundwater storage is reflected by a falling or rising piezometric head, the rate at which the storage changes is expressed in terms of piezometric head:

$$-\left(\frac{\partial q_x}{\partial x} + \frac{\partial q_z}{\partial z}\right) + W_L + W = S_S \frac{\partial h_f}{\partial t} \quad (3.21)$$

where

3.5. THE GROUNDWATER FLOW EQUATION

- W_L is the volumetric leakage flux per unit volume of the aquifer [T^{-1}],
- W is the volumetric flux from sources or to sinks per unit volume of the aquifer [T^{-1}] (positive for inflow and negative for outflow), and
- S_S is the specific storage [L^{-1}].

The specific storage is the volume of water that can be stored additionally inside a unit volume of the aquifer if the piezometric head is raised by one unit. In the confined case, it reflects the compressibility of the aquifer.

Inserting equations (3.4) and (3.10) into equation (3.21) yields the groundwater flow equation:

$$-K_x \frac{\partial^2 h_f}{\partial x^2} - K_z \frac{\partial^2 h_f}{\partial z^2} - K_z \frac{\partial B}{\partial z} + W_L + W = S_S \frac{\partial h_f}{\partial t} \quad (3.22)$$

The use of derivatives in the groundwater flow equation implies the assumption that the physical properties of the aquifer vary continually and smoothly from point to point. The aquifer is treated as a continuum, even though commonly sediment and water-filled pores inhere small scale variability and there may occur abrupt changes in the hydraulic properties on a larger scale.

Chapter 4

Numerical solution of the flow equation

The groundwater flow equation (3.22) is a second order differential equation. Analytical solutions can be found for very simple cases, such as the evaluation of pumping tests. These solutions are usually limited to rather strict assumptions like infinitely large aquifers and complete homogeneity and isotropy. For more complex hydrogeological settings, the solution to the groundwater flow equation can only be approximated by means of numerical methods. These methods are based on the discretization of space and time.

4.1 Method of finite differences

In order to find an approximation for the spatial derivatives in the groundwater flow equation, the aquifer is divided into small rectangular cells (figure 4.1). These representative elementary volumes (REVs) are large enough to be considered homogeneous in terms of porosity and hydraulic conductivity, as well as small enough to assume that the aquifer properties are constant throughout the cell. The derivatives in the groundwater flow equation can now be expressed as quotients of finite differences:

$$\frac{\partial h}{\partial x} \rightarrow \frac{\Delta h}{\Delta x} = \frac{h_2 - h_1}{x_2 - x_1} \quad (4.1)$$

$$\frac{\partial h}{\partial z} \rightarrow \frac{\Delta h}{\Delta z} = \frac{h_2 - h_1}{z_2 - z_1} \quad (4.2)$$

$$\frac{\partial h}{\partial t} \rightarrow \frac{\Delta h}{\Delta t} = \frac{h_2 - h_1}{t_2 - t_1} \quad (4.3)$$

Using a block-centered equidistant grid, each REV is represented by a single point at the center of the cell, the node. In the following, nodes and cells will be referred to by means of row and column indices (figure 4.1), starting from

As mentioned in the introduction of chapter 3 on page 11, it is assumed that the vertical profile has unit thickness rather than including thickness as third variable. Consequently, cells have unit thickness and the volumetric flux has the dimension is L^2T^{-1} . If h'_f represents the effective freshwater head during the time interval $[t, t + \Delta t]$, and the specific discharges are uniform throughout the faces of the REV, the groundwater flow into the cell can be calculated by applying equations 3.4 and 3.10. In the horizontal direction, the volumetric fluxes through the left and right face of the cell are:

$$Q_{left}(i, j) = -K_x(i, j - 0.5) \frac{h'_f(i, j) - h'_f(i, j - 1)}{\Delta x} \Delta z \quad (4.5)$$

$$Q_{right}(i, j) = K_x(i, j + 0.5) \frac{h'_f(i, j + 1) - h'_f(i, j)}{\Delta x} \Delta z \quad (4.6)$$

where

$K_x(i, j \pm 0.5)$ is the mean hydraulic conductivity at the left and right border of the cell, respectively [LT^{-1}].

The mean hydraulic conductivity at the left and right border of the cell is defined as the harmonic mean of the conductivities of the cell itself and its neighbor:

$$K_x(i, j \pm 0.5) = \frac{2K_x(i, j)K_x(i, j \pm 1)}{K_x(i, j) + K_x(i, j \pm 1)} \quad (4.7)$$

In the vertical direction, the volumetric fluxes into the cell from the top and the bottom are:

$$Q_{top}(i, j) = K_z(i - 0.5, j) \frac{h'_f(i - 1, j) - h'_f(i, j)}{\Delta z} \Delta x \quad (4.8)$$

$$Q_{bottom}(i, j) = -K_z(i + 0.5, j) \frac{h'_f(i, j) - h'_f(i + 1, j)}{\Delta z} \Delta x \quad (4.9)$$

where

$K_z(i \pm 0.5, j)$ is the mean hydraulic conductivity at the lower and upper border of the cell, respectively [LT^{-1}].

The mean vertical conductivities can be obtained in the same way as the mean horizontal conductivities:

$$K_z(i \pm 0.5, j) = \frac{2K_z(i, j)K_z(i \pm 1, j)}{K_z(i, j) + K_z(i \pm 1, j)} \quad (4.10)$$

The buoyancy terms in equations (4.8) and (4.9) are calculated from the arithmetic mean of the groundwater densities in two adjacent cells (*Oude Essink*, 1996):

$$B(i \pm 0.5, j) = \frac{\rho(i, j) + \rho(i \pm 1, j)}{2\rho_f} - 1 \quad (4.11)$$

According to equation (3.19), the volumetric flux due to leakage is calculated using the hydraulic gradient across the semi-pervious layer:

$$W_L = \frac{q_L}{\Delta z} \quad (4.12)$$

with

$$q_L = \left[(H_S - z_{bottom}) \frac{\rho_S}{\rho_f} + z_{bottom} - h_f^*(i, j) \right] C_S \quad (4.13)$$

where

$h_f^*(i, j)$ is the equivalent freshwater head at the base of the semi-pervious layer ($z_{bottom} - m_L$) [L].

Note that the freshwater head at the base of the semi-pervious layer may be different from the freshwater head at the node. Therefore, the ‘fictive’ hydraulic gradient given by equation (3.9) is used to express the freshwater head at the base of the semi-pervious layer in terms of the freshwater head at the node:

$$h_f^*(i, j) = h_f'(i, j) - (z_{bottom} - m_L - z(i, j)) \left(1 - \frac{\rho(i, j)}{\rho_f} \right) \quad (4.14)$$

where

$z(i, j)$ is the elevation of the node [L].

Inserting equation (4.14) into equation (4.13) yields:

$$q_L = \left[(H_S - z_{bottom}) \frac{\rho_S}{\rho_f} + z_{bottom} - h_f'(i, j) + (z_{bottom} - m_L - z(i, j)) \left(1 - \frac{\rho(i, j)}{\rho_f} \right) \right] C_S \quad (4.15)$$

For convenience, equation (4.15) may also be written as:

$$q_L = [L - h_f'(i, j)] C_S \quad (4.16)$$

with

$$\begin{aligned}
 L = & (H_S - z_{bottom}) \frac{\rho_S}{\rho_f} + z_{bottom} \\
 & + (z_{bottom} - m_L - z(i, j)) \left(1 - \frac{\rho(i, j)}{\rho_f} \right) \quad (4.17)
 \end{aligned}$$

If the freshwater head in the boundary cell falls below the base of the streambed, the leakage flux is controlled by the thickness of the streambed rather than by the hydraulic gradient between the surface water and the groundwater. In this case, equation (4.13) is simplified to:

$$q_L = \left[(H_S - z_{bottom}) \frac{\rho_S}{\rho_f} + m_L \right] C_S \quad (4.18)$$

Substituting the right hand sides of equations (4.5), (4.6), (4.8), (4.9), and (4.12) for the corresponding terms in equation (4.4), and dividing both sides by the volume of the cell and the length of the time interval yields the finite differences approximation of the groundwater flow equation for transient two-dimensional density-dependent flow in an anisotropic, inhomogeneous vertical cross-section through an aquifer:

$$\begin{aligned}
 S_S \frac{h_f^{t+\Delta t}(i, j) - h_f^t(i, j)}{\Delta t} = & -\frac{K_x(i, j-0.5)}{\Delta x^2} (h'_f(i, j) - h'_f(i, j-1)) \\
 & + \frac{K_x(i, j+0.5)}{\Delta x^2} (h'_f(i, j+1) - h'_f(i, j)) \\
 & + \frac{K_z(i-0.5, j)}{\Delta z^2} \left((h'_f(i-1, j) - h'_f(i, j) + B(i-0.5, j)\Delta z) \right) \\
 & - \frac{K_z(i+0.5, j)}{\Delta z^2} \left((h'_f(i, j) - h'_f(i, j+1) + B(i+0.5, j)\Delta z) \right) \\
 & + (L - h'_f(i, j)) \frac{C_S}{\Delta z} + W(i, j) \quad (4.19)
 \end{aligned}$$

As mentioned above, it is assumed that $h'_f(i, j)$ represents the effective freshwater head at the node (i, j) during the time interval $[t, t+\Delta t]$. Commonly, the effective head h'_f is approximated by a weighted mean of the freshwater heads at the beginning and at the end of the time interval to account for changes during the time interval Δt :

$$h'_f = \alpha h_f^{t+\Delta t} + (1 - \alpha) h_f^t \quad (4.20)$$

where

α is the weighting factor ($0 < \alpha < 1$) [-].

Applying equation (4.19) to each cell of a grid consisting of N_C columns and N_R rows leads to a linear system of $N = N_C \times N_R$ equations that can be solved numerically by means of an iteration algorithm (figure 4.2). Given the initial freshwater heads at the time $t = 0$, the iteration process starts from a guessed distribution of freshwater heads $h_f^m(t_1)$ at the end of the first time interval.

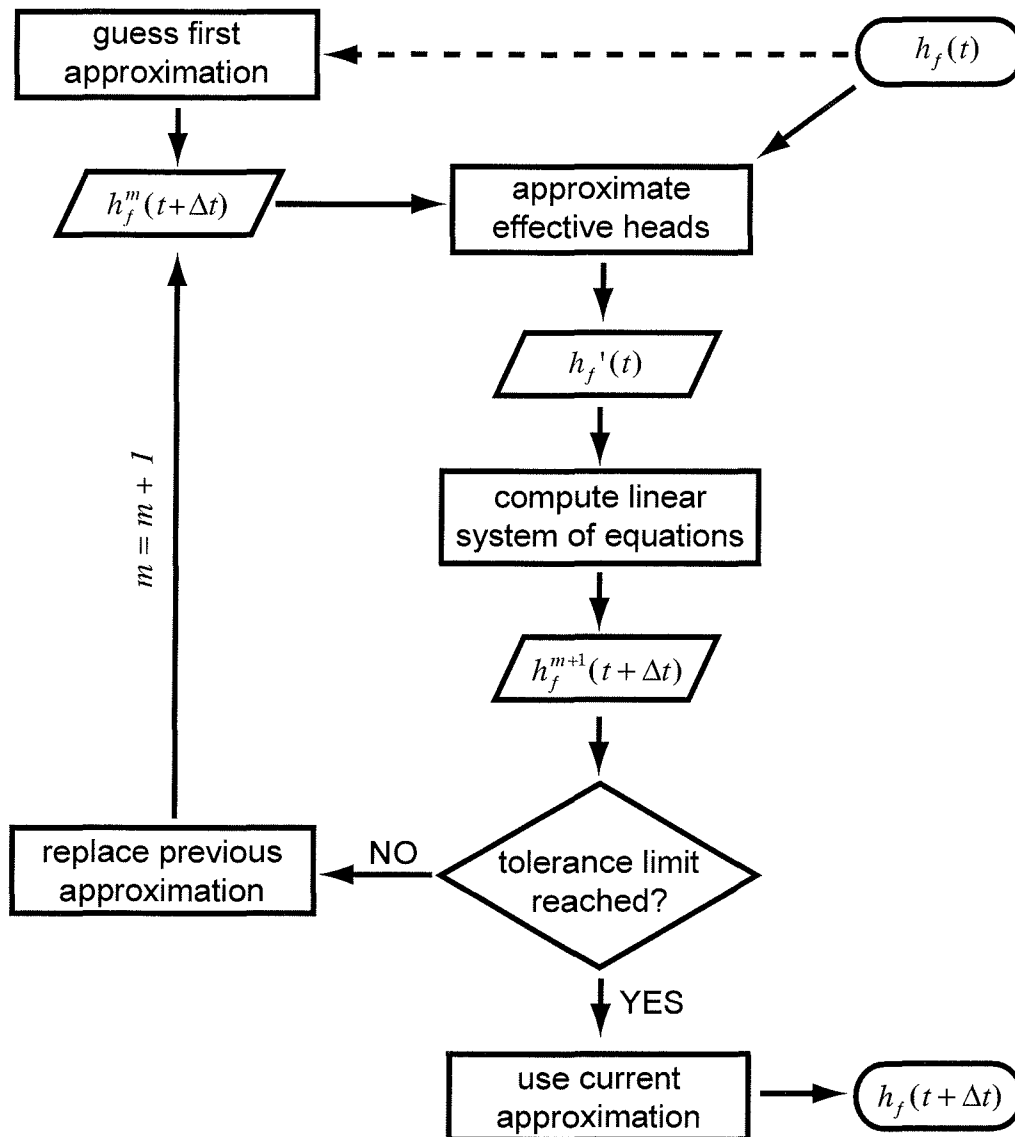


Figure 4.2: Starting from the known distribution of heads $h_f(t)$ at the beginning of the time step, the first approximation of the solution is found by guessing. As indicated by the dashed arrow, this first guess is usually based on the known values. In the course of every iteration step, the effective heads are interpolated from the known values at the beginning and the approximated values at the end of the time step. If the process converges, the approximations should successively approach the solution of the linear system of equations. The maximum change during a single iteration step is used as a criterion to evaluate the accuracy of the solution. The iteration loop stops if the maximum change is smaller than a tolerance limit defined by the user.

Based on this first guess, the effective freshwater heads $h'_f(t_1)$ are calculated according to equation (4.20). Using these values, the linear system of equations (4.19) can be solved for the freshwater heads at the end of the time interval. Then this first approximation $h_f^{m+1}(t_1)$ is used to replace the initially guessed distribution of heads $h_f^m(t_1)$. The second iteration step starts by updating the effective freshwater heads and generates the second approximation $h_f^{m+2}(t_1)$. In case the iteration process converges, the solution should improve with each iteration step until the desired accuracy is reached and the final approximation $h_f(t_1)$ is obtained.

4.2 Explicit solution

Different techniques can be applied to solve the linear system of equations through modification of the weighting factor α in equation (4.20). Setting the weighting factor α equal to zero leaves the freshwater head at the node (i, j) at the end of the time interval as the only unknown variable in each equation:

$$\begin{aligned}
 h_f^{t+\Delta t}(i, j) = & \frac{\Delta t}{S_S} \left[-\frac{K_x(i, j-0.5)}{\Delta x^2} (h_f^t(i, j) - h_f^t(i, j-1)) \right. \\
 & + \frac{K_x(i, j+0.5)}{\Delta x^2} (h_f^t(i, j+1) - h_f^t(i, j)) \\
 & + \frac{K_z(i-0.5, j)}{\Delta z^2} \left((h_f^t(i-1, j) - h_f^t(i, j) + B(i-0.5, j)\Delta z) \right. \\
 & \left. - \frac{K_z(i+0.5, j)}{\Delta z^2} \left((h_f^t(i, j) - h_f^t(i, j+1) + B(i+0.5, j)\Delta z) \right) \right) \\
 & \left. + (L - h_f^t(i, j)) \frac{C_S}{\Delta z} + W(i, j) \right] + h_f^t(i, j)
 \end{aligned} \tag{4.21}$$

This 'explicit' solution of the finite differences flow equation solves each equation of the system directly and separately. However, since the explicit solution is constrained to very strict stability criteria, the application of this simple method is limited. Large time steps or dense grids may generate oscillations in the iteration process that finally lead to unrealistically high calculation results.

4.3 Implicit solutions

Using a weighting factor greater than zero in equation (4.20) to approximate the effective head during the flow step leaves more than one unknown variable in each equation. Since the resulting system of equations cannot be solved equation-by-equation, the solution is found by means of 'implicit' methods. The system of equations resulting from a weighting factor of $\alpha = 0.5$ is commonly referred to as Crank-Nicholson scheme, while methods involving a weighting factor of $\alpha = 1$ are called 'fully implicit'. Other weighting factors are also possible but less commonly used. Implicit methods require high calculation effort. However, implicit methods are generally more stable than the explicit solution, allowing larger time steps as well as the implementation of

more accurate grids. The fully implicit solution of the finite differences flow equation (4.19) is obtained by setting $h'_f = h_f^{t+\Delta t}$ and can be written as follows:

$$\begin{aligned}
 h_f^{t+\Delta t}(i, j) & \left(-\frac{K_x(i, j-0.5)}{\Delta x^2} - \frac{K_x(i, j+0.5)}{\Delta x^2} - \frac{K_z(i-0.5, j)}{\Delta z^2} - \frac{K_z(i+0.5, j)}{\Delta z^2} - \frac{C_S}{\Delta z} - \frac{S_S}{\Delta t} \right) \\
 & + h_f^{t+\Delta t}(i, j-1) \left(\frac{K_x(i, j-0.5)}{\Delta x^2} \right) + h_f^{t+\Delta t}(i, j+1) \left(\frac{K_x(i, j+0.5)}{\Delta x^2} \right) \\
 & + h_f^{t+\Delta t}(i-1, j) \left(\frac{K_z(i-0.5, j)}{\Delta z^2} \right) + h_f^{t+\Delta t}(i+1, j) \left(\frac{K_z(i+0.5, j)}{\Delta z^2} \right) \\
 & = -\frac{K_z(i-0.5, j)}{\Delta z} B(i-0.5, j) + \frac{K_z(i+0.5, j)}{\Delta z} B(i+0.5, j) \\
 & \quad - \frac{C_S}{\Delta z} L - W(i, j) - \frac{S_S}{\Delta t} h_f^t(i, j)
 \end{aligned} \tag{4.22}$$

To transform the implicit flow equation into a more convenient form, the row and column indices are replaced by a single index. If N_C is the number of columns and N_R is the number of rows, then each cell of the model grid can be addressed using a single index k as defined by equation (4.23).

$$k = iN_C + j \tag{4.23}$$

The numbering of the grid cells using a single index is illustrated in table 4.1. Note that i , j , and k are all starting from zero.

Table 4.1: Applying the single index numbering scheme as given by equation (4.23), the first cell in the upper left corner has the index $k = 0$ while the last cell in the lower right corner of the grid has the greatest index.

0	1	2	3	...	$N_C - 1$
N_C	$N_C + 1$
$2N_C$
$3N_C$
\vdots	\vdots	\vdots	\vdots	\ddots	\vdots
$N_R - 1$	$N - 1$

Using the single index k instead of the row and column indices, the two vectors $h_f^{t+\Delta t}(k)$ and $b(k)$ are defined, containing the freshwater heads and the right hand side of equation (4.22), respectively. The coefficients of $h_f^{t+\Delta t}(k)$ are written as elements of the matrix $a(k, l)$.

$$\sum_{l=0}^{N-1} a(k, l) h_f^{t+\Delta t}(l) = b(k) \tag{4.24}$$

The matrix $a(k, l)$ consists of N rows and N columns. However, no more than five elements per row can be non-zero. As an example, the following equation shows the coefficient matrix for $N = 9$. Each non-zero element of the matrix

is marked by a bullet:

$$a(k, l) = \begin{pmatrix} \bullet & \bullet & 0 & \bullet & 0 & 0 & 0 & 0 & 0 \\ \bullet & \bullet & \bullet & 0 & \bullet & 0 & 0 & 0 & 0 \\ 0 & \bullet & \bullet & 0 & 0 & \bullet & 0 & 0 & 0 \\ \bullet & 0 & 0 & \bullet & \bullet & 0 & \bullet & 0 & 0 \\ 0 & \bullet & 0 & \bullet & \bullet & \bullet & 0 & \bullet & 0 \\ 0 & 0 & \bullet & 0 & \bullet & \bullet & 0 & 0 & \bullet \\ 0 & 0 & 0 & \bullet & 0 & 0 & \bullet & \bullet & 0 \\ 0 & 0 & 0 & 0 & \bullet & 0 & \bullet & \bullet & \bullet \\ 0 & 0 & 0 & 0 & 0 & \bullet & 0 & \bullet & \bullet \end{pmatrix} \quad (4.25)$$

4.3.1 Convergence condition for iteration methods

Iteration methods for solving linear systems of equations are said to converge for an initial h_f^m if the corresponding iterative sequence $h_f^{m+1}, h_f^{m+2}, \dots$ converges towards a solution of the given system of equations. All iterative methods described here will converge if the coefficient matrix is diagonally dominant (e.g. *Kreyszig, 1999*):

$$|a(k, k)| \geq \sum_{l=0, l \neq k}^{N-1} |a(k, l)| \quad (4.26)$$

If for every row, the absolute value of the element on the main diagonal is greater than the sum of the absolute values of all other elements in the row, then the method will converge. Using equation (4.23) to convert from double to single indices, it can be seen that each cell of the grid is represented by an element of the main diagonal, while the neighboring cells occupy the other non-zero elements of the row. Equation (4.22) shows that the corresponding coefficient consists of the sum of all other coefficients plus the leakage and the storage terms. Therefore, the coefficient matrix is always diagonally dominant.

Furthermore, the coefficient matrix in equation (4.25) shows that all non-zero elements are contained in a diagonal band from the upper left to the lower right corner of the matrix, while the two remaining corners of the matrix are filled with zeros. This banded structure along with the fact that the coefficient matrix is diagonally dominant greatly facilitates the solution of the corresponding linear system of equations.

4.3.2 Jacobi method

One way to solve the linear system of equations (4.24) is to simultaneously adjust the values of the freshwater head in each cell to the neighboring cells.

Inserting any guessed distribution of freshwater heads h_f^m into equation (4.24) yields:

$$\sum_{l=0}^{N-1} a(k, l)h_f^m(l) \approx b(k) \quad (4.27)$$

This first guess merely serves as a rough, and possibly poor approximation to the solution of the system. Following the Jacobi method (*Kreyszig*, 1999), the approximation can be improved by replacing each value of h_f^m with a new value of h_f^{m+1} that complies with the equation:

$$a(k, k)h_f^{m+1}(k) + \sum_{l=0, l \neq k}^{N-1} a(k, l)h_f^m(l) = (k) \quad (4.28)$$

Or, after rewriting:

$$h_f^{m+1}(k) = \frac{1}{a(k, k)} \left(b(k) - \sum_{l=0, l \neq k}^{N-1} a(k, l)h_f^m(l) \right) \quad (4.29)$$

The matrix in equation (4.25) shows that $a(k, k) \neq 0$ is usually given for all flow problems. The approximation h_f^{m+1} can be further improved, obtaining the second approximation h_f^{m+2} in the same way, and so forth, until the desired accuracy is reached. Note that the Jacobi method as shown in equation (4.29) only uses the old approximation h_f^m to calculate the improved approximation h_f^{m+1} . All values are improved simultaneously by stepping from h_f^m to h_f^{m+1} .

4.3.3 Gauss-Seidel method

In contrast to the Jacobi method, the Gauss-Seidel method (*Kreyszig*, 1999) improves the approximation successively rather than simultaneously, using the fact that for each $l < k$, the new value $h_f^{m+1}(l)$ has already been calculated:

$$h_f^{m+1}(k) = \frac{1}{a(k, k)} \left(b(k) - \sum_{l=0}^{k-1} a(k, l)h_f^{m+1}(l) - \sum_{l=k+1}^{N-1} a(k, l)h_f^m(l) \right) \quad (4.30)$$

Since the old value from $h_f^{m+1}(l)$ is used only if $l > k$, the Gauss-Seidel method incorporates all new values in the iteration process as soon as they have been calculated. Consequently, the Gauss-Seidel method usually converges faster than the Jacobi method.

4.3.4 Iterative Alternating Direction Implicit method (IADI)

A more sophisticated method to solve the system of equations is given by the Iterative Alternating Direction Implicit (IADI) method. It is derived from the

non-iterative Alternating Direction Implicit method developed by *Peaceman and Rachford* (1955) for solving the heat flow equation. *Pinder and Bredehoeft* (1968) applied the Alternating Direction Implicit method to groundwater flow problems. *Bennett* (1976) and *Kinzelbach* (1986) describe iterative versions of the Alternating Direction Implicit method that are based on the work of *Prickett and Lonquist* (1971). *Trescott and Larson* (1976) further modified the Iterative Alternating Direction Implicit method by introducing over-relaxation parameters that improve the convergence. The calculation of these parameters is beyond the scope of this work, however. The method used here is similar to the method described by *Kinzelbach* (1986).

While both the Gauss-Seidel and the Jacobi method change the value of the freshwater head in a single cell of the grid at a time, the IADI method solves the flow equation for all cells in a row or column simultaneously. In the course of one iteration step, the freshwater heads are calculated first row-by-row and then again column-by-column. This way, each freshwater head is calculated twice during a single iteration step (figure 4.3). In the original version of the Alternating Direction Implicit method, the rows are calculated implicitly in row-direction and explicitly in column-direction, while the column equations are implicit in column-direction and explicit in row-direction. The time step is split in two halves: The first half of the time step is calculated using the row equations and the second half is calculated using the column equations. This way, the direction of implicit calculation alternates from one half-time step to the next, hence the name of the method. According to *Peaceman and Rachford* (1955), the error from the explicit part of the scheme is evened out in the course of two half-time steps. For this reason, unlike the explicit solution described in section 4.2, the Alternating Direction Implicit method is unconditionally stable and can be used for any length of time step.

In contrast to the original method, the IADI method described here solves the flow equation in an iterative way, alternating the direction of implicit calculation from iteration step to iteration step. Always using the most recent values, the approximation is improved successively, similar to the Gauss-Seidel method. All values of h_f^{m+1} are incorporated as soon as they are calculated. The old value h_f^m is used only as long as a more recent value h_f^{m+1} is not yet available. In practice, this can easily be achieved by storing all values in the same matrix. The calculation of rows is described by equation (4.31). Keeping i fixed, the freshwater heads in the row above and below are assumed constant.

$$\begin{aligned}
 h_f^{t+\Delta t}(i, j) & \left(-\frac{K_x(i, j-0.5)}{\Delta x^2} - \frac{K_x(i, j+0.5)}{\Delta x^2} - \frac{K_z(i-0.5, j)}{\Delta z^2} - \frac{K_z(i+0.5, j)}{\Delta z^2} - \frac{C_S}{\Delta z} - \frac{S_S}{\Delta t} \right) \\
 & + h_f^{t+\Delta t}(i, j-1) \left(\frac{K_x(i, j-0.5)}{\Delta x^2} \right) + h_f^{t+\Delta t}(i, j+1) \left(\frac{K_x(i, j+0.5)}{\Delta x^2} \right) \\
 & = -h_f^t(i-1, j) \left(\frac{K_z(i-0.5, j)}{\Delta z^2} \right) - h_f^t(i+1, j) \left(\frac{K_z(i+0.5, j)}{\Delta z^2} \right) \\
 & \quad - \frac{K_z(i-0.5, j)}{\Delta z} B(i-0.5, j) + \frac{K_z(i+0.5, j)}{\Delta z} B(i+0.5, j) \\
 & \quad - \frac{C_S}{\Delta z} L - W(i, j) - \frac{S_S}{\Delta t} h_f^t(i, j)
 \end{aligned} \tag{4.31}$$

The calculation of columns is analogous. Keeping i fixed, equation (4.32) is

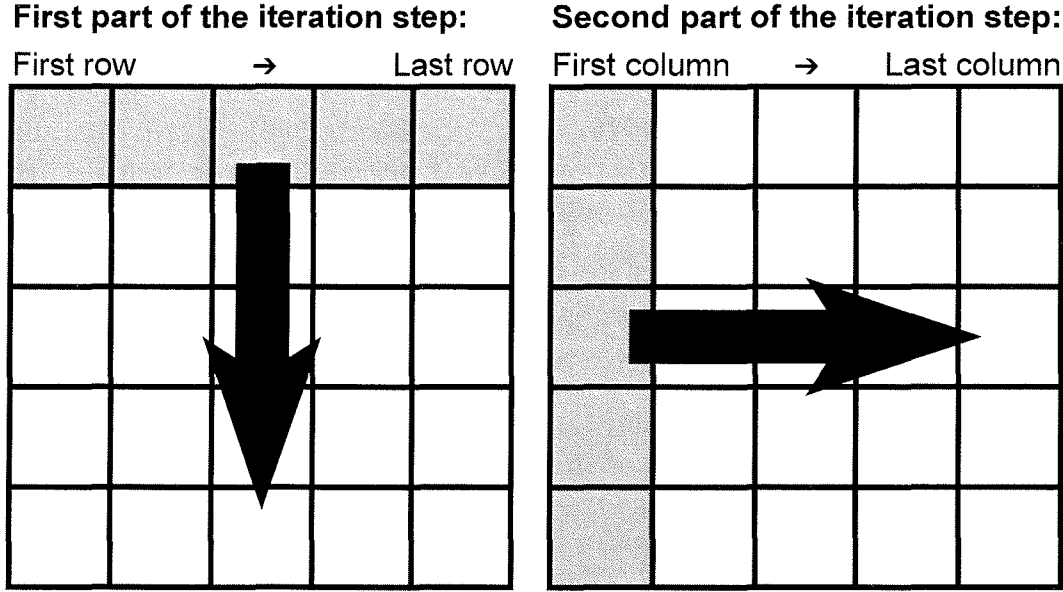


Figure 4.3: The Iterative Alternating Direction Implicit (IADI) method solves the flow equation for all cells in a row or column simultaneously. In the first half of the iteration step, the system of equations is solved row-by-row, the second half processes the grid column-by-column. This way, each value is improved twice during a single iteration step.

solved for all freshwater heads in one column, while the freshwater heads in the columns to the right and to the left are treated as constants.

$$\begin{aligned}
 h_f^{t+\Delta t}(i, j) & \left(-\frac{K_x(i, j-0.5)}{\Delta x^2} - \frac{K_x(i, j+0.5)}{\Delta x^2} - \frac{K_z(i-0.5, j)}{\Delta z^2} - \frac{K_z(i+0.5, j)}{\Delta z^2} - \frac{C_S}{\Delta z} - \frac{S_S}{\Delta t} \right) \\
 & + h_f^{t+\Delta t}(i-1, j) \left(\frac{K_z(i-0.5, j)}{\Delta z^2} \right) + h_f^{t+\Delta t}(i+1, j) \left(\frac{K_z(i+0.5, j)}{\Delta z^2} \right) \\
 & = -h_f^t(i, j-1) \left(\frac{K_x(i, j-0.5)}{\Delta x^2} \right) - h_f^t(i, j+1) \left(\frac{K_x(i, j+0.5)}{\Delta x^2} \right) \\
 & \quad - \frac{K_z(i-0.5, j)}{\Delta z} B(i-0.5, j) + \frac{K_z(i+0.5, j)}{\Delta z} B(i+0.5, j) \\
 & \quad - \frac{C_S}{\Delta z} L - W(i, j) - \frac{S_S}{\Delta t} h_f^t(i, j)
 \end{aligned} \tag{4.32}$$

Both equation (4.31) and equation (4.32) can be simplified by writing the right hand side and the coefficients of the unknown variables on the left hand side as vectors. Because the calculation of rows and columns is completely analogous, in the following only the calculation of the rows will be explained in detail. Writing the right hand side as b and the coefficients as a_0 , a_1 , and a_2 , the simplified version of equation (4.31) is:

$$a_0(j)h_f^{m+1}(i, j-1) + a_1(j)h_f^{m+1}(i, j) + a_2(j)h_f^{m+1}(i, j+1) = b(j) \tag{4.33}$$

with

$$\begin{aligned}
 a_0(j) & = \frac{K_x(i, j-0.5)}{\Delta x^2} \\
 a_1(j) & = -\frac{K_x(i, j-0.5)}{\Delta x^2} - \frac{K_x(i, j+0.5)}{\Delta x^2} - \frac{K_z(i-0.5, j)}{\Delta z^2}
 \end{aligned} \tag{4.34}$$

$$-\frac{K_z(i+0.5, j)}{\Delta z^2} - \frac{C_S}{\Delta z} - \frac{S_S}{\Delta t} \quad (4.35)$$

$$a_2(j) = \frac{K_x(i, j+0.5)}{\Delta x^2} \quad (4.36)$$

$$\begin{aligned} b(j) = & -h_f^t(i-1, j) \left(\frac{K_z(i-0.5, j)}{\Delta z^2} \right) - h_f^t(i+1, j) \left(\frac{K_z(i+0.5, j)}{\Delta z^2} \right) \\ & - \frac{K_z(i-0.5, j)}{\Delta z} B(i-0.5, j) + \frac{K_z(i+0.5, j)}{\Delta z} B(i+0.5, j) \\ & - \frac{C_S}{\Delta z} L - W(i, j) - \frac{S_S}{\Delta t} h_f^t(i, j) \end{aligned} \quad (4.37)$$

From the boundaries of the grid at $j = 0$ and $j = N_C - 1$ follows that $a_0(0) = 0$ and $a_2(N_C - 1) = 0$. Accordingly, there are two unknown variables in the first and the last equation of the system given by (4.33), while three variables are unknown in each of the remaining equations. In every equation, the unknown variables are directly related to each other, because they correspond to adjacent grid cells. For that reason, the resulting coefficient matrix $a(k, l)$ has a tri-diagonal structure:

$$\begin{pmatrix} a_1(0) & a_2(0) & 0 & 0 & \cdot & 0 & 0 & 0 \\ a_0(1) & a_1(1) & a_2(1) & 0 & \cdot & 0 & 0 & 0 \\ 0 & a_0(2) & a_1(2) & a_2(2) & \cdot & 0 & 0 & 0 \\ \cdot & \cdot \\ 0 & 0 & 0 & 0 & \cdot & a_0(N_C - 2) & a_1(N_C - 2) & a_2(N_C - 2) \\ 0 & 0 & 0 & 0 & \cdot & 0 & a_0(N_C - 1) & a_1(N_C - 1) \end{pmatrix}$$

Since the IADI systems of equations given by (4.31) and (4.32) only cover one row or one column each, they are significantly smaller than the systems of equations (4.29) and (4.30) used in the Jacobi and Gauss-Seidel method, respectively. Furthermore, all IADI systems are strictly of tri-diagonal structure and can be solved using direct methods, such as the Thomas Algorithm. The IADI method usually converges faster than the Gauss-Seidel method.

Note that in the algorithm described by *Kinzelbach* (1986), the sequence of row and column calculations also alternates from one iteration step to the next. Starting the calculations for one iteration step with the first row and the first column, then the next step will start with the last row and the last column. This has been found unnecessary in practice. Therefore the algorithm implemented in the numerical model described here does not change the sequence of calculations.

4.3.5 Thomas algorithm

The Gauss elimination method is widely used for solving tri-diagonal systems of equations. The Thomas algorithm, sometimes also referred to as TDMA (= Tri-diagonal Matrix Algorithm) is a special form of the Gauss elimination

method (*Thomas, 1949*). In contrast to the Jacobi or Gauss-Seidel method, the Thomas algorithm is not an iterative method. The exact solution to a system of equations is calculated directly, without any approximations. In combination with the iterative ADI method, the Thomas algorithm can be applied to conveniently solve the row and column equations. Setting $j = 0$ and $j = 1$ in equation (4.33) yields the equations for the first two cells in row i :

$$a_1(0)h_f^{m+1}(i, 0) + a_2(0)h_f^{m+1}(i, 1) = b(0) \quad (4.38)$$

$$a_0(1)h_f^{m+1}(i, 0) + a_1(1)h_f^{m+1}(i, 1) + a_2(1)h_f^{m+1}(i, 2) = b(1) \quad (4.39)$$

From equation (4.38) follows that the freshwater head of the first cell can be expressed in terms of the freshwater head in the second cell:

$$h_f^{m+1}(i, 0) = -\frac{a_2(0)}{a_1(0)}h_f^{m+1}(i, 1) + \frac{b(0)}{a_1(0)} \quad (4.40)$$

Consequently, the term can be eliminated from equation (4.39) by inserting equation (4.40):

$$\begin{aligned} a_0(1) \left(-\frac{a_2(0)}{a_1(0)}h_f^{m+1}(i, 1) + \frac{b(0)}{a_1(0)} \right) \\ + a_1(1)h_f^{m+1}(i, 1) + a_2(1)h_f^{m+1}(i, 2) = b(1) \end{aligned} \quad (4.41)$$

As a result, the freshwater head in the second cell can be written in terms of the freshwater head in the third cell, making it possible to eliminate the term $h_f^{m+1}(i, 1)$ in the equation for the third cell, and so on. In general, the freshwater head in one cell can be expressed as a function of the freshwater head in the following cell:

$$h_f^{m+1}(i, j-1) = d(j-1)h_f^{m+1}(i, j) + e(j-1) \quad (4.42)$$

$$h_f^{m+1}(i, j) = d(j)h_f^{m+1}(i, j+1) + e(j) \quad (4.43)$$

Substituting the right hand side of equation (4.42) for the corresponding term in equation (4.33) and solving for $h_f^{m+1}(i, j)$ yields:

$$\begin{aligned} h_f^{m+1}(i, j) = \frac{a_2(j)}{a_0(j)d(j-1) + a_1(j)}h_f^{m+1}(i, j+1) \\ + \frac{b(j) - a_0(j)d(j-1)}{a_0(j)d(j-1) + a_1(j)} \end{aligned} \quad (4.44)$$

Comparing equation (4.43) and equation (4.44) shows:

$$d(j) = -\frac{a_2(j)}{a_0(j)d(j-1) + a_1(j)} \quad (4.45)$$

$$e(j) = \frac{b(j) - a_0(j)d(j-1)}{a_0(j)d(j-1) + a_1(j)} \quad (4.46)$$

From equation (4.38) can be concluded:

$$d(0) = -\frac{a_2(0)}{a_1(0)} \quad (4.47)$$

$$e(0) = \frac{b(0)}{a_1(0)} \quad (4.48)$$

From $a_2(N_C - 1) = 0$ follows that $d(N_C - 1) = 0$. Now, $d(j)$ and $e(j)$ for all $j = (0, 1, 2, \dots, N_C - 1)$ can be calculated. The equation for the freshwater head in the last cell of the row can be solved directly:

$$h_f^{m+1}(i, N_C - 1) = e(N_C - 1) \quad (4.49)$$

Then, the solutions to all other equations are obtained according to equation (4.43) by starting with $j = N_C - 2$ and going backwards to $j = 0$.

Chapter 5

Solute transport

Solute transport in groundwater can generally be divided into three different processes. The most obvious solute transport process is advection, the transport of particles along with the groundwater flow at the same speed and into the same direction. Both the speed and the direction of advective transport are expressed as mean values for a representative elementary volume. However, the real velocity of groundwater varies considerably. As a result, some particles are transported faster than the average groundwater flow while others are progressing more slowly. Depending on the scale of reference, some particles may be transported in different directions. The sum of these factors related to the distribution of the real groundwater velocity around the mean velocity value as calculated through the groundwater flow equation is referred to as dispersion. The third solute transport process is the diffusive mixing of particles on a molecular scale caused by the Brownian motion. While dispersion directly relates to advection, diffusion is an independent solute transport process.

5.1 Advection

Advection is the transport of particles at the same speed and into the same direction as the average groundwater flow. Consequently, the advective flux is a function of the groundwater velocity. For a vertical cross-section through an aquifer, the components in the two principal directions are:

$$j_{adv,x} = v_x n_e c = q_x c \quad (5.1)$$

$$j_{adv,z} = v_z n_e c = q_z c \quad (5.2)$$

where

$j_{adv,x}$, $j_{adv,z}$ are the advective fluxes per unit area in horizontal and vertical direction [$\text{ML}^{-2}\text{T}^{-1}$], respectively, and

c is the concentration of the solute in the groundwater [ML^{-3}].

In case the groundwater flow is the result of density differences within the aquifer, the resulting advective transport may also be called convection.

5.2 Dispersion

To describe groundwater flow and advective transport, the cross-section through the aquifer is divided into representative elementary volumes (REVs). Consequently, for each REV the properties of the aquifer, such as conductivity or porosity, as well as the velocity of groundwater flow are calculated as average values. On a smaller scale, however, the REVs consist of sediment and pore space, with transport occurring in the continuous pore space only. As illustrated in figure 5.1a, friction causes the groundwater velocity to vary from the edge to the center of every single pore, similar to the velocity profile in a tube. As a result, the particles in the center of a pore are transported fastest. Moreover, advective transport through a REV cannot follow a straight line, but is bound to the structure of the pore space (figure 5.1b), resulting in further scattering of the solute particles in the aquifer. On a larger scale, additional spreading may occur due to changes in the hydraulic properties of the aquifer. However, such large scale properties are often not known well enough to be incorporated in the calculation of groundwater flow. Dispersion, or more precisely ‘hydrodynamic dispersion’, is the sum of transport processes that accompany advection due to the heterogeneity of the porous medium.

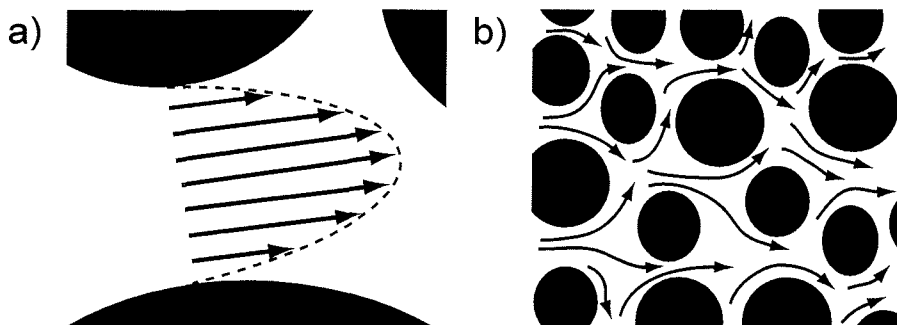


Figure 5.1: a) On a small scale, the groundwater velocity varies due to friction at the grains. As a result, solute particles at the center of a pore are moved faster than at the edges, causing dispersion. b) Both the direction and the speed of groundwater flow are affected by the structure of the pore space, causing dispersive spreading of solute particles in all directions.

Dispersion depends on the speed and direction of groundwater flow. The fact that even in isotropic porous media, dispersive transport in the direction of flow is always greater than perpendicular to the direction of groundwater flow is

accounted for by distinguishing longitudinal and transversal dispersion. The longitudinal and transversal dispersion are characterized by separate coefficients:

$$j_{disp} = j_L + j_T \quad (5.3)$$

with

$$j_L = -n_e D_L \frac{\partial c}{\partial s_L} \quad (5.4)$$

$$j_T = -n_e D_T \frac{\partial c}{\partial s_T} \quad (5.5)$$

where

j_{disp} is the total dispersive flux per unit area [$\text{ML}^{-2}\text{T}^{-1}$],
 j_L, j_T are the longitudinal and transversal dispersive fluxes [$\text{ML}^{-2}\text{T}^{-1}$],
 D_L, D_T are the corresponding coefficients of dispersion [L^2T^{-1}], and
 $\frac{\partial c}{\partial s_L}, \frac{\partial c}{\partial s_T}$ are the concentration gradients in the direction of flow and perpendicular to the direction of flow [ML^{-4}], respectively.

Scheidegger (1961) shows that the dispersivity of an isotropic aquifer may be defined in terms of two constants. The longitudinal and transverse dispersion coefficients can be approximated from the dispersivity and the speed of groundwater flow:

$$D_L = \alpha_L |v| \quad (5.6)$$

$$D_T = \alpha_T |v| \quad (5.7)$$

where

α_L, α_T are the longitudinal and transversal dispersivities of the aquifer, respectively [L], and
 $|v|$ is the magnitude of groundwater velocity [LT^{-1}] (or the speed of the groundwater flow).

In case the direction of the groundwater flow is not parallel to one of the main axes defined for the flow calculation, it is convenient to introduce additional dispersion coefficients that characterize horizontal and vertical dispersive flux. Since both horizontal and vertical concentration gradients affect the dispersive flux in each direction, four dispersive fluxes can be distinguished:

1. horizontal dispersive flux due to a horizontal concentration gradient,

2. horizontal dispersive flux due to a vertical concentration gradient,
3. vertical dispersive flux due to a vertical concentration gradient, and
4. vertical dispersive flux due to a horizontal concentration gradient.

According to *Scheidegger* (1961), the appropriate coefficients can be derived from the longitudinal and transverse dispersion coefficients, and the horizontal and vertical components of groundwater velocity using the following suite of equations from (5.8) to (5.14):

$$j_{xx} = -n_e D_{xx} \frac{\partial c}{\partial x} \quad (5.8)$$

with

$$D_{xx} = D_L \frac{v_x^2}{|v|^2} + D_T \frac{v_z^2}{|v|^2} = \alpha_L \frac{v_x^2}{|v|} + \alpha_T \frac{v_z^2}{|v|} \quad (5.9)$$

where

j_{xx} is the dispersive flux in horizontal direction due to a horizontal concentration gradient [$\text{ML}^{-2}\text{T}^{-1}$], and

D_{xx} is the corresponding dispersion coefficient [L^2T^{-1}].

and

$$j_{zz} = -n_e D_{zz} \frac{\partial c}{\partial z} \quad (5.10)$$

with

$$D_{zz} = D_T \frac{v_x^2}{|v|^2} + D_L \frac{v_z^2}{|v|^2} = \alpha_T \frac{v_x^2}{|v|} + \alpha_L \frac{v_z^2}{|v|} \quad (5.11)$$

where

j_{zz} is the dispersive flux in vertical direction due to a vertical concentration gradient [$\text{ML}^{-2}\text{T}^{-1}$], and

D_{zz} is the corresponding dispersion coefficient [L^2T^{-1}].

Dispersive fluxes perpendicular to the concentration gradients are calculated as:

$$j_{xz} = -n_e D_{xz} \frac{\partial c}{\partial z} \quad (5.12)$$

$$j_{zx} = -n_e D_{zx} \frac{\partial c}{\partial x} \quad (5.13)$$

with

$$D_{xz} = D_{zx} = (D_L - D_T) \frac{v_x v_z}{|v|^2} = (\alpha_L - \alpha_T) \frac{v_x v_z}{|v|} \quad (5.14)$$

where

j_{xz} is the dispersive flux in horizontal direction due to a vertical concentration gradient $[\text{ML}^{-2}\text{T}^{-1}]$,

j_{zx} is the dispersive flux in vertical direction due to a horizontal concentration gradient $[\text{ML}^{-2}\text{T}^{-1}]$, and

D_{xz}, D_{zx} are the corresponding dispersion coefficients $[\text{L}^2\text{T}^{-1}]$.

Note that D_{xz} and D_{zx} may have negative values if the two components of velocity have opposite signs. D_{xx} and D_{zz} are always positive.

5.3 Diffusion

While dispersion is very closely connected to advection, diffusion is a completely independent process. It results from the Brownian motion of the solute particles and ultimately leads to the removal of concentration gradients even if the groundwater is at rest. The diffusive flux in water is a function of the concentration gradient and is described by Fick's law (*Appelo and Postma, 1996*):

$$j_{diff} = -D_{M,water} \frac{\partial c}{\partial n} \quad (5.15)$$

where

j_{diff} is the diffusive flux per unit area perpendicular to the direction of n $[\text{ML}^{-2}\text{T}^{-1}]$,

$D_{M,water}$ is the diffusion coefficient in water $[\text{L}^2\text{T}^{-1}]$, and

$\frac{\partial c}{\partial n}$ is the concentration gradient in the direction of n $[\text{ML}^{-4}]$.

The diffusion coefficient is a temperature-dependent property of the solute and the fluid medium. In saturated porous media, the diffusion coefficients are smaller than in a water body, because the diffusive flux has to follow the structure of the pore space:

$$D_M = \tau D_{M,water} \quad (5.16)$$

where

D_M is the diffusion coefficient in the porous medium $[\text{L}^2\text{T}^{-1}]$, and

τ is the tortuosity of the porous medium [-].

The tortuosity factor is the ratio of the straight transport distance and the real length of the transport path within the porous medium (*Appelo and Postma, 1996*). The values of τ for groundwater aquifers typically range between 0.5 and 0.8.

In porous media the sediments hamper diffusion. In order to calculate the diffusive flux through a porous medium, equation (5.15) must be multiplied by the effective porosity. Hence, the horizontal and vertical components of diffusion in a vertical cross-section through an aquifer are:

$$j_{diff,x} = -n_e D_M \frac{\partial c}{\partial x} \quad (5.17)$$

$$j_{diff,z} = -n_e D_M \frac{\partial c}{\partial z} \quad (5.18)$$

where

$j_{diff,x}$, $j_{diff,z}$ are the horizontal and the vertical diffusive fluxes per unit vertical and horizontal area, respectively [$\text{ML}^{-2}\text{T}^{-1}$].

5.4 Solute mass flux at sources and sinks

At sources or sinks of groundwater flow, the solute mass flux into or out of the model domain is calculated from the rate of flow and the concentration the water. The calculation is similar to that of advective solute mass flux. While an arbitrary value is assumed for the concentration of the injected water, that of abstracted water is equal to the concentration of the groundwater in the aquifer.

$$j_L = W_L c_L \quad (5.19)$$

$$j_W = W c_W \quad (5.20)$$

where

j_L is the solute mass flux per unit volume of the aquifer due to leakage [$\text{ML}^{-3}\text{T}^{-1}$],

c_L is the concentration of the leakage flow [ML^{-3}],

j_W is the solute mass flux per unit volume of the aquifer due to other sources or sinks [$\text{ML}^{-3}\text{T}^{-1}$], and

c_W is the concentration of the injected or abstracted water [ML^{-3}].

5.5 Transport equation

The two-dimensional transport equation for vertical cross-sections of heterogeneous aquifers can be derived through the combination of the three transport processes described above and the solute mass flux due to external sources or sinks into a balance equation for an infinitesimal control volume:

$$\begin{aligned} \frac{\partial(n_e c)}{\partial t} &= \frac{\partial}{\partial x} \left(n_e (D_{xx} + D_M) \frac{\partial c}{\partial x} + n_e D_{xz} \frac{\partial c}{\partial z} \right) \\ &+ \frac{\partial}{\partial z} \left(n_e (D_{zz} + D_M) \frac{\partial c}{\partial z} + n_e D_{zx} \frac{\partial c}{\partial x} \right) \\ &- \frac{\partial(q_x c)}{\partial x} - \frac{\partial(q_z c)}{\partial z} + W_L c_L + W c_W \end{aligned} \quad (5.21)$$

The left hand side of equation (5.21) represents the rate of change in solute mass stored in the infinitesimal control volume. On the right hand side, the first two terms represent the dispersive and diffusive transport, and the second two terms stand for the advection. Analogously to the equation of groundwater flow (3.22), the last two terms denote solute mass flux due to external sources or sinks. Equation (5.21) is rewritten by expanding the derivatives of the left hand side and the advection terms:

$$\begin{aligned} n_e \frac{\partial c}{\partial t} + c \frac{\partial n_e}{\partial t} &= \frac{\partial}{\partial x} \left(n_e (D_{xx} + D_M) \frac{\partial c}{\partial x} + n_e D_{xz} \frac{\partial c}{\partial z} \right) \\ &+ \frac{\partial}{\partial z} \left(n_e (D_{zz} + D_M) \frac{\partial c}{\partial z} + n_e D_{zx} \frac{\partial c}{\partial x} \right) \\ &- q_x \frac{\partial c}{\partial x} - q_z \frac{\partial c}{\partial z} - c \frac{\partial q_x}{\partial x} - c \frac{\partial q_z}{\partial z} + W_L c_L + W c_W \end{aligned} \quad (5.22)$$

From the groundwater flow equation (3.22) can be seen:

$$- \left(\frac{\partial q_x}{\partial x} + \frac{\partial q_z}{\partial z} \right) = S_S \frac{\partial h_f}{\partial t} - W_L - W \quad (5.23)$$

Substituting the right hand side of equation (5.23) for the corresponding terms in equation (5.22) yields:

$$\begin{aligned} n_e \frac{\partial c}{\partial t} &= \frac{\partial}{\partial x} \left(n_e (D_{xx} + D_M) \frac{\partial c}{\partial x} + n_e D_{xz} \frac{\partial c}{\partial z} \right) \\ &+ \frac{\partial}{\partial z} \left(n_e (D_{zz} + D_M) \frac{\partial c}{\partial z} + n_e D_{zx} \frac{\partial c}{\partial x} \right) \\ &- q_x \frac{\partial c}{\partial x} - q_z \frac{\partial c}{\partial z} - c \left(S_S \frac{\partial h_f}{\partial t} - W_L - W - \frac{\partial n_e}{\partial t} \right) \\ &+ W_L c_L + W c_W \end{aligned} \quad (5.24)$$

Since groundwater is assumed to be incompressible, all changes in groundwater storage are reflected by changes in the effective porosity of the aquifer.

Therefore, continuity demands that the time derivatives of storage and effective porosity are equal:

$$S_S \frac{\partial h_f}{\partial t} = \frac{\partial n_e}{\partial t} \quad (5.25)$$

Substituting the right hand side of equation (5.25) for the storage term in equation (5.24) and dividing both sides by the effective porosity yields:

$$\begin{aligned} \frac{\partial c}{\partial t} = & \frac{1}{n_e} \left[\frac{\partial}{\partial x} \left(n_e (D_{xx} + D_M) \frac{\partial c}{\partial x} + n_e D_{xz} \frac{\partial c}{\partial z} \right) \right. \\ & \left. + \frac{\partial}{\partial z} \left(n_e (D_{zz} + D_M) \frac{\partial c}{\partial z} + n_e D_{zx} \frac{\partial c}{\partial x} \right) \right] \\ & - v_x \frac{\partial c}{\partial x} - v_z \frac{\partial c}{\partial z} + \frac{W_L(c_L - c) + W(c_W - c)}{n_e} \end{aligned} \quad (5.26)$$

From equation (5.25) follows that the effective porosity is not constant in time, unless groundwater flow is in a steady-state equilibrium. The change in effective porosity is a function of the change in hydraulic head (*Goode, 1992*):

$$n_e(t) = n_e(t_0) + \int_{t_0}^t S_S \frac{\partial h_f}{\partial t} dt = n_e(t_0) + S_S (h_f(t) - h_f(t_0)) \quad (5.27)$$

or

$$\Delta n_e = S_S \Delta h_f \quad (5.28)$$

Equation (5.27) or (5.28) can be used to adjust the effective porosity according to the changes in groundwater storage in the course of the simulation. *Goode and Konikow (1991)* evaluate this approach by comparing the results from numerical simulations with and without correction of effective porosity. Ignoring changes in the effective porosity during transient groundwater flow leads to incorrect calculation of the dilution volume, the dispersive fluxes and the velocities of groundwater flow and may result in large errors in the mass balance.

The advection terms in the transport equation (5.26) consist of first order derivatives, while both the dispersion and diffusion terms are second order differential quotients. The advection terms are hyperbolic, whereas the dispersion and diffusion terms are parabolic. Thus, the transport equation is of mixed type (e.g. *Pinder and Shapiro, 1979*). In case advective transport is dominating over dispersion and diffusion, the equation is more hyperbolic. On the other hand, if diffusion and dispersion are the important transport mechanisms, the parabolic character of the equation is emphasized. A simple way of finding the key process in a transport problem is to determine the Peclet-number (*Kinzelbach and Rausch, 1995*):

$$Pe = \frac{|v|l}{D_L} \quad (5.29)$$

where

Pe is the Peclet-number [-], and

l is a characteristic length of the transport problem [L].

For Peclet-numbers smaller than one, dispersion and diffusion are dominant (*Kinzelbach and Rausch, 1995*). Larger Peclet-numbers show that advection is the more important transport process.

Chapter 6

Method of characteristics

Parabolic differential equations like the groundwater flow equation (3.22) or the dispersion and diffusion terms of the transport equation (5.26) can conveniently be solved numerically using the method of finite differences. Applying this method to hyperbolic equations such as the advection-dominated transport equation, however, may lead to severe inaccuracies in the modeled concentrations. This phenomenon is called 'numerical dispersion' and is illustrated in figure 6.1. During the time step, a sharp concentration front leaving the first cell of a one-dimensional column is transported to somewhere within the second cell. The method of finite differences demands that the solute particles entering the cell are immediately spread over the entire cell. As a result, the concentration front does not remain sharp, but it is widened over the entire second cell. The finite differences technique does not properly represent advective transport.

The method of characteristics was originally developed for the solution of hyperbolic differential equations. *Garder et al.* (1964) first adapted it to problems of flow through porous media. Further developments have been presented e.g. by *Pinder and Cooper* (1970), *Reddell and Sunada* (1970), *Bredehoeft and Pinder* (1973), *Konikow and Bredehoeft* (1978), *Sanford and Konikow* (1985), *Konikow et al.* (1996), and *Kipp et al.* (1998). Even though compared to other modeling techniques the method of characteristics may seem underrepresented in the scientific literature (*Holzbecher*, 1998), various applications of the method to hypothetical test cases as well as to field problems have been documented during the past decades (e.g. *Goode and Konikow*, 1991; *Calvache and Pulido-Bosch*, 1997; *Konikow et al.*, 1997; *Oude Essink*, 2000, 2001a; *Van denbohede and Lebbe*, 2002).

Basic to the method of characteristics is the conversion of the transport equation from the Eulerian form to the Lagrangian form. The Eulerian form describes concentration changes at fixed points within a stationary coordinate system due to passing fluid of varying concentration. In contrast, the Lagrangian form of the transport equation describes the concentration changes as observed from points that are moving with the fluid. The latter is also called

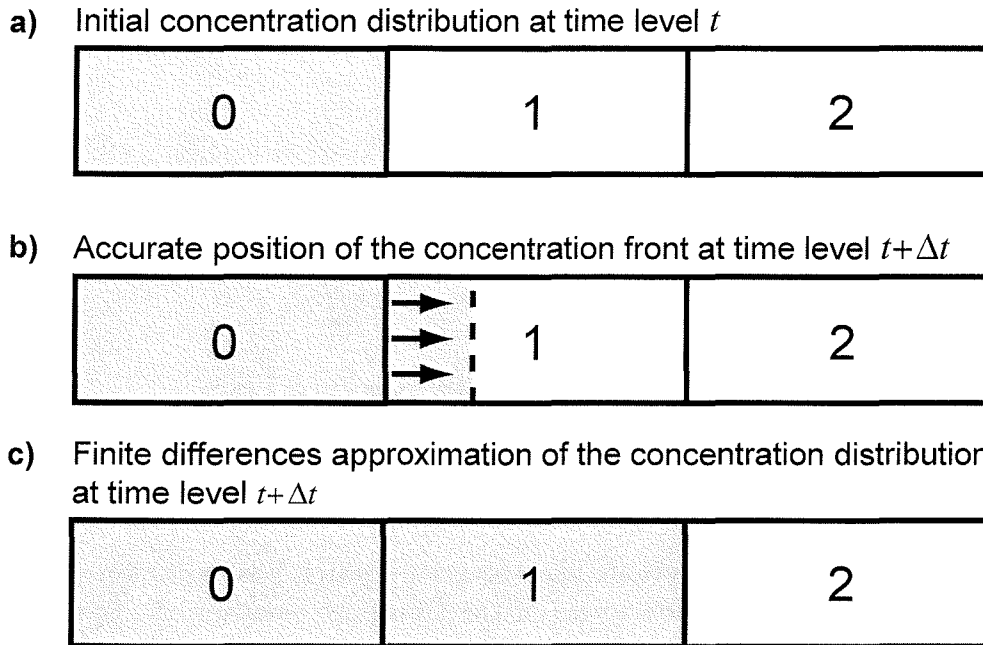


Figure 6.1: The illustration shows a hypothetical one-dimensional aquifer. A concentration front leaving the first cell at the time t (a) has reached a position somewhere within the second cell at the end of the time interval t (b). In the method of finite differences, however, each cell is represented by a single value. For numerical reasons, the solute mass is spread over the entire area of the cell, destroying the sharp concentration front (c). (*Rausch et al.*, 2002, modified)

the ‘material derivative’. For two-dimensional flow in a vertical cross-section, it may be defined as:

$$\frac{dc}{dt} = \frac{\partial c}{\partial t} + \frac{\partial c}{\partial x} \frac{dx}{dt} + \frac{\partial c}{\partial z} \frac{dz}{dt} \quad (6.1)$$

where

$\frac{dc}{dt}$ is the rate of change in concentration as observed from a point flowing with the fluid [$ML^{-3}T^{-1}$], and

$\frac{\partial c}{\partial t}$ is the rate of change in concentration as observed from a fixed point [$ML^{-3}T^{-1}$].

The material derivatives of position are defined by the normal components of groundwater velocity:

$$\frac{dx}{dt} = v_x \quad (6.2)$$

$$\frac{dz}{dt} = v_z \quad (6.3)$$

The time derivative of concentration as observed from a fixed point is given by the transport equation (5.26). Substituting the right hand sides of equations (5.26), (6.2), and (6.3) for the corresponding terms in equation (6.1) yields:

$$\begin{aligned} \frac{dc}{dt} = & \frac{1}{n_e} \left[\frac{\partial}{\partial x} \left(n_e(D_{xx} + D_M) \frac{\partial c}{\partial x} + n_e D_{xz} \frac{\partial c}{\partial z} \right) \right. \\ & \left. + \frac{\partial}{\partial z} \left(n_e(D_{zz} + D_M) \frac{\partial c}{\partial z} + n_e D_{zx} \frac{\partial c}{\partial x} \right) \right] \\ & + \frac{W_L(c_L - c) + W(c_W - c)}{n_e} \end{aligned} \quad (6.4)$$

The solution to the system of equations comprising equations (6.2), (6.3), and (6.4) may be written as:

$$x = x(t) \quad (6.5)$$

$$z = z(t) \quad (6.6)$$

$$c = c(t) \quad (6.7)$$

These functions are called the characteristic curves of the transport equation. Given solutions to equations (6.2), (6.3), and (6.4), the transport equation may be solved by following the characteristic curves. This is accomplished numerically by tracing a set of moving reference points within the stationary coordinates of the finite differences grid (*Konikow and Bredehoeft, 1978*).

The main advantage of the method of characteristics is that it avoids numerical dispersion by separately solving the hyperbolic and the parabolic part of the transport equation. In a first step, the advective transport is calculated by means of particle tracking, resulting in a new concentration distribution which reflects the concentration changes due to advection. In the second step, an explicit scheme is applied to determine the concentration changes due to dispersion, diffusion, and external sources or sinks. The concentration distribution at the new time level is then obtained by adding the concentration change that was calculated in the second step to the concentration determined in the first step. Because the calculation of concentration changes at the position of every single particle would require an enormous computational effort, the concentration changes at the nodes are used as an approximation.

At the end of each time step, the concentrations associated with the particles are updated by applying the same concentration change to the particle that was calculated for the associated node. This way, numerical dispersion is avoided, and concentration fronts remain sharp when passing through a cell.

6.1 Particle tracking

Based on the solution of the finite differences groundwater flow equation, the first step of the method of characteristics consists of tracing particles along

the streamlines. In contrast to other particle tracking methods such as the Random-Walk method, the traced particles are not solute particles, but should be considered as observation points moving along with the groundwater. Thus, a cluster of particles cannot be interpreted as a high concentration and neither does the absence of particles reflect a low concentration. Instead, the method used here is based on maintaining an even distribution of observation points (=particles) throughout the simulation.

For each particle, a record is kept that contains the exact position of the particle as well as a concentration value associated with it. At the beginning of the simulation, tracer particles are placed into each cell of the model grid. It is possible to start from random distributions, however, in the context of this work, each cell initially contains the same number of particles and the particles are spread evenly throughout the area of the cell. Figure 6.2 illustrates that it is convenient to allow only square numbers of particles in each cell, in order to make sure that the initial spacing of the particles is even.

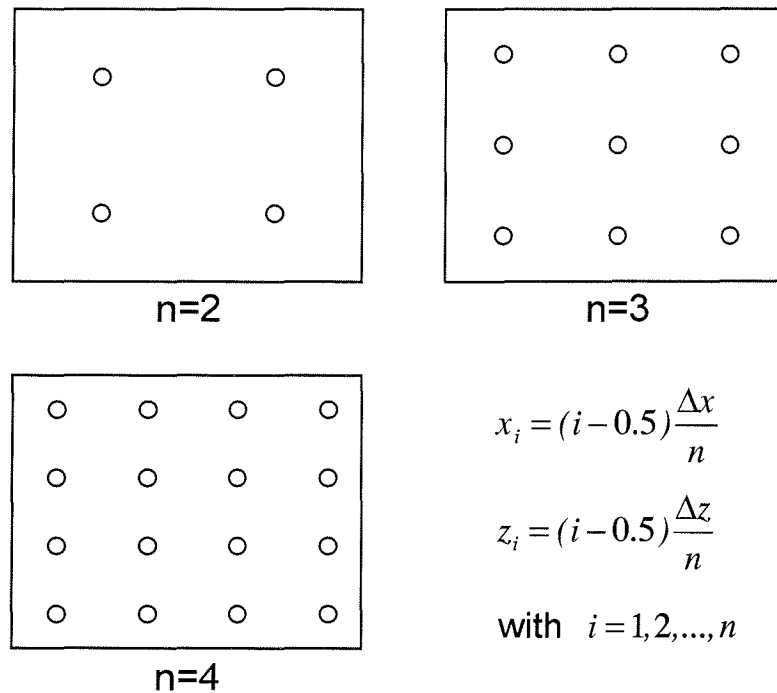


Figure 6.2: In order to ensure an even distribution of tracer points, initially only square numbers of particles are placed into the cells. The initial coordinates of the particles are given by x_i and z_i , relative to the lower left corner of the cell.

Initially, the concentration of the cell is assigned to each particle in the cell:

$$c_0(p_k) = c_0(i, j) \tag{6.8}$$

where

-
- p_k refers to particle number k , which is initially placed into cell (i, j) ,
- $c_0(p_k)$ is the initial concentration value associated with particle p_k [ML^{-3}],
and
- $c_0(i, j)$ is the initial concentration at the node (i, j) [ML^{-3}].

There are several possibilities to calculate the paths of the tracer points. The most common methods are based on either linear or bilinear interpolation of the velocity at the position of the particle. Bilinear particle tracking is used in the original two-dimensional versions of MOC (*Konikow and Bredehoeft, 1978*) and MOC DENSE (*Sanford and Konikow, 1985*), as well as in the version of MOC that was adapted for variable density flow by *Oude Essink (1996)*. The three-dimensional MOC3D (*Konikow et al., 1996*) offers the possibility to choose between linear and bilinear interpolation of horizontal velocity components, while the vertical component is always calculated through linear interpolation. *Goode (1990)* reviews linear and bilinear velocity interpolation and introduces another interpolation method based on piezometric head gradients. *Schafer-Perini and Wilson (1991)* point out that bilinear interpolation as applied by *Konikow and Bredehoeft (1978)* is inconsistent with the flow equation and propose a scheme based on the linear interpolation of specific flow. A very similar algorithm is used in MODPATH (*Pollock, 1994*).

Linear interpolation is consistent with the flow equation and therefore mass-conserving. It preserves discontinuities in velocity caused by abrupt changes in hydraulic conductivity, but it may yield unrealistic velocities in homogeneous aquifers. In these cases, bilinear interpolation gives velocities that are more realistic, but it does not preserve discontinuities in velocity in case of abrupt changes in hydraulic conductivity. Bilinear interpolation is inconsistent with the flow equation and may cause errors in the mass balance. The model that is described here allows the user to choose between linear and bilinear interpolation of velocity. Therefore, both the linear and the bilinear particle tracking scheme are described briefly. A more in-depth discussion of the methods can be found in the publications mentioned above.

6.1.1 Linear interpolation

Assuming that the normal components of groundwater flow are constant along the respective faces of the cell, the flow at an arbitrary point within the cell can be described by two linear functions of the position. For simplification, the coordinates of the point are relative to the lower left corner of the cell and the cell indices (i, j) are omitted.

$$q_x = q_{left} + xm_x \quad (6.9)$$

$$q_z = q_{bottom} + zm_z \quad (6.10)$$

with

$$m_x = \frac{q_{right} - q_{left}}{\Delta x} \quad (6.11)$$

$$m_z = \frac{q_{top} - q_{bottom}}{\Delta z} \quad (6.12)$$

where

q_{left} , q_{right} , q_{top} , q_{bottom} are the specific discharges across the respective faces of the cell [LT^{-1}].

In order to maintain consistency with the groundwater flow equation, the specific discharges are calculated using the harmonic mean of the hydraulic conductivities of the two adjacent cells. Upward flow and flow to the left are positive. The slope m_x or m_z is zero if the corresponding normal component of groundwater flow is constant throughout the cell. Assuming that the porosity is constant within each cell, equations (6.9) and (6.10) can be used in order to express the groundwater flow as time derivative of fluid displacement (*Schafer-Perini and Wilson, 1991*):

$$v_x = \frac{dx}{dt} = \frac{q_{left} + xm_x}{n_e} \quad (6.13)$$

$$v_z = \frac{dz}{dt} = \frac{q_{bottom} + zm_z}{n_e} \quad (6.14)$$

Given that neither of the velocity components is equal to zero, equations (6.13) and (6.14) can be rewritten to obtain:

$$dt = \frac{n_e}{q_{left} + xm_x} dx \quad (6.15)$$

$$dt = \frac{n_e}{q_{bottom} + zm_z} dz \quad (6.16)$$

In this approach, each component of the velocity depends only on one coordinate, the interpolated value of the horizontal velocity does not change with the vertical position, and the vertical velocity is independent of the horizontal position within the cell. Thus, equations (6.15) and (6.16) may be integrated analytically, allowing the relationship of travel distance and time to be determined (*Goode, 1990; Pollock, 1994, e.g.*). The time $\Delta t = t_1 - t_0$ a particle needs to travel from x_0 to x_1 is:

$$\Delta t = \frac{n_e}{m_x} \ln \left| \frac{q_{left} + x_1 m_x}{q_{left} + x_0 m_x} \right| \text{ for } m_x \neq 0 \quad (6.17)$$

$$\Delta t = \frac{n_e}{q_{left}} (x_1 - x_0) \text{ for } m_x = 0 \quad (6.18)$$

Analogously, the time of travel from z_0 to z_1 is:

$$\Delta t = \frac{n_e}{m_z} \ln \left| \frac{q_{bottom} + z_1 m_z}{q_{bottom} + z_0 m_z} \right| \text{ for } m_z \neq 0 \quad (6.19)$$

$$\Delta t = \frac{n_e}{q_{bottom}} (z_1 - z_0) \text{ for } m_z = 0 \quad (6.20)$$

If $v_x(x_0)$ and $v_z(z_0)$ are the components of the initial velocity of a particle that is located at the coordinates (x_0, z_0) in the cell, the path of the particle through the cell can be calculated by transforming equations (6.17) through (6.20). The horizontal position of the particle as a function of time is given by:

$$x(t) = \frac{1}{m_x} \left[v_x(x_0) \exp\left(\frac{tm_x}{n_e}\right) - q_{left} \right] \text{ for } m_x \neq 0 \quad (6.21)$$

$$x(t) = x_0 + tv_x(x_0) \text{ for } m_x = 0 \quad (6.22)$$

In the vertical direction, the path is described by:

$$z(t) = \frac{1}{m_z} \left[v_z(z_0) \exp\left(\frac{tm_z}{n_e}\right) - q_{bottom} \right] \text{ for } m_z \neq 0 \quad (6.23)$$

$$z(t) = z_0 + tv_z(z_0) \text{ for } m_z = 0 \quad (6.24)$$

The linear particle tracking algorithm implemented in the numerical model starts by calculating the initial velocity of the particle in the cell. The signs of the velocity components determine through which two faces of the cell the particle will possibly leave the cell, e.g. if the horizontal component is positive, the particle is forced to exit through the right face of the cell. The times of travel to the exit face in horizontal and in vertical direction can be calculated by applying equations (6.17) through (6.20), as appropriate. The time until the particle reaches the exit face in the horizontal direction is:

$$\Delta t_{Exit,x} = \frac{n_e}{m_x} \ln \left| \frac{q_{left} + x_{Exit} m_x}{v_x(x_0)} \right| \text{ for } m_x \neq 0 \quad (6.25)$$

$$\Delta t_{Exit,x} = \frac{n_e}{v_x(x_0)} (x_{Exit} - x_0) \text{ for } m_x = 0 \quad (6.26)$$

where

$\Delta t_{Exit,x}$ is the time until the particle reaches the horizontal position of the exit face [T], and

x_{Exit} is the horizontal position of the exit face [L], either $x_{Exit} = 0$ for the left face or $x_{Exit} = \Delta x$ for the right face of the cell.

The time until the particle reaches the exit face in the vertical direction is calculated similarly:

$$\Delta t_{Exit,z} = \frac{n_e}{m_z} \ln \left| \frac{q_{bottom} + z_{Exit} m_z}{v_z(z_0)} \right| \text{ for } m_z \neq 0 \quad (6.27)$$

$$\Delta t_{Exit,z} = \frac{n_e}{v_z(z_0)} (z_{Exit} - z_0) \text{ for } m_z = 0 \quad (6.28)$$

where

$\Delta t_{Exit,z}$ is the time until the particle reaches the vertical position of the exit face [T], and

z_{Exit} is the vertical position of the exit face [L], either $z_{Exit} = 0$ for the lower face or $z_{Exit} = \Delta z$ for the upper face of the cell.

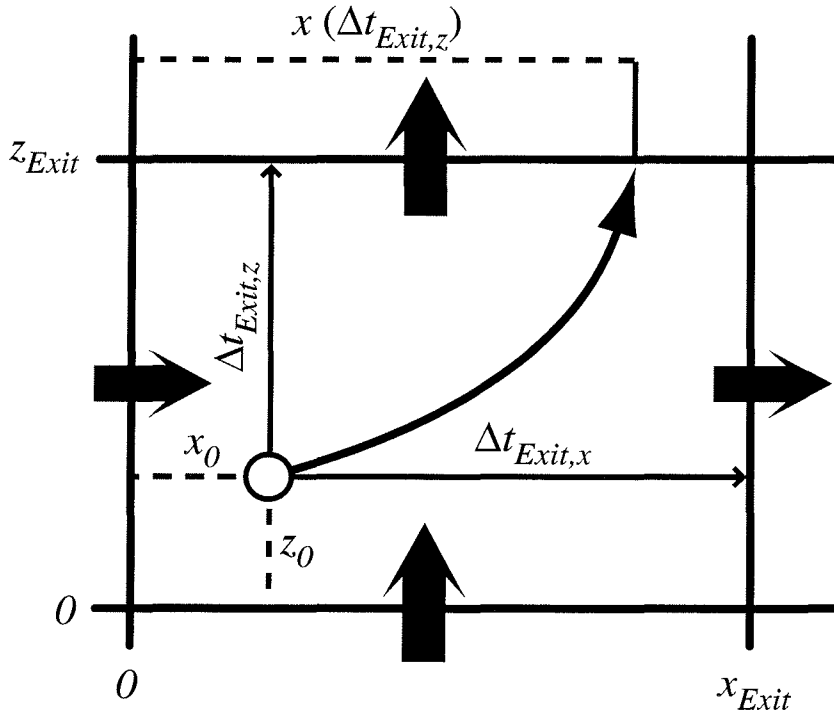


Figure 6.3: At the beginning of the tracking step, the particle is at the position marked by the circle. The linear tracking algorithm first calculates the initial velocity of the particle by linear interpolation from the specific discharges through the faces of the cell (black arrows). Next, the algorithm compares the times of travel to the potential exit faces determined by the initial velocity. In the illustrated case, the particle reaches the upper face of the cell first. The x -coordinate on the exit face is given by $x(\Delta t_{Exit,z})$. (Pollock, 1994, modified)

Special care must be taken if groundwater flows into the cell from two opposite directions. In this case, the particle cannot leave the cell in either of these two

directions. Consequently, the exit time in the respective direction cannot be calculated. If groundwater is flowing into the cell from all four sides, the cell is a strong sink, from which no particle can escape. As described later, particles that enter into sinks are removed from the model domain.

The value Δt_{Exit} indicates the time after which a particle leaves the cell of observation. If $\Delta t_{Exit,x}$ is smaller than $\Delta t_{Exit,z}$, the particle will leave the cell through the left or right face of the cell. If $\Delta t_{Exit,z}$ is smaller than $\Delta t_{Exit,x}$, the particle will leave through the upper or lower face of the cell (figure 6.3). Thus, the smallest value determines the time after which the particle leaves the cell:

$$\Delta t_{Exit} = \min(\Delta t_{Exit,x}, \Delta t_{Exit,z}) \quad (6.29)$$

where

Δt_{Exit} is the time until the particle leaves the cell [T].

If the exit time Δt_{Exit} is smaller than the given transport time step, the particle will leave the current cell before the end of the transport time step. In this case, the particle is moved to the coordinates $(x(\Delta t_{Exit}), z(\Delta t_{Exit}))$ on the exit face and the exit time is subtracted from the transport time step. Since the interpolation functions are not valid outside the area of the current cell, the procedure must be repeated using the values of the new cell, into which the particle is entering. Depending on the length of the transport time step it is possible that this procedure must be repeated several times within a single transport step. The length of the transport time step has no effect on the accuracy of the solution, because the interpolation function was integrated analytically. Nevertheless, any changes in groundwater flow during the transport time step are neglected. Therefore, it is advisable to choose small transport time steps if the groundwater flow is not at steady state.

6.1.2 Bilinear interpolation

In case bilinear interpolation is applied, each component of the velocity at the position of the particle is expressed as a function of both the horizontal and the vertical position of the particle (figure 6.4). These functions cannot be integrated analytically. Therefore, every particle is moved proportionally to its initial velocity and the length of the transport time step, applying an explicit finite differences scheme:

$$x_{t+\Delta t}(p_k) = x_t(p_k) + \Delta t v_x(p_k) \quad (6.30)$$

$$z_{t+\Delta t}(p_k) = z_t(p_k) + \Delta t v_z(p_k) \quad (6.31)$$

where

$x_{t+\Delta t}(p_k), z_{t+\Delta t}(p_k)$ are the coordinates of the particle at the end of the transport time step [L],

$x_t(p_k), z_t(p_k)$ are the coordinates of the particle at the beginning of the transport time step [L], and

$v_x(p_k), v_z(p_k)$ is the velocity of the particle at the beginning of the time step [LT⁻¹].

Equations (6.30) and (6.31) will move the particle closely along the streamline, as long as the transport time step is sufficiently small. In contrast to the linear particle tracking scheme, the length of the transport time step directly affects the accuracy of the calculated path, even if groundwater flow is at steady state.

6.1.3 Concentration after advection

After all of the particles have been moved to their new positions by either linear or bilinear tracking, the simulation of advection during the current transport step is complete and subsequently the concentration distribution after advection is determined. Therefore the mean value of the concentrations associated with the particles in a cell is calculated by:

$$c^{t+adv}(i, j) = \frac{1}{n} \sum_{k=1}^n c(p_k) \quad (6.32)$$

where

$c^{t+adv}(i, j)$ is the average concentration of the particles in cell (i, j) after particle tracking [ML⁻³],

n is the number of particles in the cell, and

$c(p_k)$ is the concentration value associated with the particle p_k [ML⁻³].

This average particle concentration only reflects the concentration change caused by advective transport within the model domain. The change in concentration due to diffusion, dispersion, sources, and sinks is calculated in a separate step.

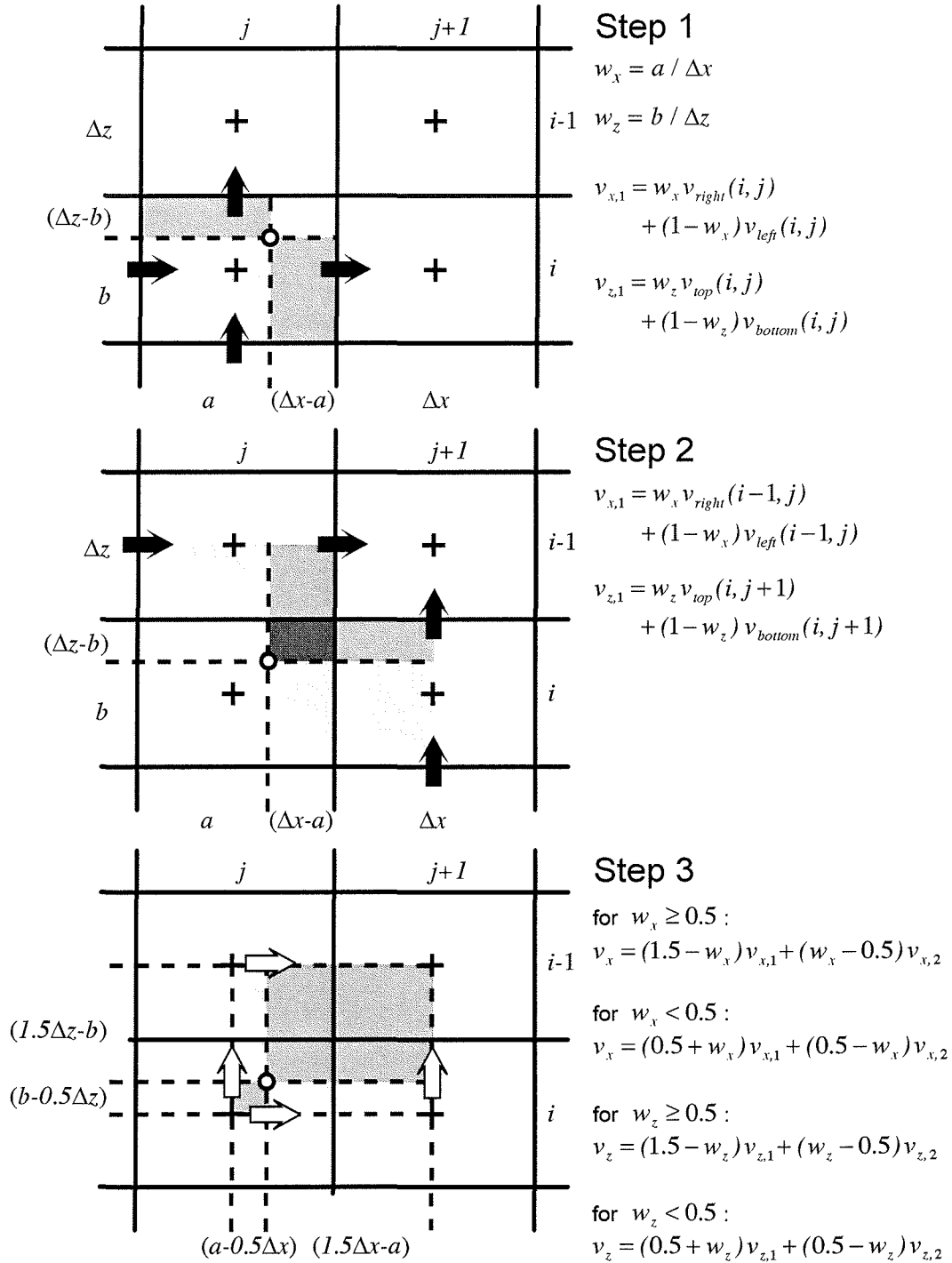


Figure 6.4: v_{left} , v_{right} , v_{top} , v_{bottom} are the velocity components normal to the respective faces of the cell. They are indicated by black arrows. The white arrows represent interpolated velocity components. The bilinear interpolation scheme involves three steps. In the first step, a velocity value is interpolated from the internodal velocities that are closest to the position of the tracer point. Another value is obtained in the same way from the second-closest internodal velocities in the next step. In the last step, the velocity at the position of the tracer point is interpolated using the velocity values found in the first two steps. (Kinzelbach, 1986, modified)

6.1.4 Redistributions

At the beginning of the simulation, each cell of the model grid contains the same number of tracer particles. However, it is possible that some cells in areas of divergent flow become void of particles in the course of the simulation process. Advective transport into and out of such void cells can not be calculated. Consequently, this phenomenon results in inaccuracies of the solution. This problem can be reduced by increasing the initial number of particles per cell, though it cannot be abolished completely. In order to constrain the numerical error, the number of void cells allowed should be limited to a small percentage of the grid (*Konikow and Bredehoeft, 1978*). If this limit is exceeded, the particle distribution can be reinitialized using the most current concentration values, albeit this results in some numerical dispersion.

6.2 Dispersion, diffusion, sources and sinks

The effects of diffusion, dispersion, and external sources and sinks on the concentration distribution are determined in the second step of the method of characteristics. The transport equation (5.26) indicates that advection, diffusion, dispersion, and the concentration changes due to external sources or sinks are interrelated and occur at the same time. Consequently, all terms of the transport equation should be solved simultaneously. However, using the method of characteristics, this is not possible, since the advective transport is determined by means of particle tracking, while the other terms of the transport equation are calculated separately. In order to account for changes in concentration due to advection, the mean value of the concentration at the beginning of the time step and the concentration after advective transport is used to calculate the required concentration gradients (*Konikow et al., 1996*):

$$c'(i, j) = \frac{c^t(i, j) + c^{t+adv}(i, j)}{2} \quad (6.33)$$

where

$c'(i, j)$ is the mean value of the concentration at the beginning of the transport time step and the average concentration of the particles in the cell after particle tracking [ML^{-3}], and

$c^t(i, j)$ is the concentration at the node (i, j) at the beginning of the transport time step [ML^{-3}].

A finite differences approximation of the diffusive and dispersive transport processes can be derived by calculating the concentration change in a representative elementary volume (REV) during the time step $[t, t + \Delta t]$:

$$\begin{aligned} \Delta c(i, j) = & \frac{\Delta t}{n_e} \left(\frac{J_{left}(i, j) + J_{right}(i, j) + J_{top}(i, j) + J_{bottom}(i, j)}{\Delta x \Delta z} \right. \\ & + W_L(i, j)(c_L(i, j) - c'(i, j)) \\ & \left. + W(i, j)(c_W(i, j) - c'(i, j)) \right) \end{aligned} \quad (6.34)$$

where

$\Delta c(i, j)$ is the concentration change at the node due to dispersive and diffusive transport and from sources or sinks [ML^{-3}], and

$J_{left}, J_{right}, J_{top}, J_{bottom}$ are the solute mass fluxes across the respective faces of the cell (i, j) [$\text{ML}^{-1}\text{T}^{-1}$] (positive for inflow and negative for outflow).

Analogous to the derivation of the finite differences flow equation in section 4.1 on page 21, solute mass fluxes into the REV are positive, while fluxes leaving the REV are negative. The solute mass fluxes caused by dispersion and diffusion are calculated as described in sections 5.2 and 5.3 (p. 38ff).

The solute mass flux across the left face of the cell is:

$$\begin{aligned} J_{left}(i, j) = & n_e(i, j - 0.5) \left[- (D_{xx}(i, j - 0.5) + D_M) \frac{\Delta c_x(i, j - 0.5)}{\Delta x} \right. \\ & \left. - D_{xz}(i, j - 0.5) \frac{\Delta c_z(i, j - 0.5)}{\Delta z} \right] \Delta z \end{aligned} \quad (6.35)$$

where

$n_e(i, j - 0.5)$ is the mean effective porosity [-] at the left face of the cell,

$D_{xx}(i, j - 0.5)$ is the coefficient for the dispersive flux due to a horizontal gradient [L^2T^{-1}],

$D_{xz}(i, j - 0.5)$ is the coefficient for the dispersive flux due to a vertical gradient [L^2T^{-1}],

$\frac{\Delta c_x(i, j - 0.5)}{\Delta x}$ is the horizontal concentration gradient [ML^{-4}], and

$\frac{\Delta c_z(i, j - 0.5)}{\Delta z}$ is the vertical concentration gradient at the left face of the cell [ML^{-4}].

The solute mass flux across the right face of the cell is:

$$\begin{aligned}
 J_{right}(i, j) = n_e(i, j + 0.5) & \left[(D_{xx}(i, j + 0.5) + D_M) \frac{\Delta c_x(i, j + 0.5)}{\Delta x} \right. \\
 & \left. + D_{xz}(i, j + 0.5) \frac{\Delta c_z(i, j + 0.5)}{\Delta z} \right] \Delta z \quad (6.36)
 \end{aligned}$$

where

$n_e(i, j + 0.5)$ is the mean effective porosity at the right face of the cell [-],

$D_{xx}(i, j + 0.5)$ is the coefficient for the dispersive flux due to a horizontal gradient [L^2T^{-1}],

$D_{xz}(i, j + 0.5)$ is the coefficient for the dispersive flux due to a vertical gradient [L^2T^{-1}],

$\frac{\Delta c_x(i, j + 0.5)}{\Delta x}$ is the horizontal concentration gradient [ML^{-4}],

$\frac{\Delta c_z(i, j + 0.5)}{\Delta z}$ is the vertical concentration gradient at the right face of the cell [ML^{-4}].

The solute mass flux across the upper face of the cell is:

$$\begin{aligned}
 J_{top}(i, j) = n_e(i - 0.5, j) & \left[(D_{zz}(i - 0.5, j) + D_M) \frac{\Delta c_z(i - 0.5, j)}{\Delta z} \right. \\
 & \left. + D_{zx}(i - 0.5, j) \frac{\Delta c_x(i - 0.5, j)}{\Delta x} \right] \Delta x \quad (6.37)
 \end{aligned}$$

where

$n_e(i - 0.5, j)$ is the mean effective porosity at the upper face of the cell [-],

$D_{zz}(i - 0.5, j)$ is the coefficient for the dispersive flux due to a vertical gradient [L^2T^{-1}],

$D_{zx}(i - 0.5, j)$ is the coefficient for the dispersive flux due to a horizontal gradient [L^2T^{-1}],

$\frac{\Delta c_z(i - 0.5, j)}{\Delta z}$ is the vertical concentration gradient [ML^{-4}], and

$\frac{\Delta c_x(i - 0.5, j)}{\Delta x}$ is the horizontal concentration gradient at the upper face of the cell [ML^{-4}].

The solute mass flux across the lower face of the cell is

$$J_{bottom}(i, j) = n_e(i + 0.5, j) \left[- (D_{zz}(i + 0.5, j) + D_M) \frac{\Delta c_z(i + 0.5, j)}{\Delta z} - D_{zx}(i + 0.5, j) \frac{\Delta c_x(i + 0.5, j)}{\Delta x} \right] \Delta x \quad (6.38)$$

where

$n_e(i + 0.5, j)$ is the mean effective porosity at the lower face of the cell [-],

$D_{zz}(i + 0.5, j)$ is the coefficient for the dispersive flux due to a vertical gradient [L²T⁻¹],

$D_{zx}(i + 0.5, j)$ is the coefficient for the dispersive flux due to a horizontal gradient [L²T⁻¹],

$\frac{\Delta c_z(i+0.5)}{\Delta z}$ is the vertical concentration gradient [ML⁻⁴], and

$\frac{\Delta c_x(i+0.5, j)}{\Delta x}$ is the horizontal concentration gradient at the lower face of the cell [ML⁻⁴].

6.2.1 Mean effective porosity

In analogy with the mean hydraulic conductivities, the horizontal and vertical mean effective porosities are defined as harmonic means of the value of the cell and its neighbor. In the horizontal direction the mean effective porosity of two adjacent cells is:

$$n_e(i, j \pm 0.5) = \frac{2n_e(i, j)n_e(i, j \pm 1)}{n_e(i, j) + n_e(i, j \pm 1)} \quad (6.39)$$

and in the vertical direction, the mean effective porosity is:

$$n_e(i, j \pm 0.5) = \frac{2n_e(i, j)n_e(i \pm 1, j)}{n_e(i, j) + n_e(i \pm 1, j)} \quad (6.40)$$

6.2.2 Velocity components at cell faces

Both components of the groundwater velocity at all four borders of the cell are needed to calculate the dispersion coefficients according to equations (5.9),

(5.11), and (5.14). The calculation of the velocity component normal to the respective cell face is straightforward:

$$v_x(i, j - 0.5) = \frac{q_{left}}{n_e(i, j - 0.5)} \quad (6.41)$$

$$v_x(i, j + 0.5) = \frac{q_{right}}{n_e(i, j + 0.5)} \quad (6.42)$$

$$v_z(i - 0.5, j) = \frac{q_{top}}{n_e(i - 0.5, j)} \quad (6.43)$$

$$v_z(i + 0.5, j) = \frac{q_{bottom}}{n_e(i + 0.5, j)} \quad (6.44)$$

where

$v_x(i, j - 0.5)$ is the horizontal velocity at the left face of the cell [LT^{-1}],

$v_x(i, j + 0.5)$ is the horizontal velocity at the right face of the cell [LT^{-1}],

$v_z(i - 0.5, j)$ is the vertical velocity at the upper face of the cell [LT^{-1}], and

$v_z(i + 0.5, j)$ is the vertical velocity at the lower face of the cell [LT^{-1}].

The velocity components parallel to the faces of the cell can be interpolated as follows:

$$v_z(i, j - 0.5) = \frac{v_z(i - 0.5, j - 1) + v_z(i + 0.5, j - 1)}{2} + \frac{v_z(i - 0.5, j) + v_z(i + 0.5, j)}{2} \quad (6.45)$$

$$v_z(i, j + 0.5) = \frac{v_z(i - 0.5, j + 1) + v_z(i + 0.5, j + 1)}{2} + \frac{v_z(i - 0.5, j) + v_z(i + 0.5, j)}{2} \quad (6.46)$$

$$v_x(i - 0.5, j) = \frac{v_x(i - 1, j - 0.5) + v_x(i - 1, j + 0.5)}{2} + \frac{v_x(i, j - 0.5) + v_x(i, j + 0.5)}{2} \quad (6.47)$$

$$v_x(i + 0.5, j) = \frac{v_x(i + 1, j - 0.5) + v_x(i + 1, j + 0.5)}{2} + \frac{v_x(i, j - 0.5) + v_x(i, j + 0.5)}{2} \quad (6.48)$$

where

$v_z(i, j - 0.5)$ is the vertical velocity at the left face of the cell [LT⁻¹],

$v_z(i, j + 0.5)$ is the vertical velocity at the right face of the cell [LT⁻¹],

$v_x(i - 0.5, j)$ is the horizontal velocity at the upper face of the cell [LT⁻¹], and

$v_x(i + 0.5, j)$ is the horizontal velocity at the lower face of the cell [LT⁻¹].

6.2.3 Concentration gradients at cell faces

While only four hydraulic gradients need to be calculated for the finite differences flow equation, the dispersion terms in equations (6.35) through (6.38) make use of eight different concentration gradients. In the context of this work, they are defined according to equations (6.49) through (6.56) (e.g. *Kinzelbach, 1986; Rausch et al., 2002*). Figure 6.5 illustrates which cells are involved in the calculation of the gradients.

The concentration gradients at the left face of the cell are:

$$\frac{\Delta c_x(i, j - 0.5)}{\Delta x} = \frac{c'(i, j) - c'(i, j - 1)}{\Delta x} \quad (6.49)$$

$$\begin{aligned} \frac{\Delta c_z(i, j - 0.5)}{\Delta z} &= \frac{c'(i - 1, j - 1) - c'(i + 1, j - 1)}{4\Delta z} \\ &+ \frac{c'(i - 1, j) - c'(i + 1, j)}{4\Delta z} \end{aligned} \quad (6.50)$$

The concentration gradients at the right face of the cell are:

$$\frac{\Delta c_x(i, j + 0.5)}{\Delta x} = \frac{c'(i, j + 1) - c'(i, j)}{\Delta x} \quad (6.51)$$

$$\begin{aligned} \frac{\Delta c_z(i, j + 0.5)}{\Delta z} &= \frac{c'(i - 1, j + 1) - c'(i + 1, j + 1)}{4\Delta z} \\ &+ \frac{c'(i - 1, j) - c'(i + 1, j)}{4\Delta z} \end{aligned} \quad (6.52)$$

The concentration gradients at the upper face of the cell are:

$$\frac{\Delta c_z(i - 0.5, j)}{\Delta z} = \frac{c'(i - 1, j) - c'(i, j)}{\Delta z} \quad (6.53)$$

$$\begin{aligned} \frac{\Delta c_x(i - 0.5, j)}{\Delta x} &= \frac{c'(i - 1, j + 1) - c'(i - 1, j - 1)}{4\Delta z} \\ &+ \frac{c'(i, j + 1) - c'(i, j - 1)}{4\Delta x} \end{aligned} \quad (6.54)$$

The concentration gradients at the lower face of the cell are:

$$\frac{\Delta c_z(i+0.5, j)}{\Delta z} = \frac{c'(i, j) - c'(i+1, j)}{\Delta z} \quad (6.55)$$

$$\begin{aligned} \frac{\Delta c_x(i+0.5, j)}{\Delta x} &= \frac{c'(i+1, j+1) - c'(i+1, j-1)}{4\Delta z} \\ &+ \frac{c'(i, j+1) - c'(i, j-1)}{4\Delta x} \end{aligned} \quad (6.56)$$

6.2.4 Concentration changes at the nodes

The concentration change due to diffusion, dispersion, sources, and sinks at the node (i, j) during the time interval $[t, t + \Delta t]$ can be calculated by substituting the right hand sides of equations (6.35) through (6.38) for the corresponding terms in equation (6.34):

$$\begin{aligned} \Delta c = & \left[\frac{n_e(i, j-0.5)}{\Delta x} \left((D_{xx}(i, j-0.5) + D_M) \frac{\Delta c_x(i, j-0.5)}{\Delta x} - D_{xz}(i, j-0.5) \frac{\Delta c_z(i, j-0.5)}{\Delta z} \right) \right. \\ & - \frac{n_e(i, j+0.5)}{\Delta x} \left((D_{xx}(i, j+0.5) + D_M) \frac{\Delta c_x(i, j+0.5)}{\Delta x} + D_{xz}(i, j+0.5) \frac{\Delta c_z(i, j+0.5)}{\Delta z} \right) \\ & - \frac{n_e(i-0.5, j)}{\Delta z} \left((D_{zz}(i-0.5, j) + D_M) \frac{\Delta c_z(i-0.5, j)}{\Delta z} + D_{zx}(i-0.5, j) \frac{\Delta c_x(i-0.5, j)}{\Delta x} \right) \\ & + \frac{n_e(i+0.5, j)}{\Delta z} \left((D_{zz}(i+0.5, j) + D_M) \frac{\Delta c_z(i+0.5, j)}{\Delta z} + D_{zx}(i+0.5, j) \frac{\Delta c_x(i+0.5, j)}{\Delta x} \right) \\ & \left. + W_L(c_L - c') + W(c_W - c) \right] \frac{\Delta t}{n_e(i, j)} \end{aligned} \quad (6.57)$$

The concentration change calculated for the node cannot be applied directly to the particles in all cases in the same way, because this could result in assigning negative concentration values to the particles. If the concentration change is positive, the increase can simply be added to the concentration values associated with the particles in the cell:

$$c^{t+\Delta t}(p_k) = c^t(p_k) + \Delta c(i, j) \quad (6.58)$$

where

$c^{t+\Delta t}(p_k)$ is the new concentration value associated with the particle p_k at the new time level $t + \Delta t$ [ML^{-3}], and

$c^t(p_k)$ is the old concentration value from the previous time level t [ML^{-3}].

On the other hand, if the concentration change is negative, the concentration values of the particles in the cell are decreased using the same factor as the relative decrease of the concentration at the node:

$$c^{t+\Delta t}(p_k) = c^t(p_k) \frac{c^{t+\Delta t}(i, j)}{c^t(i, j)} \quad (6.59)$$

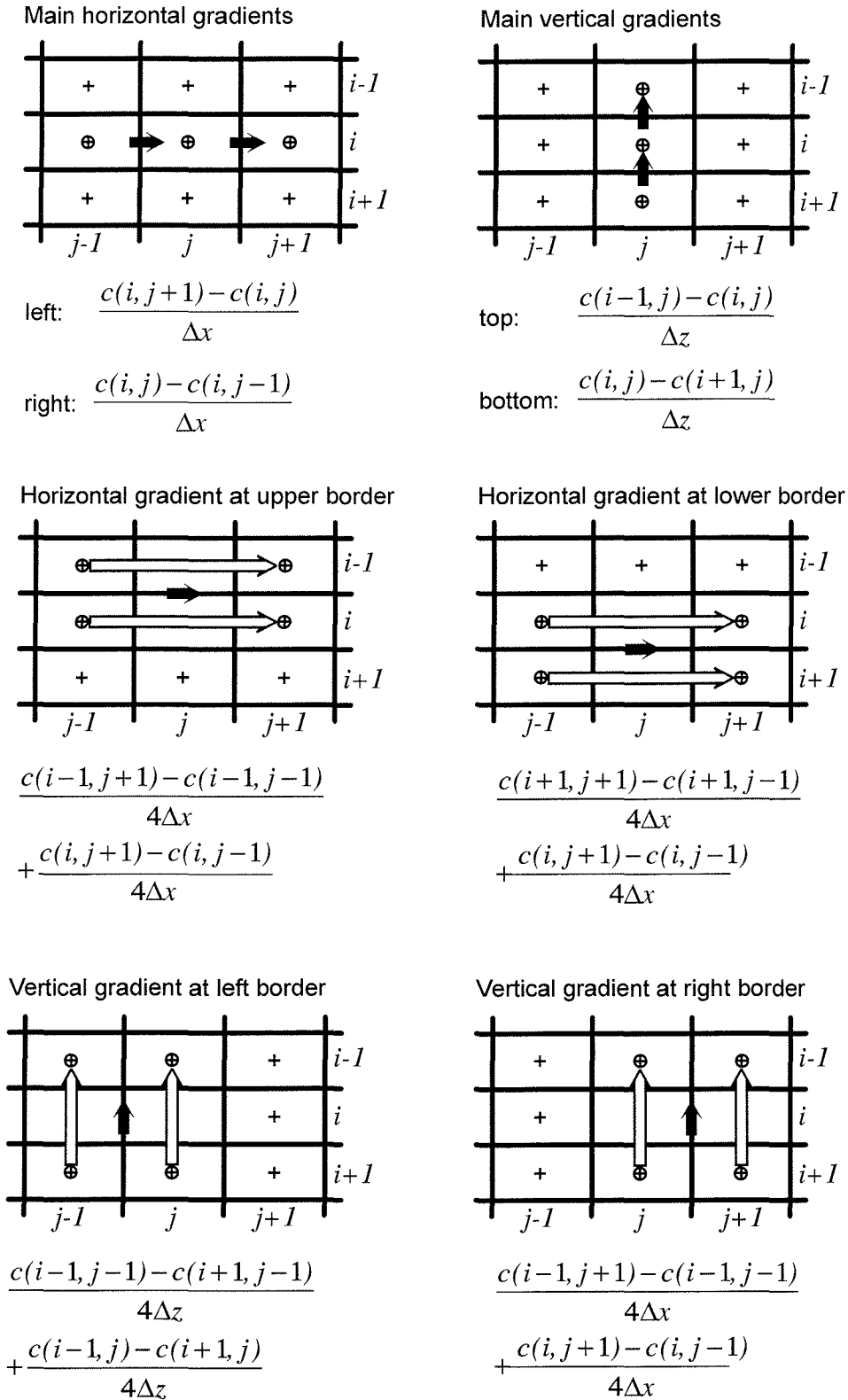


Figure 6.5: Eight different concentration gradients are used for the calculation of the dispersive flux between a cell and the four adjacent cells. The black arrows indicate the location and the positive direction of the required gradients, whereas the white arrows represent the concentration gradients used for interpolation. (Kinzelbach, 1986, modified)

where

$c^{t+\Delta t}(i, j)$ is the new concentration [ML⁻³], and

$c^t(i, j)$ is the old concentration at the node (i, j) [ML⁻³].

This technique is mass conserving for the cell, avoiding the calculation of negative concentration values which could result from routine subtraction of the nodal concentration changes.

6.3 Determination of the transport time step

The solution of the groundwater flow equation by means of an implicit numerical method as described above is unconditionally stable for any length of time step, although short time steps improve the accuracy of the result. Since the explicit solution of the dispersive transport is associated with several stability criteria that restrict the length of the time step, the transport simulation often requires shorter time steps than the flow simulation. In case shorter transport time steps are needed, the flow time step can be subdivided into several transport time steps:

$$\Delta t_F = \Delta t_T + \Delta t_T + \Delta t_T + \dots \quad (6.60)$$

where

Δt_F is the length of the flow time step [T], and

Δt_T is the length of the transport time step [T].

The time step used in the transport part of the model must satisfy all of the three criteria described below.

6.3.1 Travel distance criterion

The accuracy of bilinear particle tracking directly depends on the length of the employed time step. Since both the linear and the bilinear particle tracking scheme neglect that the velocity field may change in the course of the time step, the length of the time step must be chosen very carefully to avoid inaccuracies resulting from transient groundwater flow. A simple way to limit the length of the time step is to define a maximum relative distance across a grid cell, which a particle is allowed to move during a single time step:

$$|v_x(p_k)| \Delta t < \beta \Delta x \quad (6.61)$$

$$|v_z(p_k)| \Delta t < \beta \Delta z \quad (6.62)$$

where

β is the fraction of the cell width and height, which a particle is allowed to travel during a single transport time step ($0 < \beta < 1$) [-].

Consequently, the limit for the transport time step is derived from the minimum and maximum values of the velocity components between the nodes over the entire model grid:

$$\Delta t < \min_{grid} \left(\frac{\beta \Delta x}{\max_{grid} |v_x|}, \frac{\beta \Delta z}{\max_{grid} |v_z|} \right) \quad (6.63)$$

In particular, it should be avoided that a particle crosses an entire cell during a single time step ($\beta > 1$). This criterion is in fact quite similar to the Courant criterion for the stability of explicit solutions of the flow equation.

6.3.2 Neumann-criterion

The Neumann-criterion defines a second limit for the transport time step. It states that a concentration gradient must not be reversed by dispersive or diffusive transport alone. The Neuman criterion is explained through the following example (*Bear, 1979*):

Consider one cell of the grid and its four direct neighbors. Let the concentration in the cell be c_1 , while the concentration in all of the four other cells is c_2 , with $c_2 > c_1$. Consequently, the concentration gradients into the cell from all sides are equal. Neglecting advection, the total dispersive and diffusive flux into the cell is given by

$$J_{total} = 2n_e \left((D_{xx} + D_M) \frac{c_2 - c_1}{\Delta x} \Delta z + (D_{zz} + D_M) \frac{c_2 - c_1}{\Delta x} \right) \quad (6.64)$$

where

J_{total} is the sum of the solute mass fluxes into the cell [$ML^{-1}T^{-1}$].

The flux caused by dispersion and diffusion during the time interval must be equal to the change in solute mass storage within the cell:

$$2n_e \left((D_{xx} + D_M) \frac{c_2 - c_1}{\Delta x} \Delta z + (D_{zz} + D_M) \frac{c_2 - c_1}{\Delta x} \right) \Delta t = n_e \Delta c \Delta x \Delta z \quad (6.65)$$

Or, after rewriting:

$$\left(\frac{D_{xx} + D_M}{\Delta x^2} + \frac{D_{zz} + D_M}{\Delta z^2} \right) \Delta t = \frac{\Delta c}{2(c_2 - c_1)} \quad (6.66)$$

where

Δc is the concentration change in the cell $[\text{ML}^{-3}]$ during the time step Δt .

At the end of the time step Δt , the concentration in the cell cannot be greater than the initial concentration in the surrounding cells. The concentration change in the cell during the time interval must be equal to or less than the concentration difference. It follows the Neumann-criterion:

$$\Delta t \leq \min_{grid} \left(\frac{1}{2 \left(\frac{D_{xx} + D_M}{\Delta x^2} + \frac{D_{zz} + D_M}{\Delta z^2} \right)} \right) \quad (6.67)$$

6.3.3 Source criterion

External sources or sinks define another limit for the length of the time step in the explicit scheme. In a grid cell, the concentration change Δc due to mixing of groundwater with the concentration c and recharged water with the concentration c_W cannot exceed the difference between those two concentrations:

$$\frac{\Delta c}{c_W - c} \leq 1 \quad (6.68)$$

From equation (6.57) can be seen that the change in solute mass storage due to recharge from an external source or sink is:

$$n_e \Delta c \Delta x \Delta z = W \Delta x \Delta z (c_W - c) \Delta t \quad (6.69)$$

Or, after rewriting:

$$\frac{\Delta c}{c_W - c} = \frac{W}{n_e} \Delta t \quad (6.70)$$

Comparing equations (6.68) and (6.70) shows that the limit for the transport time step is:

$$\Delta t \leq \min_{grid} \left(\frac{n_e}{W} \right) \quad (6.71)$$

Chapter 7

Coupling flow and transport

Most solute transport models consist of two parts. In the first, the groundwater flow equation is solved, providing information about the velocity field. In the second part this velocity field is used to solve the transport equation. Commonly, smaller time steps are used for the transport simulation compared to the flow simulation, because the latter is less error-prone. If density differences due to variable solute concentrations are neglected, the coupling between the flow and transport part of the model is unidirectional. Thus the simulated velocity field determines the transport simulation. No feedback effects on groundwater flow occur.

In contrast, the variable density flow model described here involves bi-directional coupling of flow and transport. The concentration changes computed by the transport model directly translate into density changes, which in turn affect the flow of groundwater. Consequently, the density distribution has to be recalculated from the new concentration distribution at the beginning of each flow step.

7.1 Conversion from concentration to density

In the context of this work, it is assumed that the density of groundwater depends solely on the solute concentration, and that the relation between density and concentration is linear. The conversion from solute concentration to density is given by:

$$\rho(i, j) = \rho_f + c(i, j) \frac{\rho_{ref} - \rho_f}{c_{ref}} \quad (7.1)$$

where

ρ_{ref} is the reference density [ML⁻³], and

c_{ref} is the reference concentration [ML⁻³].

7.2 Simulation process

The simulation process presented here is divided into a flow part and a transport part (figure 7.1). Starting with an initial distribution of freshwater heads and densities, the implicit solution of the flow equation yields the new distribution of freshwater heads at the end of each time step. These new head values along with the densities at the beginning of the time step are used to calculate the velocity field, which then forms the interface to the second part of the simulation process.

The transport equation is solved following to separate tracks. First the advection terms are calculated and subsequently the terms related to dispersion, diffusion, sources, and sinks are solved. Advective transport is calculated by moving the tracer particles according to the velocity field which was previously calculated in the flow part. The particle tracking procedure generates a new concentration distribution, reflecting the changes due to advection. Then, an intermediate concentration distribution is calculated considering the concentrations at the beginning of the time step and those after advection.

The calculation of the dispersion coefficients occurs following the second track, also using the velocities calculated in the flow part. Applying an explicit algorithm, the concentration changes due to dispersion, diffusion, sources, and sinks are derived using the intermediate concentration values together with the dispersion coefficients. These concentration changes are applied to the concentration values after advection to obtain the new concentration distribution at the end of the time step. Finally, the new concentration values are converted into the new density distribution, which will be reflected in the flow part of the next simulation step.

Consequently, the density distribution is the second interface between flow and transport. While the velocity field links the transport part to the flow part, the density distribution connects the flow part to the transport part of the simulation, resulting in bi-directional coupling between flow and transport in density-dependent flow models.

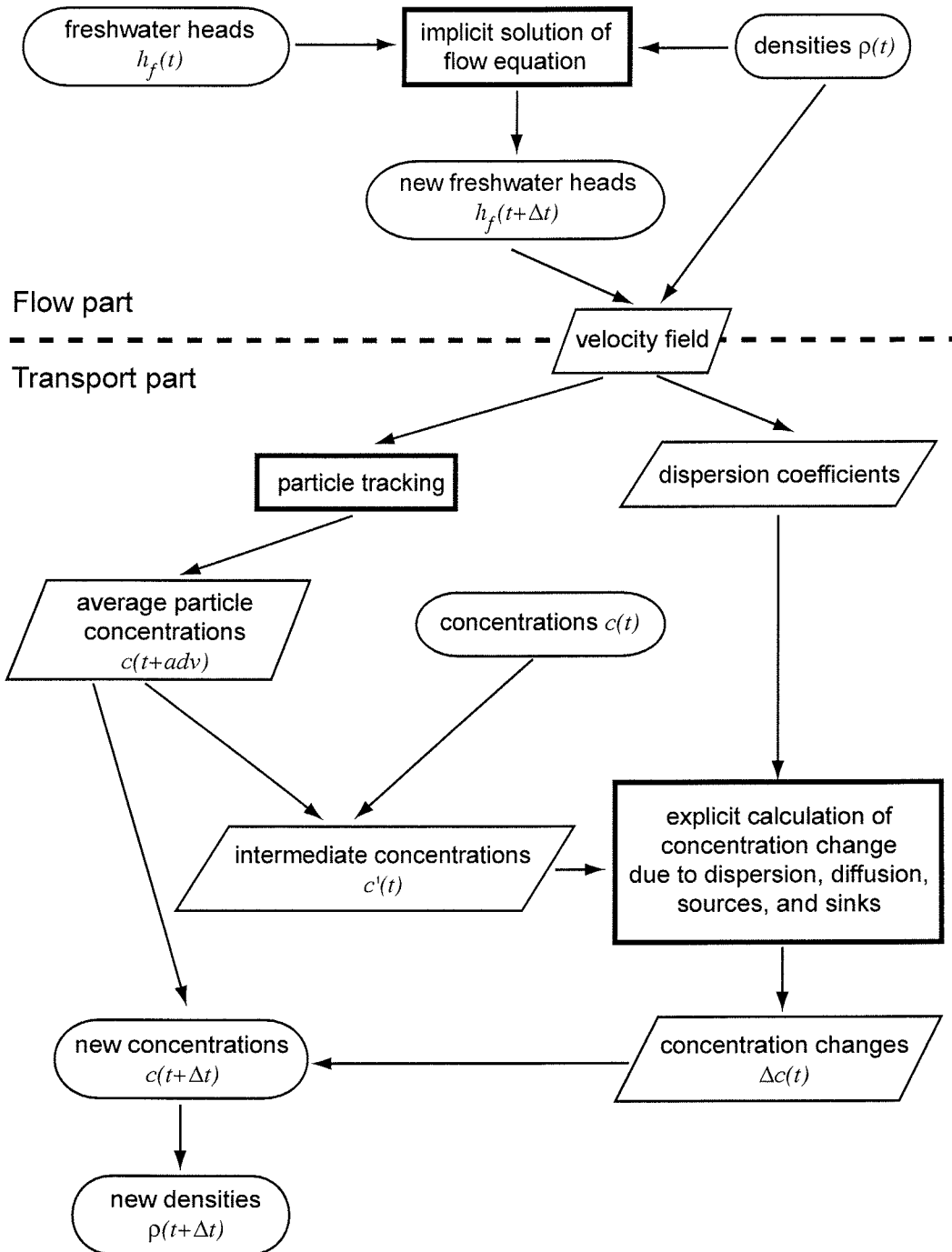


Figure 7.1: In the first part of the simulation process, the velocity field is calculated from the distributions of freshwater heads and densities at the beginning of the time step. The velocity field forms the interface to the transport part of the simulation process: The calculation of both the advection and dispersion terms of the transport equation are based on the velocities. The transport simulation generates the new concentration values, that are converted into the new density values at the end of the time step. Because the new density distribution directly affects the flow part of the next simulation step, the coupling between flow and transport is bi-directional.

Chapter 8

Initial values and boundary conditions

The solution of the flow equation and the transport equation requires the definition of initial values and boundary conditions concerning both flow and transport. The initial values comprise the hydraulic heads and the solute concentrations at the beginning of the simulation. Just like the hydraulic properties of the aquifer (e.g. specific storage, porosity, or hydraulic conductivity), the initial values and boundary conditions are defined separately for each cell. In the computer model described here, five different types of boundary conditions can be used. They will be described briefly and only as far as modeling practice is concerned. A more detailed discussion of both boundary conditions and initial values is given by *Franke et al. (1987)*.

8.1 Initial values

In practice, the initial values for a groundwater transport problem can be obtained from field data as well as from previous simulations. However, the user should be aware that any simulation results may be sensitive to variations or errors in the initial values (*Konikow and Bredehoeft, 1978*). A model not only responds to the imposed boundary conditions but also to the initial values (*Trescott and Larson, 1976*).

Groundwater flow and transport at a steady-state equilibrium is characterized by constant hydraulic heads and constant concentrations. The sum of all volumetric fluxes and solute mass fluxes into the model domain is balanced by corresponding outflows. The volume of groundwater as well as the mass of solute stored in the aquifer remains constant in time. One way to obtain a steady-state solution for a transport problem is the continuous simulation using constant boundary conditions, until the hydraulic heads and the concentrations become stable. The flow equation can be forced in to a steady-state solution

by setting the specific storage equal to zero in all cells of the model grid. The simulation run has to go on until the concentrations reached a constant value and the solute mass stored in the aquifer does not change any more. At the beginning of every flow step, the model will simply calculate a new steady state of flow, accounting for the updated concentrations.

An unambiguous solution of a steady-state transport problem requires at least one constant concentration boundary and one constant head or leakage boundary. The steady-state simulation result is independent of the initial values. Transient problems are defined clearly by the initial values. Therefore, transient simulations do not require boundary conditions to obtain unambiguous results.

8.2 Definition of boundary conditions

Boundary conditions can be used to describe the real boundaries of the aquifer as well as artificial boundaries for the model. Mathematically, three different types of boundary conditions can be distinguished: Boundary conditions of the first kind are called Dirichlet conditions. They involve the definition of either a constant hydraulic head or constant concentration. Boundary conditions of the second kind, referred to as Neumann conditions, are fixed fluxes into or out of the model domain. The third kind are the Cauchy boundary conditions. Prescribing a head- or concentration-dependent gradient, the Cauchy conditions represent a mixture of the first kind and second kind. In the computer model described in this work, the user has a choice of five different combinations of these basic boundary conditions.

8.2.1 No-flow boundaries

Perhaps the simplest kind of boundary condition is the definition of a no-flow cell. It can be used to define the natural boundaries of the aquifer as well as to introduce barriers for the groundwater flow into simulations. Note that the outer boundaries of the model grid are treated as if the grid was surrounded by no-flow cells, such that no groundwater can flow into or escape from the model domain unless through user-defined boundary cells.

Such no-flow boundary cells are completely excluded from the solution of the flow and transport equations, i.e. no groundwater or particle can enter or leave the cell. Consequently, the streamlines resulting from the flow simulation do not cross any no-flow cells but lead around and along the boundary cells. If the explicit bilinear particle tracking scheme is used, a reflection technique must be applied to prevent particles from entering no-flow boundary cells.

8.2.2 Constant observed head boundary

In constant observed head boundary cells, the observed hydraulic head remains constant throughout the simulation. Depending on the hydraulic head in the neighboring cells, such constant observed head boundary cells represent sources or sinks to the groundwater flow. The character of the cell may even change from one time step to the next. The prescribed value of observed head is maintained by adding or removing water of the same concentration as the groundwater in the boundary cell. Therefore, constant observed head boundaries may change the solute mass storage, but they have no effect on the concentration in the cell.

8.2.3 Constant concentration boundary

At constant concentration boundaries, the solute concentration in the cell remains unchanged during the entire simulation. The boundary cells can act as both sink and source of solute mass, depending on the concentration values in the surrounding cells. A constant concentration boundary condition can be combined with a constant head boundary to describe large water bodies, for example the sea, whose hydraulic head and concentration values are assumed to be unaffected by transport and flow in the model domain. All tracer points that enter a constant concentration boundary cell are assigned the constant concentration value of the cell immediately. The concentration change in the boundary cell that would result from the exchange of solute mass between the boundary cell and the adjacent cells is compensated by an external solute mass flux. In contrast to other boundary conditions, this solute mass flux is not associated with a volumetric flux of water.

8.2.4 Constant flux boundary

Constant flux boundaries are used to represent groundwater recharge from precipitation, in- or outflow across an edge of the model grid, and abstraction or injection through wells. Fluxes into the aquifer are positive, whereas fluxes out of the aquifer are characterized by a negative sign. While the concentration of abstracted water equals the concentration of the groundwater in the cell, the concentration of inflow must be specified. Constant flux boundaries affect the groundwater flow, the concentration, and the solute mass storage. They cannot be combined with any other boundary condition in the same cell.

According to the source criterion described in the previous section, the concentration change resulting from mixing groundwater of one concentration with recharged water of another concentration cannot exceed the difference between those two concentrations. In order to avoid that some tracer points violate this

rule, all particles in a constant flux boundary cell are assigned the nodal concentration at the end of a time step, rather than applying the concentration change at the node.

8.2.5 Leakage boundary

The exchange between the aquifer and surface water bodies is described in the model by means of leakage boundaries. The parameters involved are the water level, the size of the contact area between the surface water and the aquifer, the hydraulic conductivity and the thickness of the streambed or lakebed. It is assumed that the observed hydraulic head and the concentration in the stream or lake remain constant. Consequently, leakage boundaries can be sources or sinks for both groundwater flow and transport, and they alter the concentration and the solute mass storage.

8.3 Particle tracking at boundaries

The solution of the advective part of the transport equation is associated with certain difficulties (*Konikow and Bredehoeft, 1978; Konikow et al., 1996*). Linear particle tracking ensures that the particles can only move along the streamlines. In contrast, the explicit calculation of particle paths which is used in the bilinear tracking causes deviations from the streamlines. As a result, reflection techniques have to be implemented to prevent the particles from moving into no-flow boundary cells or out of the model domain at impervious borders.

Cells that act as sources or sinks for groundwater flow often cause singularities in the velocity field. While particles will continually move out of source cells, few if any will enter the cell. On the other hand, many tracer points will move into cells that act as sinks, but hardly any will leave the cell. Therefore, it is necessary to remove particles at sinks and to replace them at sources in order to maintain a fairly even distribution of tracer points and to ensure a steady, uniform stream of particles from source cells.

Both particle tracking schemes treat a source or sink as if it was uniformly distributed throughout a boundary cell. If a source or sink boundary condition is used to represent groundwater flow across a specific face of a cell, then the accuracy of the particle paths can be improved by assigning the volumetric flux to that face (*Pollock, 1994*). However, such is possible only for boundary cells located on the border of the model domain or next to an internal no-flow boundary, else stagnation may occur in the velocity field. The flux from the direction of the impervious boundary would normally be equal to zero. Therefore, it can simply be replaced by the specified volumetric flux into or out of the boundary cell. At leakage boundaries, the volumetric flux is assigned to the upper face of the cell, if possible.

8.3.1 Reflection at no-flow boundaries

Impervious boundaries of the model domain may cause problems for bilinear particle tracking. The streamlines do not cross these boundaries. However, due to the explicit calculation of the new particle position, it is possible that the interpolated velocity of a particle near an impervious boundary is such that it would be moved out of the model domain in the course of the time step. *Konikow and Bredehoeft (1978)* solve this problem by reflecting the particle at the border of the no-flow boundary.

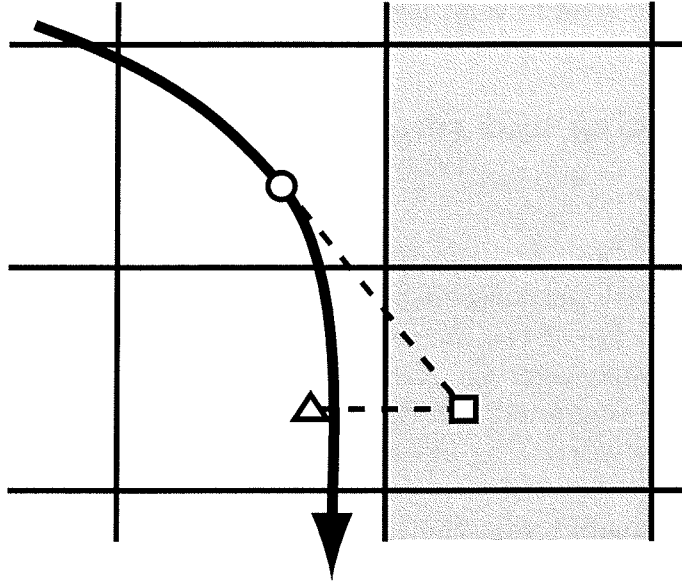


Figure 8.1: The circle marks the position of the particle at the beginning of the time step. Due to the explicit calculation of the particle path, the extrapolated position, indicated by the square, may be located within a no-flow boundary cell. In this case, the particle is relocated to the position denoted by the triangle through reflection of the position along the no-flow boundary line (*Konikow and Bredehoeft, 1978, modified*)

The reflection at a vertical border is described by:

$$x^{t+\Delta t}(p_k) = x_B - (x'(p_k) - x_B) = 2x_B - x'(p_k) \quad (8.1)$$

where

$x^{t+\Delta t}(p_k)$ is the corrected x -coordinate of the particle p_k [L],

$x'(p_k)$ is the erroneously calculated x -coordinate outside the model domain [L], and

x_b is the x -coordinate of the impervious boundary [L].

Analogously, the reflection at a horizontal border is calculated from:

$$z^{t+\Delta t}(p_k) = z_B - (z'(p_k) - z_B) = 2z_B - z'(p_k) \quad (8.2)$$

where

- $x^{t+\Delta t}(p_k)$ is the corrected x -coordinate of the particle p_k [L],
- $x'(p_k)$ is the erroneously calculated x -coordinate outside the model domain [L], and
- x_b is the x -coordinate of the impervious boundary [L].

Figure 8.1 illustrates that the correction of the path according to equations (8.1) and (8.2) will tend to relocate the particle closer to the true streamline.

8.3.2 Replacing and removing particles at sources and sinks

Following *Konikow and Bredehoeft (1978)*, SWIMMOC applies two different techniques to replace particles that move out of source cells. In case the cell is located on the edge of the model grid or next to a no-flow boundary cell, the new particle is placed at the same relative position as the particle that has left the source cell (figure 8.2). If the source cell does not border on a no-flow boundary, the new particle is placed at the original position of the particle that left the source (figure 8.3). Note that a new particle is created only for particles that originated from the source cells. Other particles, which moved into the cell, are not replaced when they leave it again.

To avoid the accumulation of particles at sinks, all particles moving into sink cells are removed after the new concentration for the node has been calculated. In case the relative magnitude of the volumetric flux out of a sink cell is not strong enough to maintain a radially convergent flow, it is possible that a particle escapes from the boundary cell (figure 8.4). Then, the particle that left the sink cell is replaced in the same way as a particle that moved out of a source cell.

The numerical creation of new particles at sources and the removal of particles at sinks is analogous to the generation and removal of fluid and solute mass. The combination of both will tend to maintain a constant number of particles in the model (*Konikow and Bredehoeft, 1978*).

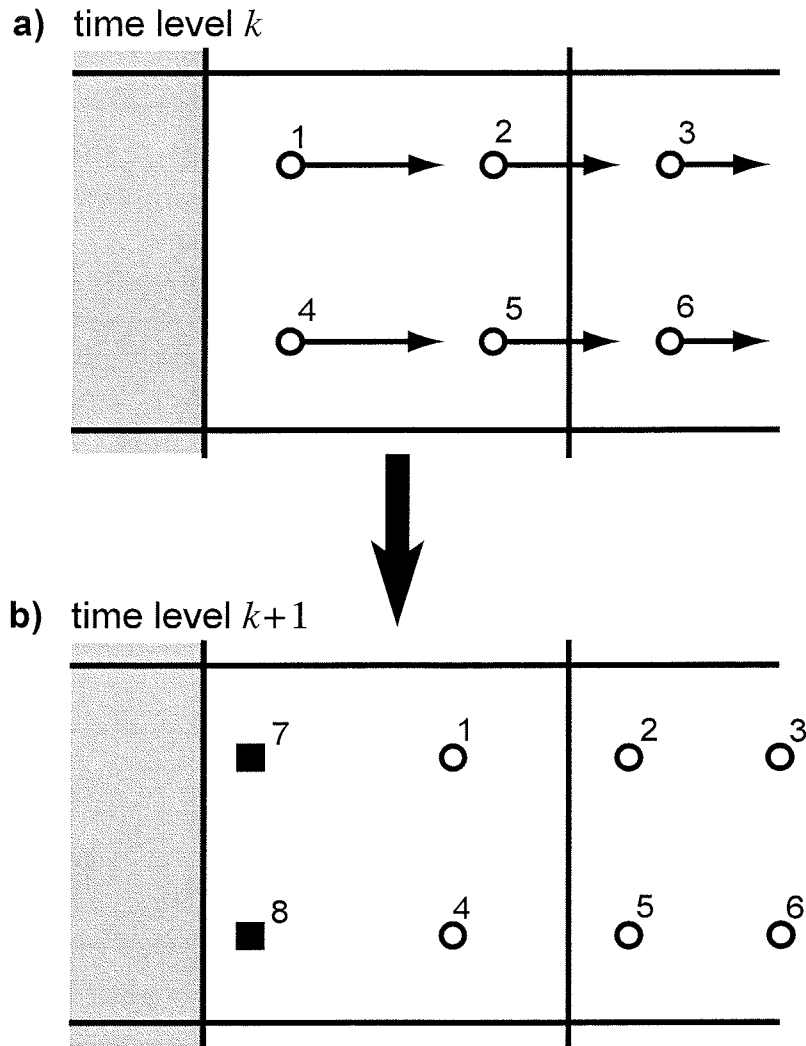


Figure 8.2: For source cells located adjacent to a no-flow boundary, a steady, uniformly spaced stream of particles can be maintained by creating a new particle in the source cell at the same relative position of the particle that moved out of the source cell. The arrows indicate the translation of the particles (white circles) during the transport step k to $k+1$. Particles no. 2 and 5 leave the source cell (a). The two new particles no. 7 and 8 are created at the positions marked by black squares to replace them (b). (*Konikow and Bredehoeft, 1978, modified*)

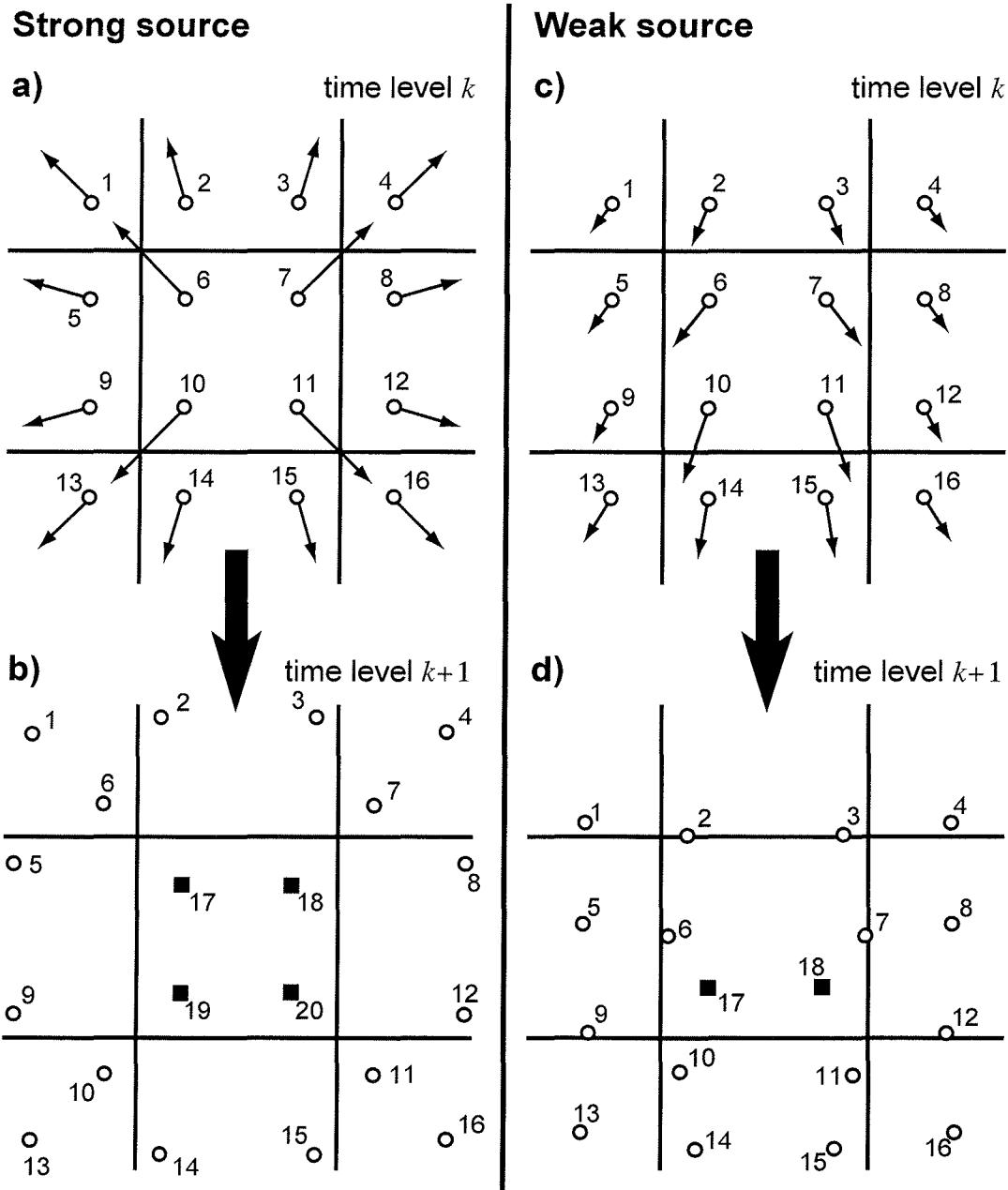


Figure 8.3: For all source cells not bordering a no-flow boundary, a uniform stream of particles from the source is maintained by generating a new particle at the original position of the particle that left the source. This technique can be applied for both, strong sources with radially symmetric flow fields and weak sources with strong regional flow. The arrows indicate the translation of the particles (white circles) during the transport step k to $k + 1$. In the case of the strong source, four particles leave the cell (a) and are replaced by the new particles no. 17 through 20, indicated by the black squares (b). After the tracking step in the weak sources cell, only two particles left the cell (c). They are replaced by particles no. 17 and 18 at the positions of the black squares (d). (Konikow and Bredehoeft, 1978, modified)

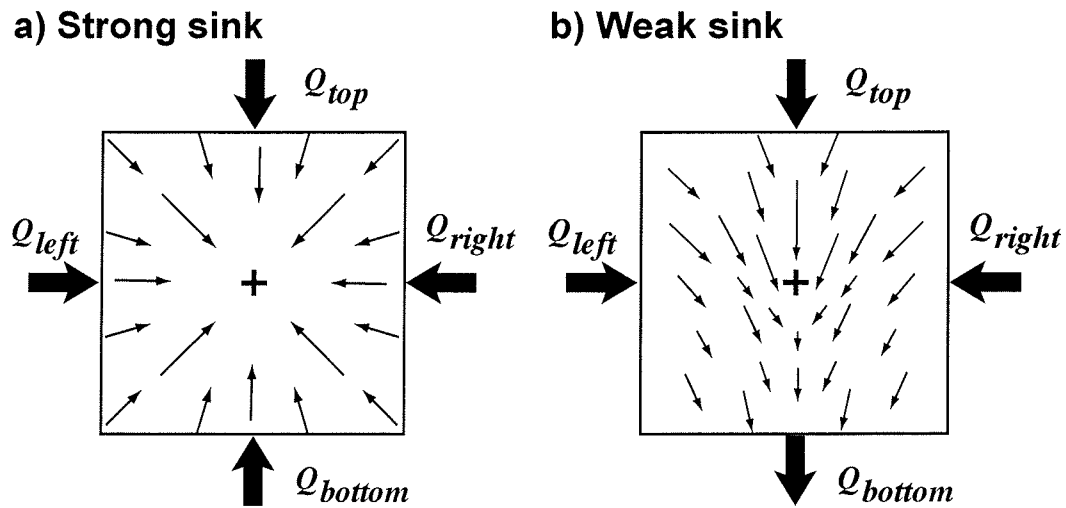


Figure 8.4: a) For conditions with a negligible regional flow field, a sink generates a radially symmetric flow field. The groundwater is flowing to strong sink cells from all sides, making it impossible for particles to escape. Consequently, particles moving into sink cells have to be removed at the end of the transport step. b) If the abstraction of groundwater is small compared to the regional flow field, it may still be possible that particles leave the sink cell with groundwater flow. Generating a new particle in the sink cell at the original position of the particle that escaped from the sink accounts for such particle loss from the cell.

Chapter 9

Accuracy of the simulation

The numerical accuracy and the precision of the solution should always be verified for each simulation run, even if (or especially if) the results meet the expectations of the user. In general, the error in the water balance is controlled by the accuracy of the solution of the flow equation, while the error in the solute mass balance depends on how precisely the transport equation was solved. Due to the bi-directional coupling of flow and transport in variable-density flow models, an inaccurate solution of the transport equation may also affect the precision of the simulated flow field. The calculation of the water balance for the simulation is explained in section 9.1, while the error estimation for the solute mass balance is described in section 9.2.

The IADI provides an unconditionally stable solution of the groundwater flow equation and the method of characteristics is a robust way of solving the transport equation. Numerical instabilities may still occur during the simulation process, resulting from the bi-directional coupling of both methods. These numerical instabilities are discussed in section 9.3.

9.1 Water balance

Continuity demands that the cumulative sum of all volumetric fluxes into and out of the model domain is balanced by a change in the volume of groundwater that is stored in the aquifer. When simulating transient problems, the volumetric change in storage is calculated from the changes in effective porosity in response to transient storage within the cells (see section 5.5 on page 43). Therefore, the volume of groundwater stored in the model domain is a function of time:

$$V(t) = \sum_i \sum_j n_e^t(i, j) \Delta x \Delta z \quad (9.1)$$

where

$V(t)$ is the volume of groundwater stored in the model domain at the time t [L^3], and

$n_e^t(i, j)$ is the effective porosity in the cell (i, j) at the time t [-].

Consequently, the volumetric change in storage from the beginning of the simulation at the time t_0 until the end of the simulation at the time t is given by:

$$\Delta V = V(t) - V(t_0) \quad (9.2)$$

where

ΔV is the change in the volume of stored groundwater [L^3].

To determine the cumulative sums of in- and outflow, at each time step the volumetric fluxes at boundaries must be recorded. At constant flux boundaries the volumetric flux is specified by the user. At constant observed head boundary cells and at leakage boundaries the volumetric flux must be calculated at the end of the flow time step.

The specific leakage flow q_L at leakage boundaries is calculated using the hydraulic gradient across the boundary at the end of the flow time step as described by equations (4.16) and (4.18). Then, the volumetric flux into the cell resulting from the leakage boundary condition in cell (i, j) is given by:

$$W_L(i, j)\Delta x\Delta z = q_L(i, j)\Delta x \quad (9.3)$$

For constant observed head boundaries, the volumetric flux across the boundary can be derived from the local flow budget:

$$W(i, j)\Delta x\Delta z = -(Q_{left}(i, j) + Q_{right}(i, j) + Q_{top}(i, j) + Q_{bottom}(i, j)) \quad (9.4)$$

If the net volumetric flux into the model domain during a single time step is positive, it is added to the cumulative inflow. Accordingly, if the net volumetric flux is negative, it is added to the cumulative outflow:

$$V_{in} = \sum_i \sum_j \sum_k (W_L(i, j) + W(i, j)) \Delta x\Delta z\Delta t(k) \quad (9.5)$$

$$\text{for } (W_L(i, j) + W(i, j)) > 0$$

$$V_{out} = \sum_i \sum_j \sum_k (W_L(i, j) + W(i, j)) \Delta x\Delta z\Delta t(k) \quad (9.6)$$

$$\text{for } (W_L(i, j) + W(i, j)) < 0$$

where

- V_{in} is the cumulative volumetric flux into the model domain [L^3],
- V_{out} is the cumulative volumetric flux out of the model domain [L^3],
and
- k is the time level.

Note that when simulating a system at a steady-state equilibrium using a homogeneous specific storage of zero, the net volumetric flux $V_{in} + V_{out}$ should be equal to zero.

The difference between the cumulative net volumetric flux and the change in the volume of groundwater stored in the model domain is the volume residual:

$$V_R = V_{in} + V_{out} - \Delta V \quad (9.7)$$

where

V_R is the volume residual [L^3].

To calculate the error in the water balance, the volume residual is either related to the cumulative in- or outflow, or to the volume of groundwater stored in the aquifer, whichever is dominant:

$$E_{W1} = 100 \frac{V_R}{V_{in}} \quad (9.8)$$

$$E_{W2} = 100 \frac{V_R}{V_{out}} \quad (9.9)$$

$$E_{W3} = 100 \frac{V_R}{V(t)} \quad (9.10)$$

where

E_{W1} , E_{W2} , E_{W3} are the percent errors in the water balance of the simulation.

The error in the water balance directly depends on the accuracy of the solution of the groundwater flow equation. Consequently, it can be controlled by choosing an appropriate tolerance limit.

9.2 Solute mass balance

The law of mass conservation demands that the cumulative sum of all solute mass fluxes into and out of the model domain, i.e. the net solute mass flux, is equal to the total change in solute mass storage. This law can be used to test the accuracy of the model. The change in mass storage for the entire model domain is calculated from the current and the initial concentration distribution. Changes in effective porosity of the aquifer in response to transient groundwater storage are accounted for by using the adjusted effective porosity. The total solute mass stored in the model domain is written as a function of time:

$$M(t) = \sum_i \sum_j c(i, j) n_e^t(i, j) \Delta x \Delta z \quad (9.11)$$

where

$M(t)$ is the solute mass stored in the model domain at the time t [M].

Thus, the change in solute mass storage between the start of the simulation at the time t_0 and the simulation end at the time t is:

$$\Delta M = M(t) - M(t_0) \quad (9.12)$$

where

ΔM is the change in the solute mass storage [M].

In order to determine the cumulative sums of solute mass fluxes into and out of the model domain, for each time step the fluxes at boundary cells have to be recorded. First, the volumetric flux across constant head and leakage boundaries must be calculated as described in the previous section. Then, the solute mass that is added to or removed from the cell as a result of the boundary condition is given by:

$$M_W(i, j) = (W_L(i, j)c_L(i, j) + W(i, j)c_W) \Delta x \Delta z \Delta t \quad (9.13)$$

where

$M_W(i, j)$ is the the solute mass added to (positive) or removed from (negative) the boundary cell [M].

As mentioned in section 5.4 on page 42, the outflow concentration is always equal to the concentration of the groundwater in the boundary cell. By definition, the same applies to the concentration of inflow at constant observed head boundaries.

At constant concentration boundaries, the changes in concentration that would result from advective, dispersive, and diffusive transport between the boundary cell and the adjacent cells are balanced by a solute mass flux across the boundary that is not associated with a volumetric flux of water. The concentration change in the boundary cell due to advection is calculated after particle tracking:

$$\Delta c_{adv}(i, j) = c^{t+adv}(i, j) - c^t(i, j) \quad (9.14)$$

where

$\Delta c_{adv}(i, j)$ is the concentration change at the node (i, j) as a consequence of advection [ML^{-3}].

The advective change in concentration corresponds to a change in solute mass of:

$$M_{adv}(i, j) = \Delta c_{adv}(i, j)n_e(i, j)\Delta x\Delta z\Delta t \quad (9.15)$$

where

$M_{adv}(i, j)$ is the solute mass transported into or out of the cell (i, j) during the time step Δt due to advection [M].

The concentration gradients necessary to calculate the solute mass fluxes due to diffusion and dispersion between constant concentration boundary cells and the adjacent cells are determined using the constant concentration value rather than the mean value of the concentration at the beginning of the time step and the concentration after particle tracking. The change in solute mass due to dispersion and diffusion is given by:

$$M_{\Delta c}(i, j) = \Delta c(i, j)n_e(i, j)\Delta x\Delta z\Delta t \quad (9.16)$$

where

$M_{\Delta c}(i, j)$ is the solute mass transported into or out of the cell (i, j) during the time step Δt as a result of dispersion and diffusion [M].

The sum of the changes in concentration at constant concentration boundary cells due to advective, dispersive, and diffusive flux are balanced by adding or subtracting the equivalent amount of solute mass:

$$M_{CB}(i, j) = -M_{adv}(i, j) - M_{\Delta c}(i, j) \quad (9.17)$$

where

$M_{CB}(i, j)$ is the solute mass added to (positive) or removed from (negative) the boundary cell (i, j) in order to balance advective, dispersive and diffusive transport [M].

The cumulative net inflow and outflow of solute mass are calculated from the sums of the solute mass fluxes at all boundary cells for every time step. If $(M_W(i, j, k) + M_{CB}(i, j, k))$ for the time level k is greater than zero, it is added to the inflow term:

$$M_{in} = \sum_i \sum_j \sum_k (M_W(i, j, k) + M_{CB}(i, j, k)) \quad (9.18)$$

where

M_{in} is the cumulative sum of solute mass inflow [M].

On the other hand, if $(M_W(i, j, k) + M_{CB}(i, j, k))$ is negative, it is subtracted from the outflow term:

$$M_{out} = \sum_i \sum_j \sum_k - (M_W(i, j, k) + M_{CB}(i, j, k)) \quad (9.19)$$

where

M_{out} is the cumulative sum of solute mass outflow [M].

Note that even though fluxes out of the model domain are characterized by a negative sign, the cumulative sum of the solute mass fluxes out of the model domain is defined as a positive value. The difference between the net flux and the change in storage is the solute mass residual:

$$M_R = \Delta M - (M_{in} - M_{out}) \quad (9.20)$$

where

M_R is the solute mass residual [M],

Large residuals often indicate inaccuracies or even errors in the numerical solution. However, small residuals do not necessarily mean that the result of the simulation is accurate. The percent error in the solute mass balance of the model is calculated by relating the solute mass residual to an appropriate measure of the solute mass flux or solute mass stored in the model domain.

As proposed by *Konikow et al.* (1996), three different equations are used to calculate the error in the mass balance. For simulations with cumulative mass inflow larger than the outflow, the residual is related to the solute mass brought into the model:

$$E_{M1} = 100 \frac{M_R}{M_{in}} \quad (9.21)$$

where

E_{M1} is the percent error in the mass balance of the simulation.

If the solute mass flux out of the model domain is dominant, the mass balance error should be calculated from the ratio of solute mass residual and solute mass outflow:

$$E_{M2} = 100 \frac{M_R}{M_{out}} \quad (9.22)$$

where

E_{M2} is the percent error in the mass balance of the simulation.

Both E_{M1} and E_{M2} are meaningless for simulations in which the solute mass fluxes into and out of the model domain are very small compared to the solute mass stored in the aquifer. In these cases, the error in the solute mass balance is calculated as the ratio of the solute mass residual and the total solute mass stored in the model domain:

$$E_{M3} = 100 \frac{M_R}{M(t)} \quad (9.23)$$

where

E_{M3} is the percent error in the mass balance of the simulation.

Since the solute transport equation is more difficult to solve than the groundwater flow equation, the error in the solute mass balance is often larger than the error in the water balance. Besides, it should be kept in mind that the method of characteristics is based on solving the transport equation at discrete points (the positions of the particles). In contrast, the mass balance error is calculated from nodal concentrations, which represent the average concentration value of the particles in the cell. Therefore, the mass balance error will typically exhibit an oscillatory behavior over time (*Konikow et al.*, 1996). However, as this type of error is not cumulative, the oscillations should remain within a limited range and eventually balance out in the course of the simulation. *Konikow et al.* (1996) presume that the error in the mass balance does not represent a bias and is not a serious problem unless it exceeds about ten percent.

9.3 Numerical instabilities

As described in section 7.2, the coupling of the flow and transport simulation in density-dependent groundwater flow models is bi-directional. The flow simulation provides the velocity field required to calculate the paths of the tracer particles. The movement of the particles changes the concentration distribution. Changes in the concentrations are equivalent to changes in the densities. Thus they will alter the buoyancy flows and consequently lead to changed flow patterns the next time the flow equation is solved.

If there are great differences in concentration between adjacent cells of the grid, particles that move from one cell into the other will cause a significant change in the density gradient. The resulting changes in the buoyancy flow may even reverse the direction of flow between the two cells. In such cases the particles will move back into the cell which they just left, reverting the density change. Obviously, this effect can lead to oscillations in grid areas with high concentration gradients, e.g. at narrow transition zones between saltwater and freshwater. The subsequent description of how the model parameters may affect these numerical instabilities is based on the discussion in *Oude Essink* (1996).

- The initial number of particles per grid cell greatly influences the numerical stability of the simulation. The more particles are in a cell, the less abrupt are concentration changes caused by particles moving from one cell into the next, provided that the particles are evenly spaced.
- The tolerance limit for the iterative solution of the flow equation directly controls the accuracy of the generated flow field. A small tolerance limit will lead to more accurately calculated paths of the particles, which may help to counteract numerical instability.
- To meet the stability criteria for the explicit solution of the dispersion and diffusion terms, the flow time step is divided into a large number of transport time steps (section 6.3). The changes in concentration occurring in the course of one flow time step may be too large to match the solution of the flow equation. In these cases, smaller flow time steps may prevent numerical instabilities.
- The initial concentration distribution should be as smooth as possible to prevent instabilities due to high gradients at the start of the simulation.
- The accuracy of the solution of the groundwater flow equation increases with decreasing sizes of grid cells. Consequently, increasing the total number of grid cells also improves the precision of particle tracking. On the other hand, reducing the cell size does not necessarily prevent numerical instabilities. Due to the stability criteria, simultaneously the number of transport time steps during one flow time step has to increase.

- If the coefficients of dispersion and diffusion are small, the transition zone between saltwater and freshwater is likely to be narrow. As a result, there may be steep concentration gradients between adjacent cells, which may result in numerical instabilities.
- For narrow transition zones between saltwater and freshwater, the velocity of groundwater flow in adjacent cells may point into opposite directions. If the transport step is rather long, the linear particle tracking algorithm may cause the tracer particles to move away from the transition zone. As a result, the transition zone could deplete of tracer particles. In such cases, the bilinear particle tracking algorithm may yield more realistic results, because it is based on a continuous velocity field.

Chapter 10

Observation points

To compare the simulation results and field data, the solute concentration of groundwater at specified locations within the model grid should be known. In case the measured locations do not happen to coincide with the position of a node or one of the tracer particles, the required concentration values can be obtained by means of interpolation. Because the method of characteristics is applied to solve the transport equation, the most accurate values of solute concentration are available at the position of the tracer particles. Consequently, the most accurate method of interpolation is based on these values. Shepard's method of inverse distance interpolation (*Shepard, 1968*) delivers a weighted mean of the concentration values associated with all tracer particles in the vicinity of the point of interest. The hydrogeological setting of the observation point can be reflected by selecting an appropriate search radius that defines the maximum distance between the observation point and a particle included into the interpolation.

As mentioned in section 6.1.4 on page 58, it is possible that some areas of the model domain deplete of particles. Consequently, the concentration value in these areas cannot be calculated from values associated with particles. Then, the concentration value at the observation point is calculated by means of bilinear interpolation between the four closest nodal values.

10.1 Shepard's method of inverse distance interpolation

Shepard's method of inverse distance interpolation (*Shepard, 1968*) is applied to calculate a weighted mean of concentration values at given positions in the circumference of an observation point:

$$c_{obs} = \sum_{k=0}^{n-1} w_k c(p_k) \quad (10.1)$$

where

- c_{obs} is the interpolated concentration value at the location of the observation point [ML⁻³],
- n is the number of particles that contribute to the interpolated value, and
- w_k is the weighting factor for the concentration value associated with tracer particle p_k [-].

The weighting factor w_k in equation 10.1 depends on the distance between the particle and the observation point:

$$w_k = \frac{d_k^{-p}}{\sum_{i=0}^{n-1} d_i^{-p}} \quad (10.2)$$

where

- d_k is the distance between the particle and the observation point [L], and
- p is an arbitrary positive number.

The interpolation algorithm implemented in the described numerical model uses the commonly applied value of $p = 2$.

10.2 Bilinear interpolation of concentration values

The concentration value at a point of interest can be interpolated from the known values at the four closest nodes. Given that the observation point is located somewhere in-between the nodes (i, j) , $(i, j + 1)$, $(i - 1, j)$, and $(i - 1, j + 1)$, the interpolated concentration value is:

$$c_{obs} = (1 - w_x)(1 - w_z)c(i, j) + w_x(1 - w_z)c(i, j + 1) + (1 - w_x)w_zc(i - 1, j) + w_xw_zc(i - 1, j + 1) \quad (10.3)$$

where

- c_{obs} is the interpolated concentration value at the observation point [ML⁻³], and

10.2. BILINEAR INTERPOLATION OF CONCENTRATION VALUES

w_x, w_z are the horizontal and the vertical weighting factors [-].

The horizontal weighting factor w_x is calculated as:

$$w_x = \frac{x_{obs} - x(i, j)}{\Delta x} \quad (10.4)$$

where

x_{obs} is the x -coordinate of the observation point [L], and

$x(i, j)$ is the x -coordinate of the node (i, j) [L].

Analogously, the vertical weighting factor w_z is:

$$w_z = \frac{z_{obs} - z(i, j)}{\Delta z} \quad (10.5)$$

where

z_{obs} is the z -coordinate of the observation point [L], and

$z(i, j)$ is the z -coordinate of the node (i, j) [L].

Bilinear interpolation of the observed concentration value is based on nodal concentrations, which represent the average values of the concentration values associated with the tracer particles in the corresponding cell. Consequently, the method is less accurate than the inverse distance interpolation method described in the previous section.

Chapter 11

Review of assumptions

The approach to the simulation of density-dependent groundwater flow described here is based on a number of simplifications. Even though the numerical model can be applied to a variety of problems, some cases may be incompatible with the implications of this code. Therefore, the user should be aware of the assumptions and limitations that are inherent in the model. The most important assumptions are:

- Groundwater flow is two-dimensional in a vertical plane. The vertical axis of the model grid is parallel to gravity.
- Darcy's law is valid: Groundwater is considered an incompressible fluid. Transient storage is accounted for by adjusting the effective porosity. Flow is always laminar. Turbulence does not occur.
- The aquifer is confined. Unsaturated flow can be neglected.
- The hydraulic conductivity of the aquifer is constant in time. For anisotropic aquifers, it is assumed that the principal axes of the hydraulic conductivity tensor are parallel to the axes of the model grid.
- The dispersivity of the aquifer is homogeneous and constant in time.
- The density of groundwater is a linear function of the solute concentration. Other factors that may affect the density of groundwater, such as temperature, are neglected.
- The solute concentration is not changed by reactions, decay, or sorption.

Chapter 12

Introduction to SWIMMOC

The computer program SWIMMOC is a numerical modeling environment for the simulation of two-dimensional density-dependent groundwater flow. SWIMMOC is based on the method of characteristics. It is a stand alone mouse- and menu-driven application that offers an intuitive graphical user interface. SWIMMOC was designed especially to study the dynamics of the saltwater/freshwater interface in coastal aquifers. It facilitates the definition of boundary conditions that are characteristic for saltwater intrusion problems. Nevertheless, SWIMMOC can be used to model other types of density-dependent flow problems, as long as they match the assumptions mentioned in chapter 11. Still, some specific simulation questions may require modifications in the source code.

SWIMMOC was written in REALBasic 5.2.4 on Mac OS X. REALBasic is an object-oriented programming language available for both Apple Macintosh and Microsoft Windows operating systems. Executable applications can be compiled for Mac OS Classic, Mac OS X, Microsoft Windows, as well as for various Linux distributions.

12.1 Overview of the general program features

Upon start-up, SWIMMOC presents the main window and a menu bar. The white rectangular area that occupies the center of the main window is reserved to show the model grid after its definition by the user. The six text fields at the top of the window indicate the status of the model during the simulation process. The four text fields in the lower left corner of the window provide information about the position of the mouse pointer when moving across the model grid. In the lower right corner of the window the type of currently displayed information is displayed. The nine main menus are: File, Edit, Model, Units, Boundaries, Parameters, View, Simulation, and Evaluation. When defining a new flow problem, it is recommended to follow the menu order from left to the right.

The simulation of density-dependent flow problems in SWIMMOC follows an intuitive and descriptive approach. In the following the items of the main menus and the associated dialogs will be described briefly. A single cell of the model grid may be selected by simply clicking on the cell. A group of cells can be selected by keeping the mouse button pressed while dragging a frame around the desired section of the grid. All values are entered without specifying the unit. Though next to every entry field, there is a term in square brackets, which presents the expected dimension: L is length, M is mass, and T is time. Thus SWIMMOC allows the user to choose any units, as long as the parameter values are entered consistently.

12.2 The File-menu

The File-menu is used to load and save model data. The menu item *Open...* displays an Open-dialog and loads a model definition file. This routine simply reads all information that is available, including model options, sea level definition, unit definitions and boundary definitions. Note that all of the current model data will be replaced.

The complete model definition including model options, sea level definition, unit definitions and boundary definitions can be stored via the menu items *Save As...* and *Save*. The option *Save* is only available if the model has not been saved or if the model has been changed after the last time it was saved. A save dialog is displayed only if a model definition has not been saved before. If the current model has been loaded from or saved to a file, *Save* will replace the existing file. On the other hand, *Save As...* can be used at any time (except when the simulation is running) to choose a new file name. Note that neither of the two will save the current status of the simulation, i.e. the model results, but the model definition only.

SWIMMOC model definition files are written in plain text format and can be viewed and edited using any text-editor. General model parameters are written in the form “parameter: value” and must be in separate lines to be recognized when SWIMMOC is reading the file. Gridded data is written as tab-delimited text that can easily be imported into spreadsheets. The model grid must be defined at the beginning of the file. The sequence of other information is arbitrary.

The *Export* submenu offers the possibility to export the simulation results to other programs. *Concentration...*, *Density...*, *Freshwater Head...*, and *Observed Head...* each write the gridded data as space-delimited text files in the format used by the program Surfer by Golden Software. *Particles...* writes a tab-delimited list of the coordinates of each particle and the concentration value associated with it. *Observation Points...* saves a tab-delimited list of the times and concentrations that were recorded at specified observation points. The last two items *Unit Definitions...* and *Boundary Definitions...* in the submenu can

be used to save the unit or boundary definitions, respectively. This information may later be imported into other flow problems.

The submenu *Import* consists of the menu items *Unit Definitions...* and *Boundary Definitions...* which can be used to read previously exported unit definitions or boundary definitions as well as to import the relevant sections from model definition files.

12.3 The Edit-menu

The menu items *Cut*, *Copy*, *Paste*, and *Clear* are provided by the operating system. *Select All* selects all cells of the grid that are currently visible. In case the user zoomed into a section of the model grid, only the cells of this section are selected. *Select None* clears the current selection, regardless of the current zoom level. The item *Select Same* is only available if one single cell is selected. It adds all cells with the same value of the currently displayed parameter to the selection.

12.4 The Model-menu

The menu item *Grid...* opens a dialog for the definition of the geometry of the model grid. The dialog is self-explaining. Note that defining a new grid removes all of the data associated with the previous grid from the memory. Clicking the *Cancel*-button leaves the current grid untouched.

The menu item *Sea Level...* opens a dialog allowing the user to define a constant or time-varying sea level that can be referred to by boundary conditions. However, the representation of temporal changes in the sea level during the simulation is restricted to the resolution of the flow time step.

The menu item *Options...* opens a dialog for defining a number of basic simulation options may be defined, which affect the simulation process. It is divided into five different tab panels:

- The *Flow* panel is used to define the tolerance limit for the iterative solution of the flow equation and allows to choose either the Iterative Alternating Direction Implicit method (default) or the Gauss-Seidel method.
- The *Transport* panel is used for controlling the transport part of the simulation. The travel distance criterion (see section 6.3.1 on page 66) is defined in terms of the minimum number of flow steps that are required for a particle to cross a cell. The maximum percentage of void cells defines how many cells of the model grid are allowed to become void of particles during the simulation before the particles are redistributed. It

is recommended to keep this value small (default=2) in order to limit numerical dispersion through redistributions. As illustrated by figure 6.2 on page 50, only square numbers of particles can initially be placed into each cell. The default number of initial particles per cell is nine. Either linear (default) or bilinear particle tracking can be selected to simulate advective transport. The different procedures are described in section 6.1 on page 49. The dispersivity of the aquifer and the coefficient of molecular diffusion is defined in the *Dispersion* panel.

- The *Density* panel comprises the parameters required to convert from solute concentration to groundwater density (see section 7.1 on page 69). The settings of the panel *Observation Points* control the interpolation of concentration at user-specified observation points. Shepard's method of inverse distance interpolation is based on accurate concentration values at discrete locations given by the particles. The search radius defines the maximum distance between the point of observation and a particle that contributes to the interpolated value. If there are no particles within the search radius, the algorithm uses linear interpolation between nodal values instead. This method reflects the results of the simulation less accurately, because the nodal concentration values are the average values of the concentration values associated with the particles in the cell. Depending on the dimension of the cell and the number of particles, the results of the two different interpolation methods may differ significantly.

12.5 The Units-menu

The Units-menu lists all hydrogeological units that haven been defined by the user. If one or more cells of the grid are selected, choosing the name of the unit assigns all unit properties to the selected cells and also stores a reference to the unit in each of these cell. If no cells are selected, choosing the name of the unit displays a dialog that allows to change the unit properties. Note that changing the properties of a unit also changes the properties of all cells associated with the unit. In order to detach a cell from a unit, select the cell and choose *No Unit*. The menu item *New Unit...* opens a dialog for the definition of a new hydrogeological unit.

12.6 The Boundaries-menu

The Boundaries-menu is very similar to the Units-menu. Choosing the name of a boundary condition while one or more cells are selected assigns the boundary condition to the cell or cells, respectively. If no cells are selected, a dialog to change the boundary condition is displayed. Changes in the definition of a

boundary condition affect all cells on which the boundary condition was imposed. Choosing *No Boundary* detaches the boundary condition from selected cells. In addition, the status of selected cells can be switched from active to inactive and vice-versa. Inactive cells are treated as no-flow boundaries and are displayed in grey color.

The menu item *New Boundary...* is used for defining new boundary conditions. It displays a dialog that is divided into four different tab panels:

- The *Head & Concentration* panel comprises the parameters for constant observed head and constant concentration boundaries. Note that these two types are the only boundary conditions that can be combined within one cell. The constant observed head value can either be specified by the user or it can be set equal to the sea level. At sea level boundaries, the time-dependent value of the user-defined sea level function is used instead of a fixed observed head. Similarly, either an arbitrary concentration value or the saltwater concentration specified in the options dialog can be assigned to constant concentration boundaries.
- Constant flux boundary conditions are defined through the *Flux* panel. SWIMMOC offers the possibility to specify the constant volumetric flux either as absolute flux per cell or per unit horizontal or vertical area. This way, the same boundary condition can be applied to different grid spacings. For volumetric fluxes into the aquifer, the concentration of the injected water must be given either through an arbitrary value or by setting the concentration equal to the concentration of saltwater. Abstraction of groundwater from the aquifer is reflected by negative values of volumetric flux and cannot be associated with a concentration value.
- The *Leakage* panel is used for define leakage boundaries (see section 3.4 on page 16).
- The *Position* panel offers the possibility to assign volumetric fluxes resulting from a boundary condition to a specific face of the boundary cell. Note that this is only possible if the boundary cell is adjacent to a no-flow boundary (see section 8.3 on page 76). Otherwise, the volumetric flux is treated as if it was uniformly distributed over the cell.

12.7 The Parameters-menu

The items of the Parameters-menu can be used to define the initial values and the properties of selected cells. Each item displays a dialog that allows to define either a constant value or a range within which random values for the corresponding parameter may be found. Note that changing the hydraulic

properties of a cell via the Parameters-menu removes a reference to a unit stored in the cell, if present.

The menu item *Copy Current to Initial* replaces the initial values of observed head and solute concentration with the current values. This is convenient e.g. to freeze a certain stage of the simulation, such as a steady-state equilibrium. Note that this feature affects all cells regardless of the selection.

12.8 The View-menu

The View-menu controls the variable or parameter displayed in the center area of the main window. The items of the first two sections can be chosen to view the initial or current values of cell parameters. The third section of the menu offers the possibility to view parameters that are calculated in the course of the simulation process. The items *Boundary Flux* and *Boundary Mass Flux* display for each cell the volumetric flux and the solute mass flux, respectively. *Horizontal Velocity* and *Vertical Velocity* calculates the corresponding normal component of groundwater velocity at the node using the volumetric fluxes at facing borders of the cell. The item *Number of Particles* displays the number of particles present in each cell, whereas the item *Particles* marks the actual position of each particle in a cell by a black dot. During the simulation process, however, this feature is disabled in order to avoid interference with the tracking algorithm. For other all other parameters, *Update* can be chosen to show intermediate results during the simulation process.

All values are represented through the fill color of the cell. The color scale ranges from dark blue for the smallest values to dark red for the largest values and is automatically adjusted to the range of values.

The item *Zoom In* allows to zoom into selected cells and can be chosen repeatedly to increase the zoom level. *Zoom Out* always switches back to the display of the entire grid.

12.9 The Simulation-menu

The menu item *Time...* displays a dialog box used to define both, the final time of the simulation as well as the length of the flow time step. If the initial concentration distribution contains steep gradients, it may be necessary to apply shorter flow time steps at the beginning of the simulation. Therefore, a time step factor can be specified to automatically increase the length of the time step.

The remaining items of the Simulation-menu give access to the different parts of the simulation process. The availability of these items follows three basic rules:

1. The transport simulation may start only after the flow simulation reached the tolerance limit specified in the options dialog.
2. The next flow step can be commenced only if the transport simulation is at the same time level as the flow simulation.
3. The transport simulation may not surpass the flow simulation.

All simulation procedures are programmed as background processes. The current state of the simulation can be displayed at any time, by either selecting the parameter of interest or choosing *Update* from the View-menu. Choosing *Stop* interrupts the simulation process as soon as possible. Transport steps cannot be interrupted. The simulation process can be resumed from any time.

12.10 The Evaluation-menu

At any stage of the simulation process, the accuracy and the precision of the flow and transport simulation may be verified by choosing *Water Balance...* and *Mass Balance...*, respectively. The dialogs displayed through these two selections show the water balance and mass balance errors as described in sections 9.1 and 9.2. In case the simulation process is running while the dialog is open, the values can be updated by clicking the *Update* button.

The menu item *Mass Accumulation* shows a graph of the changes in solute mass storage through time for the entire model domain. Analogously to the water balance and mass balance dialogs, the graph can be updated during the simulation process. Even though the sketch is quite rough and unlabeled, it can be useful to determine whether the simulation has reached a steady-state equilibrium or not. At equilibrium, the solute mass storage should remain constant in time and the graph should approach a horizontal line. Note that the mass accumulation data can be exported via the File-menu.

At any stage of the simulation, unless the simulation process is running, the menu item *New Observation Point...* offers the possibility to specify a certain point within the model domain for which the concentration value at every transport time step will be recorded. In contrast to the concentration values at the node, the concentration values at observation points are calculated using a weighted interpolation procedure, as long as Shepard's method was selected in the options dialog. All observation points are represented by menu items upon definition. Choosing the name of an observation point displays a graph of the concentration changes with time at the point of interest. The graph can be updated during the simulation process. Observation points can only be deleted while the simulation process is not running. The recorded data at all observation points can be exported via the File-menu. Note that all previously recorded data is erased every time the simulation is restarted, but not if the simulation is resumed.

Chapter 13

Numerical solution of the Henry problem

The Henry problem for saltwater intrusion is traditionally applied to test numerical models capable of simulating density-dependent groundwater flow. Though e.g. *Voss and Souza* (1987) and *Simpson and Clement* (2004) state that the Henry problem is not very suitable to verify the bi-directional coupling of flow and transport.

The Henry problem concerns saltwater intrusion into a vertical cross-section through an isotropic, homogeneous, and confined aquifer. In his original work, *Henry* (1959) used parameter ratios to keep the problem dimensionless. For practical reasons, the problem is usually solved numerically for a cross-section of two meters width and one meter height. A constant flux of freshwater into the model domain is applied to the left boundary at $x = 0$ m, while the right boundary at $x = 2$ m is marked by a constant saltwater head of $h_{obs} = 1$ m and by a constant saltwater concentration. Both the lower border of the model domain at $z = 0$ m as well as the upper border at $z = 1$ m are no-flow boundaries. Initially, the entire aquifer is filled with freshwater. Due to its higher density, the saltwater intrudes into the model aquifer at the bottom of the cross-section, forcing the freshwater flowing in from the left upward, until a steady-state equilibrium is reached. The relatively large constant diffusion coefficient is reflected by a wide transition zone from saltwater to freshwater.

Since Henry published his semi-analytical solution for the steady-state equilibrium of the saltwater intrusion problem, a variety of numerical solutions have been described in scientific literature. *Pinder and Cooper* (1970) applied the method of characteristics to a transient version of the Henry problem, while *Lee and Cheng* (1974) used the method of finite elements to obtain a steady-state solution. Their work was followed by a series of finite elements solutions for the transient Henry problem (e.g. *Segol et al.*, 1975; *Frind*, 1982; *Huyakorn et al.*, 1987; *Voss and Souza*, 1987). *Croucher and O'Sullivan* (1995) review previous solutions of the Henry problem and present a new highly accurate so-

lution based on finite differences. More recently, *Simpson and Clement* (2004) discussed the significance of the Henry problem as a test case.

Due to a misinterpretation of the dimensionless parameters used by *Henry* (1959), two different versions of the Henry problem have been discussed in the scientific literature (*Croucher and O'Sullivan*, 1995). The two versions of the problem differ in the sets of parameter ratios used, which is reflected by different diffusion coefficients. Even though this difference may seem minor, it significantly affects the concentration distribution. Table 13.1 gives an overview of the correct parameters that are required to simulate the standard case. The geometry and the boundary conditions of the Henry problem are illustrated in figure 13.1.

Table 13.1: These parameters are required for the numerical simulation of the standard Henry problem (*Simpson and Clement*, 2004). Due to a misinterpretation of the dimensionless parameters used by *Henry* (1959), some authors have used parameters that correspond to a diffusion coefficient of $D_M = 6.6 \times 10^{-6} \text{ m}^2 \text{ s}^{-1}$ instead of the value given here.

Symbol	Quantity	Value	Unit
D_M	coefficient of molecular diffusion	1.886×10^{-5}	$\text{m}^2 \text{ s}^{-1}$
K	hydraulic conductivity	1.0×10^{-2}	m s^{-1}
Q	recharge per unit thickness	6.6×10^{-5}	$\text{m}^2 \text{ s}^{-1}$
S_S	specific storage	0.0	m^{-1}
n_e	effective porosity	0.35	
ρ_f	freshwater density	1000	kg m^{-3}
ρ_{salt}	saltwater density	1025	kg m^{-3}

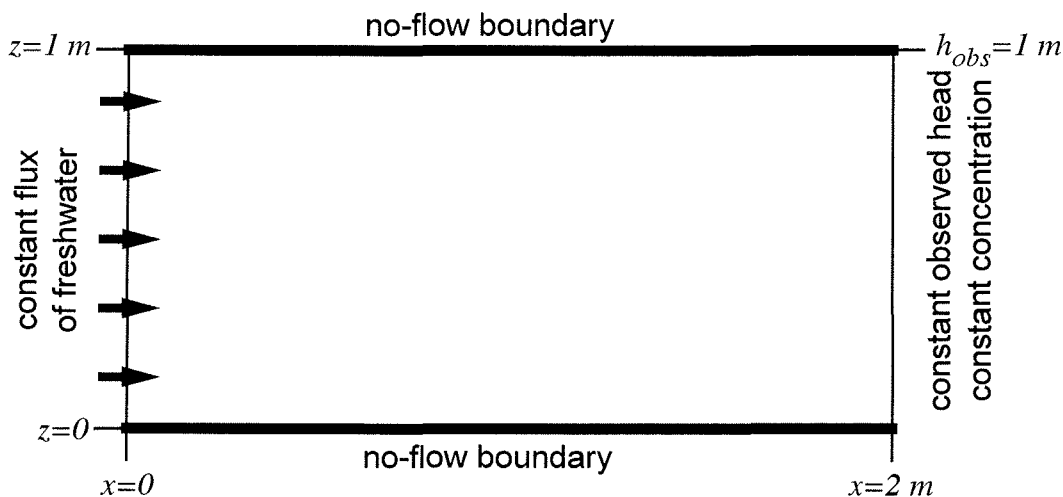


Figure 13.1: The illustration shows the geometry and boundary conditions of the standard Henry problem. The values of the corresponding parameters can be seen from table 13.1.

Following the tradition, the classic Henry problem is used to illustrate the process of creating and running a density-dependent groundwater flow simulation

in SWIMMOC. In section 13.8, a modification of the standard Henry problem as proposed by *Simpson and Clement (2004)* is described. The modified Henry problem is found to be a more suitable benchmark in density-dependent groundwater flow modeling.

13.1 Step 1: Creation of the model grid

The first step when creating a new model in SWIMMOC is to define the model grid. As illustrated in figure 13.1, the dimension of the cross-section is 2 m × 1 m. For a start, we are going to divide this area into 10 rows and 20 columns to obtain a cell size of $\Delta x = 0.01$ m and $\Delta z = 0.01$ m. An additional column is required for the correct representation of the boundary conditions. SWIMMOC uses a block-centered finite differences grid. Therefore boundary conditions are defined for the node at the center of a grid cell rather than for the border. In order to place the inflow boundary at $x = 0$ m, the left border of the model domain must be $x = -\frac{\Delta x}{2}$. Accordingly, if the seaward boundary of the model domain is located at $x = 2$ m, the right border of the model grid is at $x = 2$ m + $\frac{\Delta x}{2}$.

Table 13.2: These parameters are needed to set up the model grid for the Henry problem.

left	0.05 m	top	1 m
width	2.1 m	height	1 m
columns	21	rows	10

After choosing *Grid...* from the Model-menu, the values from table 13.2 are transferred to the corresponding entry fields. The new grid is defined by clicking the *OK* button. Then, the display shows the new grid at the center of the main window. When moving the mouse pointer across the grid, the coordinates are displayed in the lower left corner of the window.

13.2 Step 2: Specification of the aquifer properties

Next, the hydraulic properties of the aquifer will be assigned to a new unit. Choosing *New Unit...* from the Units-menu to displays the unit definition dialog. Assigning the name “Henry aquifer” and transferring the values of hydraulic conductivity, effective porosity, and specific storage from table 13.1 into the corresponding entry fields creates a new unit that comprises the properties of the aquifer in the Henry problem. After clicking the *OK* button, the new unit will appear as a new menu item in the Units-menu.

The new unit must be assigned to all cells of the model grid. After choosing *Select All* from the Edit-menu, all cells are selected and the user goes back to the Units-menu and chooses *Henry aquifer* to copy the properties of the unit to the cells in the grid. The display changes automatically to the units of the grid. To verify that all cells now possess the hydraulic properties of the unit “Henry aquifer”, any one of these properties can be displayed by choosing the corresponding menu item from the View-menu. Moving the mouse across the grid shows the cell value of the currently displayed parameter in the lower right corner of the window.

13.3 Step 3: Definition of the boundary conditions

To define the seaward boundary of the model domain, the user chooses *New Boundary...* from the Boundaries-menu and names the new boundary “Sea”. In the *Head & Concentration* panel, *Constant Observed Head Boundary* has to be selected and the value 1 entered into the corresponding field. (Alternatively, the user may select *Sea Level* and define a constant sea level of 1 m in the sea level dialog available from the Model-menu.) *Constant Concentration Boundary* and *Saltwater* must be selected. Choosing *Right* in the *Position* panel assigns the flux across the boundary to the right face of the cells. Clicking the *OK* button confirms the definition of the new boundary condition.

To define the constant flux boundary on the left hand side of the model domain, *New Boundary...* has to be chosen again, assigning the name “Recharge” to the new boundary. Choosing *Constant Flux Boundary* from the *Flux* panel allows to enter “6.6e-5” into the corresponding field and to select *Per Vertical Unit Area*. Since the flux is positive, the concentration of the inflow must be specified. The default value of 0 is correct. Selecting *Left* in the *Position* panel assigns the flux to the left face of the cell. The dialog box is closed by clicking the *OK* button.

Now, the boundary conditions must be assigned to the appropriate cells by selecting all cells of the leftmost column and choosing *Recharge* from the Boundaries-menu. Again, the view switches automatically to display the boundary conditions. Analogously, the boundary condition “Sea” is assigned to the rightmost column of the grid.

13.4 Step 4: Specification of the initial values

The simulation of the Henry problem starts with an aquifer that is completely filled with freshwater. By default, the initial concentration value is already set

to 0. This can be verified by choosing *Initial Concentration* from the View-menu. The initial observed head is also 0 by default. Thus, again choosing *Select All* from the Edit-Menu, all cells of the model grid are selected. Then, a value of 1 is assigned to all cells after choosing *Initial Observed Head* from the Parameters-Menu.

13.5 Step 5: Specification the simulation options

The last step before starting the simulation is to select the appropriate control parameters for the simulation process. The value of the tolerance limit for the flow simulation requires some thought and should be chosen carefully: In the horizontal direction, the volumetric flux between two adjacent cells solely depends on the freshwater head gradient. Consequently, the tolerance value of the calculated freshwater heads corresponds to an erroneous volumetric flux:

$$q_{tol} = K_x \frac{Tol}{\Delta x} \quad (13.1)$$

where

q_{tol} is the potential specific discharge [LT^{-1}] due to the tolerance error that is inherent to the values of the freshwater head, and

Tol is the tolerance limit [L].

Rewriting equation (13.1) yields:

$$Tol = \Delta x \frac{q_x}{K_x} \quad (13.2)$$

Inserting the parameters given in tables 13.1 and 13.2 into equation (13.2) shows that a tolerance flux equal to the recharge flux from the left boundary corresponds to a tolerance limit of $Tol = 6.6 \times 10^{-6}$ m. Obviously, the volumetric flux that could result from errors in the numerical solution should be much smaller than the recharge flux. Therefore, it is recommended to specify a tolerance limit of at least 1×10^{-8} m. Choosing *Options...* from the Model-menu displays the options dialog. The tolerance limit is set in the *Flow* panel.

In the *Dispersion* panel, the diffusion coefficient must be set to the appropriate value from table 13.1. Freshwater density, saltwater density, saltwater concentration are specified in the *Density* panel. For saltwater concentration, any desired value may be entered. It is convenient to use either the value 1 or 100,

which allows the user to read the simulated concentration values as fraction or percentage of saltwater. Note that since the seaward boundary simply is defined as saltwater boundary, the model will use whichever value specified for the constant concentration value at the boundary. For all of the remaining parameters in the options dialog, the default values should be suitable to simulate the Henry problem.

13.6 Step 6: Running the simulation

The model is now ready to start the simulation. Choosing *Time...* in the Simulation-menu, the user has to set the final time and the length of the flow time step. Because the initial concentration gradients of the Henry problem are steep, a correct solute mass balance is obtained by using a short time step at the beginning of the simulation. Starting with a time step of 1 and setting a factor of 1.1 yields acceptable results. For a start, set the final time to 1800, even though it is not necessary that the final time is a multiple of the flow time step.

The user may choose to either run the simulation automatically by selecting *Start* or follow the simulation process from step to step by selecting *Flow Step*, *Transport Step*, or *Synchronize*. Except for a single transport step, all of these procedures can be interrupted and restarted deliberately. At any time during the simulation process, intermediate results can be viewed by choosing the parameter of interest from the view menu. Selecting *Update* allows to view the most recent values of the currently selected parameter.

During the simulation process or after the simulation reached the specified final time of 1800, choosing *Mass Accumulation...* from the Evaluation-menu displays a graph of the solute mass accumulation in the model domain in the course of the simulation time. The graph did not yet approach a horizontal line asymptotically, which indicates that the saltwater intrusion is still in progress. Consequently, the simulation must be continued to obtain a solution for the steady-state equilibrium. The user may increase the final time and resume the simulation process. By repeatedly checking the mass accumulation graph, it can be observed that the solute mass storage approaches a horizontal line asymptotically after a simulation time of approximately 10000 s.

13.7 Step 7: Evaluation of the simulation results

The error in the water and mass balance can be displayed by choosing the corresponding item from the Evaluation-menu. Both errors should be within reasonable limits.

The graphical display of the simulation results in SWIMMOC is supposed to provide an idea of what is happening during the simulation process. For more sophisticated graphical presentations of the results, the user may export the values of interest through the File-menu. All grid files written by SWIMMOC are plain text files that are fully compatible with the program Surfer by Golden Software. To import the grid files into other programs, the user has to know that the files consist of a header and the gridded data. The header contains information about the dimension of the grid and the minimum and maximum values, which are required by the program Surfer. The gridded data is written as space-delimited text. The first line contains the values of the last row, the second line contains the values of the second-last row, and so on. The format of export files that contain non-gridded data, such as the concentration of the particles or the mass accumulation, is self-explaining.

Figure 13.2 shows the solute mass accumulation within the model domain during the simulation. Due to the strong gradients at the beginning of the simulation, the solute mass storage increases rapidly at the beginning. The continuous smoothing of the concentration gradients in the course of the first 10000 s is accompanied by a decreasing accumulation rate. After a simulated time of about 10000 s, the solute mass storage remains constant. At this point, the steady-state equilibrium is reached, and the mass inflow is balanced by the outflow. This time interval compares well with a value published by *Simpson and Clement* (2004). Their numerical solution of the standard Henry problem needed about 9600 s to reach the steady-state equilibrium. As they did not provide information on the mass accumulation in their solution, the two results cannot be compared in greater detail.

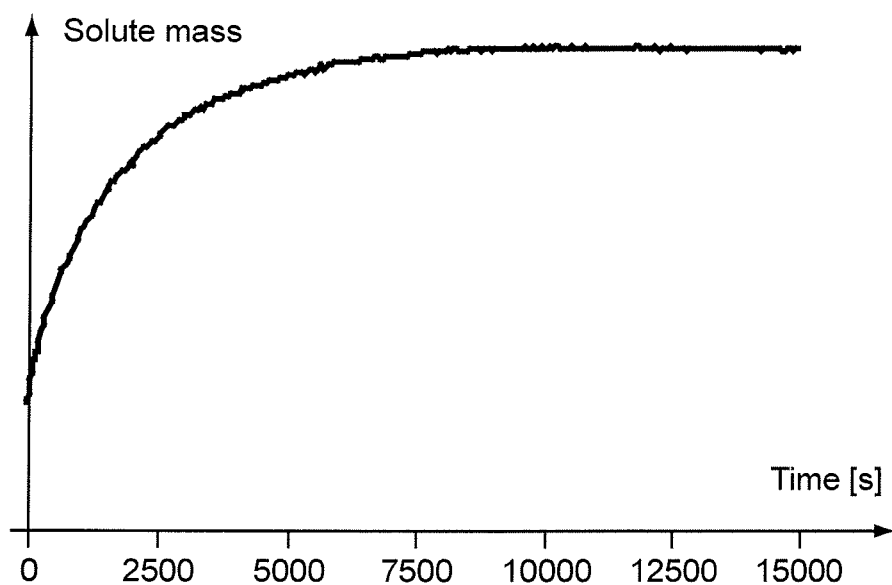


Figure 13.2: The graph shows the changes in solute mass storage within the model domain with time. The mass axis is unlabeled because the concentration of saltwater is arbitrary. The steady-state equilibrium is reached after a simulated time of about 10000 s.

Two different options for displaying the modeled concentration distribution after a simulated time of 15000 s are illustrated in figure 13.3. The first possibility is to export the concentration values at the nodes to a grid file and directly to plot lines of equal concentration (figure 13.3a). The second possibility (figure 13.3b) is to export the concentration values and the position of the tracer particles. Depending on the number of particles per cell, the interpolation of these concentration values may yield more accurate results. In the illustrated example, the two plots compare well. Figure 13.3c shows a scatter plot of the position of the tracer particles. In general, the particles are distributed evenly through the model domain, suggesting that the replacement of particles at source cells leads to the desired results. Only in those places in the grid where the velocity is highly variable, e.g. the front of the saltwater wedge, small gaps in the distribution of tracer points occur.

The observed piezometric heads and the equivalent freshwater heads for the steady -state solution of the Henry problem are illustrated in figure 13.4. The equivalent freshwater heads in the right half of the model grid clearly indicate the saltwater intrusion at the bottom of the cross-section. In the left half of the grid, the observed heads are equal to the equivalent freshwater heads, because the salt concentration of the groundwater is negligible in this part of the model aquifer.

In figure 13.5, the results of two simulations with different grid resolutions are compared to the results of numerical solutions by *Simpson and Clement* (2004). They used a finite elements grid consisting of 861 nodes. This corresponds to the resolution of the 20×41 grid used in SWIMMOC. In general, both solutions obtained from SWIMMOC show a good correspondence with the solution of *Simpson and Clement* (2004). The greatest deviations occur in the top right corner of the model grid. SWIMMOC seems to exaggerate the diffusive transport from the seaward boundary into the model domain. However, this may also be the result of a different implementation of the constant concentration boundary condition in the model used by *Simpson and Clement* (2004).

13.8 Numerical solution of the modified Henry problem

Simpson and Clement (2004) show that the Henry problem is not the most suitable test case for density-dependent flow, because the numerical quality of the bi-directional coupling between flow and transport has only minor influence on the accuracy of the simulation results. They propose a modified version of the Henry problem to be used as a benchmark and provide a semi-analytical solution that can be compared with the results of a numerical simulation. The only difference from the standard Henry problem is that the freshwater recharge flux from the left boundary in the modified Henry problem is reduced

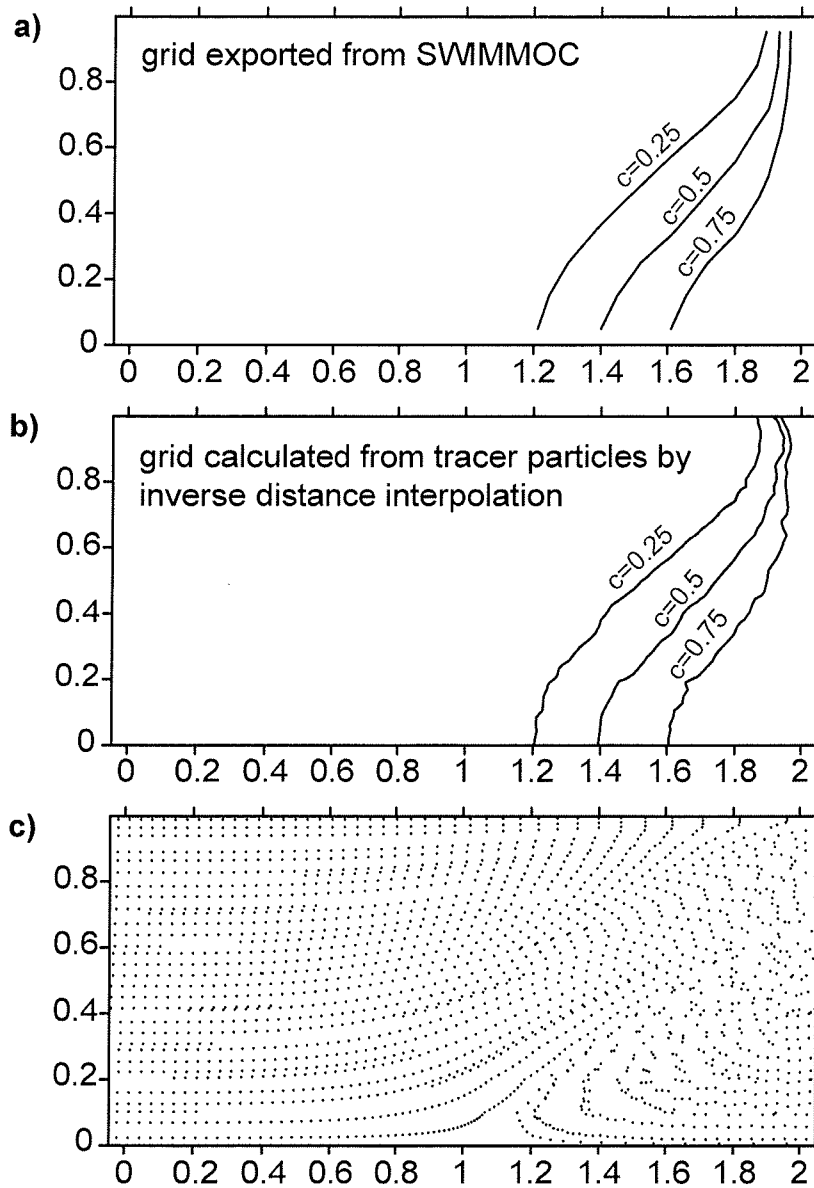


Figure 13.3: The two contour plots show the lines of equal concentration for 25, 50, and 75 percent saltwater concentration for the steady-state solution of the standard Henry problem. The grid resolution is 10×21 and 9 particles were initially placed into each cell. For the upper plot, the contour lines were drawn directly into the grid that was exported from SWIMMOC. The second contour plot is based on a grid that was calculated by inverse distance interpolation from the concentration values associated with the tracer particles. The third plot shows the position of the tracer particles.

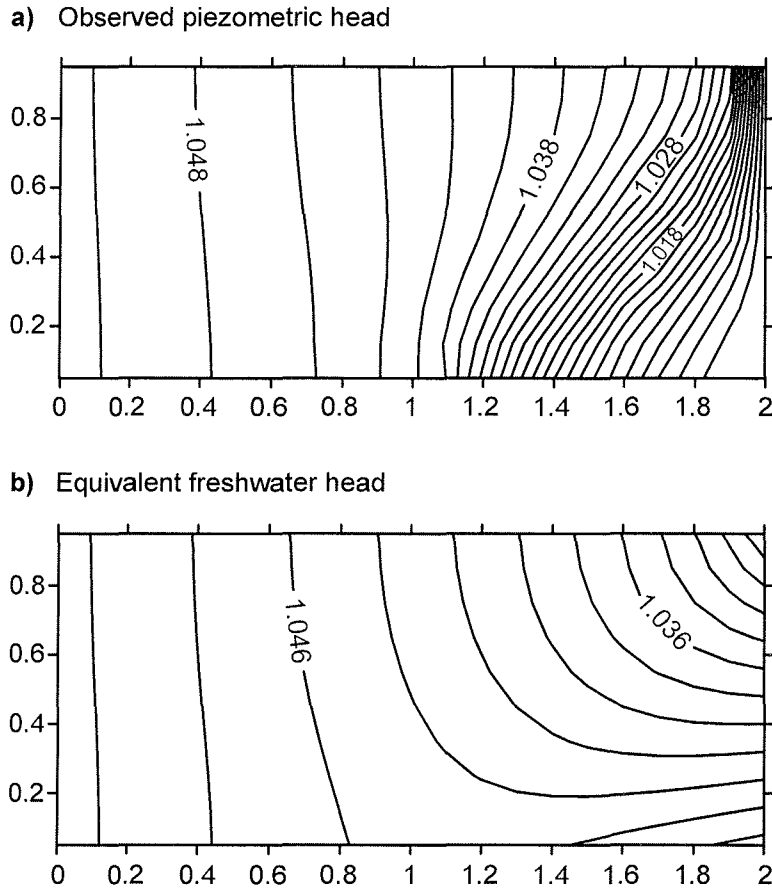


Figure 13.4: The first plot shows the lines of equal piezometric head that would be measured if the Henry problem existed in reality and could be investigated by means of observation wells (a). For the second plot, the observed piezometric heads were converted into equivalent freshwater heads (b). The difference between the two plots results from saltwater intrusion.

by 50 percent. This will cause the saltwater to intrude further into the aquifer and significantly increase the importance of correct coupling between flow and transport (*Simpson and Clement, 2004*).

In order to adapt the described SWIMMOC simulation to the modified Henry problem, the user simply chooses *Recharge* from the Boundary menu with no cells selected. This will display the definition of the “Recharge” boundary condition. In the *Flux* panel, the value of the volumetric flux rate has to be changed from $6.6 \times 10^{-6} \text{ ms}^{-1}$ to $3.3 \times 10^{-6} \text{ ms}^{-1}$. The modification is confirmed by clicking the *OK* button. The new value will automatically be applied to all boundary cells of the type “Recharge”. Now, the user may either continue a previous simulation with the changed boundary condition or restart the simulation.

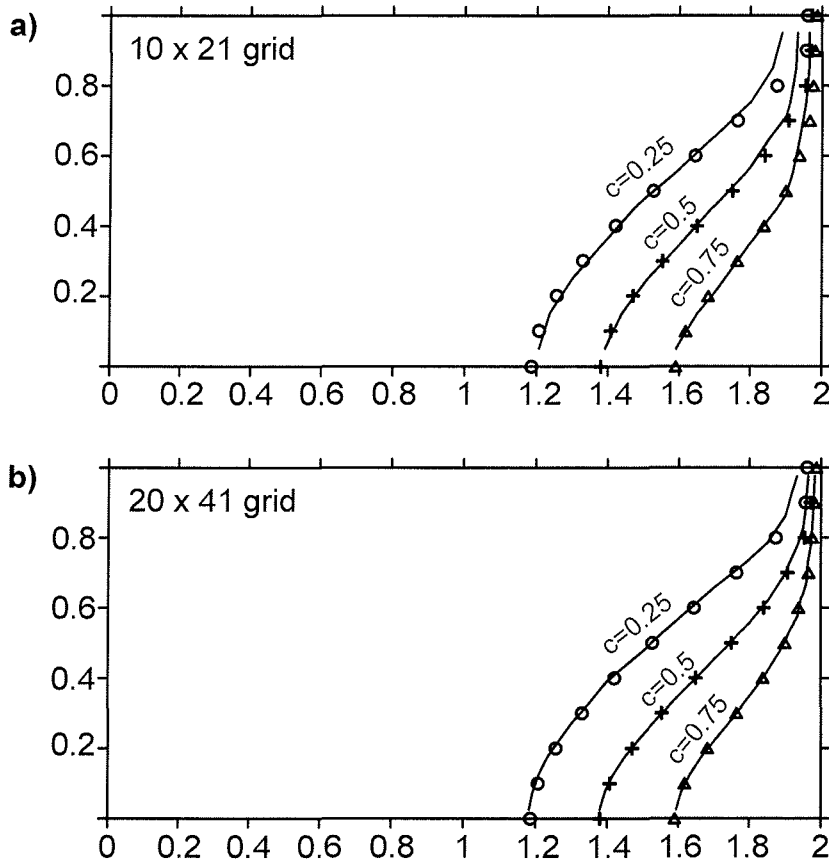


Figure 13.5: Two different simulation results obtained by using a 10×21 grid (a) and a 20×41 grid (b) in SWIMMOC are compared to a highly accurate numerical solution by *Simpson and Clement* (2004). The lines represent equal solute concentration in the SWIMMOC simulations. The points marked by the triangles, crosses, and circles indicate the points of 75, 50, and 25 percent saltwater concentration as published by *Simpson and Clement* (2004), respectively.

13.9 Comparison of the simulation results

The solute mass accumulation for the simulation of the modified Henry problem is illustrated in figure 13.6. Due to the reduced recharge flow from the left boundary, the saltwater intrudes further into the aquifer compared to the standard Henry problem. Consequently, it takes much longer, for the system to reach a steady-state equilibrium. *Simpson and Clement* (2004) state that their numerical solution required about 16500 s until no further concentration changes were observed. Figure 13.6 shows that the accumulation rate beyond this time is minor, however a balance of in- and outflow is reached much later.

Figure 13.7 shows a comparison of the simulation results obtained by using SWIMMOC and the semi-analytical solution provided by *Simpson and Clement* (2004). Both the shape and the position of the concentration contours obtained from the SWIMMOC simulation are in excellent agreement with the semi-analytical solution. According to *Simpson and Clement* (2004),

the accurate simulation of the modified Henry problem indicates that the bi-directional coupling of flow and transport is correct.

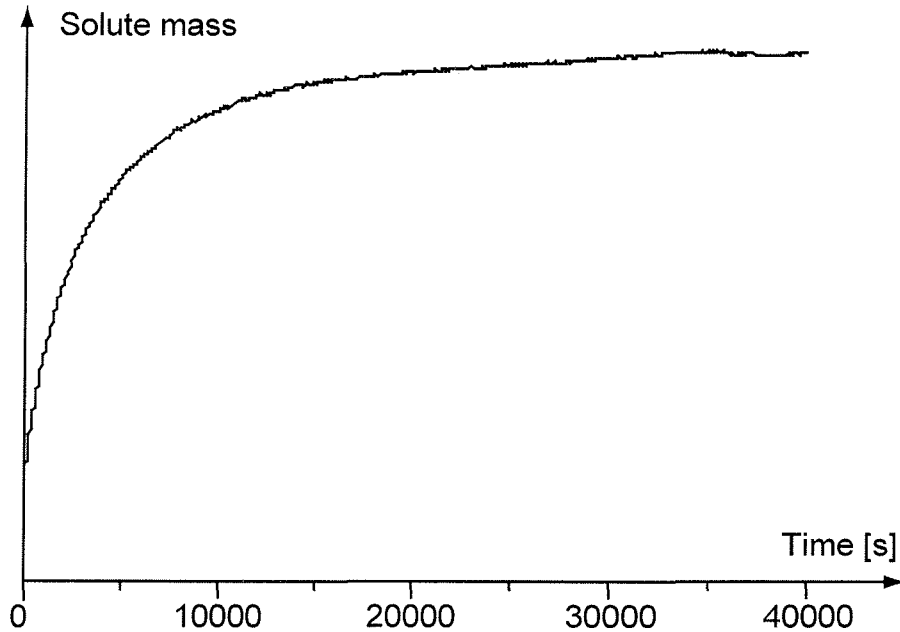


Figure 13.6: Reducing the recharge flow rate to $3.3 \times 10^{-6} \text{ ms}^{-1}$ in the modified Henry problem causes the seawater to intrude much further into the aquifer compared to the intrusion length reached in the standard Henry problem. As a result, it takes more than twice as long until the steady-state equilibrium is reached.

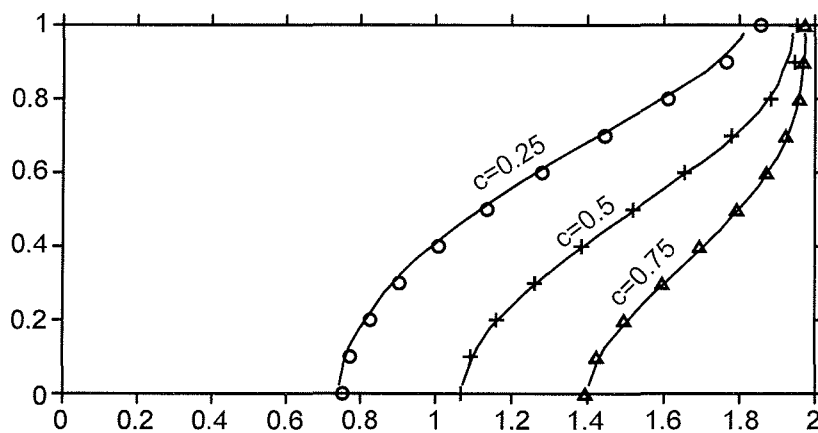


Figure 13.7: The modified Henry problem was simulated in SWIMMOC using a grid of 20 rows and 41 columns with 9 particles per cell. The lines represent equal solute concentration in the SWIMMOC solution. The points marked by the triangles, crosses, and circles indicate the points of 75, 50, and 25 percent saltwater concentration as published by *Simpson and Clement* (2004), respectively. The solution produced by SWIMMOC compares well with the semi-analytical solution.

Chapter 14

Summary

The hydrogeological and numerical background of a new numerical model for the simulation of density-dependent groundwater flow is presented. The computer program SWIMMOC is capable of simulating two-dimensional groundwater flow in vertical cross-sections. Density differences are accounted for by applying the concept of equivalent freshwater head, assuming that the groundwater density is proportional to the solute concentration.

SWIMMOC uses a finite differences formulation of the groundwater flow equation. Either the Gauss-Seidel method or the iterative alternating direction implicit (IADI) method can be used to calculate the distribution of equivalent freshwater heads and the velocity field. Both techniques are unconditionally stable.

The solution of the transport equation is based on the method of characteristics. The advection terms of the transport equation are solved by either linear or bilinear particle tracking. To ensure realistic particle paths at source and sink cells, the volumetric fluxes resulting from boundary conditions can be assigned to specific faces of the boundary cells. The bilinear tracking algorithm includes reflection techniques to correct the calculated paths close to no-flow boundaries. To avoid a crowding of tracer particles at sinks, particles entering into sink cells are removed from the model grid. Particles which move out of source cells are replaced in order to prevent that cells become depleted of tracer particles. The combination of both tends to maintain an even distribution of particles.

An explicit algorithm is applied to calculate the concentration changes due to diffusion, dispersion, sources, and sinks. To account for concentration changes resulting from advective transport, an intermediate concentration value is used to calculate the necessary concentration gradients. Assigning the concentration changes to discrete tracer particles reduces numerical dispersion to a minimum. The concentration changes are translated to changes in groundwater density, affecting the groundwater flow pattern.

Numerical instabilities may occur as a consequence of the bi-directional coupling of the flow and transport parts of the simulation. The effects of different model parameters on the stability of the solution are discussed. Recommendations and strategies to avoid numerical instabilities are derived.

In SWIMMOC, transient solute mass storage is accounted for by changes in the effective porosity of the aquifer. Groundwater flow at a steady-state equilibrium can be simulated by continuous simulation using constant boundary conditions or by setting the specific storage equal to zero, forcing the flow equation into a steady state solution. Graphs of the solute mass accumulation help to determine whether the simulation reached an equilibrium or not.

SWIMMOC allows the convenient definition of aquifer properties in terms of hydrogeological units. The creation of boundary conditions that are typical for coastal aquifers is greatly facilitated. The user has a choice of constant observed head, constant concentration, constant flux, and leakage boundary conditions. The program provides a number of visualization features to provide graphical feedback on the numerical procedures and on the state of the simulation. The accuracy of the simulation results can be evaluated by means of water balance as well as mass balance calculations.

The new numerical model is applied to simulate the classic Henry problem for saltwater intrusion as well as a modified version of the Henry problem. The simulation results for the classic Henry problem obtained by using SWIMMOC compare well with results generated by other numerical models. The accurate solution of the modified Henry problem indicates that the bi-directional coupling of groundwater flow and solute transport implemented in SWIMMOC is correct.

Part II

Streambed hydraulic conductivity

Chapter 15

In-situ measurement of low streambed hydraulic conductivity

T. Feseker and J. Seeberg-Elverfeldt

Abstract

A method for measuring the hydraulic conductivity of semi-pervious streambeds directly in the stream is described and field examples from a drainage channel in northern Germany are presented. The method is derived by increasing the sensitivity of a simple standpipe method. Error analysis shows that the tolerance of the measured values ranges between five and seven percent. However, lateral variability of the hydraulic conductivity exceeds the error of the measured values. Consequently, several tests at different locations within the channel are required to obtain a representative value of hydraulic conductivity. Comparison of the in-situ results to estimates from grain size analysis reveals deviations, which can be related to the uniformity of the streambed sediments.

15.1 Introduction

The interaction of groundwater and surface water is an important issue for water resource management in low-lying coastal areas, where the regional groundwater table is lowered through drainage networks. The drainage channels collect water from surface runoff as well as groundwater, which flows from the aquifer through the streambed into the channels. Therefore, the sustainable management of coastal groundwater resources requires an integrated approach which considers both groundwater abstraction through wells and groundwater

depletion caused by drainage networks. Excessive drainage may lead to over-exploitation and promote saltwater intrusion, but it is difficult to quantify the discharge of groundwater to the drainage network.

On a regional scale, the hydraulic relationship between surface water bodies and aquifers is controlled by the distribution and magnitude of hydraulic conductivities, both within the channel and the alluvial plain, the hydraulic gradient between the surface water levels and the adjacent groundwater hydraulic head, and the geometry and position of the stream channel within the alluvial plain *Woessner* (2000). An overview of the relevant processes is provided by *Sophocleous* (2002). The hydraulic properties of the aquifer may be assessed by means of pumping tests (e.g. *Kruseman and de Ridder*, 1994). In case the streambed sediments consist predominately of sand or gravel, the hydraulic conductivity may be estimated from grain size analysis (e.g. *Hazen*, 1893; *Beyer*, 1964). *Hvorslev* (1951) describes various permeameter tests for measuring the permeability of samples as well as in-situ tests using a single well or open bore hole. *Chen* (2000) applies a simple but efficient standpipe method to measure the streambed hydraulic conductivity in arbitrary directions directly in the stream. For practical reasons, however, this method is limited to streambeds with a relatively high permeability and cannot be applied to the semi-pervious streambeds.

This paper describes a modified version of the standpipe method used by *Chen* (2000), which can be applied to measure the hydraulic conductivity of semi-pervious streambeds in-situ. Field examples and the comparison to estimated values from grain size analysis illustrate the usefulness of this method.

15.2 Materials and methods

15.2.1 Grain size analysis

Samples of the upper 0.2 meters of the streambed sediments were taken using a mini-box corer. The grain size distribution was determined by means of wet sieving for diameters greater than 0.125 mm and through Stokes settling for smaller diameters. In order to prevent coagulation, sodium pyrophosphate ($\text{Na}_4\text{P}_2\text{O}_7 \cdot 10\text{H}_2\text{O}$) was added to the samples at a concentration of 0.5 g per liter of suspension.

The grain size distribution is used to estimate the hydraulic conductivity of the streambed sediments, applying a formula provided by *Beyer* (1964). Compared to the method described by *Hazen* (1893), this approach accounts for a larger range of uniformity coefficients. It is assumed that the hydraulic conductivity of the sediment is controlled by the effective grain size d_{10} (*Hazen*, 1893):

$$K = C d_{10}^2 \quad (15.1)$$

where

- K is the hydraulic conductivity,
 C is a proportionality factor, and
 d_{10} is the grain size diameter for which ten weight percent of the sample are finer.

Hazen (1893) employs a temperature-dependent proportionality factor, whereas the factor C used by *Beyer* (1964) depends on the temperature as well as on the uniformity coefficient, which is defined by:

$$U = \frac{d_{60}}{d_{10}} \quad (15.2)$$

where

- d_{60} is the grain size diameter for which 60 weight percent of the sample are finer.

As indicated by table 15.1, the proportionality factor is defined for a large range of uniformity coefficients. However, equation (15.1) delivers realistic results only if the value of d_{10} ranges between 0.06 mm and 0.6 mm and if the uniformity coefficient is smaller than 20 (*Beyer*, 1964).

Table 15.1: The proportionality factor C used to estimate the hydraulic conductivity from the grain size distribution depends on the uniformity coefficient U . The values given below are for a groundwater temperature of ten degrees Celsius. (*Beyer*, 1964)

U [-]	C [$1 \times 10^{-6} \text{ m}^{-1} \text{ s}^{-1}$]
1-2	0.012-0.0105
2-3	0.0105-0.0095
3-5	0.0095-0.0085
5-10	0.0085-0.0075
10-20	0.0075-0.0065
> 20	0.0065

15.2.2 In-situ tests

Chen (2000) describes a standpipe method to measure streambed hydraulic conductivity in-situ, applying evaluation formulas provided by *Hvorslev* (1951). The method uses a simple standpipe which is driven into the sediment. The

rest of the pipe is filled with water, creating a hydraulic gradient between the water levels in the pipe and in the channel. Then, the falling head in the pipe is recorded as the water flows out of the lower end of the pipe into the sediment. Assuming that the head loss in the pipe is exponential, the hydraulic conductivity of the streambed sediments enclosed in the pipe is determined using two head readings at different times (*Hvorslev*, 1951; *Chen*, 2000). In the examples provided by *Chen* (2000), the measured values of hydraulic conductivity range between $2 \times 10^{-4} \text{ ms}^{-1}$ and $2 \times 10^{-3} \text{ ms}^{-1}$. However, the time required to measure a significant change in head depends directly on the hydraulic conductivity of the sediments. In case the streambed is less permeable, the measuring time may become extremely long. Therefore, the application of the method as described by *Chen* (2000) is limited to streambeds of relatively high permeability.

As suggested by *Hvorslev* (1951), the method is modified such that the time required to measure a significant change in head is reduced. This is accomplished by using a pipe that is large in diameter to increase the area of infiltration, and a measuring tube that is small in diameter to increase the head change resulting from outflow. The quality of the results depends on both the accuracy of the head readings and the tolerance of the tube diameter. Therefore, precision tubes made for peristaltic pumps were employed as measuring tubes. The capillary rise in the tubes was measured before the tests and subtracted from the readings. Since the measuring tubes are too narrow to be used to quickly fill the device with water, a second tube with a larger diameter must be connected to the pipe (figure 15.1).

Using a hammer, the steel pipe is driven into the sediment as deep as possible. Then, the measuring tube is connected to the pipe and attached to a measuring staff, which is installed next to the pipe. Subsequently, the rest of the pipe and the measuring tube are filled by quickly pouring a bucket of water into the filling tube. As soon as the water is flowing out of the top end of the measuring tube and all air has escaped, the stopcock at the inlet of the pipe is closed to prevent that the measurement is affected by the water in the filling tube. Finally, the head loss in the measuring tube is recorded.

In practice, it has been found that the device is extremely sensitive to pressure changes in the vicinity of the pipe. Consequently, it must be avoided to walk or move in the channel during the measurement. Undisturbed readings may be obtained by either installing the measuring staff directly outside the channel or by observing the falling head from a fixed stand, such as a board placed across the channel.

According to Darcy's law (e.g. *Freeze and Cherry*, 1979), the volumetric flux through an area perpendicular to the direction of flow is proportional to the hydraulic gradient. Assuming that the hydraulic head at the lower end of the pipe is equal to the constant water level in the channel, the volumetric flux

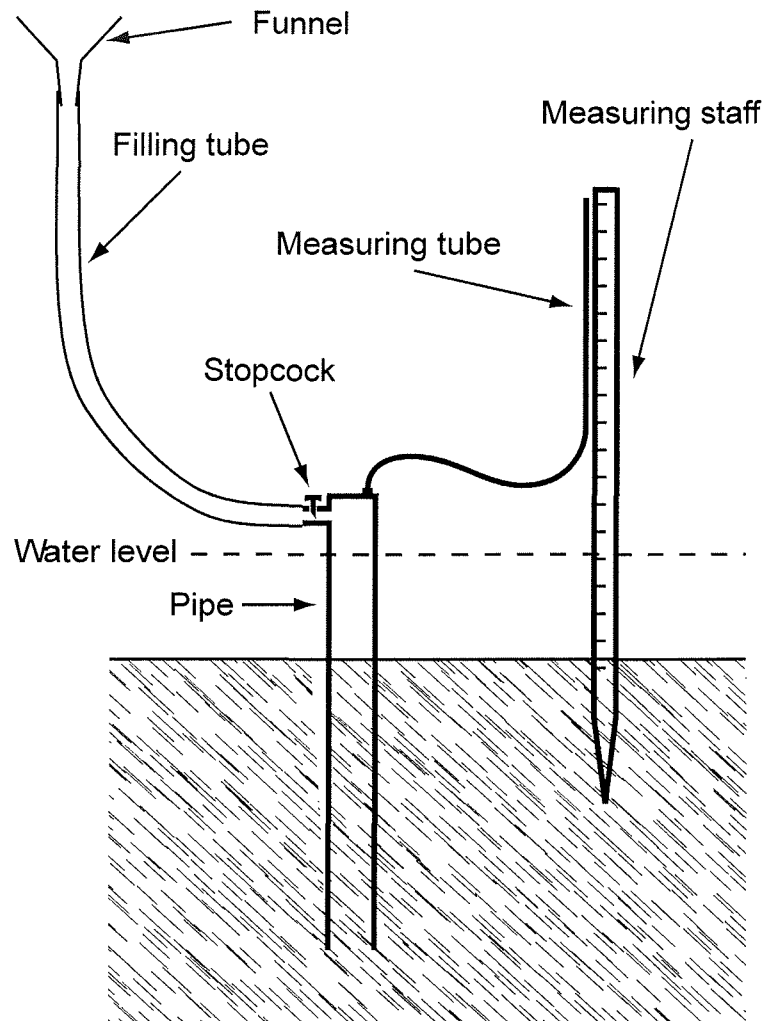


Figure 15.1: The hydraulic conductivity of the streambed sediments is measured in-situ using a steel pipe of 1 m length and 0.105 m diameter. The lower end of the pipe is open and the edge is sharpened. A steel plate bearing a connector for the measuring tube closes the top of the pipe air-tight. The small-diameter (0.00279 m) measuring tube is attached to a measuring staff, which is used to determine the distance from the hydraulic head in the tube to the water level in the channel. The pipe and the measuring tube may be filled quickly with water through a large-diameter (0.02 m) tube connected to an inlet with a stopcock close to the top of the pipe.

CHAPTER 15. IN-SITU MEASUREMENT OF LOW STREAMBED
HYDRAULIC CONDUCTIVITY

through the pipe may be calculated as:

$$Q(t) = -K_v \pi \left(\frac{D}{2} \right)^2 \frac{h(t)}{L} \quad (15.3)$$

where

- Q is the volumetric flux through the pipe,
 t is the time,
 K_v is the vertical hydraulic conductivity of the sediment enclosed in the pipe,
 D is the diameter of the pipe,
 h is the hydraulic head in the measuring tube relative to the water level in the channel, and
 L is the penetration depth of the pipe.

The rate of change in the volume of water in the measuring tube as the water is flowing out of the pipe is given by:

$$\frac{d}{dt} V(t) = \pi \left(\frac{d}{2} \right)^2 \frac{d}{dt} h(t) \quad (15.4)$$

where

- V is the volume of water in the measuring tube, and
 d is the diameter of the measuring tube.

Since the volumetric flux through the pipe is equal to the rate of change in the volume of water in the measuring tube, equations (15.3) and (15.4) may be combined to obtain:

$$\frac{d}{dt} h(t) = - \left(\frac{D}{d} \right)^2 \frac{K_v}{L} h(t) \quad (15.5)$$

The time lag is defined as the time required for water to flow out of the measuring device until a desired degree of pressure equalization is attained (*Hvorslev*, 1951). The time lag required for the hydraulic head in the measuring tube to fall from h_0 to h is determined by integrating equation (15.5) between the times t_0 and t :

$$t - t_0 = \left(\frac{d}{D} \right)^2 \frac{L}{K_v} \ln \frac{h_0}{h} \quad (15.6)$$

where

h_0, h_1 are the hydraulic heads in the measuring tube at the times t_0 and t_1 , respectively.

The length of the time lag is proportional to the natural logarithm of the ratio of the corresponding hydraulic heads in the measuring tube. For simplification, equation (15.6) may be rewritten as:

$$t = t_0 + m g(h) \quad (15.7)$$

with

$$g(h) = \ln \frac{h_0}{h} \quad (15.8)$$

where

m is the proportionality factor.

The proportionality factor m depends on the geometry of the measuring device, the penetration depth, and the vertical hydraulic conductivity of the sediment enclosed in the pipe:

$$m = \left(\frac{d}{D}\right)^2 \frac{L}{K_v} \quad (15.9)$$

Or, after rearranging:

$$K_v = \left(\frac{d}{D}\right)^2 \frac{L}{m} \quad (15.10)$$

Consequently, the vertical hydraulic conductivity may be calculated by determining the slope of a linear regression line for a sequence of measurements. Given that $(h_0, h_1, h_2, \dots, h_n)$ are the hydraulic head readings and $(t_0, t_1, t_2, \dots, t_n)$ are the corresponding times, the values of $g(h)$ at the measured points are calculated as:

$$g_i = \ln \frac{h_0}{h_i} \quad i = (1, 2, \dots, n) \quad (15.11)$$

The regression line that is fitted through the given points (g_i, t_i) is written as:

$$f(g) = t_0 + m g \quad (15.12)$$

Applying the method of least squares (e.g. *Kreyszig, 1999*), the regression line is determined such that the sum S^2 of the squares of the vertical distances from the known points to the straight line is minimum:

$$S^2 = \sum (t_i - f(g_i))^2 \quad (15.13)$$

The slope of the regression line is given by (e.g. *Kreyszig, 1999*):

$$m = \frac{n \sum g_i t_i - \sum g_i \sum t_i}{n \sum g_i - (\sum g_i)^2} \quad (15.14)$$

where

n is the number of measurements, excluding the initial values h_0 and t_0 .

The overall quality of the fit is evaluated by calculating the coefficient of determination, which is defined as:

$$r^2 = \frac{[\sum (g_i - \bar{g})(t_i - \bar{t})]^2}{\sum (g_i - \bar{g})^2 \sum (t_i - \bar{t})^2} \quad (15.15)$$

in which

$$\bar{g} = \frac{1}{n} \sum_{i=1}^n g_i \quad (15.16)$$

and

$$\bar{t} = \frac{1}{n} \sum_{i=1}^n t_i \quad (15.17)$$

where

r^2 is the coefficient of determination.

The coefficient of determination is an indicator that ranges in value between zero and one. Values close to one suggest that a strong linear relationship exists between g_i and t_i , whereas values close to zero indicate that t_i is not proportional to g_i . Provided that the assumption of a linear relationship is valid, the vertical hydraulic conductivity of the sediment enclosed in the pipe may be calculated using equation (15.10). The law of error propagation in equation (15.10) determines the error of the calculated value of K_v (e.g. *Schönwiese*, 2000):

$$\pm \Delta K_v = \sqrt{\left(\frac{\partial K_v}{\partial d} \Delta d\right)^2 + \left(\frac{\partial K_v}{\partial D} \Delta D\right)^2 + \left(\frac{\partial K_v}{\partial L} \Delta L\right)^2 + \left(\frac{\partial K_v}{\partial m} \Delta m\right)^2} \quad (15.18)$$

where

ΔK_v is the error of K_v ,

Δd is the tolerance of the diameter d of the measuring tube,

ΔD is the tolerance of the diameter D of the pipe,

ΔL is the tolerance of the penetration depth L , and

Δm is the error of the slope m of the regression line.

The partial derivatives of K_v in equation (15.18) are:

$$\frac{\partial K_v}{\partial d} = \frac{2 d L}{D^2 m} \quad (15.19)$$

$$\frac{\partial K_v}{\partial D} = -\frac{2 d^2 L}{D^3 m} \quad (15.20)$$

$$\frac{\partial K_v}{\partial L} = \frac{d^2}{D^2 m} \quad (15.21)$$

$$\frac{\partial K_v}{\partial m} = -\frac{d^2 L}{D^2 m^2} \quad (15.22)$$

The tolerance values of the diameters of the measuring tube and the pipe are $\Delta d = 0.05 \text{ mm}$ and $\Delta D = 1 \text{ mm}$, respectively. An estimated value for the accuracy of the measurement of the penetration depth in the field is $\Delta L = 1 \text{ cm}$. The standard error of the slope m is given by (*Acton, 1966; Gonick and Smith, 1993*):

$$\Delta m = \sqrt{\frac{\sum (g_i - \bar{g})^2 \sum (t_i - \bar{t})^2 - [\sum (g_i - \bar{g})(t_i - \bar{t})]^2}{n - 2}} \quad (15.23)$$

15.3 Results

Field tests were conducted at 20 locations in a drainage channel in the coastal plain of northern Germany, close to the city of Cuxhaven (figure 15.2). The channel “Norderscheidung” is part of a large tidal drainage network, which is connected to the North Sea by sluices. Since the slopes of the channels are minor, surface water flow is controlled by adjusting the water levels in different sections of the drainage network. Dewatering into the North Sea occurs during low tide.

The elevation of the ground surface ranges between 1 and 1.5 meters above mean sea level. The bottom of the channel is approximately 1.5 meters below mean sea level. The water level in the channel varies roughly between 0.2 and 1.2 meters above the bottom, while the width of the channel ranges from 0.6 to 1.5 meters. All test locations are within a section of 500 meters length, approximately 25 meters apart from each other.

15.3.1 Estimated hydraulic conductivity values based on the grain size distribution

The composition of the streambed sediments varies considerably within this section of the channel. As illustrated in figure 15.3, the grain size of the sediments is dominated by silt and fine sand. The gravel-size particles are mostly

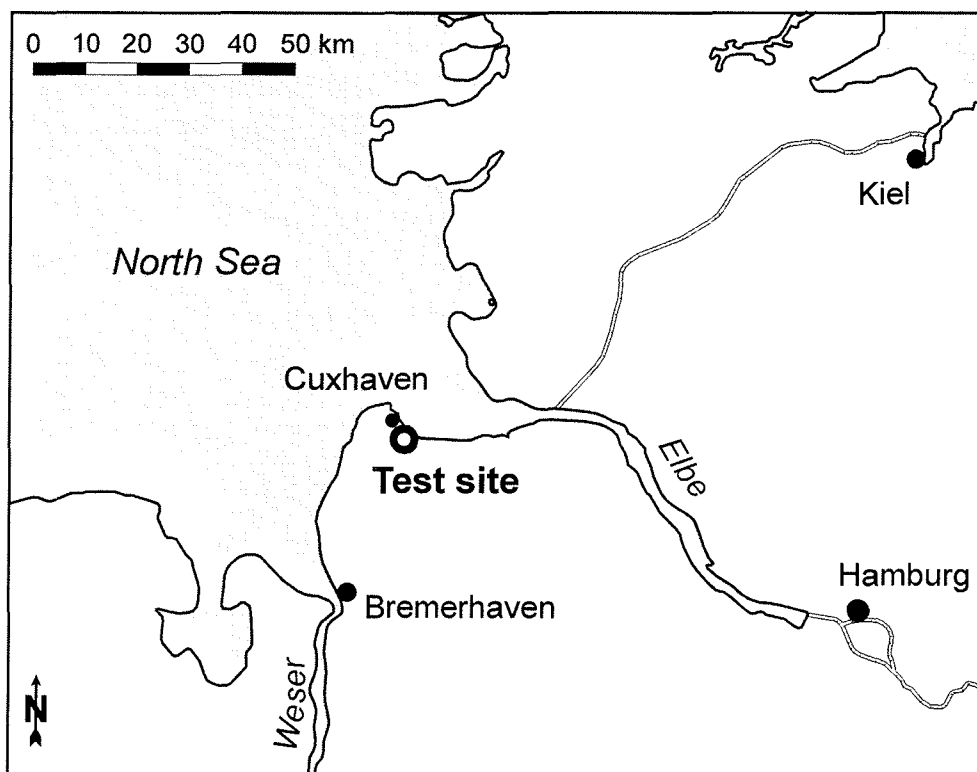


Figure 15.2: The test site (open circle) is located in north-western Germany, approximately 5 kilometers southeast of the city of Cuxhaven. The distance to the coastline is about 2.5 kilometers.

shells or pieces of shells. The sediment color ranges from grayish brown to very dark gray and the organic content is generally high. At several locations, stepping onto the sediments resulted in the release of gas bubbles.

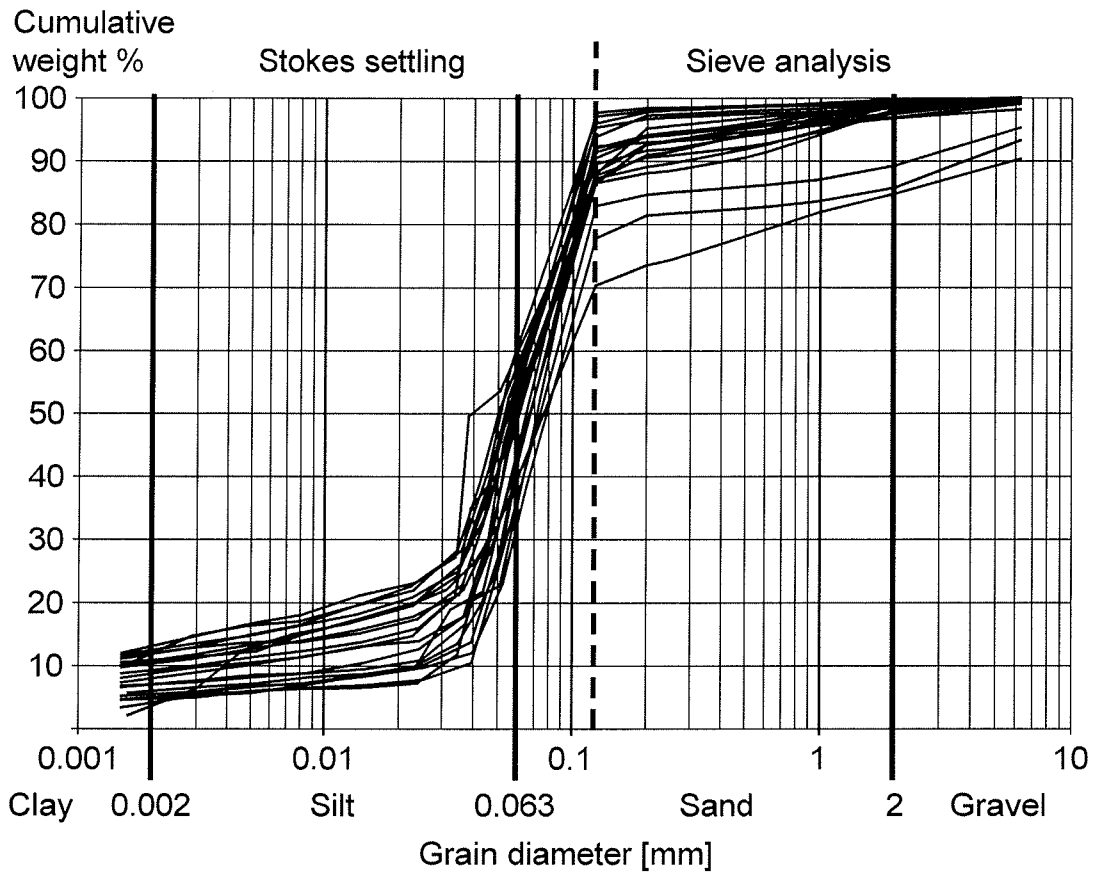


Figure 15.3: The streambed sediments at the sampled locations consist predominantly of silt and fine sand. For at least 70 weight percent of each sample, the grain sizes were smaller than 0.125 mm and had to be determined through Stokes settling.

The estimated hydraulic conductivity values obtained by applying equation (15.1) are listed in table 15.2. However, for none of the samples the effective grain size d_{10} is large enough to expect realistic estimates based on the grain size distribution. In four cases, the hydraulic conductivity could not be determined, because the effective grain size d_{10} was smaller than the minimum grain size accounted for in the hydrometer analysis. The estimated values range between $2 \times 10^{-8} \text{ ms}^{-1}$ and $1 \times 10^{-5} \text{ ms}^{-1}$. The arithmetic mean is $3 \times 10^{-6} \text{ ms}^{-1}$.

15.3.2 Results of the in-situ tests

Figure 15.4 shows the head changes in the measuring tube with time at four selected locations. The determination coefficients of the regression lines range

CHAPTER 15. IN-SITU MEASUREMENT OF LOW STREAMBED
HYDRAULIC CONDUCTIVITY

Table 15.2: Using the formula provided by *Beyer* (1964), the hydraulic conductivity of the streambed sediments is estimated from the grain size distribution in the samples. The effective grain size d_{10} of the samples from locations 11, 12, 16, and 18 is smaller than the minimum grain size accounted for in the hydrometer analysis.

Location	d_{10} [mm]	d_{60} [mm]	U [-]	C [$1 \times 10^{-6} \text{ m}^{-1} \text{ s}^{-1}$]	K [ms^{-1}]
1	0.03026	0.09173	3.03	0.0096	9×10^{-6}
2	0.02153	0.08453	3.93	0.0091	4×10^{-6}
3	0.02307	0.09841	4.27	0.0090	5×10^{-6}
4	0.0019	0.07324	38.55	0.0065	2×10^{-8}
5	0.00329	0.07785	23.66	0.0065	7×10^{-8}
6	0.02409	0.07661	3.18	0.0095	6×10^{-6}
7	0.02772	0.10052	3.63	0.0093	7×10^{-6}
8	0.03459	0.0848	2.45	0.0100	1×10^{-5}
9	0.00525	0.0822	15.66	0.0068	2×10^{-7}
10	0.00416	0.11121	26.73	0.0065	1×10^{-7}
11	–	0.07876	–	–	–
12	–	0.07044	–	–	–
13	0.00415	0.08599	20.72	0.0065	1×10^{-7}
14	–	0.0645	–	–	–
15	0.0134	0.07442	5.55	0.0084	2×10^{-6}
16	–	0.0743	–	–	–
17	0.00327	0.07111	21.75	0.0065	7×10^{-8}
18	–	0.0768	–	–	–
19	0.01908	0.07972	4.18	0.0090	3×10^{-6}
20	0.00158	0.06479	41.01	0.0065	2×10^{-8}

between $r^2 = 0.94$ and $r^2 = 0.99$ (table 15.3), suggesting that it is reasonable to assume that a linear relationship exists between the time and the natural logarithm of the corresponding ratio of hydraulic heads in the measuring tube. However, the distribution of the given points around the regression lines indicates that the measured hydraulic conductivity decreases during the test (figure 15.5). The values of vertical hydraulic conductivity determined according to equation (15.10) range from $6.98 \times 10^{-7} \text{ ms}^{-1}$ to $1.21 \times 10^{-6} \text{ ms}^{-1}$ with errors between five and seven percent (table 15.3). The arithmetic mean of the measured values is $4.03 \times 10^{-7} \text{ ms}^{-1}$.

15.3.3 Comparison of the results

Comparing the measured values and the values estimated from grain size analysis shows large deviations between the two approaches (figure 15.6). The measured values are relatively close to each other, while the estimated values vary within a range of three orders of magnitude. Figure 15.7 illustrates that

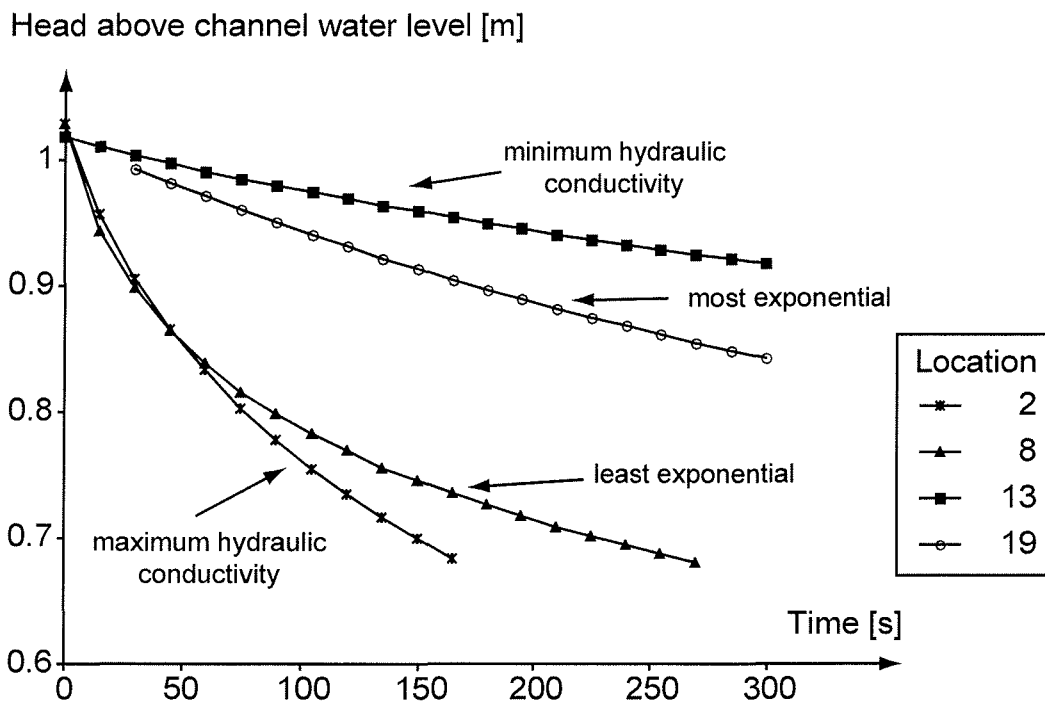


Figure 15.4: The hydraulic head in the measuring tube decreases as the water flows out of the lower end of the pipe. If the head is falling very quickly, the hydraulic conductivity of the sediment is high (location 2). Low permeability is reflected by slow changes in head (location 13). The series of measurements at locations 19 and 8 show the most and least exponential character, respectively (see also figure 15.5).

CHAPTER 15. IN-SITU MEASUREMENT OF LOW STREAMBED
HYDRAULIC CONDUCTIVITY

Table 15.3: The vertical hydraulic conductivity of the streambed sediments is calculated using the slope m of the regression line. The coefficient of determination r^2 indicates the quality of the fit. The errors of the calculated values are determined according to the law of error propagation as given by equation (15.18).

Location	r^2	m [s]	Δm [s]	K_v [ms^{-1}]	Percent Error
1	0.94	1430	37	2.36×10^{-7}	6
2	0.98	450	20	1.21×10^{-6}	6
3	0.95	1392	78	3.85×10^{-7}	7
4	0.95	2135	117	2.65×10^{-7}	7
5	0.96	1846	91	2.83×10^{-7}	7
6	0.95	886	46	6.54×10^{-7}	7
7	0.96	1071	49	5.01×10^{-7}	6
8	0.94	810	50	6.98×10^{-7}	7
9	0.96	1139	53	4.65×10^{-7}	6
10	0.94	975	57	6.23×10^{-7}	7
11	0.98	1948	73	3.01×10^{-7}	6
12	0.97	1488	66	4.03×10^{-7}	6
13	0.99	2965	51	1.88×10^{-7}	5
14	0.98	1339	43	4.22×10^{-7}	5
15	0.96	1782	83	3.21×10^{-7}	6
16	0.97	2280	98	2.57×10^{-7}	6
17	0.95	1487	80	3.42×10^{-7}	7
18	0.94	1717	99	2.84×10^{-7}	7
19	0.99	1639	28	2.76×10^{-7}	5
20	0.98	1424	52	3.52×10^{-7}	6

the estimated values are higher than the measured values in case the uniformity coefficient U is relatively small. Underestimation is associated with large values of U .

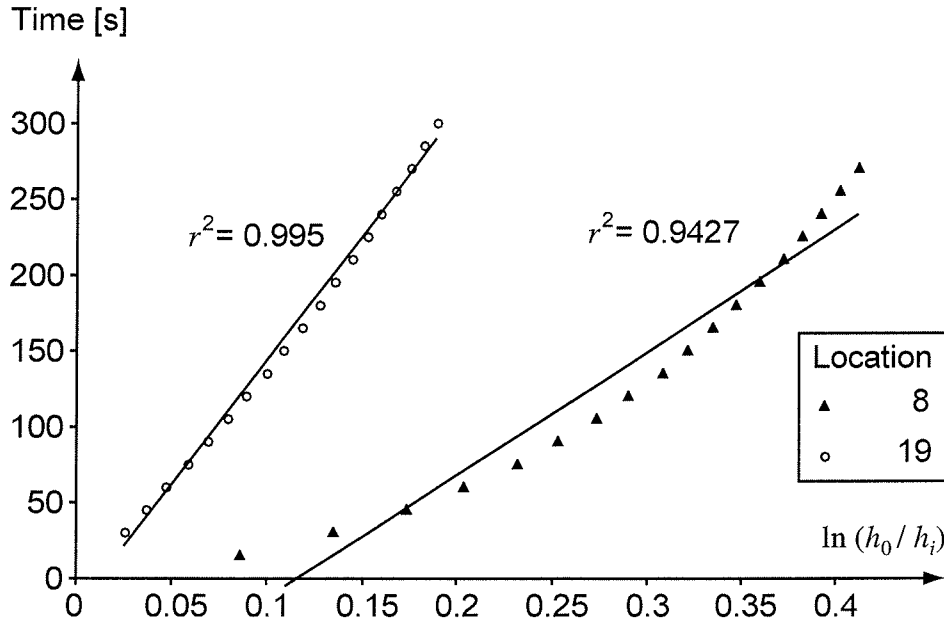


Figure 15.5: The graphs show the relationship between the time and the natural logarithm of the corresponding ratio of hydraulic heads in the measuring tube. Assuming that the hydraulic head is falling exponentially, the hydraulic conductivity of the streambed sediments can be determined by fitting a straight line through the given points. The coefficients of determination reveal that the best fit is obtained at location 19, whereas the series of measurements at location 8 shows the least exponential character. For both locations, the distribution of the points around the regression line reveals that the measured hydraulic conductivity decreases during the in-situ test.

15.4 Discussion

The evaluation of the in-situ test is simplified by assuming that the hydraulic head at the lower end of the pipe is equal to the water level in the channel and remains constant throughout the test. A more accurate evaluation formula which includes the flow out of the open end of the pipe is provided by *Hvorslev* (1951):

$$K_v = \frac{d^2 \left(\frac{\pi D}{11} \sqrt{\frac{K_v}{K_h}} + L \right)}{D^2 (t_1 - t_0)} \ln \frac{h_0}{h_1} \quad (15.24)$$

where

K_h is the horizontal hydraulic conductivity of the streambed sediments.

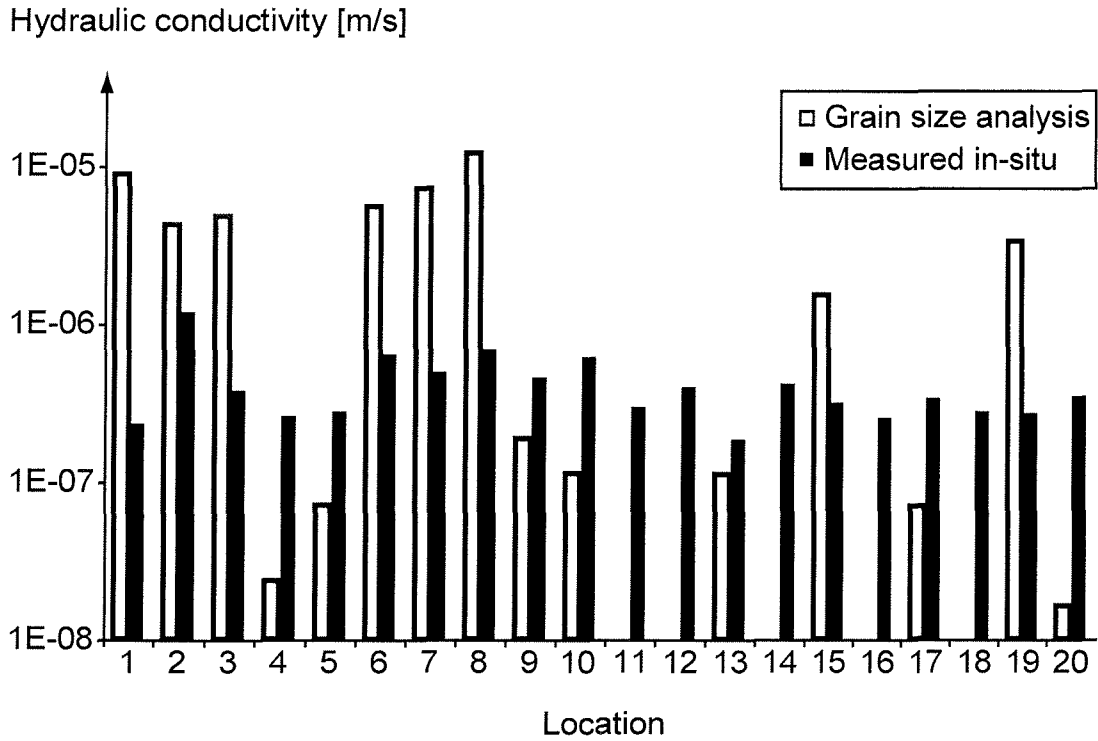


Figure 15.6: The values of hydraulic conductivity measured in-situ (black columns) are compared to the values estimated from the grain size distribution (open columns). The deviations are generally large, with estimated values both higher (locations 1, 2, 3, 6, 7, 8, 15, and 19) and lower (locations 4, 5, 9, 10, 13, and 20) than measured values. The estimated values vary within three orders of magnitude. The range of the measured values is much smaller.

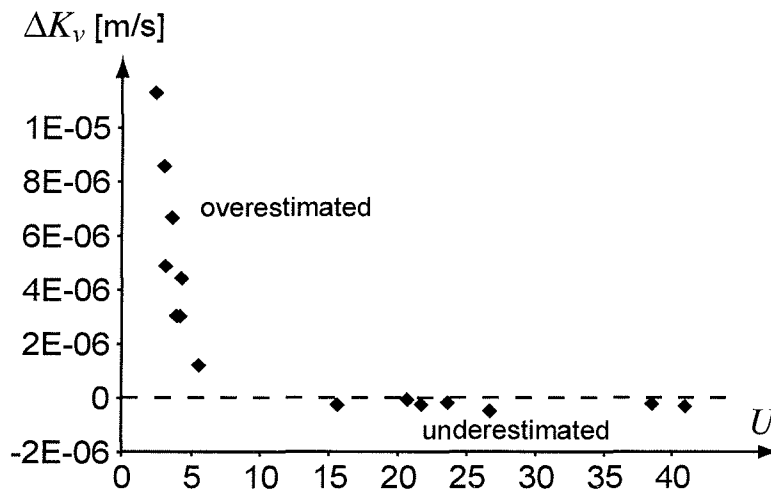


Figure 15.7: Plotting the difference ΔK_v between the estimated and the measured values of hydraulic conductivity versus the uniformity coefficient U reveals that underestimation is associated with large values of U . Small values of U result in overestimation of the hydraulic conductivity.

Equation (15.24) requires the ratio of the horizontal and vertical hydraulic conductivities to be known. However, equation (15.24) may be approximated using equation (15.10) in case the penetration depth L is several times larger than the diameter of the pipe (*Chen, 2000*).

According to equation (15.10), the vertical conductivity of the sediments enclosed in the pipe is inversely proportional to the slope of the regression line. The deviations of the given points from the straight line suggest that the measured hydraulic conductivity changes towards lower values in the course of the measurement (figure 15.5). These deviations may be caused by a real decrease in hydraulic conductivity, or they may be the consequence of transient storage within the enclosed sediments, which is neglected by both the method described by *Hvorslev (1951)* and the method used here.

A decrease in hydraulic conductivity during the test may be explained by three independent processes: 1) Fine particles which are brought into suspension when the pipe is driven into the streambed sediments will ultimately settle at the bottom of the pipe and decrease the hydraulic conductivity at the top of the sediment column. 2) The streambed sediments contain a large amount of gas. The presence of gas bubbles decreases the hydraulic conductivity, although this effect is pressure-dependent (*Hvorslev, 1951; Beckwith and Baird, 2001*). The high pressure on the enclosed sediment column at the beginning of the simulation compresses the gas bubbles, resulting in an increased permeability. Due to the falling hydraulic head in the measuring tube, the pressure in the sediment column decreases during the test, allowing the gas bubbles to expand again. As a result, the permeability of the sediments decreases. 3) Both the pressure on the sediment column and the flow of water through the column may result in the consolidation of the enclosed sediments during the test, which reduces the hydraulic conductivity.

As indicated in table 15.3, the error of the hydraulic conductivity values measured in-situ is small, suggesting that the method delivers accurate results. However, the variations in hydraulic conductivity between adjacent locations exceed the error of a single measurement by far, which suggests that the measured values only represent the hydraulic conductivity at the point of measurement. Consequently, a number of measurements is required in order to accurately characterize the permeability of streambeds.

Scheytt and Hengelhaupt (2001) describe various falling-head and constant head infiltration tests in glacial sands and compare hydraulic conductivity values measured in-situ to values estimated from grain size analysis according to *Beyer (1964)*. In all cases, the measured values were smaller than the estimates. In contrast, *Chen (2000)* found that estimates from grain size analysis using the method described by *Hazen (1893)* were lower than the values measured in-situ. Figure 15.7 indicates that the difference between the estimated values and the measured values depends on the degree of uniformity, suggesting that the formula provided by *Beyer (1964)* could be modified to obtain more realistic estimates.

15.5 Conclusions

The standpipe method can be modified for in-situ measurement of low streambed hydraulic conductivity. It provides a fast, simple, and inexpensive way to characterize the permeability of the streambed sediments. Field tests indicate that the error of the measured values is small compared to the lateral variability of the hydraulic conductivity, suggesting that several tests at different locations are required to obtain a value which is representative for a larger section of the stream.

Compared to the values measured in-situ, estimates of hydraulic conductivity from grain size analysis seem unrealistic. However, the differences between the measured and the estimated values are systematic.

Part III

Numerical studies on saltwater intrusion in a coastal aquifer in north-western Germany

Chapter 16

Numerical studies on saltwater intrusion in a coastal aquifer in north-western Germany

T. Feseker

Abstract

Saltwater intrusion in coastal aquifers depends on the distribution of hydraulic properties, on the climate, and on human interference such as land reclamation. In order to analyze the key processes which control saltwater intrusion, a hypothetical steady-state salt distribution in a representative cross-section perpendicular to the coastline is calculated using a two-dimensional density-dependent solute transport model. The effects of changes in groundwater recharge, lowering of drainage levels, and a rising sea level on the shape and position of the freshwater/saltwater interface are modeled in separate simulations. The results show that the exchange between groundwater and surface water in the marsh areas is one of the key processes influencing saltwater intrusion. A rise of the sealevel causes rapid progression of saltwater intrusion, whereas changes in groundwater recharge are compensated by the drainage network. The time scale of changes resulting from altered boundary conditions is in the order of decades and centuries, suggesting that the present-day salt distribution does not reflect a steady-state of equilibrium.

16.1 Introduction

A Coastal Aquifer Test-field (CAT-field) was established by the Leibnitz Institute for Applied Geosciences, Germany, in a representative region for the

continental European North Sea coast. The CAT-Field is located in northern Germany, bordered by the estuaries of the rivers Elbe and Weser (figure 16.1). The aim was to investigate the dynamics of groundwater flow and geochemical processes within a typical coastal aquifer in an integrated approach. The results of geophysical investigations including seismic, gravity, and airborne electromagnetic surveys are published by *Gabriel et al.* (2003). *Panteleit* (2004) provides detailed analysis of the geochemical processes in the saltwater / freshwater transition zone. *Fulda* (2002) describes first numerical studies on the position of the freshwater/saltwater interface in the study area and discusses different possibilities of simulating drainage through constant head, constant concentration or constant flux boundary conditions.

This paper focuses on the key processes which control the shape and position of the freshwater/saltwater interface. The effects of changing boundary conditions on the salt distribution are analyzed by applying a numerical model to simulate groundwater flow in a simplified representative cross-section perpendicular to the coast.

In the following, all depths are given with respect to mean sea level (MSL). Elevations above MSL are expressed as positive values, while a negative sign marks a position below MSL. The coastline is taken as the origin of the horizontal axis, which is positive in seaward direction. Consequently, the horizontal position of an inland point is denoted by a negative value.

16.1.1 Geology

The post-Permian geology of north-western Germany is characterized by up to 500 meters of sediments, which are underlain by the evaporitic deposits of the Upper Permian (Zechstein). As illustrated in figure 16.2, updoming of salt strongly affects the structure of the Tertiary and Quaternary sediments. Some salt domes even penetrate the Tertiary deposits and reach near-surface Quaternary sediments. The hydrogeology is determined by the deposits of the Neogene and the Quaternary.

The Neogene sediments consist of relatively uniformly distributed sequences of thick clay and sand layers (figure 16.2). The Quaternary sediments are dominated by gravel and sand-rich onshore deposits of the Elster and Saale glaciation. Rapid variations of the sedimentation conditions during the Pleistocene caused a more heterogeneous distribution. In the study area, two buried Pleistocene glacial valleys have been identified, which cut deeply into the Tertiary sediments (*Haertlé*, 1983; *Gabriel et al.*, 2003). It is assumed that these valleys were eroded by melt water during the Elster glaciation. However, the geological processes which formed the valleys are not yet fully understood. The main hypotheses are discussed e.g. by *Piotrowski* (1997) and *Huuse and Lykke-Andersen* (2000). During the late Elster glaciation, the valleys were refilled with gravel, sand, silt, and clay, with grain sizes generally decreasing

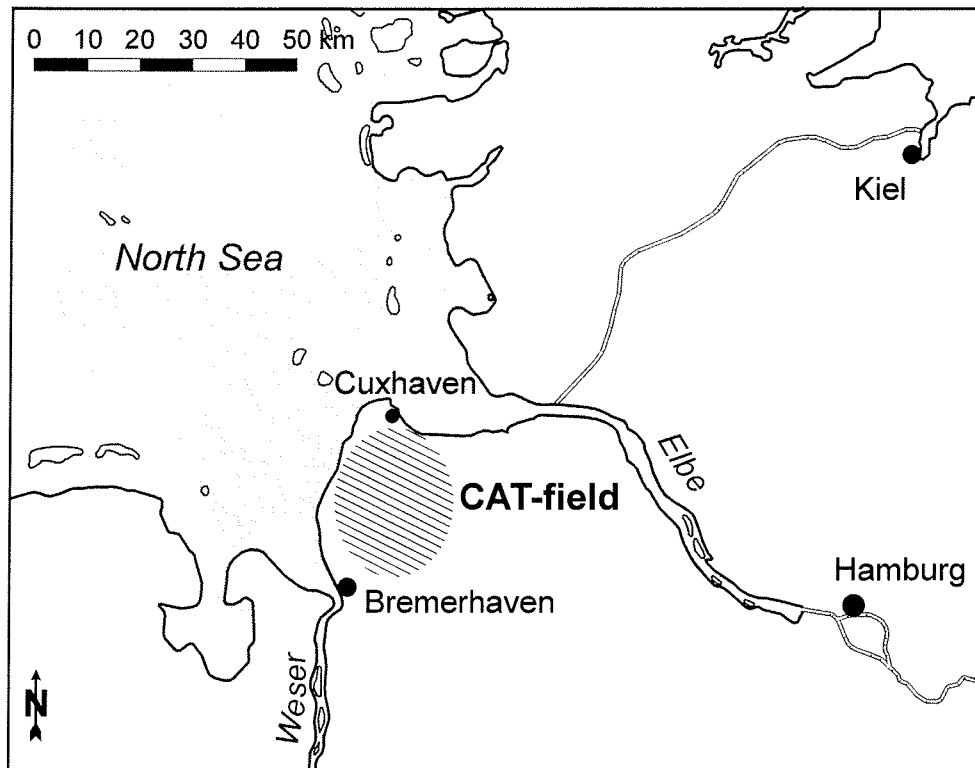


Figure 16.1: The coastal aquifer test-field (CAT-field) is located in north-western Germany, between the estuaries of the rivers Elbe and Weser.

from the bottom to the top. The upper part of the channel filling commonly consists of a thick layer of clay (Lauenburg Clay) with intercalated silts and fine sands.

The glaciogene onshore deposits outcrop at a distance of approximately five to ten kilometers from the coast and form slight ridges (geest) in the otherwise flat coastal plain. Towards the coastline, the Pleistocene deposits are covered by transgressive tidal flat sediments that are Eemian and Holocene in age, which interfinger with muds of brackish lagoonal type and with onshore peat deposits. The Holocene sequence commonly starts with a basal peat horizon. Different regressions and transgressions can be derived from intercalated layers of peat (*Gerdes et al.*, 2003; *Streif*, 2004). In the study area, the thickness of the Eemian sediments is approximately 3-5 meters, while the thickness of the Holocene sequence ranges between 15 and 20 meters (*Sindowski*, 1979).

16.1.2 Hydrogeology

On a regional scale, two main aquifers can be distinguished in the study area (*Haertlé*, 1983). The upper aquifer consists mainly of gravel and sand-rich sediments of the Pleistocene and includes fine and very fine-grained sands (Kaolin-

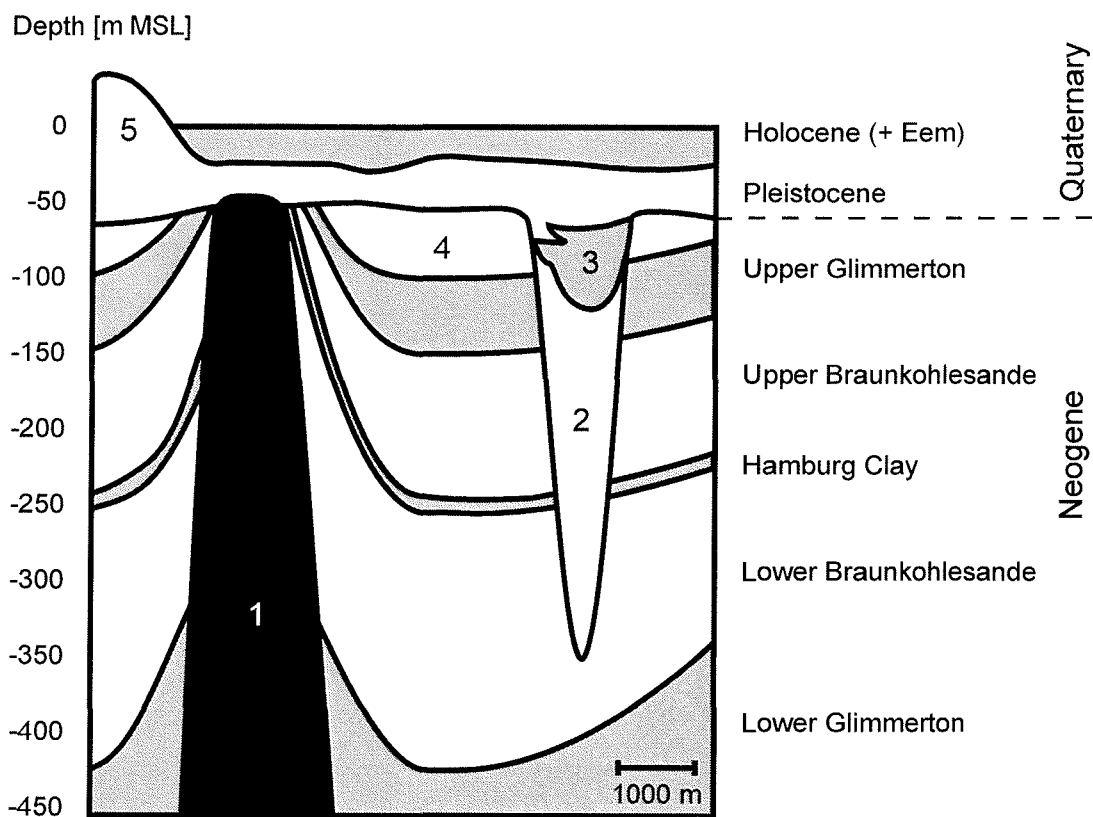


Figure 16.2: The post-Permian geology in the coastal region of north-western Germany consists of more than 400 meters of sedimentary deposits. The structure of the sediments is affected by updoming of Permian salt structures (1) and buried valleys that were eroded during the Pleistocene (2). Lauenburg Clay (3) commonly forms the top of the channel fillings. Outside the erosion channels, the Upper Miocene consists of fine sands, the so-called Kaolinsande (4). At a distance of approximately 5 to 10 kilometers from the coast, outcrops of the Pleistocene sands and gravels form slight ridges (geest, 5).

sande) that were deposited during the Pliocene and the Upper Miocene. The Quaternary sediments are generally characterized by excellent permeabilities, whereas the permeability of the Neogene deposits is medium to poor (*Panteleit, 2004*). The thickness of the upper aquifer ranges between less than 50 meters and more than 200 meters within the Pleistocene erosion channels. Silt- and clay-rich sediments of the Middle and Upper Miocene (Upper Glimmerton) form the base of the upper aquifer. The lower aquifer is made up of sand-rich sediments of the Lower and Middle Miocene (Lower and Upper Braunkohlesande). Another thick clay layer (Lower Glimmerton) forms the base of the lower aquifer.

The hydraulic resistance of the Upper Glimmerton separating the two aquifers is very large. Estimated values of hydraulic conductivity are in the range of $1 \times 10^{-9} \text{ ms}^{-1}$ and $3 \times 10^{-9} \text{ ms}^{-1}$ (*Haertlé, 1983*). According to *Haertlé (1983)*, the piezometric heads at the base of the upper aquifer are between two and six meters higher than at the top of the lower aquifer, causing downward leakage through the clay layer. However, due to the thickness of the aquitard, the very low hydraulic conductivity, and the minor pressure gradient, the leakage flux does not exceed 10 mm per year. In the area of the deep Pleistocene valleys, the separating clay layer between the two aquifers was eroded, such that there is only a single aquifer. However, *Haertlé (1983)* supposes that the Lauenburg Clay, which is commonly found at approximately the same depth as the Upper Glimmerton (figure 16.2), may act as a replacement and again lead to a subdivision into two aquifers on a local scale.

The geest ridges are the most important groundwater recharge areas in the coastal region of north-western Germany, because the permeability of the sand-rich glacial sediments is generally good and the distance from ground surface to the groundwater table is greater than in the Marsch areas. Due to extensive drainage for agricultural and land reclamation purposes, no recharge but a negative groundwater balance is expected in the Marsch areas (*Giesel and Schmidt, 1978; Fulda, 2002*). The exchange of groundwater and surface water in the marsh areas is considered a key factor in the coastal groundwater system. *Giesel and Schmidt (1978)* showed that the pattern of groundwater flow can be modeled simply by describing recharge in the geest area and drainage in the marsh area as a function of the distance from ground surface to the groundwater table. Using isotopic dating of water samples, *Suckow (2001)* calculated downward velocities between 1.2 and 1.3 meters per year. Assuming reasonable values of porosity, this corresponds to groundwater recharge in the range of 350 to 400 mm per year. Based on surface water budget calculations, *Friedhoff (2001)* estimates the net flux of groundwater into the drainage network at 120 mm per year.

As a result of the density difference between saltwater and freshwater, seawater intrudes from the North Sea into both the lower and the upper aquifer and forces the fresh groundwater upward. Electric conductivity measurements at observation wells (*Haertlé, 1983; Panteleit, 2004*) and airborne electromag-

netic surveys (*Repsold, 1990; Gabriel et al., 2003*) indicate that saltwater has intruded far into the upper aquifer. Close to the coastline, the groundwater in the upper aquifer is completely saline. At a distance of 4 kilometers from the coastline, the freshwater/saltwater interface was found at depths of between 40 and 60 meters below ground surface (*Panteleit, 2004*), suggesting that the slope of the interface is very gentle. Further inland towards the geest, the slope increases significantly (*Gabriel et al., 2003*). In the vertical direction, the transition zone between freshwater and saltwater is usually restricted to a few meters (*Panteleit, 2004*). Chemical analysis of groundwater samples show that other possible sources of salt beside the intrusion of seawater from the North Sea, such as the mobilization of residual marine waters from deeper layers (*Meinardi, 1991*) or the dissolution of halite from the underlying Permian salt, can be ruled out at least for the upper aquifer (*Panteleit, 2004*). In the lower aquifer, the saltwater intrusion extends much further inland, such that the groundwater in the lower aquifer is completely saline on a regional scale (*Haertlé, 1983*). East of the study area, however, *Haertlé (1983)* observed that the lower parts of both aquifers are saline and the upper parts are fresh.

16.2 Method

The position and shape of the freshwater/saltwater interface depends on the hydraulic properties of the aquifer as well as on the boundary conditions, such as the sea level, the rate of groundwater recharge, and the drainage levels. In case the saltwater intrusion is not at a steady-state of equilibrium, the distribution of salt in the aquifer at some initial stage and changes in the boundary conditions with time additionally influence the observed situation (cf. *Oude Essink, 2001b*). At present, the available data is insufficient to create a model which accurately represents the pattern of groundwater flow and the distribution of salt in the study area. Moreover, it would not be possible to calibrate the model due to the lack of detailed observation data from deeper layers. Therefore, a conceptual model of a representative cross-section perpendicular to the coast is derived by simplifying the hydrogeological structure of the study area.

16.2.1 Conceptual model of a representative cross-section

As illustrated in figure 16.3, the conceptual model is limited to a cross-section of ten kilometers length and reaches to a depth of 120 meters below MSL. Only the upper aquifer is considered, assuming that leakage to the lower aquifer is negligible. Within the aquifer, two regions with different hydraulic properties are distinguished. The lower part from 120 to 60 meters below MSL represents the Upper Miocene sediments, which are characterized by medium permeability. The upper part of the aquifer (above -60 m MSL) consists of

highly permeable Pleistocene deposits. The aquifer outcrops at a distance of 8 kilometers from the coast and forms a ridge two kilometers wide, representing the geest. In the marsh area, the topography is completely flat at an elevation of one meter above MSL. With the exception of the geest ridge, the entire aquifer is covered by a low-permeability layer 25 meters thick, which stands for the Eemian and Holocene deposits. Groundwater recharge only occurs in the geest area, whereas the water table in the marsh is controlled by drainage. In the conceptual model, each region is assumed to be homogenous.

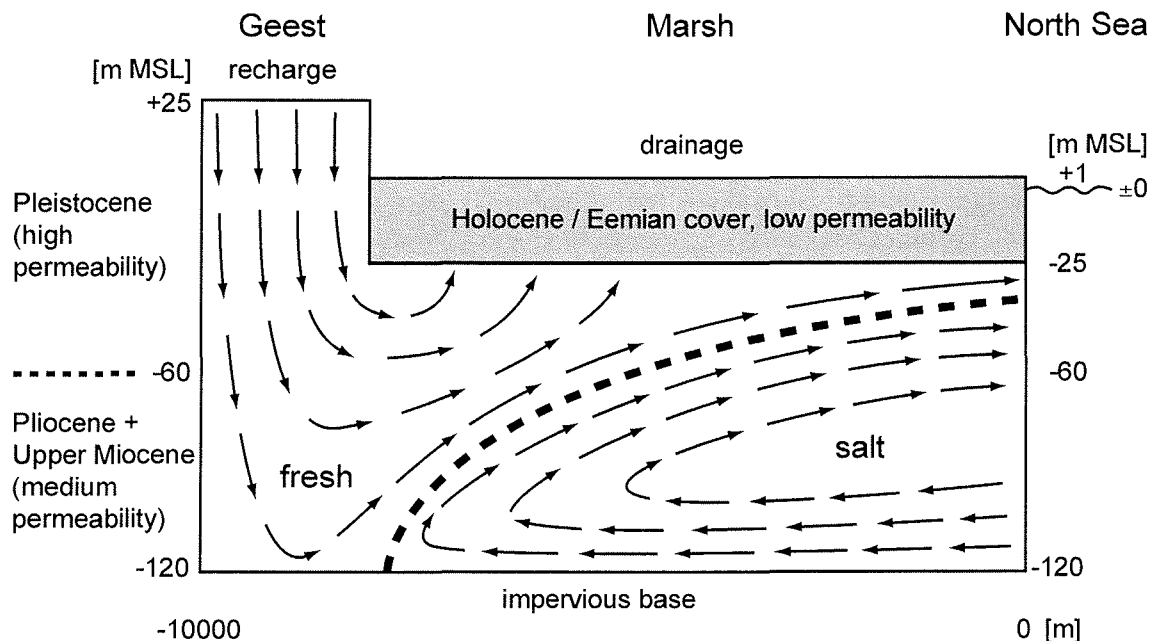


Figure 16.3: The geology of the coastal region is greatly simplified in order to develop a conceptual model of a representative cross-section through the upper aquifer perpendicular to the coastline. In the marsh region, the aquifer is overlain by a low-permeability cover layer, which stands for the Eemian and Holocene deposits. To account for the different lithologies of the upper (Pleistocene) and lower (Pliocene and Upper Miocene) part of the aquifer, it is assumed that the hydraulic conductivity is significantly lower below a depth of 60 m MSL. Groundwater recharge is limited to the geest ridge on the inland boundary of the cross-section. Saltwater intrudes into the aquifer from the seaward boundary along the impervious base and forces the fresh groundwater upward, where it is either drained or discharged into the North Sea.

16.2.2 Numerical model

A numerical model of the representative cross-section through the upper aquifer is created using the computer program SWIMMOC (*Feseker, 2004*). Based on the method of characteristics groundwater transport model MOC (*Konikow and Bredehoeft, 1978*), SWIMMOC takes advantage of the fact that relatively coarse grids can be used without numerical dispersion significantly affecting the transition zone between freshwater and saltwater. The program applies

the concept of equivalent freshwater head as described by *Oude Essink* (1996) to account for density-dependent flow. The density of groundwater is assumed to be directly proportional to the salinity, while all other factors influencing the density are neglected.

The representative cross-section is discretized using an equidistant finite differences grid consisting of 24 rows and 41 columns. The resulting grid cells are 250 meters wide and 5 meters high. As illustrated in figure 16.4, the model domain is subdivided into three subdomains, representing the Pleistocene and Pliocene/Upper Miocene parts of the aquifer and the Eemian/Holocene cover layer. The hydraulic properties of these subdomains are listed in table 16.1. For all subdomains, an anisotropy ratio is assumed such that the hydraulic conductivity in the horizontal direction is ten times larger than in vertical direction. The horizontal and vertical hydraulic conductivities of the Holocene/Eemian cover layer (subdomain C) were derived from streambed hydraulic conductivity measurements in the study area presented by *Feseker and Seeberg-Elverfeldt* (submitted). All remaining values are estimates based on the composition of the sediments.

Table 16.1: The model domain is subdivided into three subdomains A, B, and C, which describe the two different parts of the aquifer and the cover layer.

Subdomain A	
Age	Pleistocene
Lithology	dominated by sand and gravel
Horizontal hydraulic conductivity	$1 \times 10^{-3} \text{ ms}^{-1}$
Vertical hydraulic conductivity	$1 \times 10^{-4} \text{ ms}^{-1}$
Effective porosity	0.3
Subdomain B	
Age	Upper Miocene + Pliocene
Lithology	fine and very fine-grained sand with silt and clay layers
Horizontal hydraulic conductivity	$1 \times 10^{-4} \text{ ms}^{-1}$
Vertical hydraulic conductivity	$1 \times 10^{-5} \text{ ms}^{-1}$
Effective porosity	0.2
Subdomain C	
Age	Holocene + Eem
Lithology	peat, clay, silt, fine sand
Horizontal hydraulic conductivity	$3 \times 10^{-6} \text{ ms}^{-1}$
Vertical hydraulic conductivity	$3 \times 10^{-7} \text{ ms}^{-1}$
Effective porosity	0.15

In order to account for the narrow transition zone between freshwater and saltwater, which has been observed in the study area, the longitudinal and transverse dispersivities are set to 0.2 m and 0.02 m, respectively, while molec-

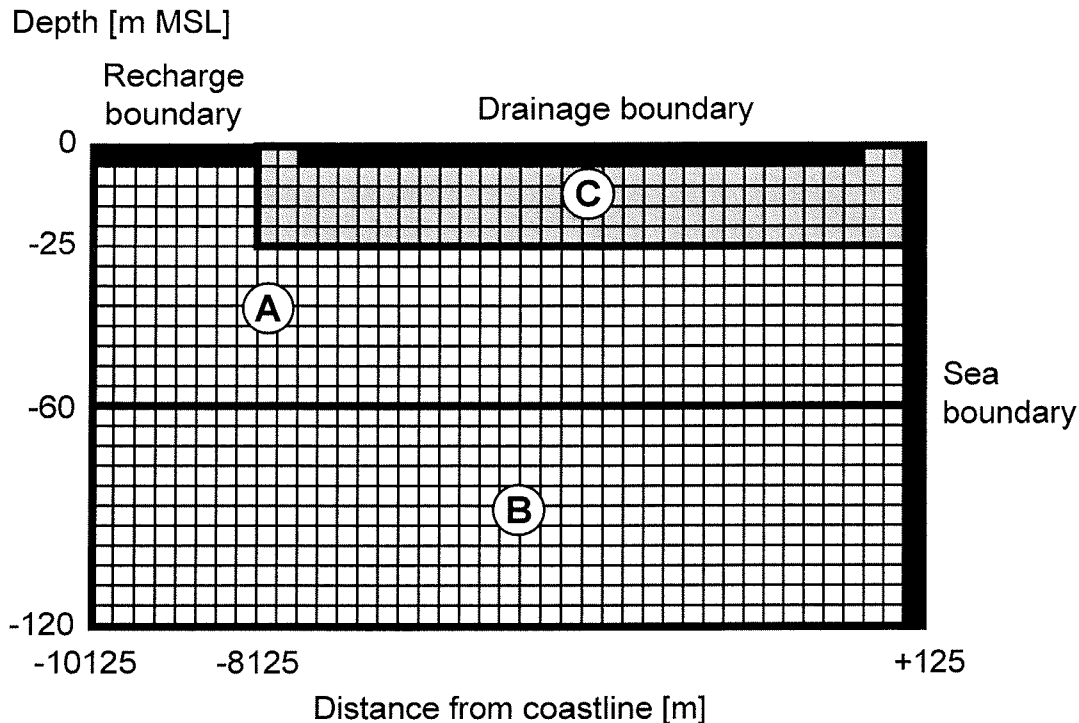


Figure 16.4: The finite differences grid consists of 24 rows and 41 columns. The model domain is subdivided into three subdomains. The upper part of the aquifer (Pleistocene) is represented by subdomain A, which is characterized by high permeability. Subdomain B describes the lower part of the aquifer (Upper Miocene and Pliocene), in which the permeability is significantly lower. The low-permeability cover layer (Eem and Holocene) is represented by subdomain C. All boundaries of the model domain are no-flow boundaries, unless a different boundary condition is defined (black cells). Groundwater recharge is simulated by means of a constant flux boundary condition, which is imposed to the outcrops of the upper aquifer (geest). A head-dependent flux boundary condition stands for drainage in the marsh region. The seaward boundary of the model domain comprises a prescribed observed head (sea level) and a constant concentration (saltwater) boundary condition.

ular diffusion is neglected. Due to the time scale of the simulations, transient storage is not considered. Since the discharge of freshwater from the rivers Elbe and Weser into the North Sea dilutes the coastal seawater, a maximum saltwater density of 1023 kg m^{-3} rather than the standard seawater value of 1025 kg m^{-3} is used. The density of freshwater is set to 1000 kg m^{-3} . The concentration values corresponding to freshwater density and maximum saltwater density are arbitrary. For convenience, a value of one is used in the context of this work to represent maximum saltwater concentration.

Three different types of boundary conditions are applied to simulate groundwater recharge, drainage, and the seaward boundary of the model domain (figure 16.4). Groundwater recharge in the geest area is represented by a constant flux (Neumann-condition) of freshwater across the upper border of the boundary cells. The boundary condition representing the North Sea is a combination of a constant concentration and a prescribed head boundary condition (Dirichlet-conditions). While the concentration of the groundwater in the boundary cells

is kept equal to the maximum saltwater concentration, the observed hydraulic head may vary with time following a predefined function.

The exchange of water between the Holocene cover layer and a drainage network in the marsh area is implemented as a head-dependent flux boundary condition (Cauchy-condition). The drainage boundary condition is defined by the thickness and vertical hydraulic conductivity of the drainage channel streambed and its elevation relative to the boundary cell. The volumetric flux across the upper border of these boundary cells depends on the hydraulic gradient between the surface water and the groundwater. In case the water level in the drainage channel is lower than the equivalent freshwater head at the base of the streambed, exfiltration of groundwater from the aquifer into the drainage channel occurs. On the other hand, a downward hydraulic gradient leads to the infiltration of freshwater from the drainage channel into the aquifer.

The effects of changing boundary conditions on the position and shape of the freshwater/saltwater interface can only be analyzed if the initial situation reflects a steady-state of equilibrium. Otherwise, it would be impossible to distinguish between the influence of the altered boundary condition and changes resulting from unsteady initial conditions. Therefore, a hypothetical steady-state position of the freshwater/saltwater interface is calculated through continuous simulation using constant boundary conditions (table 16.2), including a 'natural' drainage level which is equal to ground surface. The resulting steady-state situation is used as initial condition in the subsequent analysis of the influence of the different boundary conditions on the salt distribution in the aquifer.

16.3 Results

Using the constant boundary conditions listed in table 16.2, a balance of solute mass flux into and out of the model domain is reached after a simulated time of 3000 years. Figure 16.5 illustrates how the solute mass accumulates in the model aquifer during the progression of the saltwater intrusion. The concentration distribution at equilibrium is shown in figure 16.6. A large fraction of the recharged groundwater is drained in the marsh area close to the geest ridge, while infiltration from the drainage network into the Eemian/Holocene cover layer occurs in those boundary cells which are closer than 2000 meters to the coast (figure 16.7). The net drainage flux in the marsh area is approximately $3.17 \times 10^{-9} \text{ ms}^{-1}$ or 100 mm per year, which is about 93 percent of the total groundwater recharge.

Table 16.2: A steady state position of the freshwater/saltwater interface is modeled using the boundary conditions listed below. The groundwater recharge flux is estimated based on the present-day conditions. The hydraulic conductivity of the drainage channel streambeds were measured in-situ by *Feseker and Seeberg-Elverfeldt* (submitted).

Recharge boundary condition	
Type	constant flux
Flux concentration	freshwater
Volumetric flux	$1.2 \times 10^{-8} \text{ ms}^{-1}$ ($\approx 380 \text{ mm per year}$)
Sea boundary condition	
Type	constant concentration + prescribed observed hydraulic head
Concentration	saltwater
Observed hydraulic head	0 m MSL
Drainage boundary condition	
Type	head-dependent flux
Surface water level	+1 m MSL (= ground surface)
Surface water bottom	+1 m MSL
Streambed hydraulic conductivity	$3 \times 10^{-7} \text{ ms}^{-1}$
Streambed thickness	1 m

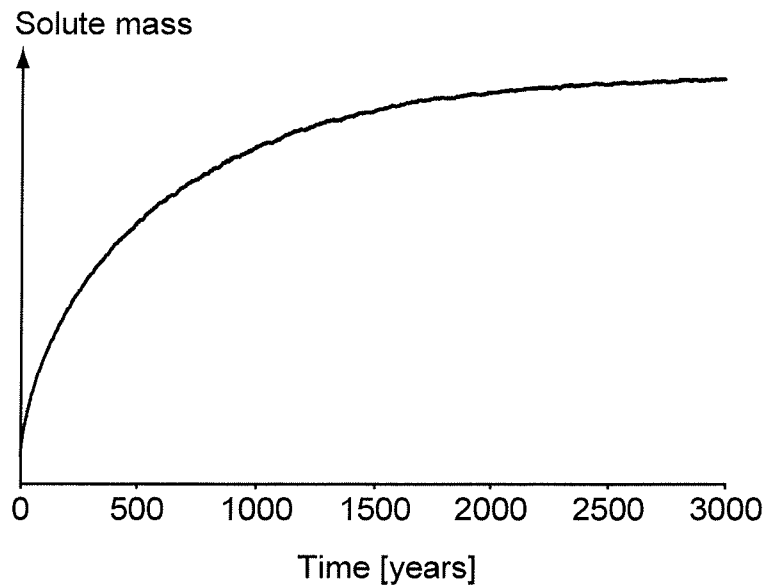


Figure 16.5: The hypothetical steady-state position of the freshwater/saltwater interface is modeled through continuous simulation with constant boundary conditions. After a simulated time of approximately 3000 years, the solute mass inflow is balanced by outflow, which indicates that the interface reached a stable equilibrium position. The solute mass axes is unlabeled because the concentration of saltwater is arbitrary.

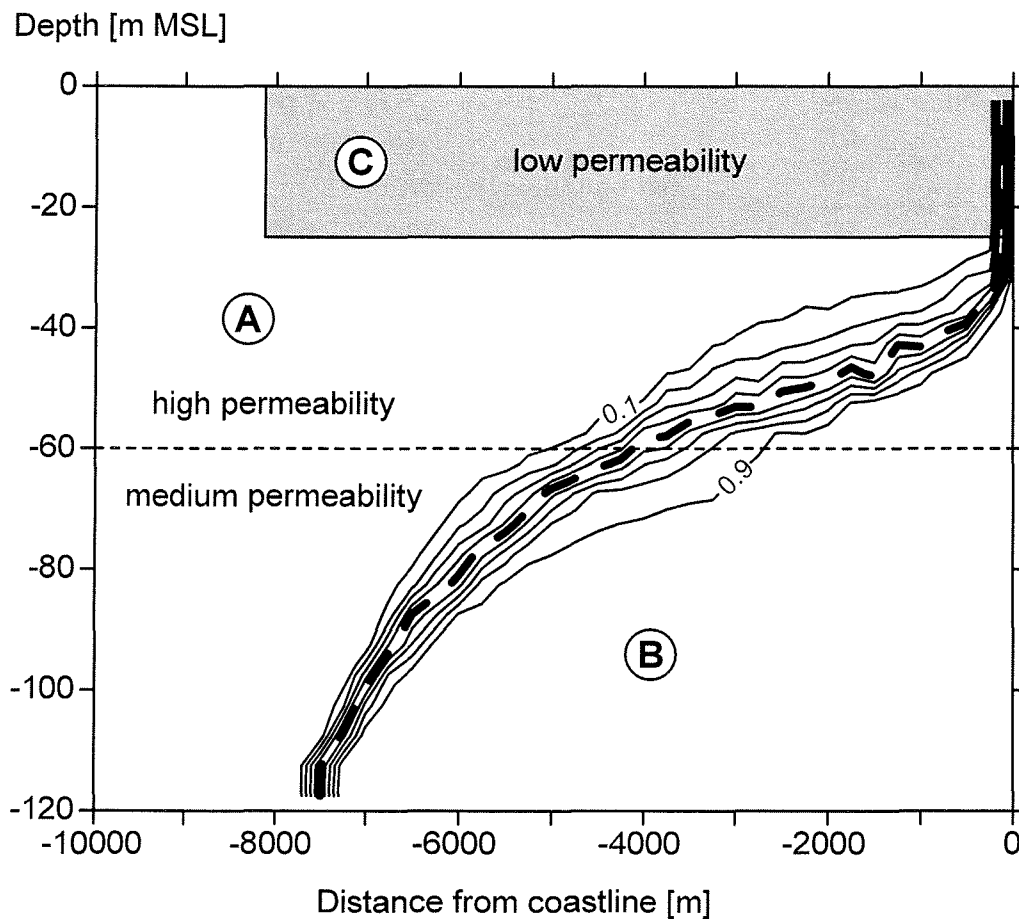


Figure 16.6: The hypothetical steady-state distribution of salt is illustrated by lines of equal concentration, with labels indicating the fraction of seawater. The position of the freshwater/saltwater interface (0.5 seawater) is marked by the thick dashed line. Close to the coast, the interface is found at a depth of approximately -30 m MSL, sloping gently inland. The slope increases significantly at a distance of about 5000 m from the coastline after the depth of the medium permeability subdomain (B) has been reached. The transition zone is widest at the border between the subdomains A and B, suggesting that the widening is associated with the corresponding change in hydraulic properties. Except for the sea boundary cells, the concentration of the groundwater in the entire area of subdomain C is lower than 0.1 seawater concentration.

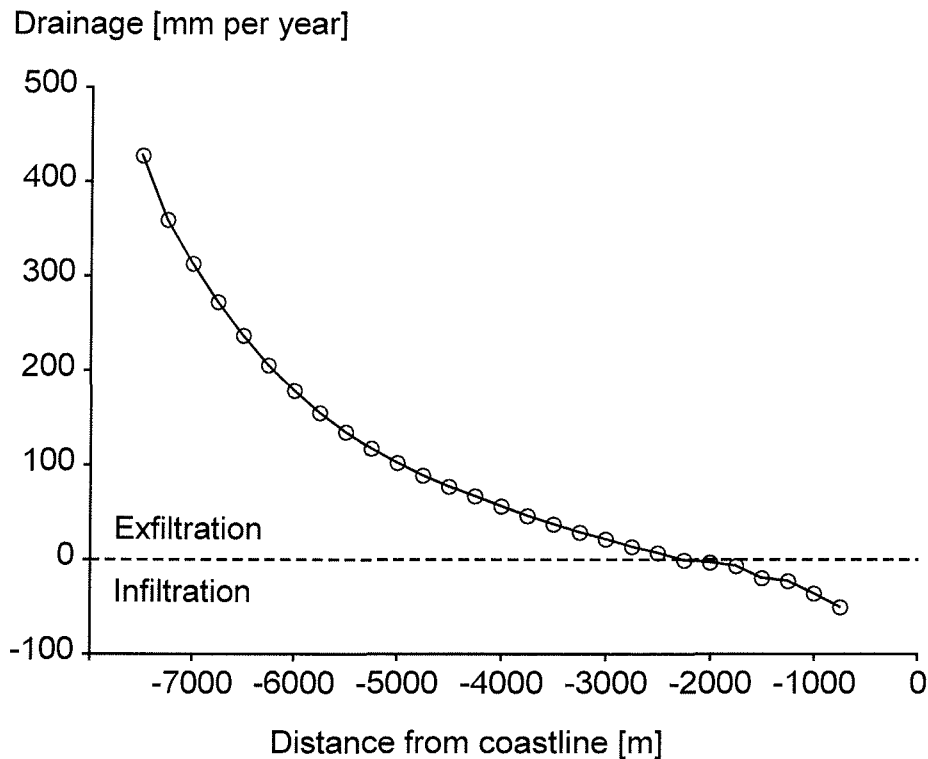


Figure 16.7: The rates of exfiltration from the Eemian/Holocene cover layer into the drainage network are highest close to the coast. Infiltration from the drainage channels into the cover layer occurs at boundary cells closer than 2000 meters to the coast line.

16.3.1 Sensitivity analysis

In order to analyze the effects of groundwater recharge, drainage, and a rising sea level on the shape and position of the freshwater/saltwater interface, the corresponding boundary conditions are changed one at a time and the influence on the groundwater system is modeled in separate simulations. For all scenarios, the hypothetical steady-state solution described above is used as initial condition.

Groundwater recharge

The sensitivity of the freshwater/saltwater interface to changes in groundwater recharge is investigated in two simulations. For the first simulation, the recharge flux in the geest area was reduced from $1.2 \times 10^{-8} \text{ ms}^{-1}$ to $8 \times 10^{-9} \text{ ms}^{-1}$, which corresponds to approximately 250 mm per year. The modeled positions of the interface for this scenario after 100, 200, 300, 400, and 500 years of simulated time are shown in figure 16.8. The decrease in groundwater recharge results in the progression of the saltwater intrusion at the base of the aquifer, while changes in the position of the interface are negligible above a depth of about -60 m MSL.

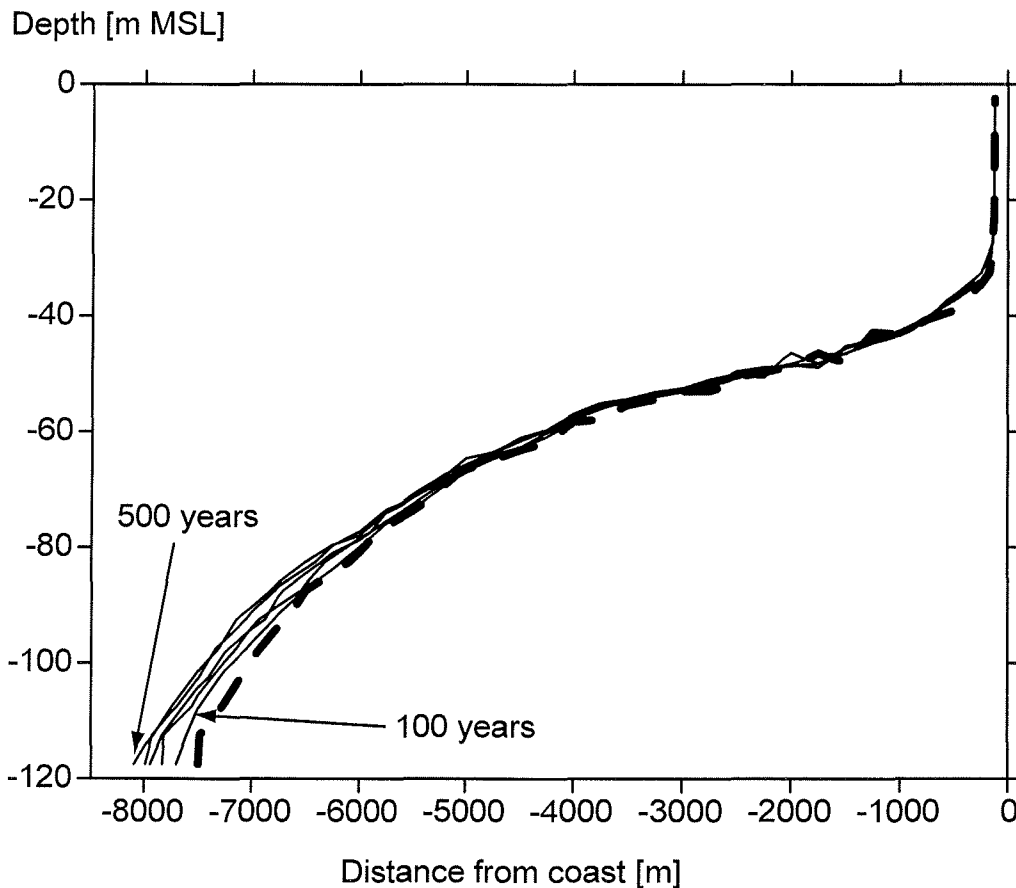


Figure 16.8: Groundwater recharge is reduced by one third. The thin lines mark the position of the freshwater/saltwater interface after 100, 200, 300, 400, and 500 years of simulated time. The thick dashed line shows the initial position of the interface, which is at equilibrium with the higher recharge rate. The reduced recharge results in the progression of the saltwater wedge at the base of the aquifer, while the interface remains almost unchanged above a depth of -60 m MSL. Significant salinization of near-surface groundwater does not occur. The changes in the position of the interface become less rapid in the course of the simulation as the system approaches a steady-state equilibrium.

The second simulation uses an increased recharge rate of $1.6 \times 10^{-8} \text{ ms}^{-1}$ or approximately 500 mm per year. The simulation results for 100, 200, 300, 400, and 500 years of simulated time are illustrated in figure 16.9. Increasing the groundwater recharge causes a retreat of the saltwater wedge at the base of the aquifer, while the shape and position of the freshwater/saltwater interface remains unchanged above a depth of approximately -60 m MSL.

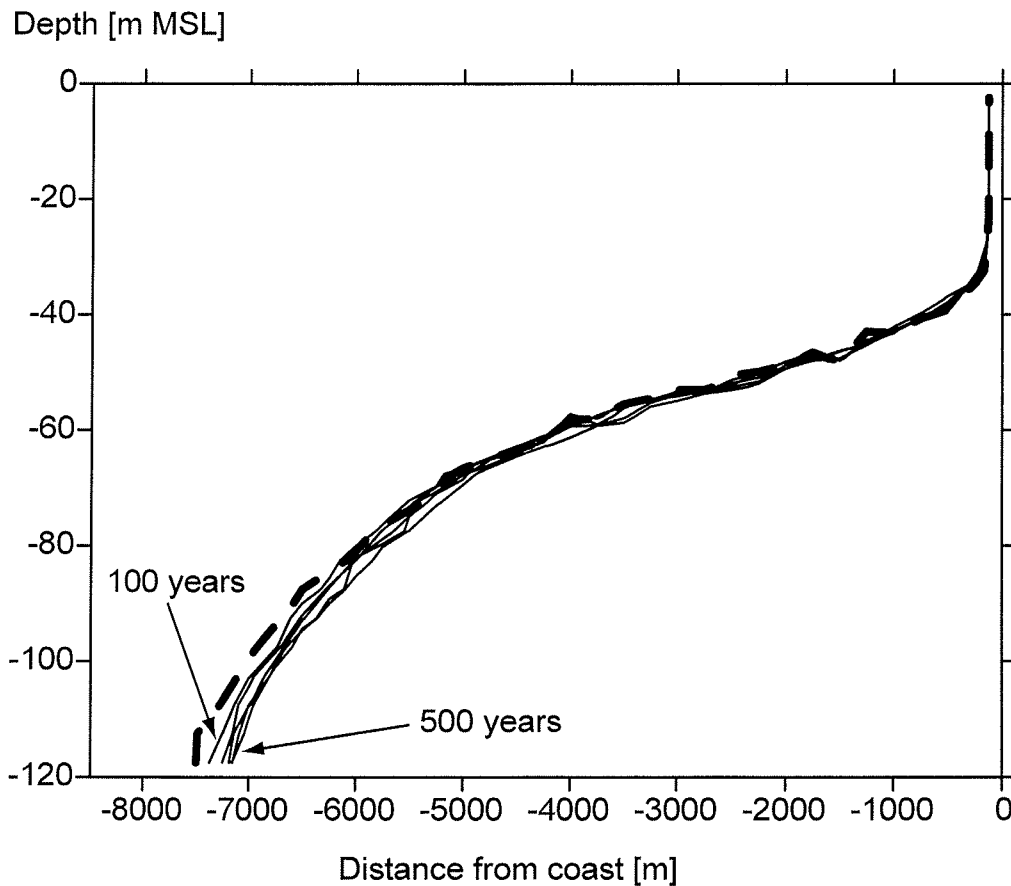


Figure 16.9: Groundwater recharge is increased by one third. The position of the freshwater/saltwater interface after 100, 200, 300, 400, and 500 years of simulated time is illustrated by the thin lines. The thick dashed line shows the initial position of the interface, which is at equilibrium with the lower recharge rate. The higher groundwater recharge flux leads to a retreat of the saltwater wedge at the base of the aquifer, while no significant changes in the position of the freshwater/saltwater interface can be observed above approximately -60 m MSL. The salinity of near-surface groundwater is negligible. As the system adjusts to the altered boundary condition, the changes become less rapid.

Comparing the rates of drainage for the two different scenarios with changed recharge flux to the drainage rates for the steady state situation (figure 16.10) shows that changes in the recharge boundary condition are compensated by drainage in the marsh area close to the geest. An increase of recharge leads to an increase of drainage, whereas a lower recharge flux is reflected by lower drainage. Infiltration of surface water from the drainage network into the Eemian/Holocene cover layer occurs in both scenarios. After 500 years of re-

duced recharge, the net drainage flux is approximately $2 \times 10^{-9} \text{ ms}^{-1}$ or 72 mm per year, which corresponds to 89 percent of the recharged groundwater. The net drainage flux resulting from 500 years of increased groundwater recharge is about $4.3 \times 10^{-9} \text{ ms}^{-1}$ or 144 mm per year, corresponding to 94 percent of the recharged groundwater.

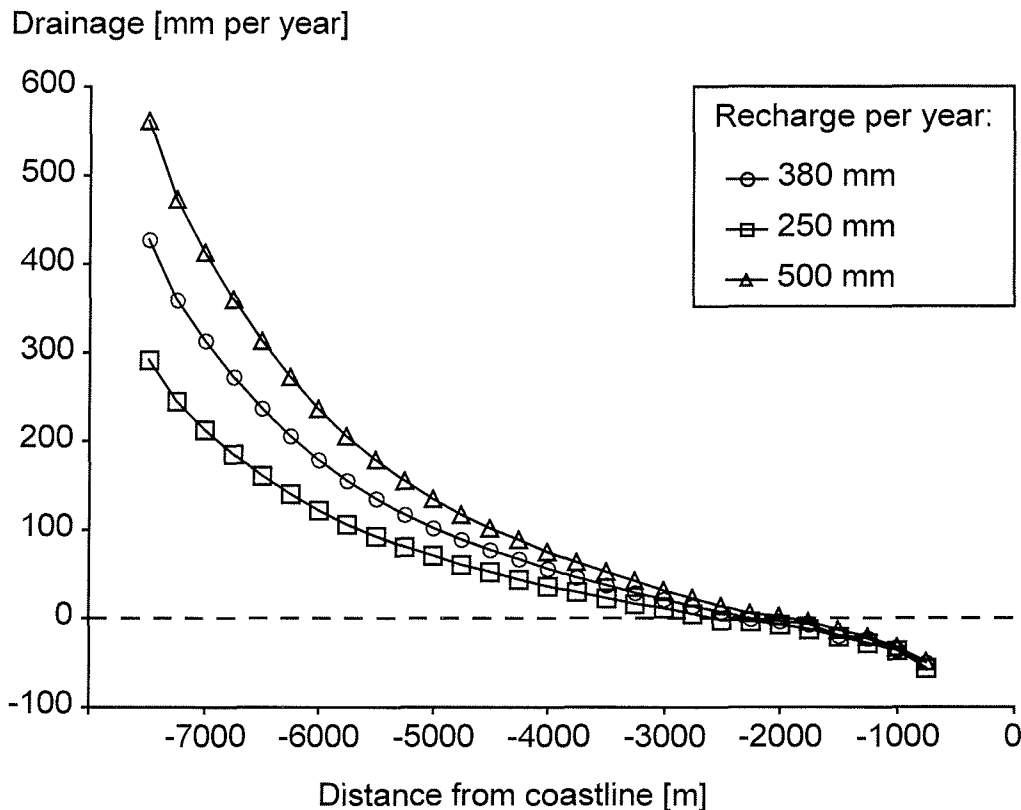


Figure 16.10: Comparing the drainage rates for the hypothetical steady-state situation (circles), the scenario with reduced recharge (squares), and the scenario with increased recharge (triangles) reveals that changes in the recharge boundary condition are compensated by changes in the drainage rates in the marsh area near the geest ridge. Closer to the coastline, the drainage flux rates remain almost unchanged, such that infiltration of water from the drainage network into the Eemian/Holocene cover layer occurs in both scenarios. (The drainage rates for the two scenarios with altered recharge boundary condition reflect the situation after 500 years of simulated time.)

Drainage

The effects of drainage on the salt distribution in the aquifer is analyzed through a simulation with the drainage level lowered from +1 m MSL to +0.5 m MSL. The calculated positions of the freshwater/saltwater interface for 100, 200, 300, 400, and 500 years of simulated time are shown in figure 16.11. The lower drainage level results in a general raise of the interface.

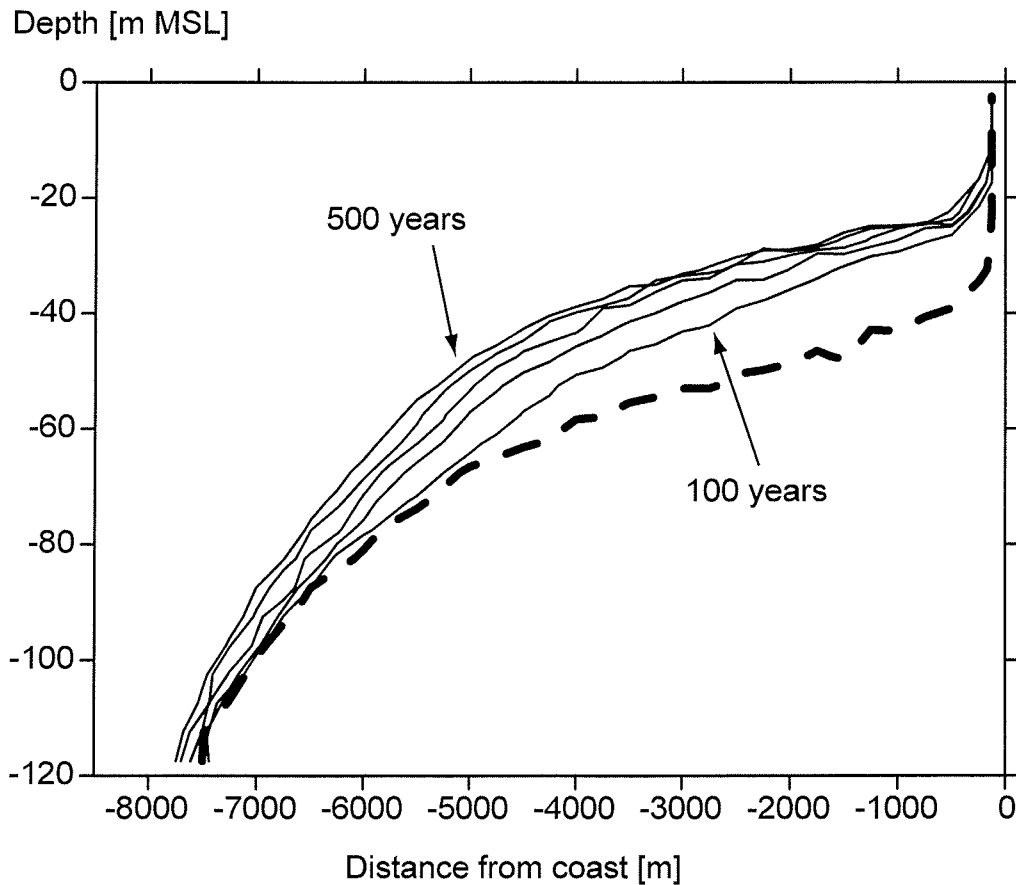


Figure 16.11: The drainage level is lowered from +1 m MSL to +0.5 m MSL. The thin lines show the position of the freshwater/saltwater interface after a simulated time of 100, 200, 300, 400, and 500 years. The thick dashed line represents the initial position of the interface at equilibrium with the higher drainage level. Lowering the drainage level results in a rapid raise of the interface. Closer than 2000 m from the coastline, the interface approaches the base of the Eemian/Holocene cover layer asymptotically, indicating that some salinization of the near surface groundwater may occur. In the course of the simulation, the rate of change becomes less as the system adjusts to the altered boundary condition.

Sea level rise

The IPCC projections of global sea level rise from 1990 to 2100 lie in the range of 0.11 m to 0.77 m (Cubasch *et al.*, 2001). In order to analyze the influence of a rising sea level on the position of the freshwater/saltwater interface, a sea level rise of 0.5 m per century is simulated, starting from the modeled steady-state of equilibrium including drainage. The model results for 50, 100, 150, 200, and 250 years of simulated time are illustrated in figure 16.12. The rising sea level causes a rapid increase of the groundwater salinity in the Eemian/Holocene cover layer close to the shore line.

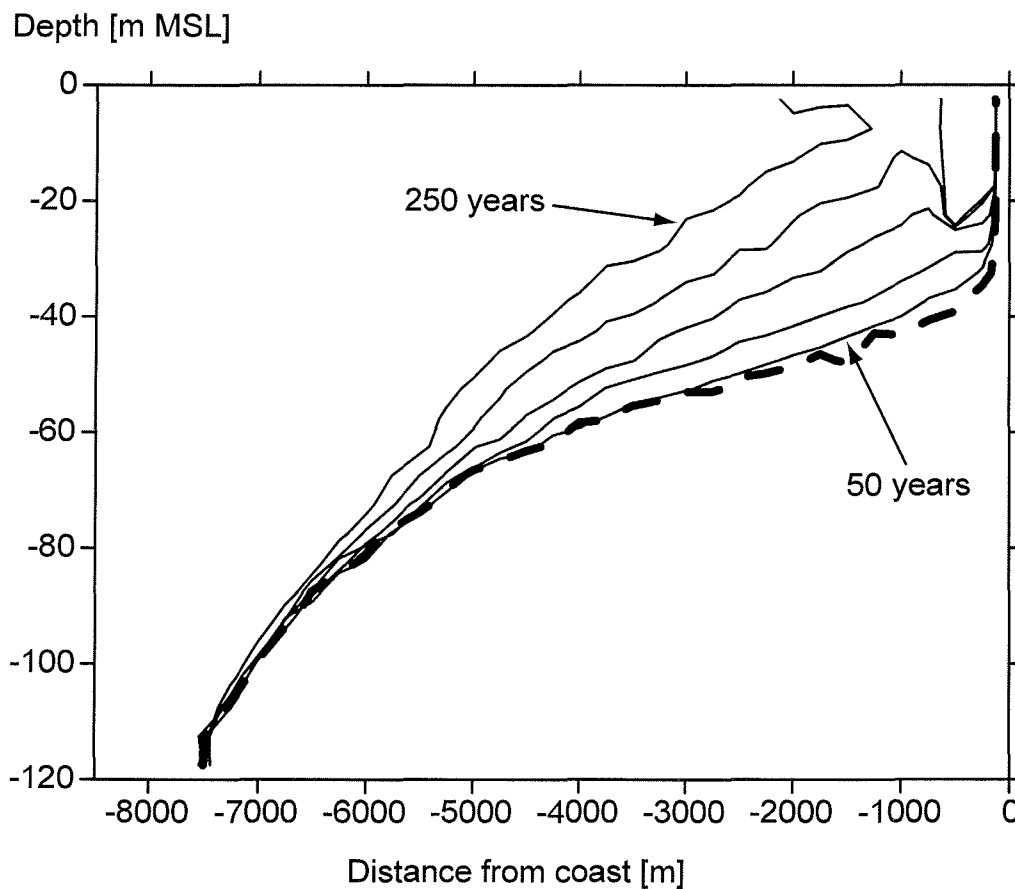


Figure 16.12: The sea level is rising at a rate of 0.5 m per century. The thin lines mark the position of the freshwater/saltwater interface after 50, 100, 150, 200, and 250 years of simulated time. The thick dashed line shows the initial position of the interface, which is at equilibrium with a sea level of 0 m MSL. The sea level rise leads to a very rapid rise of the interface close to the shore and results in severe salinization of the near-surface groundwater.

Figure 16.13 shows a comparison of the drainage rates for the hypothetical steady-state situation, the scenario with lowered drainage level, and the scenario with rising sea level. High drainage rates close to the geest area indicate that large quantities of groundwater are exfiltrated into the drainage network in all scenarios. On the other hand, infiltration of surface water into

the Eemian/Holocene cover layer close to the coastline is reduced to a minimum in the scenario with lowered drainage level, and completely abolished in the scenario with rising sea level. The lowered drainage level leads to a net drainage flux of $3.67 \times 10^{-9} \text{ ms}^{-1}$ or 116 mm per year, which is 107 percent of the groundwater recharge. The net drainage flux in the marsh area resulting from the rising sea level is $5 \times 10^{-9} \text{ ms}^{-1}$ or 158 mm per year, corresponding to 145 percent of the groundwater recharge.

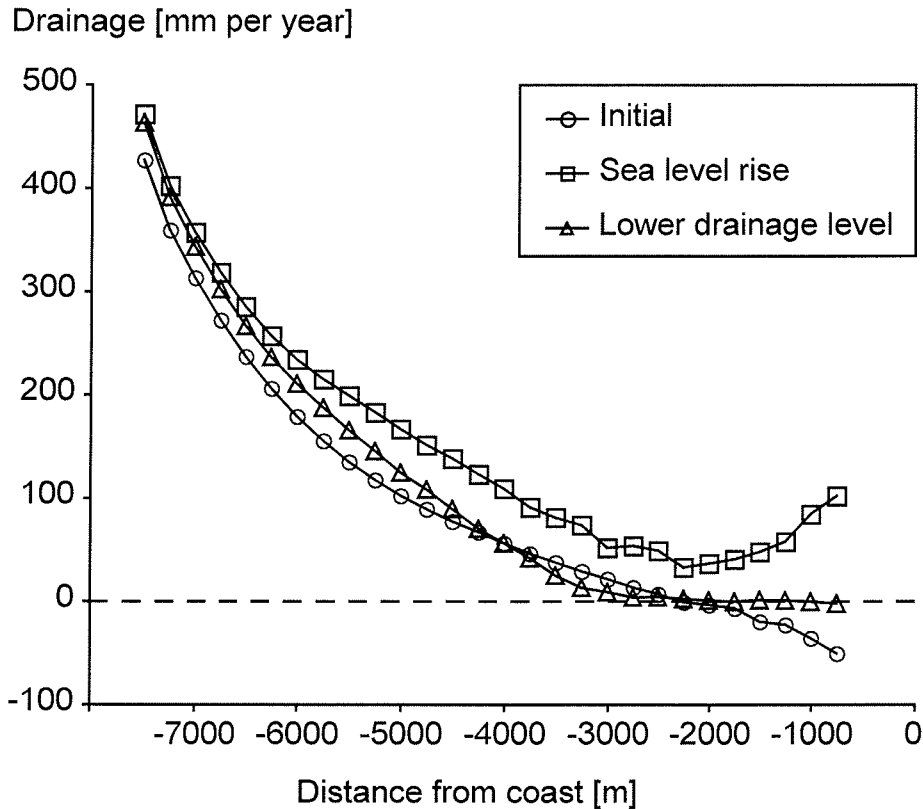


Figure 16.13: Comparing the drainage rates for the hypothetical steady-state situation (circles), the scenario with a sea level rise (squares), and the scenario with a lowered drainage level (triangles) shows that the changes in the boundary conditions mainly affect the drainage rates close to the coastline. While the initial steady-state situation includes significant infiltration of surface water into the Eemian/Holocene cover layer, the infiltration rates become negligible if the drainage level is lowered. The rising sea level even leads to a reversal of the direction of boundary flux closer than 2000 m to the coastline. (The drainage rates for the scenarios with sea level rise and lowered drainage level reflect the situation after 250 and 500 years of simulated time, respectively.)

16.4 Discussion

Observations of the salt distribution (*Repsold, 1990; Gabriel et al., 2003; Pantelait, 2004*) in the coastal aquifer show that the present extent of saltwater intrusion is considerably larger than in the hypothetical steady-state situation.

The sharpness of the freshwater/saltwater interface in the vertical direction is well reproduced by the numerical model. The horizontal widening of the transition zone associated with the change in hydraulic properties between the model subdomains A and B (figure 16.6) may be the result of unstable density-dependent flow due to heterogeneity as described by *Simmons et al.* (2001).

The time scale of changes resulting from altered boundary conditions is in the order of decades and centuries, which agrees with numerical simulations of the dynamics of the freshwater/saltwater interface in coastal aquifers in Belgium (*Vandenbohede and Lebbe*, 2002) and Greece (*Lambrakis and Kallergis*, 2001). *Oude Essink* (2001b) states that saltwater intrusion in coastal aquifers in The Netherlands is not at a steady-state equilibrium, but constantly progressing. The slow reaction of the interface in the numerical simulations presented here suggests that the same conclusion applies to the coastal aquifers in north-western Germany.

Simulating the evolution of a freshwater lens in the Belgian coastal plain, *Vandenbohede and Lebbe* (2002) observed that the modeled salt distribution was much more sensitive to changes in the drainage levels than to changes in the hydraulic conductivities, whereas the hydraulic conductivities seemed to control the time scale of the simulated processes. The sensitivity of the simulation results to the hydraulic properties of the aquifer and the cover layer was not analyzed in the study presented here. However, it seems feasible that the nature of the processes described will be the same for slightly varied hydraulic properties.

The drainage rates that were calculated in the different simulations range from 72 to 158 mm per year and compare well with the value of 120 mm per year, which was estimated by *Friedhoff* (2001). The graphs of the drainage rates at different distances from the coastline (figures 16.7, 16.10, and 16.13) provide a more detailed insight into the effects of drainage on groundwater flow. Confirming the results presented by *Giesel and Schmidt* (1978) and *Fulda* (2002), it may be concluded that the exchange of groundwater and surface water in the marsh area is one of the key processes determining the position of the freshwater/saltwater interface.

16.5 Conclusion

Considering the sluggish adjustment of the coastal groundwater system to the imposed boundary changes, it is very likely that the present-day situation does not reflect a steady-state equilibrium of saltwater intrusion, drainage, and recharge. Consequently, saltwater intrusion may progress and salinization of soils close to the coastline may increase, even if groundwater recharge does not decrease, the sea level does not rise, and the drainage levels are not lowered. On the other hand, the same time scale must be expected for countermeasures

to take effect. Therefore, further investigations of the dynamics of saltwater intrusion based on more detailed data are important to ensure a sustainable use of coastal groundwater resources.

CHAPTER 16. NUMERICAL STUDIES ON SALTWATER INTRUSION
IN A COASTAL AQUIFER IN NORTH-WESTERN GERMANY

Part IV

Modeling Groundwater Flow to a Well – User's Guide to WellFlow

License

The computer program WellFlow is free software. It can be redistributed and/or modified under the terms of the GNU General Public License as published by the Free Software Foundation; either version 2 of the license, or (at your option) any later version. This program is distributed in the hope that it will be useful, but WITHOUT ANY WARRANTY; without even the implied warranty of MERCHANTABILITY or FITNESS FOR A PARTICULAR PURPOSE. See the GNU General Public License for more details.

An electronic copy of the GNU General Public License should be included with the copy of the program. In case it is missing, write to the Free Software Foundation, Inc., 59 Temple Place - Suite 330, Boston, MA 02111-1307, USA.

Software Availability

The RealBasic source code of the computer program WellFlow as well as precompiled executables can be downloaded from <http://www.geochemie.uni-bremen.de>.

Acknowledgements

This study is part of a PhD thesis funded by the FNK at the University of Bremen. The project was encouraged and supervised by Dr. J.P. Lobo Ferreira. It was carried out during a stay as a guest scientist at the Laboratório Nacional de Engenharia Civil (LNEC) in Lisbon, Portugal. The Groundwater Research Group at LNEC and Dr. A.G. Chachadi from the University of Goa, India, supported the work.

Chapter 17

Introduction

In September 1999, a new law on groundwater protection was ratified in Portugal. It demands the delineation of three wellhead protection areas for each well used in public water supply. The first area is meant to protect the immediate surroundings of the well and is defined by a fixed radius from the wellhead. The second and third area is intended to provide enough time for intervention in case of a pollution hazard. For this reason, they are defined by the time the groundwater takes to travel from the outer limit of the area to the well.

During his stay as a trainee at GIAS in 2000, Bas Krijgsman studied the relation between the hydrogeological properties of a simple unconfined aquifer and the time of travel distance. He developed a GIS-based methodology for the delineation of wellhead protection areas in unconfined aquifer settings and supplied a case study of wells in Goa, India. However, many wells in Portugal abstract water from very heterogeneous aquifers. It is difficult to compare these multi-layer systems to simple unconfined aquifers because of the vertical exchange of water that occurs between the layers. Furthermore, at a given location with fixed hydrogeological characteristics, the penetration depth of the well and the position of the screens may have a great effect on the flow of groundwater. These parameters should be taken into account when judging the vulnerability wells.

The aim of this work is to study the influence of aquifer heterogeneity and well properties on groundwater flow and on the time it may take a pollutant to reach the well. As a suitable tool to answer these questions was not available, the computer program WellFlow has been developed. It is a user-friendly, menu- and mouse-driven stand-alone modeling tool for Windows and Mac OS. Following an axisymmetric approach where a vertical cross section of a cylinder is modeled, this program simulates steady-state groundwater flow to a well by applying the method of finite differences.

17.1 Wellhead protection areas

Wellhead protection areas are regions around a wellhead in which installations or activities capable of polluting groundwater resources are prohibited or restricted. In September 1999, Portugal ratified a new law on groundwater protection (Decreto-Lei no. 382/99 de 22 de Setembro). It demands the delineation of three different protection areas around each well used for public water supply that is abstracting more than 100 m^3 per day or serving more than 500 habitants. If the abstraction rate is lower or the well is serving fewer habitants, only the immediate protection area is required. Figure 17.1 shows a cross-sectional view of the different protection radii explained below.

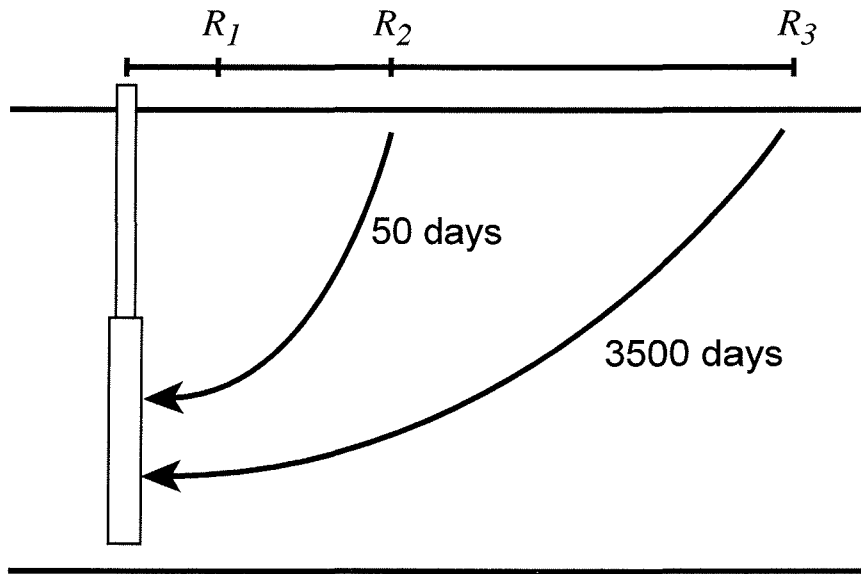


Figure 17.1: The radius R_1 of the immediate protection area is defined by a fixed distance, whereas the radii R_2 and R_3 of the intermediate and extended protection areas are defined by times of travel (tot).

1. Immediate protection area

The first protection area is intended to protect the wellhead and its immediate surroundings. Therefore, all activities are prohibited except maintenance and conservation of the installations or exploration of the aquifer. The radius of immediate protection is defined at a fixed distance from the wellhead. Depending on the type of aquifer, it varies between 20 and 60 meters in most cases.

2. Intermediate protection area

The intermediate protection area eliminates pollution hazards to groundwater that will arrive at the well in the near future. It assures that time for intervention remains in case of a contamination and that pollutants attenuate before they reach the well. The law suggests that the radius of

the second protection area should correspond to a time of travel distance of 50 days. It commonly varies between 40 and 280 meters, depending on the hydrogeological setting of the well. Installations or activities capable of polluting groundwater resources are prohibited.

3. **Extended protection area**

The extended protection area restricts or prohibits installations or activities that may cause a persistent pollution of the aquifer. The law recommends that the boundary of the extended protection area should correspond to a time of travel distance of 3500 days. Depending on the setting of the well, the radius usually varies between 350 and 2400 meters.

Chapter 18

Groundwater flow to a well

18.1 Wells in single layer systems

18.1.1 Unconfined aquifer settings

An unconfined aquifer is a layer of permeable rock or sediment in which the pressure of the groundwater is balanced by atmospheric pressure. The water table is lower than the top of the aquifer. A change in the amount of groundwater that is stored in an unconfined aquifer is reflected by a change in the elevation of the water table. An increase in groundwater storage corresponds to the filling of previously air-filled pore space or fissures with water. A decrease in storage is associated with the emptying of pores or fissures. Figure 18.1 illustrates that abstracting water from an unconfined aquifer setting creates a cone of depression in the water table.

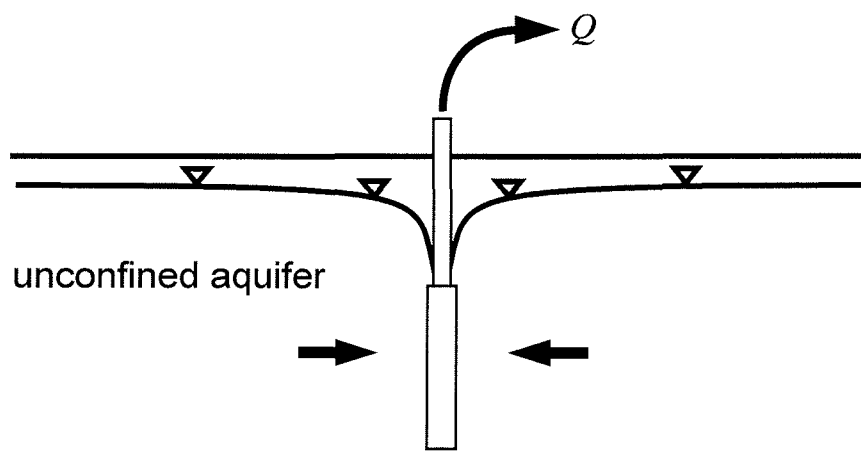


Figure 18.1: Pumping water from a well in an unconfined aquifer causes a drawdown of the watertable.

18.1.2 Confined aquifer settings

A confined aquifer is a layer of permeable rock or sediment that is overlain by an impermeable layer or a layer of significantly lower permeability. The aquifer is completely saturated with groundwater. Due to the confining layer, the pressure of groundwater is greater than atmospheric pressure. Therefore, the piezometric level is higher than the top of the aquifer. The compressibility of the groundwater or the aquifer sediment permits changes in the amount of groundwater stored in a confined aquifer. An increase of groundwater storage is accompanied by an increase in groundwater pressure and results in higher piezometric heads. A decrease in groundwater storage is reflected by lower pressure and lower piezometric heads. Abstracting groundwater from a confined aquifer creates a cone of depression in the piezometric heads (figure 18.2).

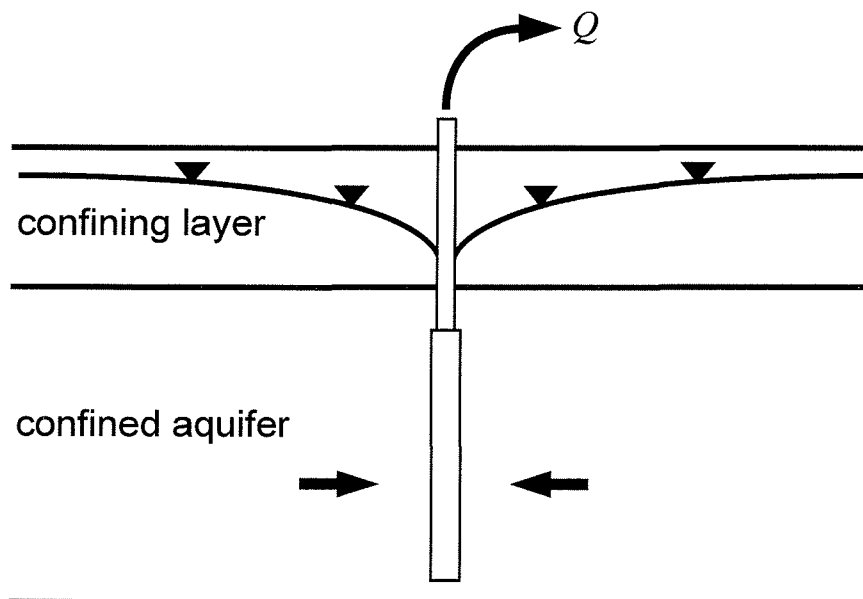


Figure 18.2: Pumping water from a well in a confined aquifer creates a cone of depression in the piezometric surface.

In the context of wellhead protection, it is important to note that perfectly confined aquifers would be invulnerable to pollution from ground surface, because it is impossible for any pollutant to pass through the impervious layer overlaying the aquifer. However, perfect confinement is rarely found in nature and even low permeability may open a way to pollution.

18.1.3 Analytical solutions for single aquifer settings

According to Darcy's law, the rate of groundwater flow is proportional to the area perpendicular to the direction of flow, the hydraulic conductivity of the

aquifer, and the hydraulic gradient (*Freeze and Cherry, 1979*):

$$Q = A \times K \times \frac{dh}{dn} \quad (18.1)$$

where

Q is the volumetric flux in the direction of n ,

A is the area perpendicular to n ,

K is the hydraulic conductivity, and

h is the hydraulic head.

The velocity of groundwater flow is obtained by dividing the volumetric flux by the area perpendicular to flow and the effective porosity of the aquifer:

$$v = \frac{Q}{An_e} = \frac{K}{n_e} \frac{dh}{dn} \quad (18.2)$$

where

v is the velocity of groundwater flow, and

n_e is the effective porosity of the aquifer.

Assuming no regional hydraulic gradient and a homogenous aquifer, groundwater flow to the well is radial. Consequently, the rate of flow is the same for any concentric shell around the well:

$$Q = 2\pi rb \times K \times \frac{dh}{dr} \quad (18.3)$$

where

r is the radial distance from the well, and

b is the thickness of the aquifer.

Approaching the well, the hydraulic gradient is increasing, because the area for flow to pass through is decreasing. Therefore, abstraction of groundwater through a well creates a cone of depression. Equation (18.2) indicates that the velocity is increasing towards the well proportionally to the hydraulic gradient.

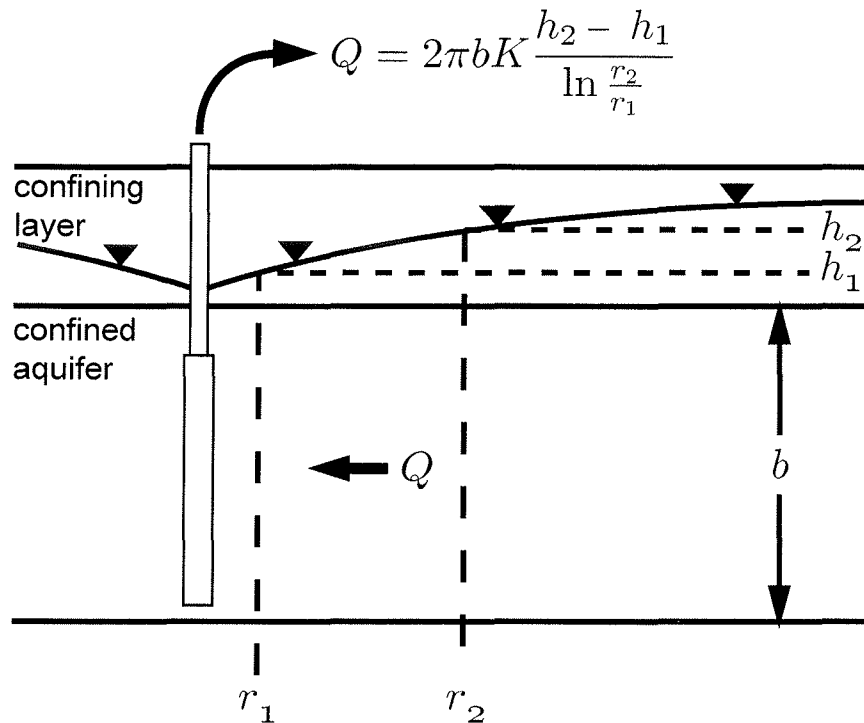


Figure 18.3: The rate of groundwater flow to a well in a confined aquifer can be expressed in terms of the piezometric heads at two observation wells. For unconfined aquifers, an approximation can be obtained by using saturated thickness instead of aquifer thickness.

By integrating equation (18.3), the radial volumetric flux towards the well can be expressed in terms of piezometric head at two observation wells within the capture area of the well:

$$\begin{aligned} \int_{h_1}^{h_2} dh &= \int_{r_1}^{r_2} \frac{Q}{2\pi bK} \frac{1}{r} dr \\ h_2 - h_1 &= \frac{Q}{2\pi bK} [\ln(r_2) - \ln(r_1)] \\ Q &= 2\pi bK \frac{h_2 - h_1}{\ln \frac{r_2}{r_1}} \end{aligned} \quad (18.4)$$

where

h_1, h_2 are the piezometric heads in the observation wells, and

r_1, r_2 are the corresponding radial distances from the pumping well.

Equation (18.4) is known as the Thiem formula and is commonly used for determining the hydraulic conductivity of confined aquifers by means of steady-state pumping tests (*Kruseman and de Ridder, 1994*). Figure 18.3 illustrates the geometry of the pumping test evaluation. For confined aquifer settings, the

area perpendicular to flow is determined by radius and aquifer thickness. In case of unconfined groundwater flow, the thickness of the aquifer in equation (18.3 is replaced by the saturated thickness:

$$Q = 2\pi rKh \frac{dh}{dr} \quad (18.5)$$

Integration of equation (18.5) between r_1 and r_2 yields the Dupuit formula for the evaluation of pumping tests in unconfined aquifers (*Kruseman and de Ridder, 1994*):

$$Q = \pi K \frac{h_2^2 - h_1^2}{\ln \frac{r_2}{r_1}} \quad (18.6)$$

Both the Thiem and the Dupuit formula can be rewritten by substituting the piezometric head with the observed drawdown at the observation wells. *Kruseman and de Ridder (1994)* show that the two formulas are equivalent if a corrected drawdown value is used in the Dupuit formula.

18.2 Wells in multi-layer systems

Aquifer systems that consist of three or more layers occur far more frequently in nature than perfectly confined single-layer aquifers or simple unconfined aquifers. While the analytical solutions described above are based on the assumption that groundwater flow occurs only horizontally towards the well, multi-layer aquifer systems cannot be described without accounting for vertical groundwater flow. As a result, analytical solutions are much more complex than the Thiem and Dupuit formulas for single layer aquifers and restricted to simple three-layer settings.

18.2.1 Three-layer aquifer settings

In a three-layer aquifer system, a low permeability layer separates two permeable layers of rock or sediment. As illustrated in figures 18.4 and 18.5, leakage through the semi-pervious layer may occur from the top to the bottom aquifer as well as vice versa. The lowering of the piezometric levels caused by abstracting water from a well may reverse the pre-pumping direction of leakage in a three-layer aquifer system (figure 18.5).

18.2.2 Analytical solutions for three-layer aquifer settings

Kruseman and de Ridder (1994) describe an analytical solution for calculating the steady-state drawdown in a leaky aquifer that was developed by De Glee.

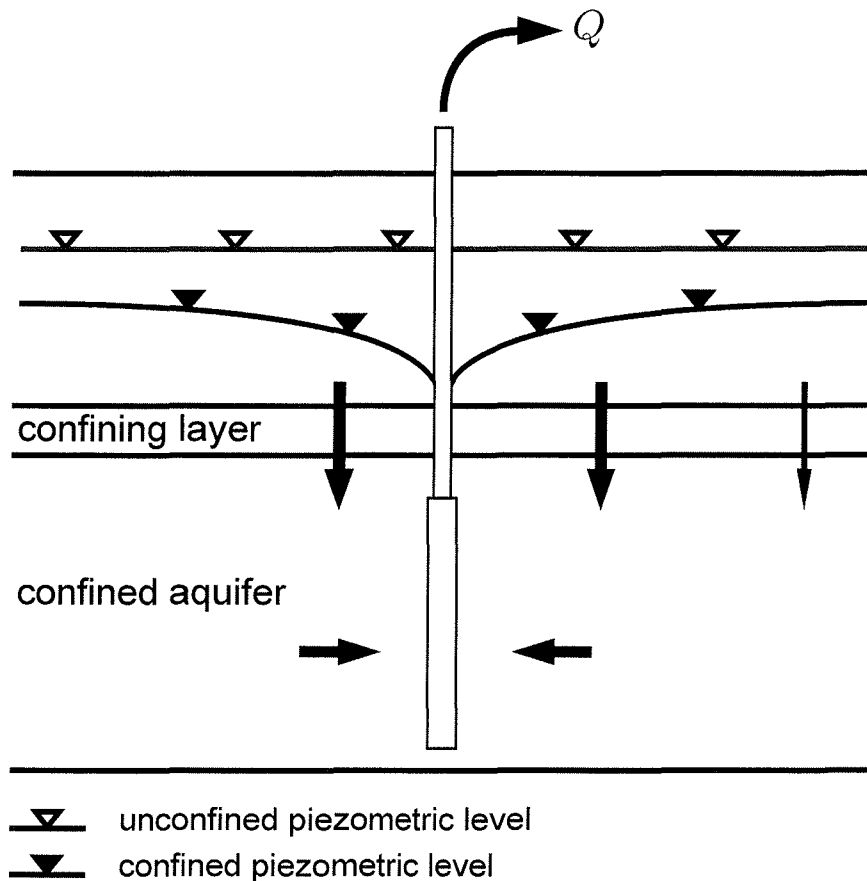


Figure 18.4: Part of the water abstracted from a well in a three-layer aquifer system with downward leakage comes from the unscreened top layer. Leakage is greater close to the well, because pumping increases the hydraulic gradient from the top to the bottom layer.

The approach involves a modified Bessel function and is solved graphically by means of a superposition method. *Hantush and Jacob (1955)* introduces an approximation of De Glee's equation, which simplifies calculations but still requires a graphical solution. For a detailed description of the methods see *Kruseman and de Ridder (1994)*.

18.2.3 Settings with more than three layers

Multi-layer aquifer systems consist of any combination of high and low permeability layers. As a result of horizontal groundwater flow and vertical leakage between the layers, the piezometric level can be different in each layer.

Wells abstracting water from multi-aquifer systems are associated with complex patterns of groundwater flow. For systems with more than three layers, there are no analytical solutions that describe the distribution of hydraulic heads and flow velocities. Hence, modeling is required to understand on what paths and how fast the groundwater reaches the screens of the well.

Chapter 19

Modeling groundwater flow to a well

There are many computer programs that can be used to simulate groundwater flow to a well. Two-dimensional flow models commonly use a horizontal discretization of the aquifer. Consequently, lateral variations of the aquifer properties or regional hydraulic gradients can be taken into account, while the vertical sequence of high- and low-permeability layers within the aquifer system and the position of the screens of the well must be neglected. Three-dimensional models allow a more precise definition of the aquifer in space, but the calculations involved are much more complex. Besides, in most cases there is not enough data available to accurately describe the distribution of hydrogeological properties of the aquifer in space.

The vertical heterogeneity of the aquifer system can be estimated from the lithology log of the well. The position of the screens of a well is commonly known. As these parameters are both readily available and important for calculating groundwater flow to a well, it is desirable to use a model that does an efficient simulation based on this data. For axisymmetric modeling, it is assumed that groundwater flow to a well is radial. In that case, a cylindrical section of the aquifer can be discretized into horizontal layers and concentric shells around the well. Hence, vertical heterogeneity can be described while lateral variations of aquifer properties are neglected.

19.1 Concept of modeling axisymmetric flow

As axisymmetric flow models are based on the assumption that ground water flow to a well is radial, any regional hydraulic gradient must be neglected. The only driving force of flow is abstraction from the well. Disregarding lateral variations of hydrogeological properties, the resulting cone of depression is perfectly axisymmetric. Figure 19.1 illustrates that a vertical cross-section

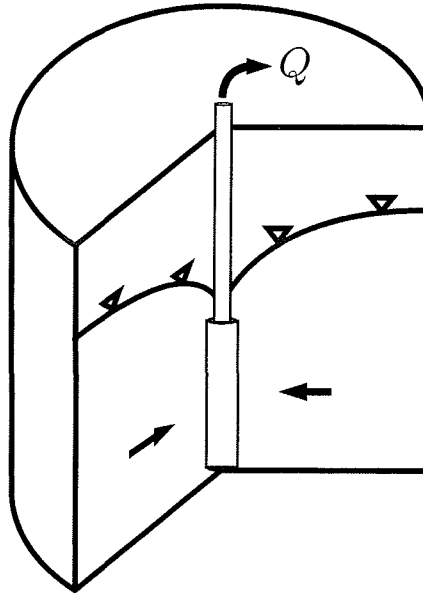


Figure 19.1: A vertical cross-section from the well to the outside of a cylinder around the well sufficiently describes the shape of the cone of depression.

of a cylinder sufficiently describes the shape of the cone of depression. Consequently, the three-dimensional draw-down can be determined by modeling the distribution of piezometric levels in two dimensions for the cross-section.

19.2 Grid design

Following the method of finite differences, the cross-sectional plane is divided into columns and rows (figure 19.2). Due to the radial symmetry of the model, the columns represent concentric shells around the well. High- and low-permeability layers can be defined in the model by assigning different hydrogeological properties to each row.

Approaching the well, the head gradient from pumping increases, because the cross-sectional area for flow to pass through is decreasing. Thus, finer discretization is required close to the well to accurately represent this increasing gradient. However, the difference in size for two neighboring cells should be small in order to avoid large numerical errors.

19.3 Finite differences flow equation

To obtain an approximation of the distribution of hydraulic heads, the value of the hydraulic head is calculated for a single point at the center of each cell. These nodes are referred to by means of row and column indices. Given that

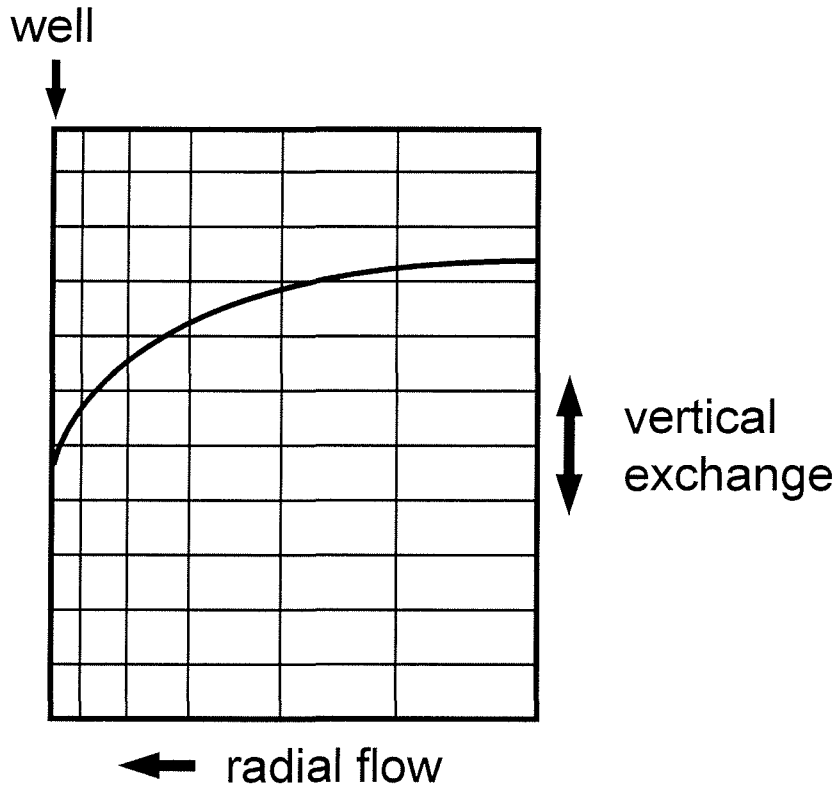


Figure 19.2: Following the method of finite differences, the cross-sectional plane is divided into columns and rows. Approaching the well, finer discretization of the mesh is required to accurately describe the increasing hydraulic gradient. The difference in size should be small for neighboring cells in order to avoid numerical errors.

flow is at a steady-state equilibrium, the in- and outflow must be balanced for each cell (figure 19.3). Assuming that inflow is positive and outflow is negative, the water balance for the cell (i, j) may be expressed as:

$$Q_z(i, j) + Q_r(i, j) = 0 \quad (19.1)$$

where

$Q_z(i, j)$ is the net volumetric flux in vertical direction, and

$Q_r(i, j)$ is the net volumetric flux in vertical direction into cell (i, j) .

In the vertical direction, the exchange of water between a cell and the upper and lower adjacent cell can be calculated by applying Darcy's law as given by equation (18.1):

$$Q_z(i, j) = A(j) \left(K_z(i - 0.5) \frac{h(i - 1, j) - h(i, j)}{z(i - 1) - z(i)} - K_z(i + 0.5) \frac{h(i, j) - h(i + 1, j)}{z(i) - z(i + 1)} \right) \quad (19.2)$$

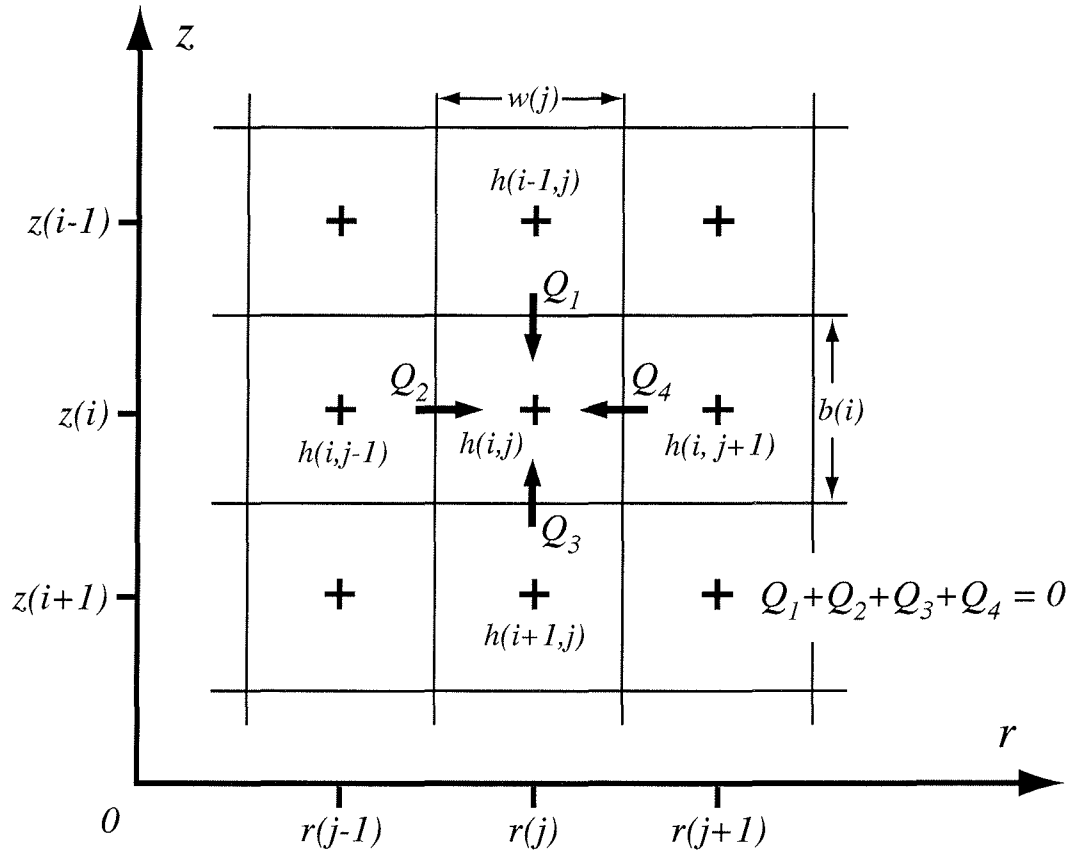


Figure 19.3: By definition, groundwater flow into a cell is positive and outflow is negative. Assuming a steady-state equilibrium, the sum of all flows is equal to zero and groundwater storage in each cell remains constant. All equations describing flow are functions of the hydraulic gradient. Consequently, the steady-state hydraulic head in each cell can be expressed in terms of the hydraulic heads in the adjacent cells.

where

$A(j)$ is the horizontal area of the j th shell,

$K_z(i - 0.5)$ is the mean vertical hydraulic conductivity of the layers i and $i - 1$,

$K_z(i + 0.5)$ is the mean vertical hydraulic conductivity of the layers i and $i + 1$,
and

$z(i)$ is the elevation of the center of the i th row of the grid, i.e. the z -coordinate of the nodes in that row.

In order to account for variable vertical hydraulic conductivity between different layers, the harmonic mean of the vertical conductivities is used in equation (19.2):

$$K_z(i \pm 0.5) = \frac{2K_z(i)K_z(i \pm 1)}{K_z(i) + K_z(i \pm 1)} \quad (19.3)$$

The horizontal area of a shell is determined by the radius and the width of the shell:

$$A(j) = 2\pi \left[\left(r(j) - \frac{w(j)}{2} \right)^2 - \left(r(j) + \frac{w(j)}{2} \right)^2 \right] \quad (19.4)$$

where

$r(j)$ is the distance from the center of the j th shell to the well, and

$w(j)$ is the width of the shell (or the column of the grid).

Horizontal flow between a cell and the two adjacent cells is calculated according to the Thiem formula as given by equation (18.4):

$$Q_r(i, j) = 2\pi b(i) K_x(i) \left(\frac{h(i, j+1) - h(i, j)}{r(j+1) - r(j)} - \frac{h(i, j) - h(i, j-1)}{r(j) - r(j-1)} \right) \quad (19.5)$$

where

$b(i)$ is the height, and

$K_x(i)$ is the horizontal hydraulic conductivity of the i th row of the grid.

For unconfined conditions, the row height $b(i)$ is replaced with the mean saturated thickness of the two adjacent cells. Substituting the right hand sides of equations (19.2) and (19.5) for the corresponding terms in equation (19.1) yields the finite differences equation for steady-state axisymmetric groundwater flow:

$$\begin{aligned} & \frac{A(j)K_z(i-0.5)}{z(i-1) - z(i)} (h(i-1, j) - h(i, j)) \\ & - \frac{A(j)K_z(i+0.5)}{z(i) - z(i+1)} (h(i, j) - h(i+1, j)) \\ & + \frac{2\pi b(i)K_x(i)}{r(j+1) - r(j)} (h(i, j+1) - h(i, j)) \\ & - \frac{2\pi b(i)K_x(i)}{r(j) - r(j-1)} (h(i, j) - h(i, j-1)) = 0 \end{aligned} \quad (19.6)$$

It follows that the hydraulic head at the node (i, j) can be expressed as a function of the heads at the four adjacent nodes. For convenience, equation (19.6) can be simplified by substituting the coefficients of the hydraulic heads:

$$h(i, j) = \frac{Mh(i, j-1) + Nh(i, j+1) + Oh(i-1, j) + Ph(i+1, j)}{M + N + O + P} \quad (19.7)$$

with

$$\begin{aligned} M &= \frac{A(j)K_z(i-0.5)}{z(i-1) - z(i)} \\ N &= \frac{A(j)K_z(i+0.5)}{z(i) - z(i+1)} \\ O &= \frac{2\pi b(i)K_x(i)}{r(j+1) - r(j)} \\ P &= \frac{2\pi b(i)K_x(i)}{r(j) - r(j-1)} \end{aligned}$$

Applying equation (19.7) to each cell of a grid that consists of N_R rows and N_C columns leads to a linear system of $N = N_R \times N_C$ equations which can be solved numerically by means of a simple iteration process:

$$\begin{aligned} h^{m+1}(i, j) &= \frac{1}{M + N + O + P} \\ &\quad \left(Mh^m(i, j-1) + Nh^m(i, j+1) \right. \\ &\quad \left. + Oh^m(i-1, j) + Ph^m(i+1, j) \right) \end{aligned} \quad (19.8)$$

where

m is the iteration level.

During each iteration step, the value of the hydraulic head at the node (i, j) is adjusted to the hydraulic heads at the adjacent nodes from the previous iteration level. By successively improving the value at each node from h^m to h^{m+1} , the iteration process approaches the solution of the system of equations.

Once the distribution of hydraulic heads is obtained at the desired accuracy, the velocity field can be calculated using the hydraulic gradients. The normal components of velocity between the nodes can be concluded from equation (18.2). The pattern of points of known hydraulic head and points of known velocity is shown in figure 19.4. In the radial direction, the velocities at the borders of the cell (i, j) are:

$$v_r(i, j-0.5) = -\frac{K_x(i)}{n_e(i)} \frac{h(i, j) - h(i, j-1)}{r(j) - r(j-1)} \quad (19.9)$$

and

$$v_r(i, j+0.5) = -\frac{K_x(i)}{n_e(i)} \frac{h(i, j+1) - h(i, j)}{r(j+1) - r(j)} \quad (19.10)$$

where

$v_r(i, j \pm 0.5)$ is the radial component of groundwater velocity at the inward and outward face of the cell, respectively. (A negative sign indicates flow towards the well.)

Accordingly, the vertical components of velocity are given by:

$$v_z(i - 0.5, j) = -\frac{K_z(i - 0.5)}{n_e(i)} \frac{h(i - 1, j) - h(i, j)}{z(i - 1) - z(i)} \quad (19.11)$$

and

$$v_z(i + 0.5, j) = -\frac{K_z(i + 0.5)}{n_e(i)} \frac{h(i, j) - h(i + 1, j)}{z(i) - z(i + 1)} \quad (19.12)$$

where

$v_z(i \pm 0.5, j)$ is the vertical component of groundwater velocity at the upper and lower face of the cell, respectively. (A negative sign indicates downward flow.)

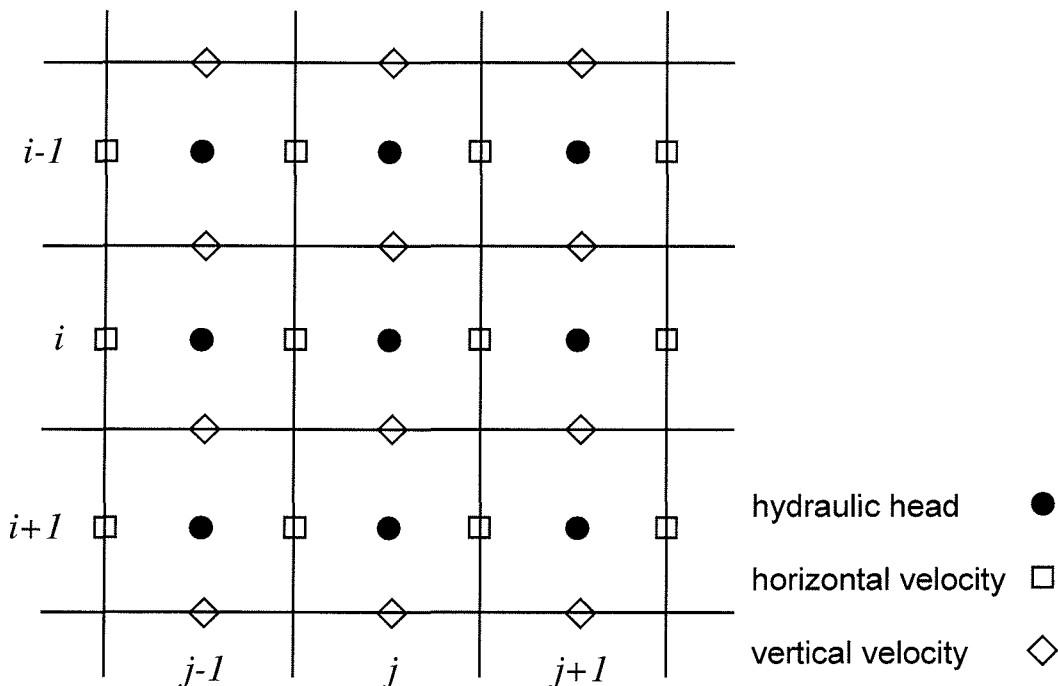


Figure 19.4: The solution of the axisymmetric flow equation yields the values of hydraulic head at the nodes. The hydraulic gradients determine the components of groundwater velocity normal to the faces of the cell. The vertical component of velocity is known at the upper and lower faces of the cells, whereas the radial component is obtained for the inward and outward borders of the cells.

19.4 Calculating times of travel

In case groundwater flow is at a steady-state equilibrium, the velocity field does not change with time, because the hydraulic heads are constant. All particles that move at the same velocity as the groundwater may only travel along fixed streamlines. Provided that groundwater flow is continuous, the position of a particle at any given time determines both the path on which it moved to this position and its path in the future. Consequently, streamlines as well as times of travel can be obtained by following a particle along its path forward or backward in time. This can be accomplished in an efficient and accurate way by means of linear particle tracking (e.g. *Schafer-Perini and Wilson (1991), Pollock (1994)*).

The normal components at the initial position of a particle are interpolated separately using the closest known values of velocity (figure 19.4). For simplification, the coordinates of the particle are written relative to the lower inward corner of the cell. Assuming that the particle is located in cell (i, j) , the initial velocity component in the radial direction is given by:

$$v_r(t_0) = v_r(i, j - 0.5) + r_0 m_r \quad (19.13)$$

with

$$m_r = \frac{v_r(i, j + 0.5) - v_r(i, j - 0.5)}{w(j)} \quad (19.14)$$

where

$v_r(t_0)$ is the initial radial velocity of the particle at the time t_0 , and

r_0 is the distance of the particle from the inward border of the cell.

The interpolation of the initial vertical velocity of the particle is analogous:

$$v_z(t_0) = v_z(i + 0.5, j) + z_0 m_z \quad (19.15)$$

with

$$m_z = \frac{v_z(i - 0.5, j) - v_z(i + 0.5, j)}{b(j)} \quad (19.16)$$

where

$v_z(t_0)$ is the initial vertical velocity of the particle, and

z_0 is the distance of the particle from the lower border of the cell.

As the velocity is the time derivative of the position, the times of travel in the radial and vertical directions can be obtained by integrating equations (19.14) and (19.16), respectively. In the radial direction, the time of travel from r_0 to r is:

$$t - t_0 = \Delta t_r = \frac{1}{m_r} \ln \left| \frac{v_r(i, j - 0.5) + m_r r}{v_r(t_0)} \right| \text{ for } m_r \neq 0 \quad (19.17)$$

$$\Delta t_r = \frac{r - r_0}{v_r(t_0)} \text{ for } m_r = 0 \quad (19.18)$$

The time of travel from z_0 to z in the vertical direction is calculated analogously:

$$t - t_0 = \Delta t_z = \frac{1}{m_z} \ln \left| \frac{v_z(i + 0.5, j) + m_z z}{v_z(t_0)} \right| \text{ for } m_z \neq 0 \quad (19.19)$$

$$\Delta t_z = \frac{z - z_0}{v_z(t_0)} \text{ for } m_z = 0 \quad (19.20)$$

Note that equations (19.17) through (19.20) are valid only within the cell (i, j) and if the respective component of initial velocity is non-zero.

Equations (19.17) through (19.20) can be rearranged to express the position of the particle as a function of time. To simplify the equations, it is assumed that $t_0 = 0$. The distance between the particle and the inward face of the cell is:

$$r(t) = \frac{\exp(m_r t) v_r(t_0) - v_r(i, j - 0.5)}{m_r} \text{ for } m_r \neq 0 \quad (19.21)$$

$$r(t) = r_0 + v_r(t_0) t \text{ for } m_r = 0 \quad (19.22)$$

In the vertical direction, the distance between the particle and the lower face of the cell is

$$z(t) = \frac{\exp(m_z t) v_z(t_0) - v_z(i + 0.5, j)}{m_z} \text{ for } m_z \neq 0 \quad (19.23)$$

$$z(t) = z_0 + v_z(t_0) t \text{ for } m_z = 0 \quad (19.24)$$

In order to calculate the path of a particle for a given time of travel, the linear particle tracking algorithm starts by calculating the velocity at the initial position of the particle. The signs of the velocity components determine through which two faces of the cell the particle may potentially leave the cell, e.g. if the radial component is positive, the particle can only exit through the outward face of the cell. The times of travel to the potential exit faces in radial and in vertical direction can be calculated by applying equations (19.17) through (19.20), as appropriate. The time until the particle reaches the exit face in the radial direction is:

$$\Delta t_{Exit,r} = \frac{1}{m_r} \ln \left| \frac{v_r(i, j - 0.5) + m_r r_{Exit}}{v_r(t_0)} \right| \text{ for } m_r \neq 0 \quad (19.25)$$

$$\Delta t_{Exit,r} = \frac{r_{Exit} - r_0}{v_r(t_0)} \text{ for } m_r = 0 \quad (19.26)$$

where

$\Delta t_{Exit,r}$ is the time until the particle reaches the radial position of the exit face $[T]$, and

r_{Exit} is the horizontal position of the exit face $[L]$, either $r_{Exit} = 0$ for the inward face or $r_{Exit} = w(j)$ for the right face of the cell.

The time until the particle reaches the exit face in the vertical direction is calculated analogously:

$$\Delta t_{Exit,z} = \frac{1}{m_z} \ln \left| \frac{v_z(i + 0.5, j) + m_z z_{Exit}}{v_z(t_0)} \right| \text{ for } m_z \neq 0 \quad (19.27)$$

$$\Delta t_{Exit,z} = \frac{z_{Exit} - z_0}{v_z(t_0)} \text{ for } m_z = 0 \quad (19.28)$$

where

$\Delta t_{Exit,z}$ is the time until the particle reaches the vertical position of the exit face $[T]$, and

z_{Exit} is the vertical position of the exit face $[L]$, either $z_{Exit} = 0$ for the lower face or $z_{Exit} = b(i)$ for the upper face of the cell.

Special care must be taken if the groundwater flows into the cell from two opposite directions. Consequently, the exit time in the respective direction cannot be calculated, because neither of the two faces are potential exit faces.

In case $\Delta t_{Exit,x}$ is smaller than $\Delta t_{Exit,z}$, the particle will exit across the inward or outward border of the cell. In case $\Delta t_{Exit,z}$ is smaller than $\Delta t_{Exit,x}$, the particle will leave through the upper or lower border of the cell (figure 19.5). The smallest value is the time after which the particle leaves the cell:

$$\Delta t_{Exit} = \min(\Delta t_{Exit,x}, \Delta t_{Exit,z}) \quad (19.29)$$

where

Δt_{Exit} is the time until the particle leaves the cell $[T]$.

If the exit time Δt_{Exit} is smaller than the given time of travel, the particle is moved to the coordinates $(r(\Delta t_{Exit}), z(\Delta t_{Exit}))$ on the exit face. Since the interpolation functions are not valid outside the cell, the values of the cell into which the particle is entering are used for the next tracking step. This procedure is repeated until the given time of travel is reached.

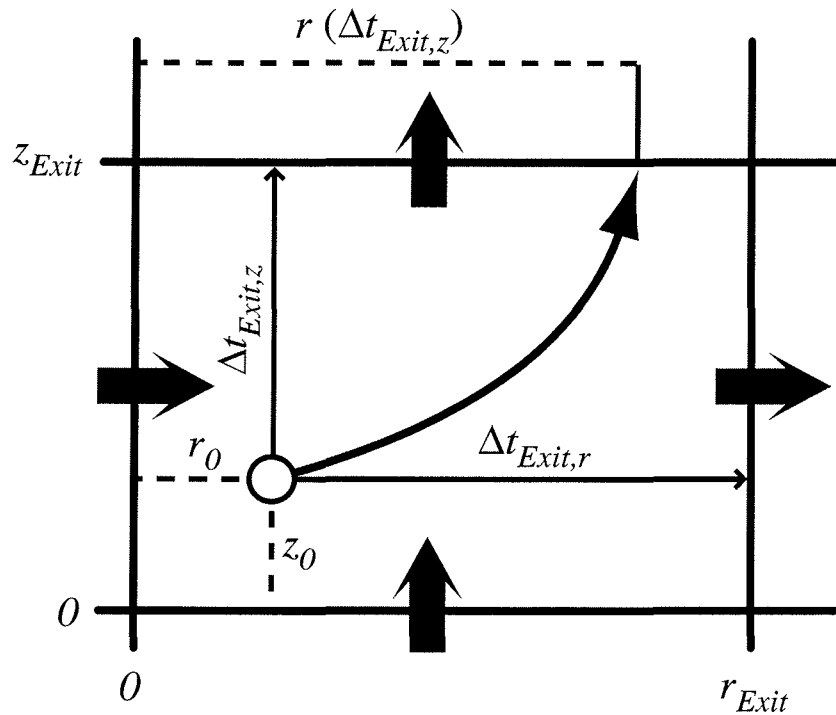


Figure 19.5: At the beginning of the tracking step, the particle is at the position marked by the circle. The linear tracking algorithm first calculates the initial velocity of the particle by linear interpolation from the velocity components normal to the faces of the cell (black arrows). Next, it compares the times of travel to the potential exit faces determined by the initial velocity. In the illustrated case, the particle reaches the upper face of the cell first. The r -coordinate on the exit face is given by $r(\Delta t_{Exit,z})$. (Pollock (1994), modified)

CHAPTER 19. MODELING GROUNDWATER FLOW TO A WELL

Chapter 20

The computer program WellFlow

The program WellFlow is a user-friendly, menu- and mouse-driven stand-alone modeling tool. It was written in RealBasic for Mac OS and can be compiled for both Windows and Macintosh operating systems. WellFlow simulates steady-state groundwater flow to a well by applying the method of finite differences, following an axisymmetric approach where a vertical cross-section of a cylinder is modeled in two dimensions. The program has been developed to study the influence of aquifer heterogeneity and the screening of a well on groundwater streamlines and times of travel. It can be used for calculating time of travel distances required for the delineation of wellhead protection areas in multi-aquifer settings.

20.1 Input data

When setting up a new WellFlow simulation, the first step is to enter all data that characterizes the hydrogeological setting of the well. Secondly, the properties of the well itself such as radius and abstraction rate must be defined. Finally, the dimensions of the model and the degree of spatial discretization have to be specified before the flow equation can be solved.

20.1.1 Hydrogeological units

Hydrogeological units at the location of the well can be defined in the layer parameters dialog that is opened by choosing *Layers...* from the Parameters-menu. A list of all layers is displayed on the left hand side of the dialog. Selecting one of the layers shows the properties of the layers on the right hand side of the dialog. If more than one layer is selected, only the properties that

both layers have in common are shown. Changing the values in the entry fields affects all selected layers.

A new layer at the bottom of the sequence is created by clicking the *Add Layer* button when no layer is selected. If one or more layers are selected, clicking the *Insert Layer* button will insert a new layer above the first selected layer. Upon creating a new layer, a title must be assigned to the layer. This title can be changed later by double-clicking on the layer in the list.

Clicking the *Remove* button will remove the selected layers from the list and shift the lower layers upward.

When the values of thickness and top or bottom of layer are changed, WellFlow automatically completes or recalculates these parameters as soon as possible. Gaps within the defined sequence are prevented by adjusting the top and bottom of other layers.

As WellFlow assumes that groundwater flow to the well is at a steady-state equilibrium, the effective porosity does not have any effect on the distribution of hydraulic heads in the surroundings of the well. However, the parameter needs to be defined correctly for the calculation of streamlines and times of travel.

For each hydrogeological unit, an individual pre-pumping hydraulic head must be entered. This value is used as a constant head boundary condition in the last column of the grid.

The screening of the layer can be toggled by checking the corresponding box. Every new layer is unscreened by default, but at least one layer within the modeled sequence must be screened in order for the model to run. The titles of screened layers are underlined in the list of layers.

The layers can be rearranged by dragging and dropping in the list of layers. When a layer has been dragged to a new position in the sequence, the top and bottom of all layers are readjusted, preserving the top of the sequence and the thicknesses of the layers.

20.1.2 Well properties

The abstraction rate and the radius of the well casing are specified in the well parameters dialog that is accessed by choosing *Well..* from the Parameters-menu. Injection can be simulated by entering a negative abstraction rate.

20.1.3 Model properties

The radius and the discretization of the modeled cylinder can be defined in the Model Parameters dialog that is opened by choosing *Model...* from the

Parameters-menu. The total radius should be larger than the radius of the cone of depression, because it is assumed that the head on the outside boundary of the model is not affected by the well. The number of shells characterizes the degree of spatial discretization of the model. The more shells there are, the more accurately the distribution of hydraulic heads can be calculated. However, a large number of shells may lead to long calculation times. The coarsening factor determines the difference in width of adjacent cells in a row.

In order to ensure a relatively even spacing of the rows in the grid, WellFlow automatically divides the layers into sublayers, if necessary. By default, the maximum thickness of a sublayer is given by the minimum thickness of the layers in the sequence. Optionally, the program can be forced to use smaller row heights by specifying the maximum thickness of a sublayer or the minimum of sublayers per layer.

As another option, recharge from precipitation surplus can be defined. The program automatically calculates the appropriate volumetric flux to the cells in the topmost row of the grid based on the horizontal area of the corresponding shell. It is also possible to simulate evapotranspiration by setting the recharge parameter to a negative value.

20.1.4 Loading and saving input data sets

All input data may be saved by choosing *Save* or *Save As...* from the File-menu. All files written by WellFlow are in plain text format and can be viewed or modified using any text editor. Previously saved input data sets can be loaded by choosing *Open...* from the File-menu.

20.2 Simulation

As long as the parameters that have been entered are inconsistent or incomplete, the center area of the main window remains blank and an error message is displayed at the bottom. Once all necessary parameters have been entered, the main window shows a simple sketch of the sequence, the position of the screens and the model grid.

Now, the axisymmetric flow equation can be solved step by step or via an automated iteration process. The automatic solution is started by choosing *Start* from the Solve-menu and entering the desired tolerance limit. The iteration process can be interrupted and resumed at any time. The effects of one single iteration step can be checked by choosing *One step* from the Solve-menu. The current tolerance is displayed in the top right corner of the main window.

20.3 Evaluation

When the flow equation has been solved at the desired accuracy, the simulation results can be evaluated by means of forward and backward particle tracking. By default, clicking somewhere on the grid area will start forward particle tracking from this position. The particle is followed until it reaches the well or the boundary of the model domain and the time of travel is displayed at the bottom of the main window. The direction of particle tracking can be changed from forward to backward in the options dialog that is opened by choosing *Options...* from the Evaluation-menu.

In order to show time-dependent capture zones of the well, choose *Plot Contour...* from the Evaluation-menu and enter the desired time of travel. The limits of the corresponding zone are marked by a black line in the grid. Note that by default, the backward particle tracking to find the time contour starts at the center of the first shell. The start radius can be changed in the options dialog. If the start radius is equal to the well radius, only those particles that are placed at a screen will be tracked. To change the accuracy of the tracking the maximum distance between two points of the contour line can be reduced or increased in the options-dialog.

The water table in the topmost layer can be displayed by choosing *Water Table* from the View-menu. If the topmost layer is unconfined, the water table is drawn as a black line across the grid. For confined conditions, the black line is drawn above the grid and marks the piezometric levels in the topmost layer.

All simulation results can be exported to other programs for further evaluation and comparison to field data. The items *Export Heads...*, *Export Water Table...*, and *Export Contour...* write the corresponding data into tab-delimited text files, which can easily be opened by other applications. The first lines of each file contain information on the order of the data.

Chapter 21

Examples

In the following, the application of WellFlow will be illustrated for a few examples. In the first example, WellFlow is used for simulating groundwater flow to a well in a single confined aquifer. This setting is simple enough to allow a comparison of the simulation results with an analytical solution. In the second example, the initial head of the confined aquifer from the first example is lowered in order to turn it into an unconfined aquifer. Once again, the simulation results may be compared to an analytical solution.

21.1 Example A: Single confined aquifer

In the first example, a well is abstracting water from a homogenous, isotropic and perfectly confined aquifer. The well fully penetrates the aquifer and is screened over the entire penetration depth. In WellFlow, a single layer is defined to represent the aquifer (table 21.1). The radius of the well casing is 0.1 m and the abstraction rate is 10 l s^{-1} . The total radius of the model is 100 m and the grid is subdivided into 20 shells, using a coarsening factor of 1.2. The tolerance limit for the iterative solution of the flow equation is set to $1 \times 10^{-4}\text{ m}$ per step.

Table 21.1: Parameters for defining the aquifer in example A

Top	0 m
Thickness	20 m
Horizontal hydraulic conductivity	$1 \times 10^{-4}\text{ m s}^{-1}$
Vertical hydraulic conductivity	$1 \times 10^{-4}\text{ m s}^{-1}$
Effective porosity	0.3
Initial head	10 m

An analytical solution for example A is obtained by applying the Thiem formula as given by equation (18.4). The radius of the well and the drawdown in the well as calculated by the model is used as a reference point. Figure 21.1 shows a comparison of the simulation results for example A with the analytical solution and the results of another simulation for the same setting, using only 10 shells. The results from both simulations are in excellent agreement with the analytical solution. Example C shows how WellFlow can be applied to calculate time of travel contour lines for a well in a three-layer aquifer system.

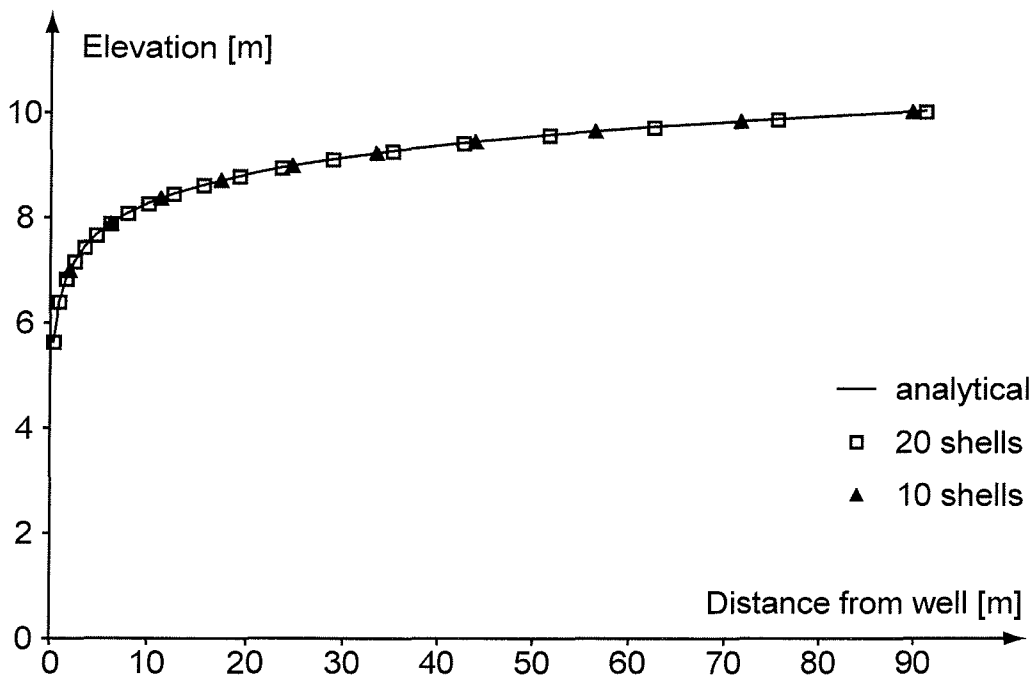


Figure 21.1: The simulation results for example A using different radial spacing of the model grid are compared to an analytical solution obtained by means of the Thiem formula. For both grids, the simulation results are in excellent agreement with the analytical solution.

21.2 Example B: Single unconfined aquifer

The second example makes use of the same layer definition as in Example A, except that the initial head is lowered from $10m$ to $-1m$ in order to turn the layer into an unconfined aquifer. All other parameters are the same as in Example A.

An analytical solution for example B is obtained by applying the Dupuit formula as given by equation (18.6). Once again, the simulated drawdown at the well and the well radius is used as a reference point. A comparison of the results of the two numerical simulations using different numbers of shells and the

analytical solution is shown in figure 21.2. Both the result of the simulation based on ten shells and the result of the simulation based on 20 shells match the analytical solution very well.

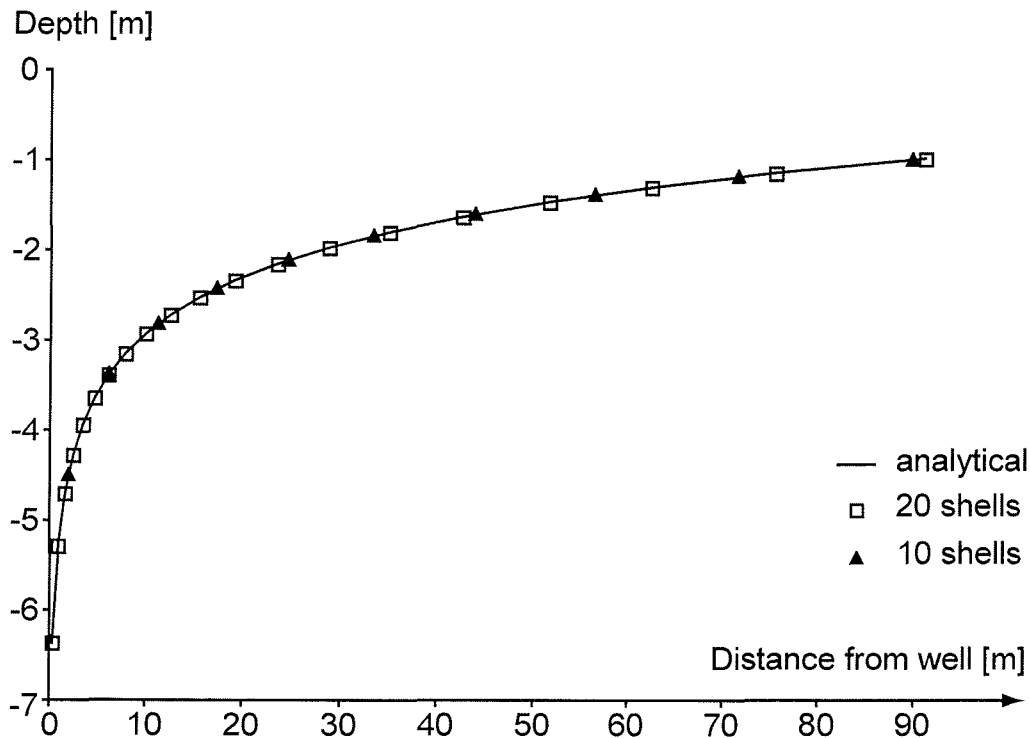


Figure 21.2: The results from two numerical simulations based on different radial grid spacings are compared to an analytical solution for example B, which was obtained by applying the Dupuit formula. Both simulations excellently match the analytical solution.

21.3 Example C: Three-layer aquifer system

Examples A and B show that the program WellFlow yields the same results as the analytical solutions for confined and unconfined single aquifer systems. The following example demonstrates that WellFlow can easily be applied to multi-aquifer systems as well.

In example C, the main aquifer has the same hydraulic properties as the aquifer in Examples A and B, but it is overlain by an aquitard and an unconfined aquifer at the top of the sequence. There are no screens in the upper aquifer. Table 21.2 summarizes the hydrogeological setting.

The total radius of the model is 500 m and the grid is subdivided into 20 shells, using a coarsening factor of 1.2. The radius of the well casing is 0.1 m, and the abstraction rate is 10 l s^{-1} . By default, WellFlow uses the minimum thickness of the layers in the sequence as a thickness limit for the sublayers.

Table 21.2: Sequence of hydrogeological layers in example C

Unconfined aquifer	Top	0 m
	Thickness	10 m
	Horizontal hydraulic conductivity	$1 \times 10^{-4} \text{ ms}^{-1}$
	Vertical hydraulic conductivity	$1 \times 10^{-4} \text{ ms}^{-1}$
	Effective porosity	0.3
	Initial head	0 m
Aquitard	Top	-10 m
	Thickness	2 m
	Horizontal hydraulic conductivity	$1 \times 10^{-9} \text{ ms}^{-1}$
	Vertical hydraulic conductivity	$1 \times 10^{-9} \text{ ms}^{-1}$
	Effective porosity	0.3
	Initial head	0 m
Confined aquifer	Top	-12 m
	Thickness	20 m
	Horizontal hydraulic conductivity	$1 \times 10^{-4} \text{ ms}^{-1}$
	Vertical hydraulic conductivity	$1 \times 10^{-4} \text{ ms}^{-1}$
	Effective porosity	0.3
	Initial head	10 m

As a result, the sequence in example C would be subdivided into a total of 17 sublayers: five for the unconfined aquifer, one for the aquitard, and ten for the confined aquifer. However, because the aquitard plays an important role in the system, it is advisable to apply a finer discretization. This is accomplished by increasing the minimum number of sublayers per layer in the model dialog. Forcing at least three sublayers per layer yields a total of 48 sublayers in the grid. The iterative solution of the flow equation was stopped after a tolerance of $1 \times 10^{-4} \text{ m}$ per step had been reached.

Figure 21.3 shows the calculated tie of travel contours for 50 days and for 3500 days. The groundwater velocity within the aquitard is very low, because of the low hydraulic conductivity. Since it takes a very long time until groundwater from the unconfined top aquifer reaches the well, the aquitard protects the groundwater in the lower confined aquifer.

The contour lines for both 50 days and 3500 days travel time are vertical within the lower confined aquifer. This indicates that the the pattern of groundwater flow is dominated by radial flow to the well while vertical leakage from the unconfined aquifer plays a minor role. Comparing the distances between the well and the two contour lines shows that the radial velocity is increasing towards the well.

In order to evaluate the protective function of the aquitard, the hydraulic conductivity of the aquitard is increased from $1 \times 10^{-9} \text{ ms}^{-1}$ to $1 \times 10^{-6} \text{ ms}^{-1}$

while all other parameters are left unchanged. The results of this simulation are shown in figure 21.4.

The time of travel contour lines reveal that increasing the hydraulic conductivity of the aquitard significantly reduces the protective effect of the aquitard. The shapes of the contour lines indicate that the flow pattern in both the upper unconfined and the lower unconfined aquifer is dominated by radial flow beyond the 50 days contour line. Closer to the well, the groundwater in the confined aquifer mixes with groundwater from the upper aquifer that is leaking through the aquitard.

Since the abstracted water comes from both the upper and the lower aquifer, the hydraulic gradients in the lower aquifer are smaller than in the first simulation. Consequently, the groundwater velocity in the confined aquifer is lower, and the distance from both the 50 days and the 3500 days contour line to the well is smaller.

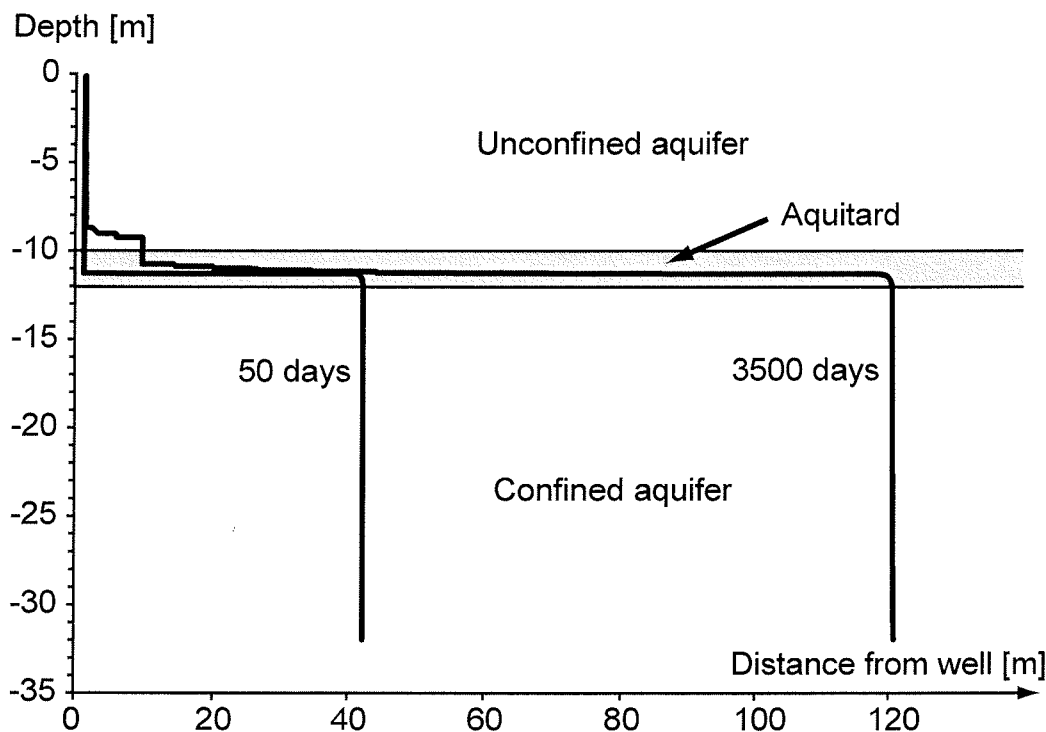


Figure 21.3: The time of travel contour lines for 50 days and 3500 days show that the low-permeability layer between the upper unconfined aquifer and the lower confined aquifer protects the groundwater in the confined aquifer from possible sources of pollution at the surface.

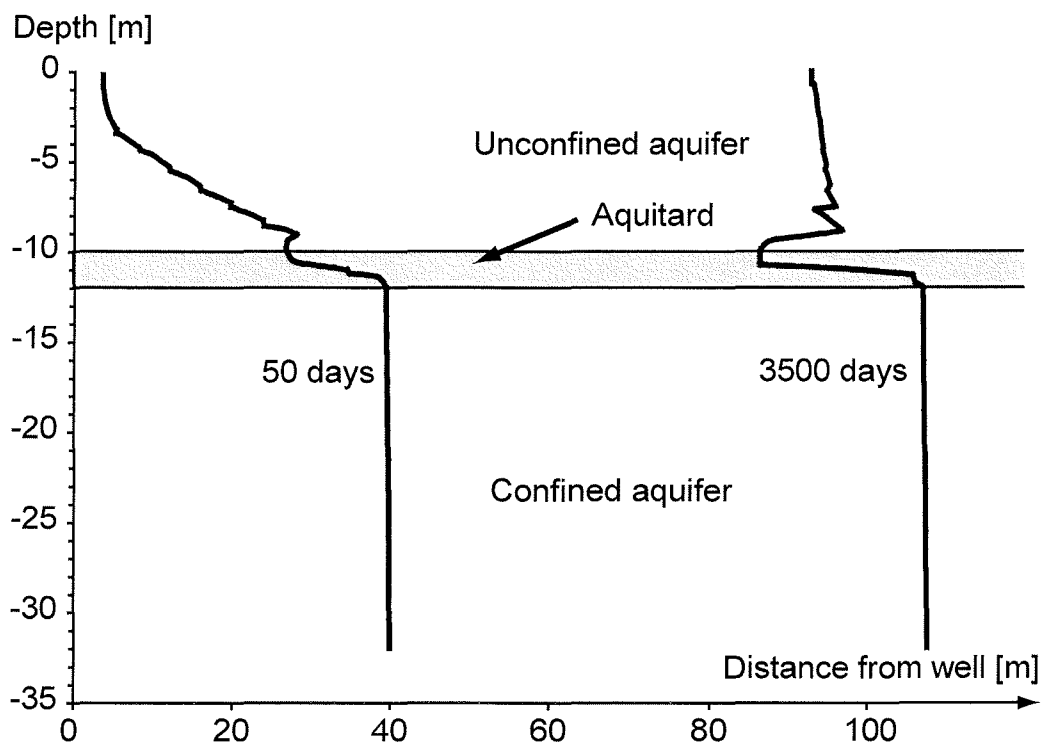


Figure 21.4: Increasing the hydraulic conductivity of the aquitard significantly reduces the protective effect. The shapes of the time of travel contour lines indicate that the groundwater in the upper aquifer first approaches the well radially and then leaks through the aquitard close to the well.

Chapter 22

Summary

The delineation of wellhead protection zones that relate to specific times of travel to the well requires the calculation of groundwater velocities in the vicinity of the well. Analytical solutions are available for simple hydrogeological settings that are characterized by up to three layers of different hydraulic conductivity. More complex settings in multi-layer aquifer systems can be described by means of numerical modeling.

Two-dimensional models that simulate groundwater flow in a horizontal plane neglect the vertical heterogeneity of the aquifer. Three-dimensional modeling involves high computational effort and requires more data than commonly available for wells. Axisymmetric groundwater models ignore regional hydraulic gradients while offering the possibility to accurately describe the vertical heterogeneity of multi-layer aquifer systems. Commonly, the data required to set up an axisymmetric flow model for a well is readily available.

The computer program WellFlow was developed for the simulation of steady-state axisymmetric groundwater flow to wells in multi-layer aquifer systems. WellFlow is based on the finite differences formulation of the axisymmetric flow equation. Hydraulic heads are calculated by means of a simple iteration process. Forward and backward linear particle tracking is applied to visualize streamlines and time of travel contours.

Comparing the results of simulations using WellFlow with analytical solutions for single aquifers shows that the program accurately simulates confined as well as unconfined groundwater flow to a well. The application of WellFlow to a well in a three-layer aquifer system yields realistic results.

Part V

Delineation of wellhead protection zones – A simplified approach

Chapter 23

Delineation of wellhead protection zones – A simplified approach

T. Feseker and J. P. Lobo Ferreira

23.1 Introduction

In September 1999, Portugal ratified a new law on groundwater protection. It demands three wellhead protection areas for each well used for public water supply that is abstracting more than 1000 cubic metres per day or serving more than 500 habitants. If the abstraction rate is lower or if the well is supplying fewer habitants, only the immediate protection zone is required. Various activities and installations capable of polluting groundwater resources are prohibited within these protection zones in order to prevent contamination of drinking water.

The immediate protection area encloses the surroundings of the wellhead including the installations used for abstracting water. Depending on the type of aquifer, the outer boundary of this inner protection zone is defined at a fixed radial distance from the wellhead and can be easily marked. On the other hand, the intermediate and the extended protection areas are defined by the time it takes for groundwater to reach the well from the outer boundary of the protection zone. Consequently, the delineation of the two outer protection areas becomes complex problem that often requires numerical modeling.

23.2 Problem definition

There are many computer programs that can be used to simulate groundwater flow to a well. Two-dimensional flow models commonly use horizontal discretization of the aquifer. Consequently, lateral variations of the aquifer properties are taken into account while the vertical sequence of high- and low-permeability layers within the aquifer system and the position of the screens of the well are neglected. Three-dimensional models allow a more precise description of the aquifer in space, but on the other hand, the calculations involved are much more complex and time-consuming. Besides, in most cases there is not enough data available to describe the distribution of hydrogeological properties at the same level of accuracy as the spatial discretization of the model grid.

The vertical heterogeneity of the aquifer can be estimated from the lithological logs of the well. The position of the screens of a well is commonly known. As these parameters are important for calculating groundwater flow to a well and because they are available without any further investigations, it is therefore desirable to develop a model that does an efficient simulation using lithological and well screen data. In axisymmetric flow modeling, it is assumed that groundwater flow to a well is radial. In that case, a cylindrical section of the aquifer can be discretized into horizontal layers and vertical shells around the well. Hence, vertical heterogeneity can be conveniently described whereas lateral variations in the hydrogeological properties are ignored. These restrictions fit well with the data that is available for most wells and make axisymmetric flow modeling as an appropriate and suitable approach for simulating groundwater flow to a well.

23.3 Concepts of modeling axisymmetric flow

As axisymmetric flow models are based on the assumption that ground water flow to a well is radial, while regional hydraulic gradient is negligible. The only driving force of flow is abstraction from the well. Disregarding lateral variations of hydrogeological properties, the resulting cone of depression is perfectly axially symmetric around the well. Thus, a vertical cross-section from the well to the outer limit of the cone of depression sufficiently describes the sloping hydraulic gradient around the well. Therefore, the three-dimensional draw-down can be determined by modeling the distribution of piezometric levels in two dimensions.

Following the method of finite differences, the cross-sectional plane of the geological system is divided into cells by columns and rows. However, it is important to note that the cells do not represent rectangular sections of the aquifer like in common two-dimensional grids. As the columns of the axisymmetric

grid are concentric cylindrical shells around the well, each cell represents a ring-shaped element. As one approaches close to the pumping well, the hydraulic gradient increases and the cross sectional area of flow decreases. Accordingly, finer discretization of the grid is required close to the well to accurately represent this increasing gradient.

As an approximation of the distribution of hydraulic heads, the head value is calculated for the midpoint of each cell. Given that the rate of abstraction is constant, and flow is in steady-state condition: In- and outflow are balanced for each cell. The vertical exchange of groundwater between two cells can be determined by applying Darcys Law. For calculating the horizontal flow of groundwater, the axial symmetry of the model has been taken into account by using the Dupuit-Thiem equation.

23.4 The computer program “WellFlow”

In order to study groundwater flow to a well and to facilitate the delineation of wellhead protection areas especially in multi-aquifer settings, the computer program WellFlow was developed. It is a user-friendly, menu- and mouse-driven stand-alone modeling tool for Windows and Mac OS. Steady-state groundwater flow to a well can be simulated by applying the method of finite differences, following an axisymmetric approach where a vertical cross-section of a cylinder is modeled in 2D.

The well is defined by abstraction rate and radius. Hydrogeological units (lithological data) at the position of the well are entered as horizontal layers that are homogenous and having a constant thickness throughout the model area. A steady-state hydraulic head is assigned to each layer. The head value serves as a fixed head boundary condition on the outer model limit, while the flow between layers resulting from different steady-state heads is taken into account during iteration. Recharge from precipitation surplus can be defined for the top layer of the modeled sequence.

The program uses this basic input data to automatically generate a finite differences grid. The distribution of hydraulic heads is solved numerically using an iteration process. Once the desired accuracy is reached, groundwater streamlines and time of travel distances can be calculated by means of forward and backward particle tracking.

23.5 Application of WellFlow – A case study

The program can be used to study the effects of different screening and vertical heterogeneity in layered aquifer systems on groundwater flow to a well. Flow

to partially penetrating wells can be simulated. In contrast to horizontal two-dimensional models, WellFlow model enables the user to calculate traveltime for different depths of particle starting points. Thus, the protective effect of low-permeability layers above the aquifer can be examined when determining the size of protection zones. Furthermore, it is possible to apply WellFlow model even before a well is sunk in order to determine the most suitable design of the well as far as protection zones are concerned.

As a first test, WellFlow model has been applied to a well in Ramalhal, Portugal. The well is situated in the cretaceous Torres Vedras aquifer, approximately 50 kilometers north of Lisbon. It is 135 meters deep and consists of 13 screened and 15 unscreened intervals. The litholog comprises 27 different layers, ranging from clays to sands and conglomerates. By combining the information on the screening of the well with the litholog, the aquifer system can be divided into 8 unscreened and 6 screened layers. The hydrogeological properties of these 14 layers have been estimated from the petrography described in the litholog. The conductivity of the high-permeability layers ranges from $1e-5$ to $1e-4$ m/s, whereas the conductivity of the low-permeability layers varies between $1e-9$ and $1e-8$ m/s. As the model yields approximately the same relation between abstraction rate and draw-down in the well as documented in the well-performance test, the chosen values conductivity seems reasonable. For particle tracking, it is assumed that the effective porosities are 0.2 and 0.1, respectively. Figure 23.1 shows the layers used in the simulation and gives an overview of the distances corresponding to a time of travel of 50 days for different depths of particle starting points.

It is obvious that the unscreened superficial aquifer and the uppermost aquitard protect the groundwater resources from pollutants injected close to ground surface. Above the first screen, flow velocities are so low that it takes a very long time until groundwater from the two upper layers reaches the well. However, if there was a way for pollutants to quickly enter the deeper layers of the aquifer system, e.g. through an abandoned well or bore hole, they would reach the well much faster.

23.6 Conclusion

Axisymmetric models are very suitable for modeling groundwater flow to a well, because all of the data that is already available for most wells may be included in the simulation. In contrast to horizontal two-dimensional models, both the vertical heterogeneity of multi-layered aquifers and the position of the screens can be taken into account. Especially in the context of the delineation of wellhead protection areas, it seems important to include the vertical dimension in travel time calculations.

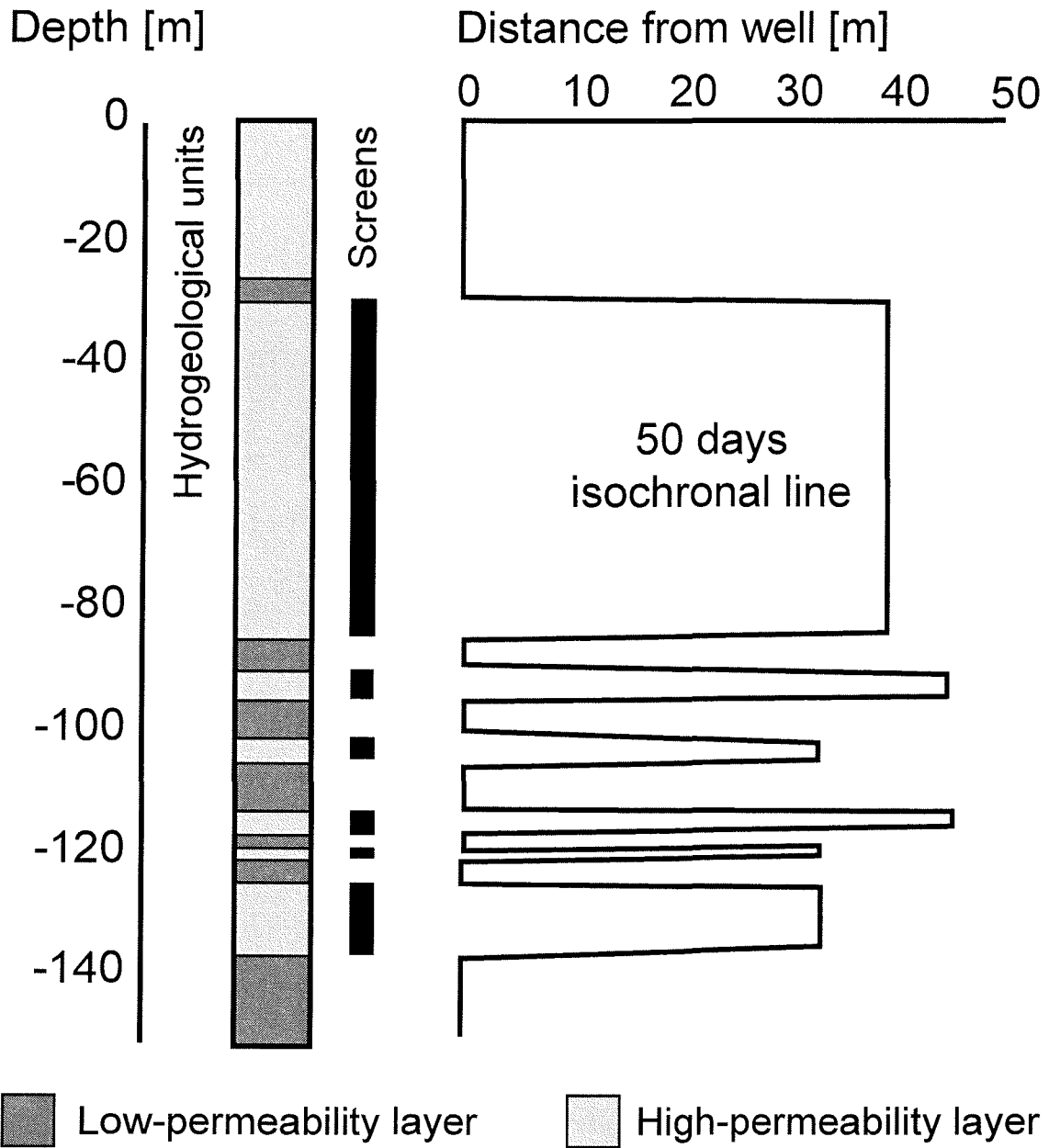


Figure 23.1: The isochronal line illustrates that the time it takes for a particle to reach the well strongly depends on the depth of the point where the particle enters the aquifer system.

CHAPTER 23. DELINEATION OF WELLHEAD PROTECTION ZONES
– A SIMPLIFIED APPROACH

References

- Acton, F. S. (1966), *Analysis of Straight-Line Data*, Dover Publication, New York.
- Appelo, C. A. J., and D. Postma (1996), *Geochemistry, Groundwater and Pollution*, A. A. Balkema, Rotterdam, Brookfield.
- Badon Ghijben, W., and J. Drabbe (1889), Nota in verband met de voorgenomen putboring nabij Amsterdam, *Tijdschrift van het Koninklijk Instituut voor Ingenieurs*, pp. 8–22.
- Bear, J. (1979), *Hydraulics of groundwater*, McGraw-Hill, New York.
- Beckwith, C. W., and A. J. Baird (2001), Effect of biogenic gas bubbles on water flow through poorly decomposed blanket peat, *Water Resources Research*, 37(36), 551–558.
- Bennett, G. D. (1976), Introduction to groundwater hydraulics, in *Techniques of Water-Resources Investigations, Book 3*, chap. B2, U.S. Geological Survey.
- Beyer, W. (1964), Zur Bestimmung der Wasserdurchlässigkeit von Kiesen und Sanden aus der Kornverteilung, *Wassertechnik - Wasserwirtschaft*, 14(6), 165–169.
- Bredehoeft, J. D., and G. F. Pinder (1973), Mass transport in flowing groundwater, *Water Resources Research*, 9(1), 194–210.
- Calvache, M. L., and A. Pulido-Bosch (1997), Effects of geology and human activity on the dynamics of salt-water intrusion in three coastal aquifers in southern Spain, *Environmental Geology*, 30(3/4), 215–223.
- Chen, X. (2000), Measurement of streambed hydraulic conductivity and its anisotropy, *Environmental Geology*, 39(12), 1317–1324.
- Cohen, J. E., C. Small, A. Mellinger, J. Gallup, and J. Sachs (1997), Estimates of coastal populations, *Science*, 278(2), 1211–1212.
- Costanza, R., R. d'Arge, R. de Groot, S. Farber, M. Grasso, B. Hannon, K. Limburg, S. Naeem, R. O'Neill, J. Paruelo, R. G. Raskin, P. Sutton, and M. van den Belt (1997), The value of the world's ecosystem services and natural capital, *Nature*, 387, 253–260.

REFERENCES

- Croucher, A. E., and M. J. O'Sullivan (1995), The Henry problem for saltwater intrusion, *Water Resources Research*, 31(7), 1809–1814.
- Cubasch, U., X. Dai, Y. Ding, D. J. Griggs, B. Hewitson, J. T. Houghton, I. Isaksen, T. Karl, M. McFarland, V. P. Meleshko, J. F. B. Mitchell, M. Noguer, B. S. Nyenzi, M. Oppenheimer, J. E. Penner, S. Pollonais, T. Stocker, and K. E. Trenberth (2001), Technical summary, in *Climate Change 2001: The Scientific Basis. Contribution of Working Group I to the Third Assessment Report of the Intergovernmental Panel on Climate Change*, edited by J. T. Houghton, Y. Ding, D. J. Griggs, M. Noguer, P. J. van der Linden, X. Dai, K. Maskell, and C. A. Johnson, Cambridge University Press, Cambridge, United Kingdom and New York, NY, USA.
- Feseker, T. (2004), *A Saltwater Intrusion Model based on the Method of Characteristics – User's Guide to SWIMMOC*, Universität Bremen, published online at www.geochemie.uni-bremen.de.
- Feseker, T., and J. Seeberg-Elverfeldt (submitted), In-situ measurement of low streambed conductivity.
- Franke, O. L., T. E. Reilly, and G. D. Bennett (1987), Definition of boundary and initial conditions in the analysis of saturated ground-water flow systems - an introduction, in *Techniques of Water-Resources Investigations, Book 3*, chap. B5, U.S. Geological Survey.
- Freeze, R. A., and J. A. Cherry (1979), *Groundwater*, Prentice Hall, Englewood Cliffs, N.J.
- Friedhoff, T. (2001), *Wasserhaushaltsuntersuchungen im tidebeeinflussten Einzugsgebiet der Medem (Land Hadeln)*, Hochschule Bremen, diploma thesis.
- Frind, E. O. (1982), Simulation of long-term transient density-dependent transport in groundwater, *Advances in Water Resources*, 5, 73–88.
- Fulda, C. (2002), Numerische Studien zur Salz-/Süßwasserverteilung im Rahmen der Cuxhavener Forschungsbohrung, *Mitteilungen der Deutschen Geophysikalischen Gesellschaft, Sonderband II*, pp. 10–26.
- Gabriel, G., R. Kirsch, B. Siemon, and H. Wiederhold (2003), Geophysical investigation of buried Pleistocene subglacial valleys in northern Germany, *Journal of Applied Geophysics*, 53(4), 159–180.
- Garder, A. O., D. W. Peaceman, and A. L. Pozzi (1964), Numerical calculation of multidimensional miscible displacement by the method of characteristics, *Society of Petroleum Engineers Journal*, 4(1), 26–36.
- Gerdes, G., B. E. M. Petzelberger, B. M. Scholz-Böttcher, and H. Streif (2003), The record of climatic change in the geological archives of shallow marine, coastal, and adjacent lowland areas of Northern Germany, *Quaternary Science Reviews*, 22(1), 101–124.

- Giesel, W., and G. Schmidt (1978), Grundwasserumsatz zwischen Geest und Marsch, in *Geologisches Jahrbuch*, vol. C 23, pp. 53–62, Schweizerbart, Stuttgart.
- Gonick, L., and W. Smith (1993), *The cartoon guide to statistics*, HaperCollins, New York.
- Goode, D. J. (1990), Particle velocity interpolation in block-centered finite difference groundwater flow models, *Water Resources Research*, 26(5), 26–36.
- Goode, D. J. (1992), Modeling transport in transient ground-water flow: an unacknowledged approximation, *Ground Water*, 30(2), 257–261.
- Goode, D. J., and L. F. Konikow (1991), Testing a method-of-characteristics model of three-dimensional solute transport in ground water, in *Symposium on Ground Water, Proceedings of the International Symposium, Nashville, Tenn., July 29 - August 2, 1991*, edited by G. Lennon, pp. 21–27, American Society of Civil Engineers, New York.
- Guo, W., and C. D. Langevin (2002), User's guide to SEAWAT: A computer program for simulation of three-dimensional variable-density ground-water-flow, in *Techniques of Water-Resources Investigations, Book 6*, chap. A7, U.S. Geological Survey.
- Haertlé, T. (1983), Geologisch-hydrogeologische und hydrochemische Untersuchungen im niedersächsischen Bereich der Unteren Elbe, Ph.D. thesis, Albert-Ludwigs-Universität Freiburg.
- Hantush, M. S., and C. E. Jacob (1955), Non-steady radial flow in an infinite leaky aquifer, *Transactions of the American Geophysical Union*, 36, 95–100.
- Hazen, A. (1893), Some physical properties of sands and gravels, *Annual Report of the Massachusetts State Board of Health*, 24, 541–556.
- Henry, H. R. (1959), Salt intrusion into fresh-water aquifers, *Journal of Geophysical Research*, 64(11), 1911–1919.
- Herzberg, A. (1901), Die Wasserversorgung einiger Nordseebäder, *Journal für Gasbeleuchtung und Wasserversorgung*, 44(44), 815–819.
- Holzbecher, E. (1998), Comments on “Constant-concentration boundary condition: Lessons from the HYDROCOIN variable-density groundwater benchmark problem” by L.F. Konikow, W.E. Sanford, and P.J. Campbell, *Water Resources Research*, 34(10), 2775–2778.
- Huuse, M., and H. Lykke-Andersen (2000), Overdeepened Quaternary valleys in the eastern Danish North Sea: morphology and origin, *Quaternary Science Reviews*, 19(12), 1233–1253.

REFERENCES

- Huyakorn, P. S., P. F. Andersen, J. W. Mercer, and H. O. White, Jr. (1987), Saltwater intrusion in aquifers: Development and testing of a three-dimensional finite element model, *Water Resources Research*, 23(2), 293–312.
- Hvorslev, M. J. (1951), Time lag and soil permeability in ground-water observations, *Bulletin 36*, Waterways Experiment Station, Corps of Engineers, U.S. Army, Vicksburg, Mississippi.
- Izuka, S. K., and S. B. Gingerich (1998), Estimation of the depth to the fresh-water/salt-water interface from vertical head gradients in wells in coastal and inland aquifers, *Hydrogeology Journal*, 6(3), 365–373.
- Kinzelbach, W. (1986), *Groundwater Modeling - An Introduction with Sample Programs in Basic*, Elsevier, Amsterdam, Oxford, New York, Tokio.
- Kinzelbach, W., and R. Rausch (1995), *Grundwassermodellierung*, Gebrüder Borntraeger, Berlin, Stuttgart.
- Kipp, K. L., Jr., L. F. Konikow, and G. Z. Hornberger (1998), An implicit dispersive transport algorithm for the U.S. Geological Survey MOC3D solute-transport model, *Water-Resources Investigations Report 98-4234*, U.S. Geological Survey.
- Konikow, L., D. Goode, and G. Hornberger (1996), A three-dimensional method-of-characteristics solute transport model (MOC3D), *Water-Resources Investigations Report 98-4267*, U.S. Geological Survey.
- Konikow, L. F., and J. D. Bredehoeft (1978), Computer model of two-dimensional solute transport and dispersion in ground water, in *Techniques of Water-Resources Investigations, Book 7*, chap. C2, U.S. Geological Survey.
- Konikow, L. F., W. E. Sanford, and P. J. Campbell (1997), Constant-concentration boundary condition: Lessons from the hydrocoin variable-density groundwater benchmark problem, *Water Resources Research*, 33(10), 2253–2261.
- Kreyszig, E. (1999), *Advanced Engineering Mathematics*, eighth ed., John Wiley and Sons, Inc.
- Kruseman, G. P., and N. A. de Ridder (1994), *Analysis and Evaluation of Pumping Test Data*, second ed., International Institute for Land Reclamation and Improvement, P.O. Box 45, 6700 AA Wageningen, The Netherlands.
- Lambrakis, N., and G. Kallergis (2001), Reaction of subsurface coastal aquifers to climate and land use changes in Greece: modelling of groundwater refreshing patterns under natural recharge conditions, *Journal of Hydrology*, 245(1-4), 19–31.

- Lee, C.-H., and T.-S. Cheng (1974), On seawater encroachment in coastal aquifers, *Water Resources Research*, 10(5), 1039–1043.
- Meinardi, C. R. (1991), The origin of brackish groundwater in the lower parts of The Netherlands, in *Hydrogeology of Salt Water Intrusion – A Selection of SWIM Papers*, edited by W. De Breuck, Heise.
- Oude Essink, G. H. P. (1996), Impact of sea level rise on groundwater flow regimes, Ph.D. thesis, Delft University of Technology, The Netherlands.
- Oude Essink, G. H. P. (2000), Density dependent groundwater at the island of Texel, the Netherlands, in *Proceedings of the 16th Salt Water Intrusion Meeting, June 2000, Miedzyzdroje-Wolin Island, Poland*, pp. 47–54.
- Oude Essink, G. H. P. (2001a), Salt water intrusion in a three-dimensional groundwater system in the Netherlands: A numerical study, *Transport in Porous Media*, 43, 137–158.
- Oude Essink, G. H. P. (2001b), Saltwater intrusion in 3d large-scale aquifers: a Dutch case, *Physics and Chemistry of the Earth, Part B: Hydrology, Oceans and Atmosphere*, 26(4), 337–344.
- Panteleit, B. (2004), Geochemische Prozesse in der Salz-Süßwasser Übergangszone, Ph.D. thesis, Universität Bremen.
- Peaceman, D. W., and H. H. Rachford, Jr. (1955), The numerical solution of parabolic and elliptic differential equations, *Journal of the Society for Industrial and Applied Mathematics*, 3(1), 28–42.
- Pinder, G. F., and J. D. Bredehoeft (1968), Application of the digital computer for aquifer evaluation, *Water Resources Research*, 4(5), 1069–1093.
- Pinder, G. F., and H. H. Cooper, Jr. (1970), A numerical technique for calculating the transient position of the saltwater front, *Water Resources Research*, 6(3), 875–882.
- Pinder, G. F., and A. Shapiro (1979), A new collocation method for the solution of the convection-dominated transport equation, *Water Resources Research*, 15(5), 1177–1182.
- Piotrowski, J. A. (1997), Subglacial hydrology in north-western Germany during the last glaciation: groundwater flow, tunnel valleys, and hydrological cycles, *Quaternary Science Reviews*, 16(2), 169–185.
- Pollock, D. W. (1994), User's guide for MODPATH/MODPATH-PLOT, version 3: A particle tracking post-processing package for MODFLOW, the U. S. Geological Survey finite-difference ground-water flow model, *Open File Report 94-464*, U.S. Geological Survey.
- Prickett, T. A., and G. Lonquist (1971), Selected digital computer techniques for groundwater resource evaluation, *Bulletin 65*, Illinois State Water Survey.

REFERENCES

- Rausch, R., W. Schäfer, and C. Wagner (2002), *Einführung in die Transportmodellierung im Grundwasser*, Gebrüder Borntraeger, Berlin, Stuttgart.
- Reddell, D. L., and D. K. Sunada (1970), Numerical simulation of dispersion in groundwater aquifers, *Hydrology Paper 41*, Colorado State University.
- Repsold, H. (1990), Geoelektrische Untersuchungen zur Bestimmung der Süßwasser-/Salzwassergrenze im Gebiet zwischen Cuxhaven und Stade, in *Geologisches Jahrbuch*, vol. C 56, pp. 3–37, Schweizerbart.
- Sanford, W. E., and L. F. Konikow (1985), A two-constituent solute-transport model for ground water having variable density, *Water-Resources Investigations Report 85-4279*, U.S. Geological Survey.
- Schafer-Perini, A. L., and J. L. Wilson (1991), Efficient and accurate front tracking for two-dimensional groundwater flow models, *Water Resources Research*, 27(7), 1471–1485.
- Scheidegger, A. E. (1961), General theory of dispersion in porous media, *Journal of Geophysical Research*, 66(10), 3273–3278.
- Scheytt, T., and F. Hengelhaupt (2001), Auffüllversuche in der wassergesättigten und ungesättigten Zone - ein Vergleich unterschiedlicher Verfahren, *Grundwasser*, 6(2), 71–80.
- Schönwiese, C. D. (2000), *Praktische Geostatistik*, Gebrüder Borntraeger, Berlin, Stuttgart.
- Segol, G., G. F. Pinder, and W. G. Gray (1975), A Galerkin finite element technique for calculating the transient position of the saltwater front, *Water Resources Research*, 11(2), 343–347.
- Shepard, D. (1968), A two-dimensional interpolation function for irregularly-spaced data, in *Proceedings of the 23rd ACM International Conference*, pp. 517–524, ACM Press.
- Simmons, T. C., T. R. Fenstemaker, and J. M. Sharp, Jr. (2001), Variable-density groundwater flow and solute transport in heterogeneous porous media: approaches, resolutions and future challenges, *Journal of Contaminant Hydrology*, 52(1-4), 245–275.
- Simpson, M. J., and T. P. Clement (2004), Improving the worthiness of the Henry problem as a benchmark for density-dependent groundwater flow models, *Water Resources Research*, 40, W01504, doi:10.1029/2003WR002199.
- Sindowski, K.-H. (1979), *Zwischen Jadebusen und Unterelbe*, *Sammlung geologischer Führer*, vol. 66, Borntraeger, Berlin, Stuttgart.
- Sophocleous, M. (2002), Interactions between groundwater and surface water: the state of the science, *Hydrogeology Journal*, 10(1), 52–67.

- Streif, H. (2004), Sedimentary record of Pleistocene and Holocene marine inundations along the North Sea coast of Lower Saxony, Germany, *Quaternary International*, 112(1), 3–28.
- Suckow, A. (2001), Isotopenhydrologische Multiparameterstudien im Rahmen des Forschungsschwerpunktes Grundwasser: erste Ergebnisse, 68. *Tagung der Arbeitsgemeinschaft Nordwestdeutscher Geologen*, Bremerhaven.
- Thomas, L. H. (1949), Elliptic problems in linear difference equations over a network., *Tech. rep.*, Watson Scientific Computing Laboratory, Columbia University.
- Trescott, G. F., P. C. Pinder, and S. P. Larson (1976), Finite-difference model for aquifer simulation in two dimensions with results of numerical experiments, in *Techniques of Water-Resources Investigations*, Book 7, chap. C1, U.S. Geological Survey.
- Vandenbohede, A., and L. Lebbe (2002), Numerical modelling and hydrochemical characterisation of a fresh-water lens in the belgian coastal plain, *Hydrogeology Journal*, 10, 576–586.
- Voss, C. I. (1987), SUTRA - a finite element simulation for saturated-unsaturated, fluid-density-dependent ground-water flow with energy transport or chemically reactive single-species solute transport, *Water-Resources Investigations Report 84-4369*, U.S. Geological Survey.
- Voss, C. I., and W. R. Souza (1987), Variable density flow and solute transport simulation of regional aquifers containing a narrow freshwater-saltwater transition zone, *Water Resources Research*, 23(10), 1851–1866.
- Woessner, W. W. (2000), Stream and fluvial plain groundwater interactions: rescaling hydrogeologic thought, *Ground Water*, 38(3), 423–429.

Publications of this series:

- No. 1** **Wefer, G., E. Suess and cruise participants**
Bericht über die POLARSTERN-Fahrt ANT IV/2, Rio de Janeiro - Punta Arenas, 6.11. - 1.12.1985.
60 pages, Bremen, 1986.
- No. 2** **Hoffmann, G.**
Holozänstratigraphie und Küstenlinienverlagerung an der andalusischen Mittelmeerküste.
173 pages, Bremen, 1988. (out of print)
- No. 3** **Wefer, G. and cruise participants**
Bericht über die METEOR-Fahrt M 6/6, Libreville - Las Palmas, 18.2. - 23.3.1988.
97 pages, Bremen, 1988.
- No. 4** **Wefer, G., G.F. Lutze, T.J. Müller, O. Pfannkuche, W. Schenke, G. Siedler, W. Zenk**
Kurzbericht über die METEOR-Expedition No. 6, Hamburg - Hamburg, 28.10.1987 - 19.5.1988.
29 pages, Bremen, 1988. (out of print)
- No. 5** **Fischer, G.**
Stabile Kohlenstoff-Isotope in partikulärer organischer Substanz aus dem Südpolarmeer
(Atlantischer Sektor). 161 pages, Bremen, 1989.
- No. 6** **Berger, W.H. and G. Wefer**
Partikelfluß und Kohlenstoffkreislauf im Ozean.
Bericht und Kurzfassungen über den Workshop vom 3.-4. Juli 1989 in Bremen.
57 pages, Bremen, 1989.
- No. 7** **Wefer, G. and cruise participants**
Bericht über die METEOR - Fahrt M 9/4, Dakar - Santa Cruz, 19.2. - 16.3.1989.
103 pages, Bremen, 1989.
- No. 8** **Kölling, M.**
Modellierung geochemischer Prozesse im Sickerwasser und Grundwasser.
135 pages, Bremen, 1990.
- No. 9** **Heinze, P.-M.**
Das Auftriebsgeschehen vor Peru im Spätquartär. 204 pages, Bremen, 1990. (out of print)
- No. 10** **Willems, H., G. Wefer, M. Rinski, B. Donner, H.-J. Bellmann, L. Eißmann, A. Müller,
B.W. Flemming, H.-C. Höfle, J. Merkt, H. Streif, G. Hertweck, H. Kuntze, J. Schwaar,
W. Schäfer, M.-G. Schulz, F. Grube, B. Menke**
Beiträge zur Geologie und Paläontologie Norddeutschlands: Exkursionsführer.
202 pages, Bremen, 1990.
- No. 11** **Wefer, G. and cruise participants**
Bericht über die METEOR-Fahrt M 12/1, Kapstadt - Funchal, 13.3.1990 - 14.4.1990.
66 pages, Bremen, 1990.
- No. 12** **Dahmke, A., H.D. Schulz, A. Kölling, F. Kracht, A. Lücke**
Schwermetallspuren und geochemische Gleichgewichte zwischen Porenlösung und Sediment
im Wesermündungsgebiet. BMFT-Projekt MFU 0562, Abschlußbericht. 121 pages, Bremen, 1991.
- No. 13** **Rostek, F.**
Physikalische Strukturen von Tiefseesedimenten des Südatlantiks und ihre Erfassung in
Echolotregistrierungen. 209 pages, Bremen, 1991.
- No. 14** **Baumann, M.**
Die Ablagerung von Tschernobyl-Radiocäsium in der Norwegischen See und in der Nordsee.
133 pages, Bremen, 1991. (out of print)
- No. 15** **Kölling, A.**
Frühdiagenetische Prozesse und Stoff-Flüsse in marinen und ästuarinen Sedimenten.
140 pages, Bremen, 1991.
- No. 16** **SFB 261 (ed.)**
I. Kolloquium des Sonderforschungsbereichs 261 der Universität Bremen (14.Juni 1991):
Der Südatlantik im Spätquartär: Rekonstruktion von Stoffhaushalt und Stromsystemen.
Kurzfassungen der Vorträge und Poster. 66 pages, Bremen, 1991.
- No. 17** **Pätzold, J. and cruise participants**
Bericht und erste Ergebnisse über die METEOR-Fahrt M 15/2, Rio de Janeiro - Vitoria,
18.1. - 7.2.1991. 46 pages, Bremen, 1993.
- No. 18** **Wefer, G. and cruise participants**
Bericht und erste Ergebnisse über die METEOR-Fahrt M 16/1, Pointe Noire - Recife,
27.3. - 25.4.1991. 120 pages, Bremen, 1991.
- No. 19** **Schulz, H.D. and cruise participants**
Bericht und erste Ergebnisse über die METEOR-Fahrt M 16/2, Recife - Belem, 28.4. - 20.5.1991.
149 pages, Bremen, 1991.